Alma Mater Studiorum – Università di Bologna

DOTTORATO DI RICERCA IN

FISICA SPERIMENTALE DELLA MATERIA

Ciclo XXV

Photoinduced electronic transitions and leakage correlation to defects/dislocations in GaN heterostructures

Presentata da: Saurabh Pandey

Coordinatore Dottorato | **Relatore**

Prof. Fabio Ortolani | **Prof. Anna Cavallini**

Settore Concorsuale di afferenza: 02/B1

Settore Scientifico disciplinare: FIS/03

Esame finale anno 2013

Alma Mater Studiorum – Università di Bologna

Dissertation for the degree of

DOCTOR OF PHILOSOPHY IN PHYSICS

in the

FACOLTÀ DI SCIENZE MATEMATICHE FISICHE E NATURALI

Cycle XXV

Photoinduced electronic transitions and leakage correlation to defects/dislocations in GaN heterostructures

Presented by:

Saurabh Pandey

PhD School Coordinator

Prof. Fabio Ortolani

Supervisor

Prof. Anna Cavallini

Settore Concorsuale di afferenza: 02/B1

Settore Scientifico disciplinare: FIS/03

Final Exam year 2013

Abstract

III-nitride materials are very promising for high speed electronics/optical applications but still suffer in performance due to problems during high quality epitaxial growth, evolution of dislocation and defects, less understanding of fundamental physics of materials/processing of devices etc. This thesis mainly focus on GaN based heterostructures to understand the metal-semiconductor interface properties, 2DE(H)G influence on electrical and optical properties, and deep level states in GaN and InAlN, InGaN materials.

The detailed electrical characterizations have been employed on Schottky diodes at GaN and InAl(Ga)N/GaN heterostructures in order to understand the metal-semiconductor interface related properties in these materials. I have observed the occurrence of Schottky barrier inhomogenity, role of dislocations in terms of leakage and creating electrically active defect states within energy gap of materials. Deep level transient spectroscopy method is employed on GaN, InAlN and InGaN materials and several defect levels have been observed related to majority and minority carriers. In fact, some defects have been found common in characteristics in ternary layers and GaN layer which indicates that those defect levels are from similar origin, most probably due to Ga/N vacancy in GaN/heterostructures. The role of structural defects, roughness has been extensively understood in terms of enhancing the reverse leakage current, suppressing the mobility in InAlN/AlN/GaN based high electron mobility transistor (HEMT) structures which are identified as key issues for GaN technology.

Optical spectroscopy methods have been employed to understand materials quality, sub band and defect related transitions and compared with electrical characterizations. The observation of 2DEG sub band related absorption/emission in optical spectra have been identified and proposed for first time in nitride based polar heterostructures, which is well supported with simulation results. In addition, metal-semiconductor-metal (MSM)-InAl(Ga)N/GaN based photodetector structures have been fabricated and proposed for achieving high efficient optoelectronics devices in future.

Keywords: III-Nitrides, GaN high electron mobility transistors (HEMT), carrier gas, sub bands, dislocations, defects, leakage current, mobility mechanims

This thesis is dedicated to my family and friends

Acknowledgements

It would be very obvious and sincerely required to first acknowledge to my thesis supervisor Prof. Anna Cavallini and to show my deep gratitude to her for giving me opportunity to work with her group. I would be thankful to her for selecting me for European project under Marie Curie fellowship program to do my PhD research work for three years. I still remember her motivation and encouragement to me to start the research in challenging area of nitride semiconductors which was very new area to me. Thanks to her for continuous support and cooperation to allow me to use different facilities within laboratory and encouragement for doing collaborations with different project partners.

I would also like to express my sincere thanks to Prof. Beatrice Fraboni and Dr. Daniela Cavalcoli for being co-supervisor of my thesis. I would be grateful to both of them for their continuous support on operation of different experimental techniques to perform different measurements. I would like to mention the special thanks to them for their continuous guidance/support to discuss scientific results, writing publications for journals and encouragement for developing skills to manage the projects.

I would like to express my gratitude to Antonio Castalldini for his enormous help and training on Deep level transient spectroscopy method and sharing his vast experience with me. I would like to thank my colleague and close friend Albert Minj for his close interactions, sharing his expertise on AFM analysis and helping me, especially to get well settled in Bologna in early days. I would also like to thanks my colleagues Alessandra Sćida, Andrea Ciavatti for their help in Photocurrent measurements.

For the continuous support on processing of GaN heterostructures I would like to thank Tomasso Brazzini and Prof. F. Calle's group members at UPM, Madrid. I would be always thankful to Tomasso fo giving his valuable time on my samples and sharing his knowledge with me during my visit at UPM, Madrid. I would like to thank Dr. Pierre Ruterana and his team at CIMAP, Caen to give me the opportunity to visit his and related groups and to perform TEM, Low frequency noise spectroscopy measurements. I would like to express special thanks to AIXTRON AG, Aachen and Alcatel, Thales teams for continuously providing the samples for characterizations. I also would like to thanks other RAINBOW partners for their invaluable discussions, knowledge sharing during various internal meetings, conferences and workshops etc.

I would like to thank European commission for funding RAINBOW-ITN project on “High quality material and intrinsic properties of InN and Indium rich nitride alloys” which was my source of funding for my PhD work. This work was supported by the EU under project no. PITN-GA-2008-213238 (RAINBOW)

I would feel delight to acknowledge to ‘Residenza Studi Superiori, Institute of Advanced Studies’, Bologna for its residential fellowship program which gave me opportunity to live in enriched multi-national environment and culture. It has certainly advanced and developed my skills and knowledge in other areas of studies apart from my own research field which will be surely helpful to me in my career.

I would be happy to acknowledge my friends and group members at Dept. of Physics Lucia Amidani, Alberto, Stefania, Martina, and others for their cooperation and help during my stay there.

I would like to take opportunity to show my special thanks and gratitude to my close friends Eze(quiel) Poodts, Ceren, Dani(elle), Cami(la), Asti, Joanna, Albert, Dhruv Kumar, Priyank, Shalini and others for always being with me and helping me. Thanks to you all for making my stay at Bologna as a special journey in my life.

Finally and most importantly, I would like to thank my parents and brothers who have always valued and encouraged me on my knowledge and education in my life.

List of Publications

Published:

1. D. Cavalcoli, **S. Pandey**, B. Fraboni, A. Cavallini, “Band gap shift in Al1-xInxN/AlN/GaN heterostructures studied by Surface Photovoltage Spectroscopy”, ***App. Phys. Lett.*** 98, 142111 (2011), also appear in “*Virtual Journal of Nanoscale Science & Technology*”, 23 (16) (April 25, 2011)
2. **S. Pandey**, B. Fraboni, D. Cavalcoli, A. Minj, A. Cavallini, “Two dimensional electron gas properties by current-voltage analysis of Al0.86In0.14N/AlN/GaN heterostructures”, ***App. Phys. Lett.*** 99, 012111 (2011)
3. **S. Pandey**, D. Cavalcoli, B. Fraboni, A. Cavallini, “Surface Photovoltage Spectroscopy characterization of Al0.86In0.14N/AlN/GaN heterostructures”, ***phys. stat. solidi (c)** 9, 693* (2012)
4. A. Minj, D. Cavalcoli, **S. Pandey**, B. Fraboni, A. Cavallini, T. Brazzini, F. Calle, “Nano-cracks induced high leakage in InAlN/AlN/GaN heterostructures”, ***Scri. Materialia*** 66, 327 (2012)
5. **S. Pandey**, B. Fraboni, D. Cavalcoli, A. Minj, A. Cavallini, “Current-voltage measurements of Al0.86In0.14N/AlN/GaN heterostructures”, ***phys. stat. solidi (c)*** 9, 986 (2012)
6. **S. Pandey**, D. Cavalcoli, A. Minj, B. Fraboni, A. Cavallini, “Mobility limiting mechanisms in polar semiconductor heterostructures”, ***Acta Materialia*** 60, 3176 (2012)
7. **S. Pandey**, D. Cavalcoli, B. Fraboni, A. Cavallini, T. Brazzini, F. Calle, “Role of surface trap states on two- dimensional electron gas density in InAlN/AlN/GaN heterostructures”, ***Appl. Phys. Lett.***, 100, 152116 (2012)
8. **S. Pandey**, D. Cavalcoli, B. Fraboni, Cavallini, P. Gamarra, M. A. Poisson, "Electronic transitions and Fermi edge singularity in polar heterostructures studied by absorption and emission spectroscopy”, ***J. Appl. Phys.***112, 123721 (2012)
9. T. Brazzini, **S. Pandey**, M. F. Romerro, P. Bokov, M. Feneberg, G. Tabares, A. Cavallini, R.Goldhahn, F. Calle, ***JJAP:IWN2012 proceeding (accepted, in press)*** (2012)

Submitted/under review :

1. T. Brazzini, M. J. Tadjer, Z. Gačević, **S. Pandey**, A. Cavallini, F. Calle, *under review, **Solid state electronics*** (2012)

Acronyms

2DE(H)G	2 dimensional electron (hole) gas
ACF	Autocorrelation function
AFM	Atomic force microscopy
BB	Blue band
BE	Bound exciton
BM	Moss-Burstein effect
BTE	Boltzmann transport equation
CV	Capacitance-voltage
CB(O)	Conduction band (offset)
DFT	Density functional theory
DLTS	Deep level transient spectroscopy
ECV	Electrochemical capacitance-voltage
EL	Electroluminescence
EQE	External quantum efficiency
FE	Free exciton
FES	Fermi edge singularity
FPE	Poole-Frenkel Emission
FWHM	Full width at half maximum
HEMT	High electron mobility transistor
HHCF	Height-height correlation fucntion
HWHM	Half width at half maximum
IV	Current-voltage
LD	Laser diode
LDA	Local density approximation
LED	Light emitting diode
LM	Lattice-matched
LT	Low temperature
MBE	Molecular beam epitaxy
MD	Misfit dislocations
MFP	Mean free path
ML	Monolayer
MFS	Minimum feature size
MOCVD	Metal organic chemical vapor deposition
MOVPE	Metal organic vapor phase epitaxy
MS	Metal-semiconductor
PC	Photocurrent spectroscopy
PL	Photoluminescence
QTH	Quartz-Tungeston-halogen
QW	Quantum well
RB	Red band
RBS	Rutherford backscattering
RMS	Root mean square
RSR	Remote surface roughness

RT	Room temperature
SBH	Schottky barrier height
SPV(S)	Surface photo voltage (spectroscopy)
SEM	Scanning electron microscopy
STM	Scanning Tunneling microscopy
TD(D)	Threading dislocation (density)
TE	Thermionic emission
TEM	Transmission electron microscopy
TFE	Thermionic field emission
UHV	Ultra high vaccum
Xe	Xenon
XRD	X-ray diffraction
YB(L)	Yellow band (luminescence)

Content

Abstract i
Dedication ii
Acknowledgment iii
List of Publications v
Acronyms vi
Table of Contents viii
List of tables xii
List of figures xiii

Chapters:

1. Introduction

1.1 Introduction to III-Nitride semiconductors ……………………………………….………..1
1.2 Objective of the thesis …………………………………………………………....……..3
References ……………………………………………………………………….....…..4

2. Background on III-V nitride materials properties

2.1 Crystal structure properties ………………………………………………………........6
2.1.1 Crystalline structure and symmetry …………………………………………….......6
2.1.2 Crystal polarity ………………………………………………………………….......9
2.1.3 Spontaneous and piezoelectric polarization ……………………………………….....10
2.1.4 Polarization in heterostructure and 2-Dimensional electron/hole gas ……………......16
2.1.5 High power high frequency HEMT’s on In(Al)GaN/GaN ………………………......19
2.1.6 Band structure of III-nitrides ……………………………………………………........21
2.2. Defects in semiconductors ……………………………………………………….......25
2.2.1 Type of defects ………………………………………………………………….......26
2.2.2 Thermodynamics of defects ……………………………………………………........28
2.2.3 Defects and HEMTs key problems ……………………………………………........29
References ……………………………………………………………………….......32

3. Experimental techniques

3.1 Current-Voltage (I-V) characterization ……………………………………………......35
3.1.1 Schottky contacts ………………………………………………………………..........35
3.1.2 Current transport mechanism in Schottky diodes …………………………………......37
3.1.3 Experimental setup ……………………………………………………………………....40
3.2. Capacitance-Voltage (C-V) characterization …………………………………………….41
3.2.1 Series resistance and equivalent circuit of the Schottky diode in C-V Measurements ……………………………………………………………..........42
3.2.2 Experimental setup ……………………………………………………………….......43
3.3 Thermal spectroscopy …………………………………………………………………......44
3.3.1 Physics of carrier emission and capture ………………………………………......44
3.3.2 Deep level transient spectroscopy (DLTS) ……………………………..…......49
3.3.3 Capture kinetics via DLTS …………………………………………………..…....52
3.3.4 Experimental setup ………………………………………………………………........55
3.4 Surface photovoltage spectroscopy ……………………………………………………......57
3.4.1 Surface electrical properties of semiconductor ………………………………….…....57
3.4.2 Surface Photovoltage (SPV) effect ……………………………………………….......58
3.4.3 SPV effect on buried interfaces ………………………………………………….......59
3.4.4 SPV experimental measurements ……………………………………………..........61
3.4.4.1 Kelvin probe method ……………………………………………………..........61
3.4.4.2 The metal-insulator-semiconductor structure ……………………………..........62
3.4.4.3 SPS set-up ………………………………………………………………….......62
3.4.5 Applications of SPS ……………………………………………………………......63
3.5 Photocurrent Spectroscopy ……………………………………………………………......64
3.5.1 Basic principles ………………………………………………………………….......65
3.5.2 Experimental tools/setup for photocurrent spectroscopy ………………….……......66
3.5.3 Applications in GaN and heterostructures/quantum wells ………………………......68
References …………………………………………………………………………………......69

Results and Discussions

4. Characterization of GaN layer

4.1 Sample details and growth information …………………………………...……..…..71
4.2 Current - voltage (I-V) characterization ……………………………………...….……..72

4.3 Capacitance -voltage (C-V) characterization ……………………………………..……..76
4.4. Deep level transient spectroscopy (DLTS) analysis …………………………..……....80
4.5 Surface photovoltage, photocurrent and photoluminescence analysis …………..….....82
References ……………………………………………………………………………..….87

5. Characterization of InAlN/AlN/GaN based heterostructures for high electron mobility transistors

5.1 Sample and growth details ………………………………………………………..……....89
5.2 Surface morphology analysis by atomic force microscopy analysis (AFM) …...……...91
5.3 Band diagram Simulation ……………………………………………………..…......92
5.4 Current-Voltage (I-V) characteristics and analysis ……………………………………93
5.4.1 'In-Ga alloy' Schottky-Schottky configuration Current-voltage measurements and 2DEG properties analysis …………………………..………………………..…93
5.4.2 (Ni/Au) Schottky junction behaviour ……………………………………………....97
5.4.2.1 Leakage and poole-frenkel emission analysis ………………………………......98
5.4.2.2 Role of the surface trap states in the formation of 2DEG …………………......101
5.4.2.3 Barrier inhomogeneity at (Ni/Au)-InAlN/AlN/GaN interface ……………......103
5.4.3 Mobility limiting mechanisms in polar nitride semiconductor heterostructures..... 105
5.5. Capacitance-Voltage (C-V) analysis …………………………………………………111
5.6. Deep level transient spectroscopy (DLTS) analysis ……………………………........113
5.6.1 Sample without 'AlN' interlayer ……………………………………………....…114
5.6.2 Sample with 'AlN' interlayer ……………………………………………….......116
5.7 Optical characterization with SPV, PC and PL …………………………………......121
5.7.1 Band gap shift in $Al_{1-x}In_xN$/AlN/GaN heterostructures studied by surface photovoltage spectroscopy ……………………………………………………......121
5.7.2 Subband energy levels and fermi edge singularity in InAlN/AlN/GaN heterostructures …………………………………………………………........125
5.7.3 Photoresponse analysis of metal-semiconductor-metal (MSM) InAlN/AlN/GaN HEMT structures …………………………………………………………......131
References ……………………………………………………………………….......136

6. Characterization of InGaN/GaN heterostructures

6.1 Sample and growth details …………………………………………………………….139
6.2 Band diagram simulation of $In_{0.19}Ga0_{.81}N$/GaN ……………………………….......140

6.3 Electrical characterization of deep levels in $In_{0.19}Ga0_{.81}N/GaN$ structure ……...…....140
6.4 Surface photovoltage spectroscopy on undoped and doped $In_xGa_{1-x}N/GaN$ heterostructure with varying Indium content …………….…………………….......145
6.5 Mesa-InGaN/GaN based photodetector structure ……………………………….....150
References …………………………………………………………………….......154

Conclusions …………………………………………..…………………………….....155

List of Tables

2.I Lattice parameters of bulk InN, GaN and AlN …………………………………………………7

2.II Experimental and theoretical stiffness constants of InN, GaN and AlN in GPa ……….......14

2.III Spontaneous and piezoelectric coefficients of various semiconductors ……………….…16

2.IV Band parameters of InN, GaN and AlN ……………………………………….…...……….23

2.V Effectives masses for electrons (m_e*/m_0), heavy ($m_{hh}*/m_0$) and light ($m_{lh}*/m_0$) hole parallel (∥) and perpendicular (⊥) to the polar [0001] axis in isotropic approximation around the point ……………………………………..……….……………….…………...24

2.VI GaN/AlN valence band offset (VBO) and conduction band offset (CBO) ……….……......25

2.VII InN/GaN band offsets ……………………………………………………….………..…....25

2.VIII InN/AlN band offsets ……………………………………………………….……….…..…25

4.I Summary of defect levels observed by DLTS, SPV, PC and PL ………….……………..…87

5.I Sample details of InAlN/AlN/GaN structures …………………………….………….…....90

5.II Parameters of deep levels in sample 1 ……………………………...………………..…116

5.III Sample details: nominal thickness of InAlN layer and %In, nominal thickness of AlN interlayer, experimentally measured 2DEG density by Hall Effect technique. It also shows the observed subband energy related to 2DEG well values from GaN valence band edge measured by SPV, PC and FES position by PL 126

5.IV Time constant for the raising of the signal for the two bias voltage used and the two photon excitation energies 135

6.I Summary of deep levels in $In_{0.19}Ga_{0.81}N$ detected by DLTS ……………..………….…....144

List of Figures

1.1 Band gap variation with lattice constant for various compound semiconductors ………...…...1

1.2 The expected GaN devices global market size in next years ………………………..………....2

1.3 Increasing market of GaN based optoelectronics market (predicated) ……………………..…....2

2.1 Wurtzite (a) and Zinc-blende (b) structures of GaN. The red and blue spheres indicate Ga and N atoms, respectively 6

2.2a Hexagonal structure with representations for the base vectors a_1, a_2 , a_3 and the lattice parameters a and c 8

2.2b The dark (red and green) shadow areas show the m-plane and a-plane, respectively, while grey shadow area shows c-plane 8

2.3. Atoms bonded in tetrahedron for (a) zinc-blende and (b) wurtzite arrangements. Interchangeable on rotation along [111] and [0001] directions for cubic and wurtzite Respectively 9

2.4. Stacking sequence for (a) (0001) planes in wurtzite ([11-20] azimuth), and (b) (111) planes in zinc-blende ([1-10] azimuth) 9

2.5 Ball and stick model of wurtzite showing polarity in GaN: (a) Ga-polar along [0001], N- polar for [000-1] (b) 10

2.6 Spontaneous polarization at AlN/GaN interfaces in a heterostructure with Ga-polarity, i.e., the c-direction bonds point from Ga to N sites. The surface also represents the Ga layer 11

2.7 Microscopic picture of spontaneous polarization in a freestanding GaN slab ……...………11

2.8 Predicted spontaneous polarization for random, ternary alloys with wurtzite crystal structure. The dependence of P_{SP} on x can be approximated with high accuracy by quadratic equations (2.3). The nonlinearity can be described by positive bowing parameters increasing from AlGaN to InGaN and AlInN 12

2.9 Bound surface density of wurtzite GaN, InN and AlN crystals caused by a gradient in piezoelectric and spontaneous polarization at the surfaces in dependence of biaxial strain applied in the basal plane (a). (b) Bound interface density of pseudomorphic AlGaN/GaN, InGaN/GaN and AlInN/GaN heterostructures grown on relaxed GaN buffer layers with Ga-face polarity. Positive (negative) polarization-induced interface charges are screened by electrons (holes) in n-type (p-type) samples, causing the formation of two-dimensional carrier gases 18

2.10 Polarization directions and sheet carrier density in GaN and AlN for different conditions of strain in: (a) unstrained GaN or AlN or InN (b) tensile strained AlN grown on relaxed GaN buffer (c) Compressive strained GaN on relaxed AlN buffer, (d) Compressive strained InN on relaxed GaN buffer 18

2.11 Schematic description of the potential profile at nitride heterojunctions …………………...…19

2.12 Calculated band structure of GaN (left) AlN (right) ……………………………………...…21

2.13 Schematic representation of the valence band splitting in wurtzite GaN 22

2.14 Valence band structure of (a) GaN (b) AlN, indicating the anisotropy 24

2.15 Presence of shallow and deep levels in GaN semiconductor ……………………………..…27

2.16 Representation of Edge and Screw dislocation with respect to burger vector ……………......28

2.17 Representation of stacking faults for GaN/sapphire ……………………………………......28

2.18 Variation of leakage current of heterojunction bipolar transistors (HBT) on lateral epitaxial overgrowth (LEO) window and wing regions. The leakage is reduced for the wing region by four orders of magnitude as compared to the window region ………………………..…....30

2.19 Experimental drain-current versus time waveform in response to a constant drain voltage of 10 V and gate-source voltage stepped from (a) -7 to 0 V and (b) -12 to -4 V. The HEMT was in series with a 50 - resistor attached to the drain terminal. This HEMT exhibits varying degrees of gate-induced lag due to trapped charge ……………………..………....31

2.20 Possible mechanisms contributing to HEMT degradation and failure are represented ……....31

3.1 Unbiased band structure of a metal/n-type semiconductor contact ………………………….....36

3.2 Block diagram for the I-V characterization ……………………………………....……40

3.3 Equivalent circuit for Schottky diode ……………………………………………....…..42

3.4 Block diagram for capacitance-voltage characterization ……………………………..……..43

3.5 The processes possible for a deep level involving transitions to or from a band are (a) electron capture and (b) electron emission to conduction band and (c) hole capture and (d) hole emission to the valence band 45

3.6 Effect of a forward bias pulse with V'>0 applied on a reversely biased junction in presence of a majority carrier trap 48

3.7 Effect of a forward bias pulse with V'>0 applied on a reversely biased junction in presence of a minority carrier trap …………………………………………………………...………..49

3.8 Schematic illustration of the effect of capture and emission of electrons from an electron trap. (a) The sample is biased in the fill pulse regime to allow ET to fill with electrons. The fill pulse bias is always greater than the measurement bias to allow traps to fill. The bottom part of the figure shows the bias scheme as a function of time while the other graph shows the resulting capacitance. (b) At the start of the measurement, the levels are completely filled resulting in a lower charge density in the depletion region. This dictates the depletion depth and capacitance. (c) As the traps emit, the charge density increases due to the uncovered fixed charge of the traps. In this case, the depletion region shrinks as the same total charge can be uncovered in a smaller volume, and the capacitance increases. This is the standard intuitive process for a deep level exposed to a voltage change …………………………......50

3.9 Discharge capacitance transients at different temperatures, with the rate window t_1-t_2 in

evidence (a), associated DLTS signal (b) ……………………………………………………........52

3.10 Before capture (top), the defect is uncharged and has no Coulombic barrier associated with it. After capture begins (bottom), a time dependent barrier forms reducing the capture rate of the next electron. In order for the effect to be observed, neighboring defects have to be close enough to be influenced by the resultant Coulombic potential ……………….……......53

3.11 Simulated DLTS spectra of interacting levels for a bandlike energy distribution [30] (a). Measured minority carrier bandlike distribution of states in $Si_{0.7}Ge_{0.3}/Si$ [32] (b). The simulation uses a broader distribution of states, which causes the larger distortion of the DLTS curve at larger fill pulse times. The features of the bandlike distribution are the decrease in peak temperature and increase in peak height at longer fill pulse times and the high temperature side of the curves typically nearly overlap 54

3.12 Block diagram of the instrumentation for the DLTS measurements, evidencing the correlator and the double boxcar average 56

3.13 Schematic band diagram of semiconductor surface SCR at equilibrium 58

3.14 Schematic band diagrams of the semiconductor depleted n-type surface space-region under different illumination conditions 59

3.15 Schematic band diagrams of thin film structure in the dark (solid curve) and under illumination (dashed curve), where the interface SCR (a) is the dominated contribution and the surface SCR (b) to the SPV effect ………………………………………………………..60

3.16 Parallel plate capacitor band diagram formed from two different metals with the two plates isolated (a), short-circuited (b) and connected through a d.c. bias equal and opposite to the contact potential difference (c) ………………………………………………………………61

3.17 Block diagram of SPS set-up …………………………………………………………………63

3.18 SPV spectra showing the GaN band gap and YL related transition 64

3.19 Band-to- band and intraband transitions induced by photons ……………………..……......64

3.20 Light wavelength dependence of the absorption coefficient α and of the photoconductivity σ in the regions above (I), near (II) and below (III) bandgap 66

3.21 Block diagram of Photocurrent setup 67

3.22 Showing Deep levels in GaN layers 68

3.23 Showing presence of 2DEG related absorption in AlGaN/GaN based HEMTs 68

4.1 Schematic of GaN layer on sapphire with Schottky (filled dot) and Ohmic contacts (empty dots) 71

4.2 Forward and reverse bias characteristics of Pt-GaN at different tempearatures 72

4.3a Apparent Schottky barrier height and ideality factor variation versus tempearature …...……73

4.3b Apparent Schottky barrier height variation with temperature ……………………………......73

4.4 Variation of Schottky barrier height with ideality factor. The linear extrapolation for n = 1 gives the ideal barrier height for Pt-GaN 74

4.5 Conventional Richardson plot for the measurement of barrier height and Richardson constant ……………………………………………………………………75

4.6 Conventional Richardson's plot for calculation of barrier height and Richardson constant 76

4.7 Variation of saturation current and tunneling parameter with temperature varitaion with TFE Model ……………………………………………………………………………...77

4.8 Variation ln(J/Es) with electric field for 218 K- 318 K …………………………...…...78

4.9 Variation of R(T) and S(T) with 1000/T to calculate high frequency constant for GaN (a) and trap barrier height (b) ……………………………………………………………...…....78

4.10 C-V characteristics of Pt-GaN at 300 K (a) diagram of 1/C2 vs V (b) ……………….…..79

4.11 Carrier concentration profile with depth (a) and reverse bias (b) …………………...…..80

4.12 DLTS spectra for Pt-GaN (left axes), and ΔC vs. temperature (right axes) ………………....81

4.13 Arrhenius plot of GaN sample. Activation energy and capture cross section of the levels detected are reported ……………………………………………………………...…..82

4.14a SPV spectra of GaN layer recorded by using QTH and Xe lamps ……………………..…....83

4.14b SPV, PC spectra at 300 K and PL spectra at 300 K and 5 K ……………………...…....84

4.15 SPV, PC spectra at 300 K and PL spectra at 5 K ……………………………………..…....85

4.16 Emission mechanism of Yellow Band in GaN ……………………...…………………..…....86

5.1a Schematic of InAlN/AlN/GaN heterostructure for electrical measurements, Ohmic contacts have been deposited by Ti/Al/Ni/Au (shown as Ω, squares in orange color) and Schottky dots of Ni/Au or Pt (circle in red color) 90

5.1b Effect of annealing on Ohmic contact behavior for sample 3, shows the achieved Ohmicity at high temperature annealing in comparison to unannelaed condition 91

5.2 Surface morphology analyses of samples with variation in AlN interlayer 91

5.3 Conduction band profiles of InAlN/AlN/GaN heterostructure with varying AlN layer thickness (a), and Carrier concentration variation with AlN layer thickness variation in heterostructures (b) 92

5.4a Current vs. Voltage plot showing difference between change of slope as 2DEG conduction in samples with 1 nm AlN (blue) and 7.5 nm AlN thickness (red). It also shows the depletion of reverse-biased Schottky with increasing bias (inset) …………………………......94

5.4b V_{2DEG} as a function of the AlN interlayer thickness ……………………………………….....94

5.5 2DEG concentration as a function of the AlN interlayer thickness. Our data are obtained from I-V curves (solid squares) and Hall measurements (open squares) and they are compared with results form the literature, obtained with C-V (solid triangles) and Hall measurements (circles), on similar samples. The last point (7.5 nm) of our I-V curve has

been extrapolated (see text). The lines are plotted only for eye-guidance(a). 2DEG Hall mobility (left axis) and sheet resistance (right axis) variation with AlN interlayer thickness (b) 96

5.6a Variation of reverse bias leakage current with different AlN interlayer thickness. Variation of Dislocation density (V-Pit) is also shown in the inset 98

5.6b Measured reverse-bias current divided by electric field vs square root of electric field for Schottky contact on the $Al_{0.86}In_{0.14}N$/AlN/GaN heterostructure (semi-log scale) 99

5.7 Temperature dependent I-V and ln(J/Es) vs. Es plot to show the Pool-Frenkel emission in samples 1, 3 and 6 (lines are used only for eye guide lines) 100

5.8 R(T) vs. 1/T allows calculating high frequency relative dielectric constant (a) and S(T) vs. 1/T allows calculating the emission barrier height of trap (b) 100

5.9a Variation of Schottky barrier height (in red solid squares, left axis) and 2DEG density (in blue open squares, right axis) on AlN layer thickness variation. The lines are a guide to the eye 101

5.9b Measured 2DEG density variation with barrier height (red solid circles) and linear fitting (straight line) 102

5.10 The variation in 2DEG density (dashed line for 15 nm and dotted line for 30 nm) ……........103

5.11 Apparent Schottky barrier height and ideality factor variation with tempearature (a). Variation of Schottky barrier height with ideality factoe. The linear extrapolation for n = 1 gives the ideal barrier hright for (Ni/Au)-InAlN/AlN/GaN (b) 104

5.12 Surface roughness (open squares) V-pit density (solid squares) (top layer) and Hall mobility at 300 K (solid triangle) and 77 K (solid dots), and also 2DEG density at 300 K (in dash line) and 77 K (dot line), (bottom layer) plotted as a function of AlN layer thickness. The sketch of $In_xAl_{1-x}N$/AlN/GaN heterostructure is also shown in the inset 107

5.13 Band diagram, calculated from Schrodinger-Pöisson solver, showing the fluctuation in different subband energy wave functions at heterointerface for different AlN interlayer thickness ……………………………………………………………………………...…...108

5.14 Typical topography maps of In_xAlN_{1-x}/AlN/GaN heterostructure with AlN layer thickness of 2 nm obtained by AFM (a) and STM (b). The fitting of the one-dimensional height-height correlation function H is also shown in the inset of Fig (a) for the AFM line profile, of Fig (b) for the STM line profile ………………………………………………………......109

5.15 Remote surface scattering mobility calculated vs surface roughness for different correlation length values (a). Experimental Hall mobility at 77 K (black triangle), calculated mobility limited by surface roughness scattering (solid squares), dislocation scattering (solid circles) and total calculated mobility (solid circle) plotted as a function of surface roughness(b) ……………………………………………………………………………....110

5.16 C-V characterisctics of different sampels with Ni/Au (a) and Pt (b) Schottky diodes, showing $1/C^2$ vs V plot to calculate Schottky barrier height ……………………………....112

5.17 The calculated Carrier concentration (N_d) from C-V measurements with Ni/Au (a) and Pt (b) Schottky diodes ……………………………………………………………………….....113

5.18 The comparison of calculated 2DEG density from conventional Hall Effect measurements (red circles), C-V measurements (black squares) and I-V model (blue triangles) 113

5.19 DLTS spectra for sample 1 for different emission rates at different bias and pulses …….114

5.20 Arrhenius plot reporting the signatures of the deep levels (majority carriers) detected in sample1 ………………………………………………………………………………......115

5.21 Schematic diagram of traps level position and dislocation related energy levels in InAlN barrier layer ……………………………………………………………………………....115

5.22 C-DLTS spectra for sample 3 for different bias conditions shown as (a) and (b) for a constant filling pulse duration ……………………………………………………….....117

5.23 Arrhenius Plot reporting the signatures of the deep levels (majority carriers) detected in sample 3 ………………………………………………………………………………......117

5. 24 C-DLTS spectra for sample 6 for constant filling pulse duration, showing the presence of deep levels (majority and minority carriers) ……………………………………………......119

5.25 C-DLTS spectra for sample 6 in low (a) and high temperature (b) regime for constant filling pulse duration ……………………………………………………………………….....119

5. 26 Arrhenius Plot reporting the signatures of the deep levels (majority and minority carriers) detected in sample 6 ……………………………………………………………….......120

5.27 Deep level positions in sample 3 and 6 ……………………………………………....…...120

5.28 SPV (a.u.) spectra, normalized to the maximum values, measured in the AlInN/AlN/GaN heterostructures (a) and in the GaN template (b). In Figure 5.28 (a) the spectra have been shifted with increasing AlN layer thickness for clarity ……………..…..122

5.29 Transmission coefficient T (λ) of GaN template (red, short dashed dot) and of AlInN/AlN (1 nm)/ GaN heterostructure (black, solid line), and SPV (λ) of AlInN/AlN (1 nm)/ GaN (blue, dashed line) ……………………………………………………………………......122

5.30 2DEG density vs interlayer AlN thickness measured by Hall Effect at 300 K ………...…...123

5.31 Experimental values (red filled squares) and fitted curve (red solid line) of the band gap shift ΔE_G as a function of free carrier concentration n_e. Calculated values of the electron effective mass are plotted in the inset as a function of free carrier concentration n_e ……....125

5.32 Schematic of the band structure for InAlN/AlN/GaN heterostructures calculated at 300 K (for SPV) and 5 K (for PL) from Schrodinger-Pöisson equation to show the possible photoexcited electronic transitions (marked as 1, 2, 3) 127

5.33 Surface Photovoltage signal plotted against photon energy for all samples. The lines are only a guide for the eyes 128

5.34 Y signal and SPV signal variation measurements for sample 1 which shows n-type of conductivity for 2DEG channel layer in within GaN layer 129

5.35 Typical measured Photocurrent spectra plotted against photon energy for sample 1, mentioned in table II 129

5.36 normalized PL spectra for all three samples at 5 K showing above GaN energy gap related transitions (a). The normalized PL spectra for sample 1 (b). The inset shows the GaN edge related transition for both samples (b) 130

5.37 Schematic of MSM structure (a) and top view (b) …………………………………..…...132

5.38 Leakage current measured for Pt-MSM on both samples ……………………………..…....133

5.39 ER measurements of the two samples analysed. The measurements were performed with a bias voltage (8 V sample A and 10 V sample B) with a superposition of a modulating voltage of 1 V ……………………………………………………………………….…....133

5.40 Responsivity versus applied voltage for the two samples ……………………………...…...134

5.41 Transient behaviour of sample 1&2 analysed for two different excitation energies and two bias voltages. low (1 V) and high (2/5 V) ……………………………………………......135

6.1 Schematic of InGaN/GaN heterostructure for electrical measurements, Ohmic contacts are shown as Ω, (squares in orange color) and Schottky dot of Pt (circle in red color) …..…....139

6.2 Simulated band diagram for InGaN/GaN structure showing the hole accumulation (2DHG) at interface ………………………………………………………….…..………....……140

6.3a Current-voltage spectra for Pt-(InGaN/GaN) at 300 K …………………………………......141

6.3b Capacitance-voltage spectra for Pt-(InGaN/GaN) at 300 K. The inset shows the calculation for barrier height from C^{-2} vs V plot ………………………………………………...…...141

6.4 Calculated carrier concentration profiling of InGaN/GaN structure at 300 K ………....…..142

6.5 C-DLTS spectra for InGaN/GaN structure for constant filling pulse duration ………....…143

6.6 Simulated band diagram for InGaN/GaN at 0 and 2 V (in reverse bias) …………….…....143

6.7 Arrhenius Plot reporting the signatures of the deep levels (majority carriers) and minority carriers detected in InGaN/GaN structure ……………………………………………...…144

6.8 SPV spectra of some samples (a) Calculation of bowing parameter for $In_xGa_{1-x}N$ layers (%In up to 22) with experimental results (solid squares), calculated results (solid circles) and comparison with earlier reported results (solid triangle, open circles) in references. The line shows the fit for linear region (up to 20% In) (b) 146

6.9a Normalized SPV spectra with photonflux showing against photon energy for all samples. GaN, InGaN band to band and Si donor related transitions are indicated in the spectra …....147

6.9b Comparison of the Surface Photovoltage (SPV) spectra of Si doped and undoped structures for 14% and 19% In in InGaN barrier layer …………………………………………......148

6.10 1-D Schrodinger-Pöisson simulation shows conduction and valence band profile of InGaN/GaN undoped structures (a) and Si-doped structures (b). The straight line (short dashed) drawn at 0 is just to show Fermi level of heterostructure for eye guide line 149

6.11 Variation of deep donor levels (solid triangle) in conduction band of InGaN with %In is shown and variation of doping density (solid circle) is also shown in inset 150

6.12a Optical microscope image of mesa structure of InGaN/GaN based photodetector structure. ‘Pt’ metal Schottky-InGaN, is shown in gold color while black shades show the Ti/Al/Ni/Au metal stack on GaN, as Ohmic contacts 151

6.12b The Current-voltage characteristics of device at InGaN-GaN heterojunction 151

6.13a Photocurrent spectra for Pt-InGaN surface (solid) and InGaN-GaN heterojunction (dashed) without any bias 152

6.13b The EQE for device at Pt-InGaN surface (solid) and InGaN-GaN heterojunction (dashed), showing high efficiency at interface of InGaN-GaN 153

6.14 PC spectra of Pt-InGaN surface and InGaN-GaN heterojunction at -5 V 153

Chapter 1

Introduction

1.1 Introduction to III-Nitride semiconductors

Compound semiconductor research has played a major role in technological improvement in last decades and put the world at a new front. Recent progress in semiconductor research show the capability of III-nitride based semiconductor research as most promising for optoelectronics devices application and possibly as well as for high speed/mobile transistors development etc. In 1992, Nakamura [1] successfully realized the p-type doping for GaN and this invention can be considered as a key date for applications in optoelectronic devices. Since then, light emitting diodes (LEDs) and laser diodes (LDs) have become possible in a spectral range which could not be achieved using conventional semiconductors like Si, (Al)GaAs or AlInGaP. In particular, the blue and white LEDs have shown non-comparable advantages ever since. They are the materials of choice for ultravioletblue- green optoelectronics and they hold the potential to complement and even challenge silicon in a number of electronic applications. The main reason for the continuously increasing success and research in GaN systems for optoelectronic devices is due to ability of tuning its direct band gap along a wide range of energies. Figure 1.1 represents the band gap range for various semiconductors and wurtzite III-N, showing that this semiconductor family covers the whole visible spectrum. On the other hand, in 1993, Khan [2] realized a heterostructure field effect transistor based on an AlGaN/GaN layer structure for the first time, considered as a breakthrough for electronic device research with nitrides. The two-dimensional electron gas (2DEG) in combination with superior material properties in terms of large bandgap, high breakdown voltage and high saturation carrier velocity is an ideal precondition for application in electronic devices.

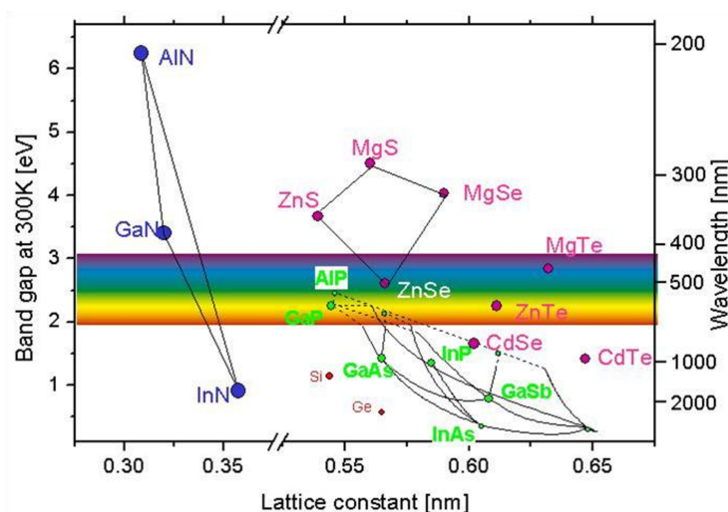

Figure 1.1 Band gap variation with lattice constant for various compound semiconductors [3]

The gallium nitride (GaN) and Aluminium Nitride (AlN) materials were synthesized first in 1930 and 1907 [4, 5] and then grown epitaxially by means of hydrid phase vapour epitaxy (HVPE) in 1969 by Maruska *et al.* [6]. In later years, the important breakthroughs were achieved by realization of the growth *via* metal organic chemical vapor phase epitaxy (MOVPE), molecular beam epitaxy [7, 8]. Since then the scientific work done on this material system and it's exploding market as depicted in Figure 1.2 according to *electronic industry market research and knowledge network* statistics [9]. In the 1992´s the *p*-type doping was discovered leading to the first high-brightness light emitting diode (LED) [10]. This pushed forward the development of the InGaN ternary alloy and consequently the blue laser diode [11]. Indeed, it is an attractive candidate for optical and electronic devices, with a bandgap covering an unprecedented spectral range from ultraviolett (UV) to infrared (IR). The predicated market size for various applications with GaN devices for optoelectronics applications is shown in Fig. 1.3. On the other hand, there are several main drawbacks which causes the efficiency droop in nitride based devices still need to be understood and improved with epitaxial quality, fabrication etc. The drawbacks have motivated a huge research effort on the growth of III-nitrides using non-polar and semi-polar crystallographic orientations by reducing the effects of the polarization-induced internal electric field.

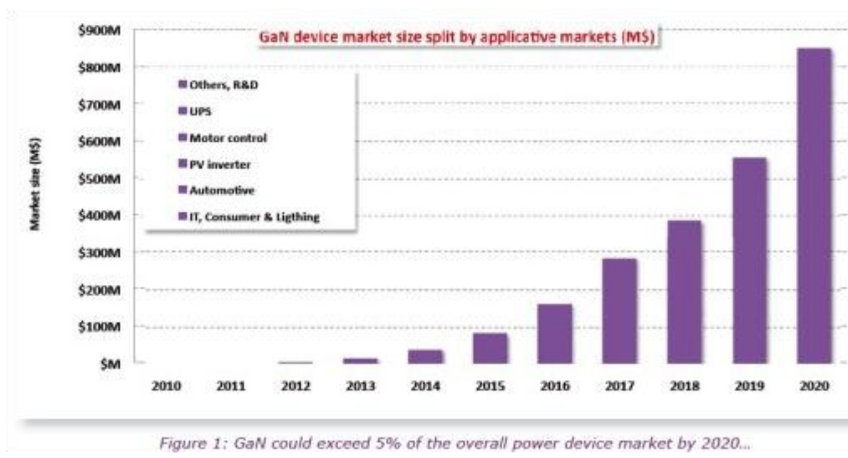

Figure 1.2 The expected GaN devices global market size in next years [9]

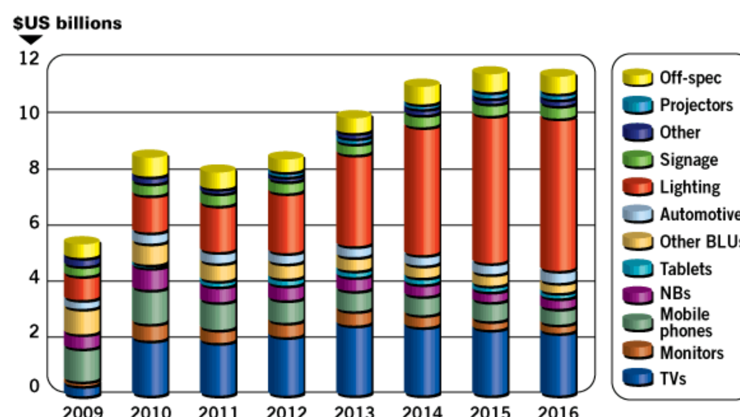

Figure 1.3 Increasing market of GaN based optoelectronics market (predicated) [12]

One of the main drawbacks of III-nitride semiconductors is the large lattice-mismatch (LM) issue of it's binary compounds with each other which results starined epitaxial layers and limitation on the thicknesses for the growth of heterostructures. Apparently, AlInN has the capability of reducing the lattice mismatch by growing the alloy of AlN or InN grown on GaN templates and thus allowing strain-free, LM heterostructures which offers a new degree of freedom in designing nitride based heterostructures for various applications. Recently, Kuzmik et. al [13] reported that the combination of strain-free AlInN epi-layers together with high polarization properties would lead to superior device performance with respect to AlGaN/GaN heterostructures. Therefore, the LM AlInN/GaN system is an ideal candidate for high power/frequency electronics etc.

Due to optimization of LM structure with strain free AlInN/GaN heterostructure which is considered 'state of art' for electronic devices research and have been reported with superior high mobility and 2DEG density properties by Gonschrek [14]. As a further research work, it was found that unfortunately these electrons forming the 2DEG suffer from poor in-plane transport properties. As a development/improvement part, it was proposed that insertion of thin AlN layer could improve the quality of this 'state of art' heterostructures based transistor for next generation power devices.

1.2 Objective of the thesis

The objective of this thesis is concerned with various prospects of III-nitride based heterostructure for different applications. The focus has been given in order to provide the detailed investigation on general properties investigation to the physical phenomena for electronic application and very new results on defect related investigation on AlInN/GaN based heterostructures with varying AlN interlayer thickness. Additionally, InGaN based structures have been investigated in order to understand the defect levels and their properties followed by optical properties of photodetector structure.

The thesis starts with ***chapter 1*****,** an introduction to III-nitride semiconductors and it's achievement in research and development over other semiconductors also with it's increasing market size for electronic and optoelectronics applications. The chapter finishes with the introduction with organization of the thesis.

Chapter 2 gives an overview on III-nitride semiconductor materials properties i.e. structural, electrical and optical which is kind of unique among all semiconductors, particularly with the existing polarization within the materials which offers the possibility of 2DEG and 2DHG systems. This also provides information on type of defects in semiconductors and their influences on nitride based heterostructures performance and issues.

Chapter 3 mainly describes the main experimental techniques used for research during the thesis work. The experimental techniques used in for this thesis ranges from basic electrical characterization to Deep level Transient spectroscopy (DLTS) followed by optical methods such as Surface Photo Spectroscopy (SPS) and Photo-Current spectroscopy (PC).

Chapter 4 deals with detailed characterization of GaN layer by in order to understand the electrical properties such as Schottky barrier inhomogeneity, leakage mechanism, and optical and defect related studies. The defects extracted by using DLTS technique are compared with optical methods and found in good agreement with each other. The 'yellow luminescence' related issue has also been discussed by considering the nature of dislocations.

Chapter 5 describes the a very detailed investigation of lattice mismatched InAlN/AlN/GaN based heterostructures with varying AlN interlayer thickness in order to understand the role of AlN layer on electrical and optical properties. It has been observed that thin AlN layers enhance the performance of the device while thick AlN layers cause structural deformation and results in substantial reduction in performance [15, 16]. The electrical analysis allow understanding the properties like mobility, 2DEG density variation with varying AlN thickness which can be used to optimizing the interlayer thickness by growers to improve the quality and properties [17]. DLTS analysis gives information to identify the deep levels in structures and also allows defining them as extended defects connecting to the trap responsible for Poole-Frenkel mechanism [18]. The defect levels identified have not been reported in literature so far. Moreover, we have also observed the effect of 2DEG density variation on optical properties which have never been reported in terms of 2DEG related transitions above GaN bandgap in such heterostructures [19]. In addition, we have observed similar phenomena in case of LM structures and also proposed the observation of Fermi Edge singularity (FES) phenomena attributed to high 2DEG density in heterostructures. In later part, MSM based photodetector structure has been fabricated and the possibility of developing optoelectronic devices with high efficiency is discussed.

Chapter 6 is mainly dedicated to study InGaN/GaN heterostructures to detect the deep levels, understand the optical properties and propose an efficient Photodetector structure. DLTS investigation detects majority and minority carrier related traps, where minority carrier related trap emission is attributed to InGaN/GaN interface. Surface photovoltage spectroscopy studies mainly focus on energy gap determination for varying In content in InGaN layer, which also defines the bowing parameter for InGaN alloys. In later part, MSM based photodetector structure has been fabricated and surface and heterojunction (interface) related efficiency is compared, which gives a possibility of developing optoelectronic devices with high efficiency.

References

1. S. Nakamura, N. Iwasa,M. Senoh, and T.Mukai, Jpn. J. Appl. Phys. 31 (1992)
2. M. Asif Khan, A. Bhattarai, J. N. Kuznia, and D. T. Olson, Appl. Phys. Lett. 63 1214 (1993)
3. http://www-opto.e-technik.uni-ulm.de/lehre/cs/
4. F. Fichter, Z. Über Aluminiumnitrid. Anorg. Chem. 54, 322 (1907)
5. W. C. Johnson, J. B. Parsons, M. C. Crew, J. Phys. Chem. 234, 2651 (1932)
6. H. P. Maruska, and J. J. Tietjen, Appl. Phys. Lett. 15, 327 (1969)
7. H. M. Manasevi, F. M. Erdmann, and W. I. Simpson, J. Electrochem. Soc. 118, 1864 (1971)
8. S. Yoshida, S. Misawa, A. Itoh, Appl. Phys. Lett. 26, 461 (1975)
9. *http://www.electronics.ca/publications/products/Power-GaN-2012.html*
10. S. Nakamura, M. Senoh, and T. Mukai, Jpn. J. Appl. Phys. 2 30, L1708 (1991)
11. S. Nakamura, T. Mukai, and M. Senoh, Appl. Phys. Lett. 64, 1687 (1994)
12. http://www.electroiq.com/articles/sst/2012/01/gan-led-market-growth-starts-in-2012.html
13. J. Kuzmik, IEEE Electron Device Lett. 22, 510 (2001)
14. M. Gonschorek, J.-F. Carlin, E. Feltin, M. A. Py, and N. Grandjean, Appl. Phys. Lett. 89, 062106 (2006)
15. S. Pandey, B. Fraboni, D. Cavalcoli, A. Minj, A. Cavallini, Appl. Phys. Lett. 99, 012111 (2011)
16. A. Minj, D. Cavalcoli, S. Pandey, B. Fraboni, A. Cavallini, T. Brazzini, F. Calle, Scrip. Mate. 66, 327 (2012)
17. S. Pandey, D. Cavalcoli, A. Minj, B. Fraboni, A. Cavallini, D. Skuridina, P. Vogt, Michael Kneissl, Acta mat. 60, 3176 (2012)

18. S. Pandey, D. Cavalcoli, B. Fraboni, A. Cavallini, T. Brazzini, F. Calle, Appl. Phys. Lett. 100, 152116 (2012)
19. D. Cavalcoli, S. Pandey, B. Fraboni, A. Cavallini, Appl. Phys. Lett. 98, 142111 (2011)

Chapter 2

Background on III-V nitride materials properties

(In, Al, Ga)N based system is very promising for various applications such as high frequency, high power HEMTs, in addition for optoelectronic devices as solar blind UV detectors, UV LEDs, UV laser diodes, biosensors, pressure sensors, and MEMS [1-5]. Focusing on the properties that give nitrides a huge advantage in HEMT applications, a number of material metrics combine to give GaN-based devices great potential. This Chapter gives an introduction to important material properties of wurtzite nitride semiconductors: crystal structure, polarization field and defects in III-nitride and key issues.

2.1 Crytall structure properties

2.1.1 Crystalline Structure and Symmetry

(In, Al, Ga)N mainly exists in two crystallographic types, known as zinc-blende (β-phase) and wurtzite (α-phase). The wurtzite phase is thermodynamically stable in comparison to metastable cubic, with energy gain/atom of 18.4 meV, 9.9 meV and 11.4 meV for AlN, GaN and InN, respectively. The possibility of co-existence of wurtzite and cubic phases is high because energy barrier is not high enough to prevent the mixing, demanding critical tuning of growth conditions.

The *wurtzite* GaN phase shows hexagonal symmetry [shown in Fig. 2.1(a)] and belongs to the space group P63mc (C46v). The lattice consists of two merged hexagonal sub-lattices shifted by 3/8[0001] for GaN. The two sub-lattices are composed of group-III metal and nitrogen atoms, respectively. Fig. 2.1(b) represents the GaN in *zinc blende* phase, with cubic symmetry. Cubic GaN belongs to F43m (T2d) space group consisting of two face-centered cubic structures shifted by ¼[111], with both metal and nitrogen atoms occupying appropriate sites.

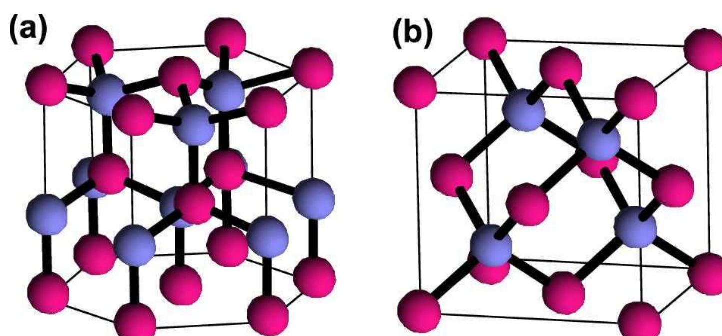

Figure 2.1 (a) Wurtzite and **(b)** Zinc-blende structures of GaN. The red and blue spheres indicate Ga and N atoms, respectively

The hexagonal crystal structure of III-Ns, illustrated in Fig. 2.2a, is represented by the edge length *a* of the basal hexagon along the [11-20] axis, height *c* of the hexagonal prism along the [0001] axis, and the anion-cation bond length *u* along the [0001] axis. The anion-cation bond length is considered because it changes with different cations and ionic radii [6]. The notation for the four indices *(h k i l)* is assigned to the three base vectors a_1, a_2, a_3 and *c*. The third index *i* is defined as -*h*-*k*. All the three base vectors are separated by angle of 120°. It must be remembered that, unlike the cubic orientations, the Miller indices of hexagonal orientations do not lead to identical planes on permutation. In the hexagonal system, equivalent crystallographic planes can be identified by permutation of the three basal Bravais indices *h k i*. In addition, different type of planes (polar) have been also shown in Fig. 2.2b, where a_1, a_2 are at 120° and a_3 is parallel to c-axis. The lattice parameters of binary GaN, InN and AlN are indicated in Table 2.I. For ternary compounds like $A_xB_{1-x}N$ the lattice parameters can be deduced using Vegard's law [7]:

$$a_{AB} = xa_A + (1-x)a_B \qquad (2.1)$$

Table 2.I Lattice parameters of bulk InN, GaN and AlN

	InN	**GaN**	**AlN**
c (A^o)	5.693	5.186	4.982
a (A^o)	3.533	3.189	3.112
c/a	1.611	1.626	1.600
u	0.377	0.377	0.382

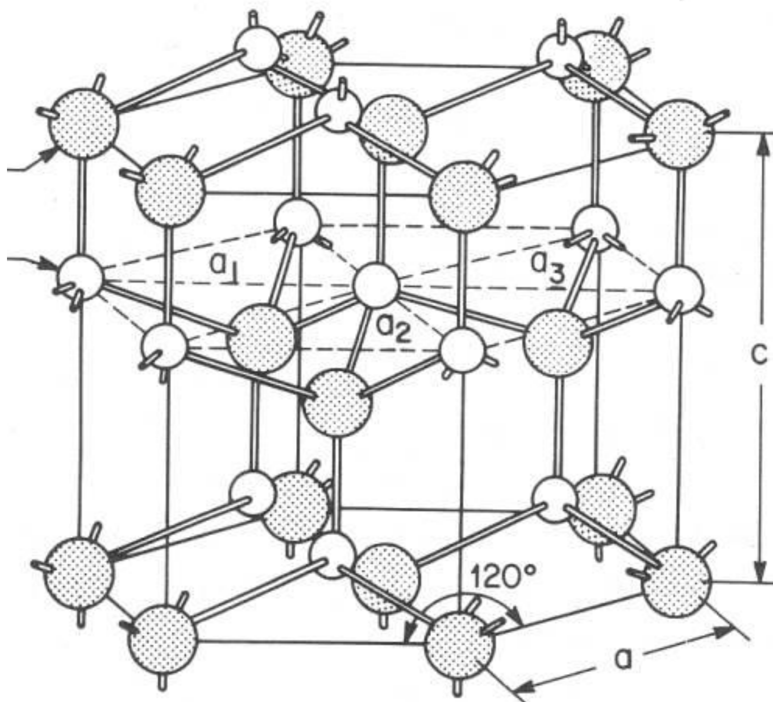

***Figure* 2.2a** Hexagonal structure with representations for the base vectors a_1, a_2 , a_3 and the lattice parameters *a* and *c*

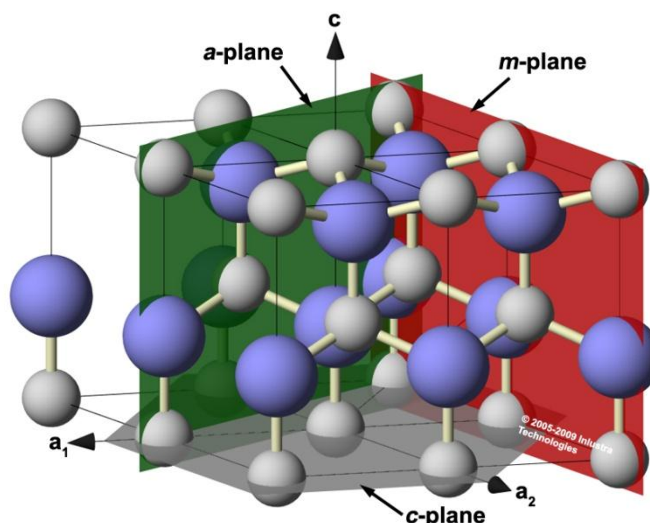

Figure 2.2b The dark (red and green) shadow areas show the m-plane and a-plane, respectively, while grey shadow area shows c-plane [8]

In both cubic and hexagonal phases, the atoms are tetrahedrically bonded and the structures if rotated along equivalent axis by 60° can be transformed into either zincblende or wurtzite ([111] or [0001], respectively, as indicated in Fig. 2.3. As a result, the major aspect which differentiates the wurtzite and cubic crystalline structures is the stacking sequence shown in Fig 2.4. The wurtzite phase (0001) plane is stacked in ABAB… sequence and cubic phase (111) plane exhibits ABCABC… stacking.

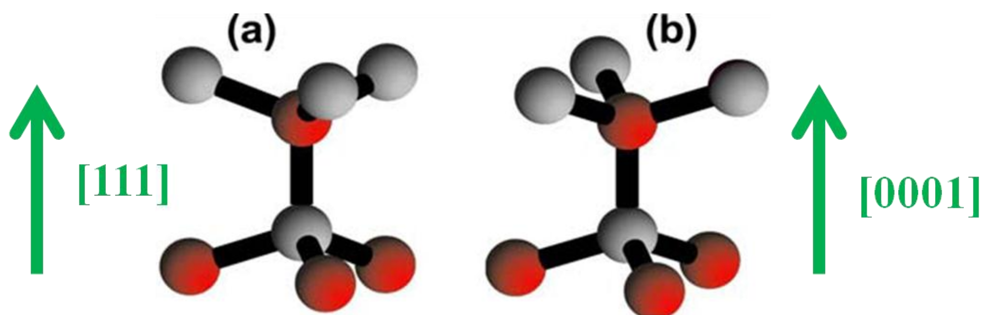

***Figure* 2.3**. Atoms bonded in tetrahedron for **(a)** zinc-blende and **(b)** wurtzite arrangements. Interchangeable on rotation along [111] and [0001] directions for cubic and wurtzite respectively

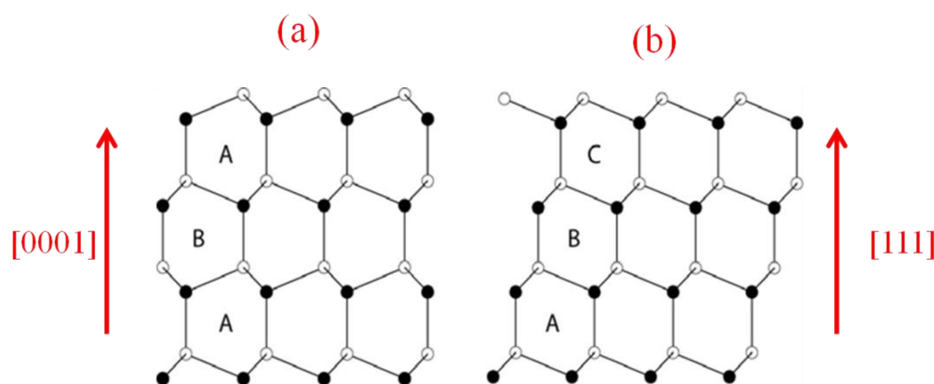

***Figure* 2.4**. Stacking sequence for **(a)** (0001) planes in wurtzite ([11-20] azimuth), and **(b)** (111) planes in zinc-blende ([1-10] azimuth)

The wurtzite crystals being non-centrosymmetric, the barycenters of positive and negative charges carried by group III metal (In, Al, Ga) do not necessarily coincide along the *c*-axis. The presence of polarization is strongly connected to the unit cell symmetry of the crystal. This asymmetry is the origin of the pyroelectric nature of wurtzite (In, Al, Ga)N, which will be discussed in next section.

2.1.2 Crystal Polarity

The hexagonal lattice is not centrosymmetric and, as a result, [0001] ≠ [000-1], as shown in Fig. 2.5. If we consider the bonds between Ga-N along the <0001> direction, the vector pointing from Ga to N is arbitrarily identified as [0001], and the material grown along this direction called Ga-polar, whereas the material grown in the opposite direction is called N-polar. Therefore, the Ga-polar structure is the mirror image of N-polar structure. However, the surface properties in terms of chimica behavior, morphology or thermal stability are strongly affected depending on whether the structure is Ga or N polar. The polarity of the films can be confirmed by various methods like wet chemical etching, characterization of physical morphology and convergent beam electron diffraction.

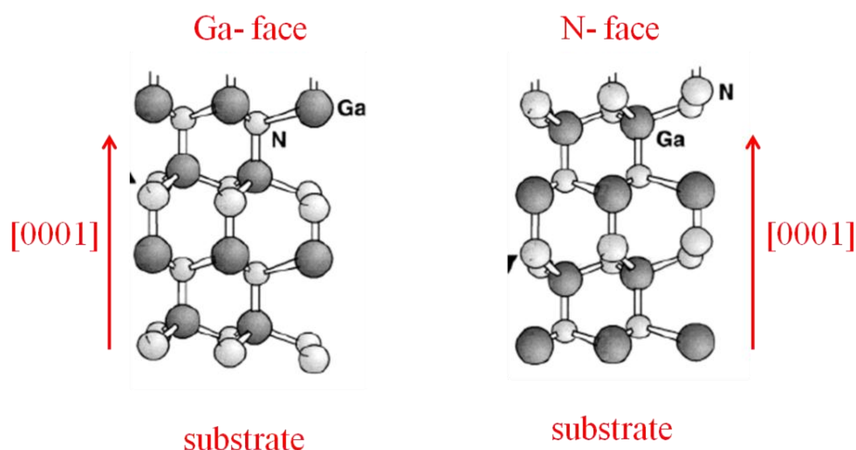

***Figure* 2.5** Ball and stick model of wurtzite showing polarity in GaN: **(a)** Ga-polar along [0001], **(b)** N-polar for [000-1]

Ga-polar GaN is usually preferred because it favors two-dimensional growth; on the contrary, N-polar GaN usually displays rough surface morphology. The GaN grown on sapphire is systematically Ga-polar when grown by MOVPE, but in the case of MBE growth, the polarity depends on the substrate preparation (nitridation or not) and on the nature of the buffer layer [9, 10, 11, 12, 13]. In contrast, in the case of growth on SiC (either 4H or 6H), the polarity is imposed by the polarity of the substrate. Thus, III-N deposition on the (0001) face of SiC, also called Si-face, will result in metal polarity, whereas growth on the (000-1) face of SiC, the so-called C-face, gives rise to N-polar material [14, 15, 16, 17].

2.1.3 Spontaneous and piezoelectric polarization

The existence of polarization make III-nitride semiconductors special and this has been one of the main driving force for research community. The presence of polarizations is strongly connected to the unit cell symmetry of the crystal. The polarization properties exist for nitride semiconductors in both the zincblende and wurtzite phases, which are closely related to each other. The polarization phenomena exist in two different ways as (1) Spontaneous Polarization (P_{sp}) and (2) Piezoelectric Polarization (P_{pz}). Thus total Polarization can be expressed as

$$P_{total} = P_{sp} + P_{pz} + P_{ext} \qquad (2.2)$$

Thus, in case of absence of external electric field, the total Polarization contribution is mainly from spontaneous and piezoelectric polarization in solids.

Spontaneous polarization In the case of zincblende, compound semiconductors, such as GaAs or GaN, have four symmetry equivalent polar <111> axes whose contributions eliminate each other in equilibrium. Hence, these materials are free of electrical polarization at equilibrium. In contrast, the wurtzite phase has a singular polar axis, namely, the [0001] axis as shown in Fig. 2.6 [18]. Thus, the wurtzite phase carries spontaneous polarization along [0001] even at equilibrium. One typical example of spontaneous polarization is shown in Fig. 2.6 for AlN/GaN interface structure on Ga-face GaN substrate.

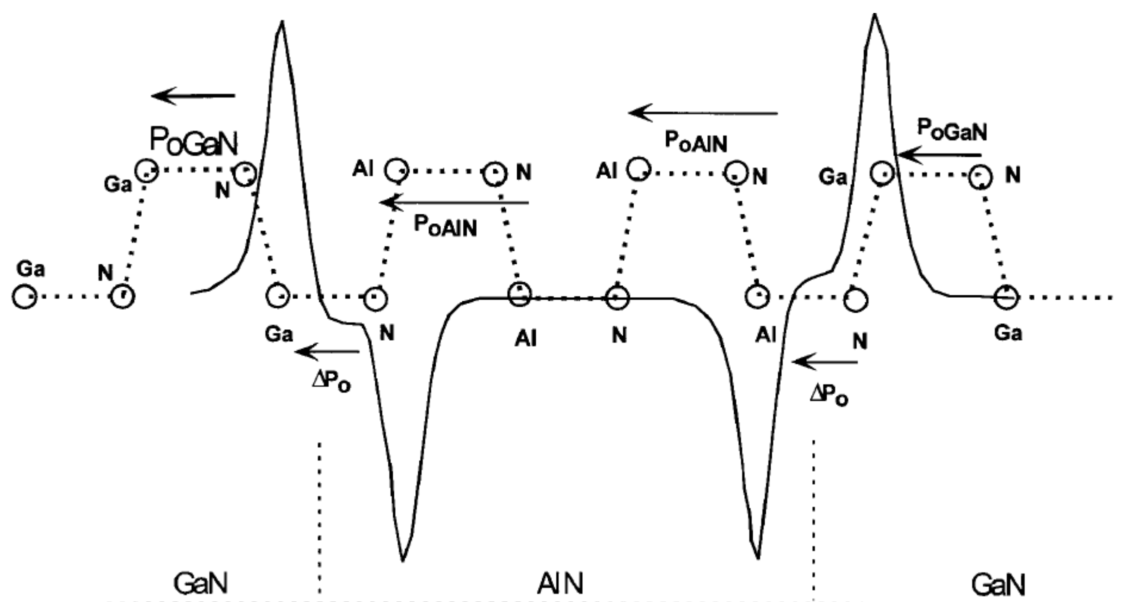

***Figure* 2.6** Spontaneous polarization at AlN/GaN interfaces in a heterostructure with Ga-polarity, i.e., the c-direction bonds point from Ga to N sites. The surface also represents the Ga layer [18].

Figure 2.7 illustrates the microscopic picture of polarization in a slab of strain-free GaN [19]. Each unit cell can be thought to contain a charge dipole that is formed due to the spatial separation of the barycentre of the negative charges due to the electron clouds and the positive charge due to the nuclei. The dipoles in every layer of unit cells neutralize each other in the bulk of the semiconductor, but form sheet charges $\pm\sigma_\pi$ on the surfaces. A free Ga-face surface develops a negative sheet charge, and a positive sheet charge forms on the N-face surface. The net electric field in the bulk of the semiconductor is therefore not zero, but $E_\pi = \sigma_\pi / \varepsilon$ by Gauss's law. Note that this is the field if the bound sheet charge dipole that forms on the free surfaces is not neutralized by the flow of mobile charges.

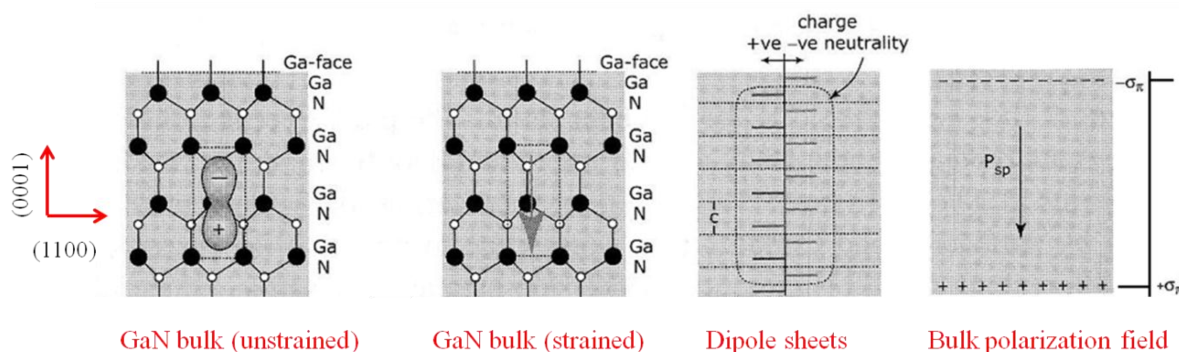

***Figure* 2.7** Microscopic picture of spontaneous polarization in a freestanding GaN slab.

An estimate of the electric field in III-nitrides arising from the polarization sheet charges gives $E_\pi \approx 1$ - 10 MV/cm. Such large fields cause a major redistribution of charges in the system. What is interesting is that these large fields are frozen into the system by means of the crystal structure and they do have striking effects on the band diagrams, charge accumulation and depletion. In general, the steady-state picture is much different from the flat-band situation one finds in standard heterostructure device physics. In a compositionally uniform, unstrained bulk polar material that possesses spontaneous polarization, the total

polarization **P** is constant in space and the volume density of polarization charge vanishes (mathematically, $(\nabla.P)=0$ but $(P \neq 0)$. Due to the absence of net charge in the bulk, the macroscopic electric field has a magnitude $E_\pi = \sigma_\pi / \varepsilon$, where ε is the dielectric constant of the semiconductor. This electric field can be related to the surface charges $\sigma_\pi = P.n$ of a slab of the material by Gauss' law.

Bernardini et al. [20] and Ombacher et al [21] theoretically calculated the spontaneous polarization in ternary alloy $A_xB_{1-x}N$ as a function of the *x*. Because of the nonlinear dependence of the cell internal parameter on alloy composition a nonlinear behavior of the spontaneous polarization versus *x* has to be expected. Bernardini *et al.* pointed out that the different response to the hydrostatic pressure of the binary constituents of the alloy should contribute significantly to the nonlinear behaviour of spontaneous polarization in ternary random alloys [21]. Thus, the spontaneous polarization of the random ternary nitride alloys is given to second order in *x* by (in Cm^{-2}):

$$
\begin{aligned}
P^{sp}_{ABN}(x) &= P^{sp}_{AN}x + P^{sp}_{BN}(1-x) + bx(1-x) \\
P^{sp}_{AlGaN}(x) &= -0.090x - 0.034(1-x) + 0.021x(1-x) \\
P^{sp}_{AlInN}(x) &= -0.090x - 0.042(1-x) + 0.070x(1-x) \\
P^{sp}_{InGaN}(x) &= -0.042x - 0.034(1-x) + 0.037x(1-x)
\end{aligned} \quad (2.3)
$$

The first two terms in the equations are the usual linear interpolation between the binary compounds (such as InN, GaN, AlN). The third term embodies nonlinearity to quadratic order (see also figure 2.8). Higher-order terms are neglected as their effect was estimated to be less than 10%. The *b* parameter is defined as bowing parameter for band gap calculations in alloys which will be discussed in next sections.

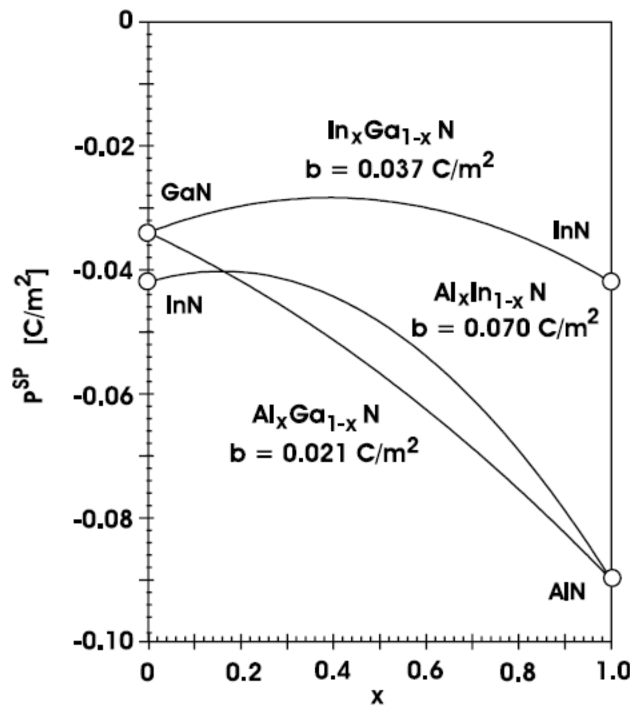

Figure 2.8 Predicted spontaneous polarization for random, ternary alloys with wurtzite crystal structure. The dependence of P_{SP} on *x* can be approximated with high accuracy by quadratic

equations (2.3). The nonlinearity can be described by positive bowing parameters increasing from AlGaN to InGaN and AlInN [21].

Piezoelectric polarization In practice, semiconductor layers are often grown under strain due to the lattice mismatch to the underlying layer. In other words, the asymmetry in the unit cell or the lack of inversion symmetry can be further enhanced when strained on materials with a lattice mismatch, a source of additional piezoelectric polarization. The contributions of the four polar axes of zincblende structures eliminate each other for growth along a <111> direction. However, growth along one of the polar axes lifts the symmetry and the crystal exhibits piezoelectric polarization. In contrast, the wurtzite structure with its unique polar [0001] axis always carries piezoelectric polarization for any growth direction.

The piezoelectric polarization field, P_{pz}, is expressed in terms of piezoelectric constants e_{ij} and deformation of a crystal ε_j as follows:

$$P_{pz} = \sum e_{ij}\varepsilon_j \qquad (2.4a)$$

The equation indicates that the applied strain changes the dipole moment along the [0001] axis; as a consequence it induces macroscopic polarization with magnitude linearly dependent on the polarization tensor of the material. The equation can be written in a different form:

$$P_{pz} = \sum d_{ij}\sigma_j \qquad (2.4b)$$

Where, P_{pz} is linearly related to all components of general stress σ_j and piezoelectric moduli d_{ij}. Both the above equations tell the same concept and are related by Hooke' law, which state that, for small stress, the amount of strain is proportional to the magnitude of the applied stress. Therefore,

$$\sigma_i = \sum C_{ij}\varepsilon_j \qquad (2.4c)$$

Where, C_{ij} is the stiffness or elastic constant tensor. In this thesis we will stick to e_{ij} (d_{kj} C_{jl}) for theory and calculations for the sake of uniformity. In the case of wurtzite structure, due to the crystal symmetry, the elastic constant tensor contains five independent coefficients, as described below:

$$C_{ij=} \begin{pmatrix} C_{11} & C_{12} & C_{13} & 0 & 0 & 0 \\ C_{12} & C_{11} & C_{13} & 0 & 0 & 0 \\ C_{13} & C_{13} & C_{33} & 0 & 0 & 0 \\ 0 & 0 & 0 & C_{44} & 0 & 0 \\ 0 & 0 & 0 & 0 & C_{44} & 0 \\ 0 & 0 & 0 & 0 & 0 & \frac{1}{2}(C_{11}-C_{12}) \end{pmatrix} \qquad (2.5)$$

The value of elastic coefficients, experimentally measured and theoretically calculated by several groups for InN, GaN and AlN are summarized in Table 2. II

Table 2.II Experimental and theoretical stiffness constants of InN, GaN and AlN in GPa

	C_{11}	C_{12}	C_{13}	C_{33}	C_{44}	References
InN	271	124	94	200	46	[22] theory
	223	115	92	224	48	[23] theory
GaN	374	106	70	379	101	[24] exp.
	396	144	100	392	91	[22] theory
	367	135	103	405	95	[23] theory
AlN	410	140	100	390	120	[25] exp.
	396	137	108	373	116	[23] theory

During heteroepitaxy of III-nitrides on the (0001) plane, the in-plane stress is uniform $(\sigma_x = \sigma_y = \sigma)$ and there is no stress along the *c*-axis or shear stress. In that particular case (biaxial stress configuration), equation (2.4c) gives:

$$\varepsilon_y = \varepsilon_x ; \varepsilon_z = -2(C_{13} / C_{33})\varepsilon_x \qquad (2.6)$$

where, $\varepsilon_z = (c - c_0) / c_0,\ and\ \varepsilon_x = \varepsilon_y = (a - a_0) / a_0, c_0\ and\ a_0$ are unstrained parameters.
Due to crystal symmetry we have only three non-zero independent constants e_{33}, e_{31} and e_{15}, so that equation (2.4a) can be written as

$$\overrightarrow{P_{pz}} = \begin{pmatrix} 0 & 0 & 0 & 0 & e_{15} & 0 \\ 0 & 0 & 0 & e_{15} & 0 & 0 \\ e_{31} & e_{31} & e_{33} & 0 & 0 & 0 \end{pmatrix} x \begin{pmatrix} \varepsilon_1 \\ \varepsilon_2 \\ \varepsilon_3 \\ \varepsilon_4 \\ \varepsilon_5 \\ \varepsilon_6 \end{pmatrix} \qquad (2.7)$$

With eq. (2.6) and (2.7), we obtain that the in the case of biaxial strain piezoelectric polarization vector is along [0001] axis and the module can be obtained by:

$$P_{pz[0001]} = 2\,\varepsilon_z \left(e_{31} - e_{33} \frac{C_{13}}{C_{33}} \right) \qquad (2.8)$$

with the piezoelectric constants e_{33} and e_{31} and the elastic constants C_{13} and C_{33}. Hence, the piezoelectric polarization is along [0001].

As a consequence of equation (2.7) and of the linear interpolation of the elastic and piezoelectric constants, the piezoelectric polarization is nonlinear in terms of the alloy composition. The nonlinear dependence of the piezoelectric polarization on the alloy composition can be approximated with accuracy better than 1% by the following quadratic equations [21]:

$$P^{pz}_{AlGaN/InN}(x)=[-0.28x-0.113(1-x)+0.042x(1-x)]\, in\, C\, m^{-2}$$
$$P^{pz}_{AlGaN/GaN}(x)=[-0.0525x+0.0282x(1-x)]\, in\, C\, m^{-2} \qquad (2.9)$$
$$P^{pz}_{AlGaN/AlN}(x)=[-0.026(1-x)+0.0248x(1-x)]\, in\, C\, m^{-2}$$
$$P^{pz}_{AlInN/InN}(x)=[-0.28x+0.104x(1-x)]\, in\, C\, m^{-2}$$
$$P^{pz}_{AlInN/GaN}(x)=[-0.0525x+0.148(1-x)+0.0938x(1-x)]\, in\, C\, m^{-2} \qquad (2.10)$$
$$P^{pz}_{AlInN/AlN}(x)=[-0.182(1-x)+0.092x(1-x)]\, in\, C\, m^{-2}$$
$$P^{pz}_{InGaN/InN}(x)=[-0.113(1-x)-0.0276x(1-x)]\, in\, C\, m^{-2}$$
$$P^{pz}_{InGaN/GaN}(x)=[+0.148x-0.0424x(1-x)]\, in\, C\, m^{-2} \qquad (2.11)$$
$$P^{pz}_{InGaN/AlN}(x)=[+0.182(x)+0.026(1-x)-0.0456x(1-x)]\, in\, C\, m^{-2}$$

For heterostructures with barriers under moderate strain [21], these equations can be used as an input, either directly as polarization, as interface-bound sheet charge, depending on the implementation, in a self-consistent Schrödinger–Poisson solver based for example on effective-mass or tight-binding theory.
The calculated nonlinear piezoelectricity of the binary compounds can be described by the relations (in C-m^{-2}):

$$P^{pz}_{AlN} = -1.808\varepsilon + 5.624\varepsilon^2 \quad for\ \varepsilon \le 0 \qquad (2.12a)$$
$$P^{pz}_{AlN} = -1.808\varepsilon - 7.888\varepsilon^2 \quad for\ \varepsilon \ge 0 \qquad (2.12b)$$
$$P^{pz}_{GaN} = -0.918\varepsilon + 9.541\varepsilon^2 \qquad (2.12c)$$
$$P^{pz}_{GaN} = -1.373\varepsilon + 7.559\varepsilon^2 \qquad (2.12d)$$

Therefore, the calculation of the piezoelectric polarization of an $A_xB_{1-x}N$ alloy at any strain becomes straightforward. One can choose a value for x, calculate the strain $\varepsilon_1 = \varepsilon(x)$ from Vegard's law, and the piezoelectric polarization by

$$P^{pz}_{ABN}(x) = xP^{pz}_{AN}(\varepsilon(x)) + (1-x)\, P^{pz}_{BN}(\varepsilon(x)) \qquad (2.13)$$

where, $P^{pz}_{AN}(\varepsilon(x)), P^{pz}_{BN}(\varepsilon(x))$ are the strain dependent bulk piezoelectric field polarizations of the relevant binary compounds mentioned above.

Polarization constants The spontaneous and piezoelectric polarization constants for InN, GaN and AlN are indicated in Table 2. III. Usually, materials constants of group-III nitrides are determined by *ab initio* density-functional theory (DFT) calculations in the framework of the local-density approximation (LDA). In the case of spontaneous and piezoelectric polarization constants, it is important to note that these materials constants critically rely on structural data such as, e.g., the lattice constant ratio *c/a* and the anion-cation bond length *uc* along the [0001] axis. We observe that the magnitude of piezoelectric constants is ten times higher than GaAs or CdTe compounds, due to

the strong ionic character of the III-N bond. In bulk materials, rearrangement of surface charges cancels spatially uniform polarization-induced electric fields. However, for heterostructures, variation in composition and strain induces internal electric fields in the layers.

Table 2.III Spontaneous and piezoelectric coefficients of various semiconductors [19, 21]
Note: no spontaneous coefficients for GaAs and CdTe (cubic symmetry materials)

	P_{sp} ($C\ m^{-2}$)	**e_{31}($C\ m^{-2}$)**	**e_{33}($C\ m^{-2}$)**
InN	-0.032	0.57	0.97
GaN	-0.029	0.49	0.73
AlN	-0.081	0.60	1.46
GaAs	-	0.06	0.12
CdTe	-	-0.01	0.03

2.1.4 Polarization in Heterostructure and 2-Dimensional Electron/Hole Gas

The band gap of GaN is narrower in comparison to that of AlN. Any abrupt change in material results in abrupt band offset at the semiconductor heterointerface which must be step-like in normal cases. However, the difference in spontaneous and piezoelectric polarization across the heterointerface affects the band structure to a large extent in III-N, leading to charge depletion or interface charge accumulation. The amount of charges at the interface depends on the strain and material composition.

As mentioned above, the total polarization P is the sum of the piezoelectric and spontaneous polarization,

$$P_{ABN} = P_{ABN}^{pz} + P_{ABN}^{SP} \qquad (2.14)$$

Associated with a gradient of polarization in space is a polarization-induced charge density given by

$$\rho_P = -\nabla P \qquad (2.15)$$

As a special case, at the surface of a relaxed or strained $A_xB_{1-x}N$ layer, as well as at the interfaces of a $A_xB_{1-x}N$ /GaN heterostructure, the total polarization changes abruptly, causing a fixed two-dimensional polarization charge density σ, given by

$$\sigma_{pol} = \sigma_{ABN} = P_{ABN} = P_{ABN}^{pz} + P_{ABN}^{SP} \qquad \text{for surfaces} \qquad (2.16a)$$

$$\begin{aligned}\sigma_{pol} &= \sigma_{ABN/GaN} = P_{GaN} - P_{ABN} \\ &= (P_{GaN}^{pz} + P_{GaN}^{SP}) - (P_{ABN}^{pz} + P_{ABN}^{SP})\end{aligned} \qquad \text{for interfaces} \qquad (2.16b)$$

Figures 2.9 (a) and (b) show the polarization-induced surface and interface sheet density σ/e ($e = -1.602 \times 10^{-19}$ C) for relaxed and strained binary nitrides as well as for pseudomorphic $A_xB_{1-x}N$/GaN heterostructures. The (spontaneous) polarization-induced bound surface density of relaxed InN, GaN and AlN crystals is determined to be 2.62×10^{13}, 2.12×10^{13} and 5.62×10^{13} cm^{-2}, respectively, which is equivalent to approximately two and five electron charges per every 100 surface atoms. If a biaxial compressive strain of e.g. $\varepsilon_1 = -0.02$ is applied to the crystals, the surface charges are reduced to 0.72×10^{13}, 0.74×10^{13} and 3.22×10^{13} cm^{-2}, respectively (figure 2.9 (a)). For compressive strains in InN, GaN and AlN of $\varepsilon_1 = -0.025$, -0.030 and -0.045 the piezoelectric polarization compensates the spontaneous polarization and the strained crystals should be without surface charge and internal electric field. As can be seen from figure 2.9 (a), compressive strain reduces and tensile strain enhances the bound surface charge. It should be mentioned that for relaxed layers grown along the *c*-axis on a substrate of choice, the surface charge is positive (negative) for material with N-face (Ga-face) polarity.

As in ferroelectrics, the bound surface charge can be screened by oppositely charged surface defects and adsorbed charges from the environment [26]. If the screening of the surface charge by defects or the ambient is not complete, the carrier concentration profiles inside the crystals will be affected [27]. For example in slightly n-type doped Ga-face GaN grown on *c*-Al2O3 substrates free electrons are expected to accumulate at the GaN/Al_2O_3 interface compensating the positive bound (mainly spontaneous) polarization-induced interface charge $+\sigma$, whereas the negative surface charge on top of the GaN layer $-\sigma$ is only partially compensated by the ionized donors. As a consequence a significant band bending at the Ga-face GaN surface is expected.

Since screening by charges from the ambient at $A_xB_{1-x}N$/GaN interfaces can be excluded, polarization-induced effects are much easier to study in heterostructures in comparison with single epitaxial layers. For pseudomorphic Ga-face $Al_xGa_{1-x}N$/GaN ($0 < x \leq 1$) and $Al_xIn_{1-x}N$/GaN ($0.71 < x \leq 1$) heterostructures, the polarization-induced interface charges are predicted to be positive (figure 2.9 (b)). In both cases the bound charge increases nonlinearly with x up to 7.06×10^{13} cm^{-2}, estimated for the AlN/GaN heterostructure. For Ga-face $In_xGa_{1-x}N$/GaN ($0 < x \leq 1$) and $Al_xIn_{1-x}N$ /GaN ($0 < x \leq 0.71$) heterostructures σ is found to be negative. Again the polarization-induced interface density changes in a nonlinear manner if the alloy composition is varied. For pseudomorphic InN/GaN heterostructures a very high value of the bound sheet density of 14.4×10^{13} cm^{-2} is calculated.

In n-type heterostructures it has to be taken into account that free electrons will accumulate at interfaces with positive bound sheet charges, compensating $+\sigma$. As a consequence a 2DEG with a sheet carrier concentration close to the concentration of the bound interface density $+\sigma/e$ can be formed. It should be pointed out that these 2DEGs are realized without any need of a modulation-doped barrier. This is of special interest for the fabrication of high-frequency and high power HEMTs, as the growth and processing of these devices is significantly simplified.

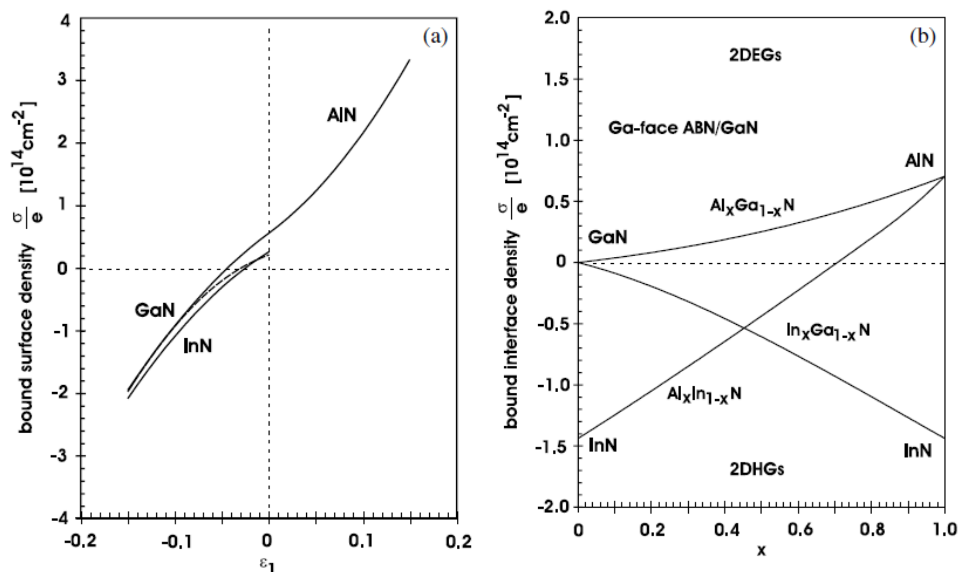

Figure 2.9 (a) Bound surface density of wurtzite GaN, InN and AlN crystals caused by a gradient in piezoelectric and spontaneous polarization at the surfaces in dependence of biaxial strain applied in the basal plane. (b) Bound interface density of pseudomorphic AlGaN/GaN, InGaN/GaN and AlInN/GaN heterostructures grown on relaxed GaN buffer layers with Ga-face polarity. Positive (negative) polarization-induced interface charges are screened by electrons (holes) in n-type (p-type) samples, causing the formation of two-dimensional carrier gases [19, 21]

The polarization difference results in a fixed charge sheet, σ_{pol} at the heterointerface. Now, let us try and identify the modification in the band diagram introduced by this fixed interface charge. In general, heterostructures are grown Ga-face GaN substrate so we will focus on GaN based heterojunctions. Figure 2.10 shows the sign of the polarization vectors and the resulting σ_{pol} for different cases.

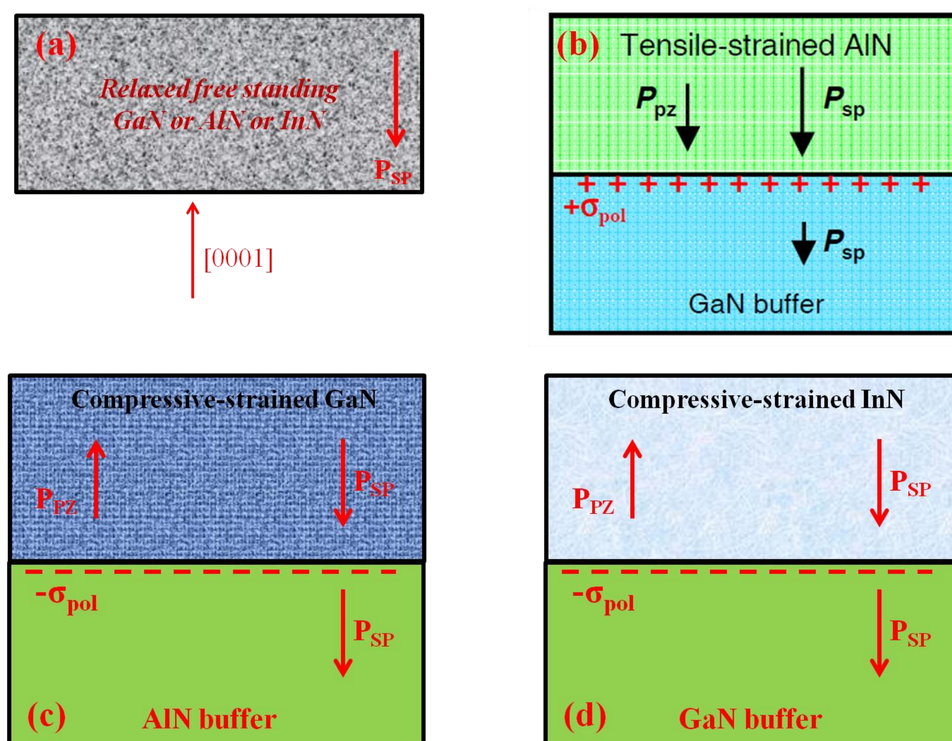

Figure 2.10 Polarization directions and sheet carrier density in GaN and AlN for different conditions of strain in: (a) unstrained GaN or AlN or InN (b) tensile strained AlN grown on relaxed GaN buffer (c) Compressive strained GaN on relaxed AlN buffer, (d) Compressive strained InN on relaxed GaN buffer.

For instance, in the case of AlN strained on GaN, both the difference in spontaneous and piezoelectric polarization lies in the same direction, leading to positive σ_{pol} at the interface and hence to the formation of a two dimensional electron gas (2DEG) in GaN by rearrangement of free carriers. Conversely, when GaN is compressively strained on an AlN buffer layer, the polarization difference have opposite sense, leading to negative σ_{pol}, and hence to a depletion region in the GaN. The corresponding band diagrams are depicted in fig. 2.11.

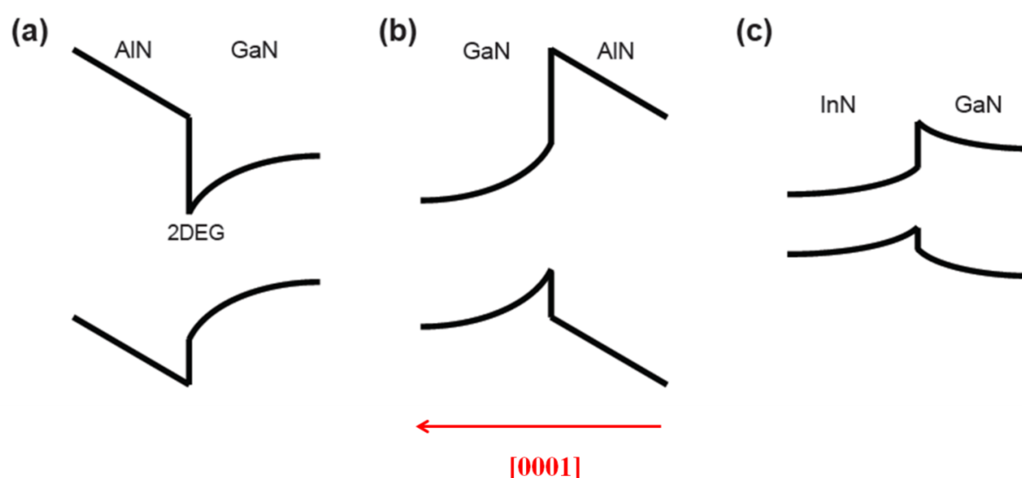

Figure 2.11 Schematic description of the potential profile at nitride heterojunctions

The built-in electric field in III-N heterostructures offers many interesting properties to emerge, which can be either engineered according to our advantage for device design. For instance, the 2DEG formed at the GaN/AlGaN interface can be used to fabricate high electron mobility transistors (HEMTs), with sheet carrier concentration comparable to those obtained by doping the channel. Since the structures are non-intentionally doped, the mobility is not degraded on scattering by the presence of ionized donors which is the case.

2.1.5 High Power High Frequency HEMT's on In(Al)GaN/GaN

Until recently, AlGaN/GaN material quality has been insufficient to produce high quality microwave devices. The recent improvements in GaN material quality that allow the fabrication of high frequency transistors have largely been driven by the commercialization of GaN for optical applications. These applications were made possible by the implementation of p-type doping in GaN by Amano *et al.* and the improved p-type doping concentrations by Nakamura in 1992 [28, 29]. The original applications for the Group III-Nitride material system were laser diodes, light emitters, and UV detectors. Due to the direct, wide bandgap of these materials, these devices have been implemented in a wide range of color applications from the UV to visible including displays by incorporating varying amounts of Al, In, and Ga with a large degree of commercial success [29]. More recently, AlGaN/GaN has been used for HEMT's in highfrequency, high-power devices. Taking advantage of the piezoelectric charge forming a two-dimensional electron gas (2-DEG) at

the AlGaN/GaN interface, many researchers have been able to implement HEMT's with channel current-carrier densities an order of magnitude higher than those formed with AlGaAs/GaAs. The high temperature stability of GaN compounds and high breakdown voltage of these materials allow very high density power operations which greatly exceed the power handling abilities of all other material systems to date with the exception of SiC. While HBT's would yield superior frequency response and power handling, their implementation has been largely unsuccessful due to the inability to make high enough quality p-type GaN and reliable ptype ohmic contacts [30, 31]. The p-type ohmic contacts being used for LED's are not good enough for microwave devices. Ohmic contacts to n-type GaN have been highly successful [32, 33]. Most III-Nitride microwave device research is currently focused on HEMT's, which require only n-type ohmic contacts.

Nevertheless, a great deal of research is currently focused on the substitution of the AlGaN barrier with an $In_xAl_{1-x}N$ barrier [34, 35, 36].[The motivation for such a shift when AlGaN/GaN HFETs are already near adoption is essentially the ability to induce an even larger carrier density (>2.5 x 10^{13} cm^{-2}) due to the relatively large difference in polarization at the interface where the 2-dimensional electron gas (2DEG) resides coupled with the larger conduction band offset afforded to InAlN as compared to typical AlGaN barrier layers, resulting in better carrier confinement in the quantum well [37]. Additionally, the pairing of InAlN with GaN is attractive because these materials can be lattice matched, circumventing strain related maladies that plague the AlGaN/GaN system [34].

High sheet density coupled with respectable mobilities at room temperature (for example, n_s=2.6 x 10^{13} cm^{-2} and μ=1170 cm^2/V/s for a product of over 3x10^{16} V^{-1} s^{-1}) [22] promises high current density in InAlN channels. In fact, record current densities of 2.3A/mm and 2.8A/mm have been achieved with forward biased gates in DC and pulsed modes, respectively [38] Regarding device scaling, Medjdoub *et al.* showed no change in sheet carrier density down to 9 nm and operation down to 3 nm InAlN barrier thicknesses, demonstrating the benefits in terms of scalibility of InAlN barrier layers over AlGaN barriers. Additionally, the same group [38] demonstrated FET performance at 1000ºC, which may have never been demonstrated in ANY device prior to this point and upon returning to room temperature after operation at up to 1000^0C, it appears that I_D, gate leakage, and pinchoff voltages are all preserved. These factors motive the further development on InAlN-based HFETs. In the following we will discuss our own results, discuss the spectre of hot phonon lifetime, which limits the ultimate performance of the HFETs, and provide experimental evidence of the ability to tune the hot phonon effects, resulting in enhanced microwave performance and reliability of InAlN-based HFET devices.

State of the Art Transistors Even though GaN and related compounds still have a large number of growth related defects compared to other materials, HEMT's made from AlGaN/GaN heterostructures have impressive performance. As early as 2001, with 0.12 µm gate devices, f_T and f_{MAX} as high as 101 and 150 GHz have been reported for AlGaN/GaN HEMT's on SiC substrates [23, 25] Other researchers report very high power operation with saturated output powers as high as 10.7 W/mm at 10 GHz [31-33]. There have been many successful attempts at making HEMT's on various substrates for improved power dissipation. Microwave applications include mobile-phone base stations, non-mobile wireless systems such as fixed wireless access systems, wireless local loop systems, or local multipoint distribution systems, and military applications such as tracking systems, communications, and frequency jammers. GaN based devices are touted as being the material of choice for high performance devices for use in harsh operating environments since they require less cooling. InAlN/GaN based transistors are more promising as they offer better propertied to AlGaN/GaN based devices.

2.1.6 Band structure of III-Nitrides

a) Band diagram

The bandgaps of III-nitride semiconductors cover a wide energy range that goes from the near infrared to the deep ultraviolet (Several groups have investigated the band structures of both GaN and AlN using different methods such as the all-electron relativistic, full potential, linearized augmented plane wave (FLAPW) method [39, 40]. The band structures of GaN and AlN are represented in fig. 2.12, showing direct band gap with the conduction and valence band minima situated at the Γ point.

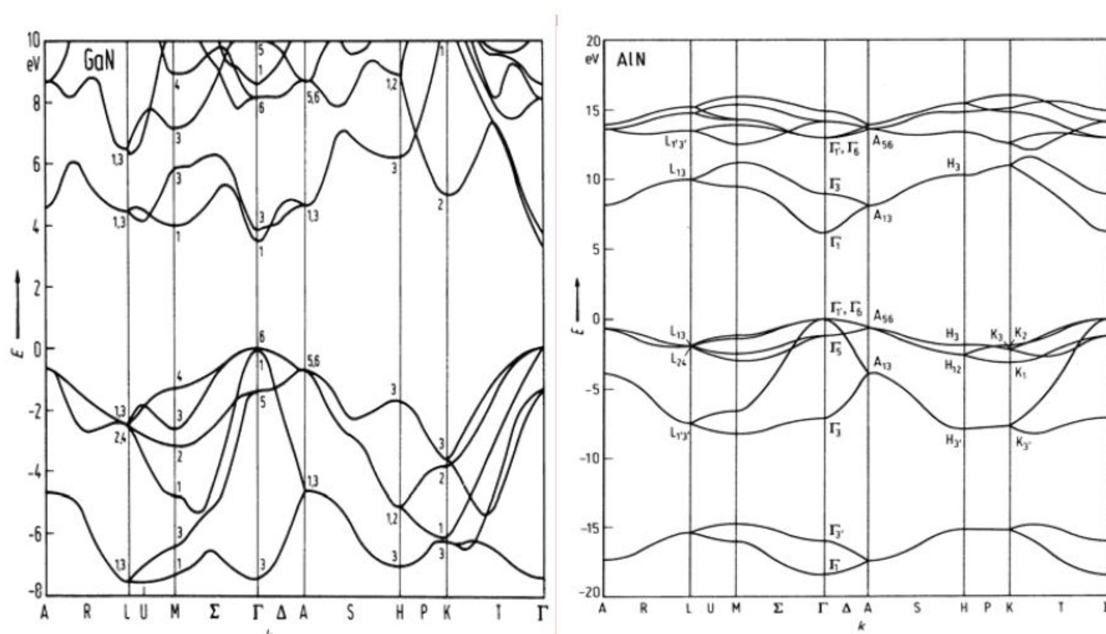

Figure 2.12 Calculated band structure of GaN (left) AlN (right) [39, 40]

Due to the asymmetric nature of wurtzite structure the valence band degeneracy is lifted due to the crystal field and spin-orbit coupling. Thus the heavy hole (A), light hole (B) and spin-orbit, crystal field splitting (C) subbands are separated. The bands have their symmetry at the Γ point with Γ9 for A and Γ7 for B and C subbands, as shown in Fig 2.13. In the case of GaN, the energy difference between the valence band subbands is given by ΔE_{AB} = 6 meV, ΔE_{CB} = 37 meV, with the values of degeneracy by the crystal-field and spin-orbit Δ_{cr} = 10 meV and Δ_{so} = 17 meV respectively [41]. In the case of AlN, Δ_{cr} = -169 meV, i.e. the top of the C subband is at higher energy than the A or B subbands.

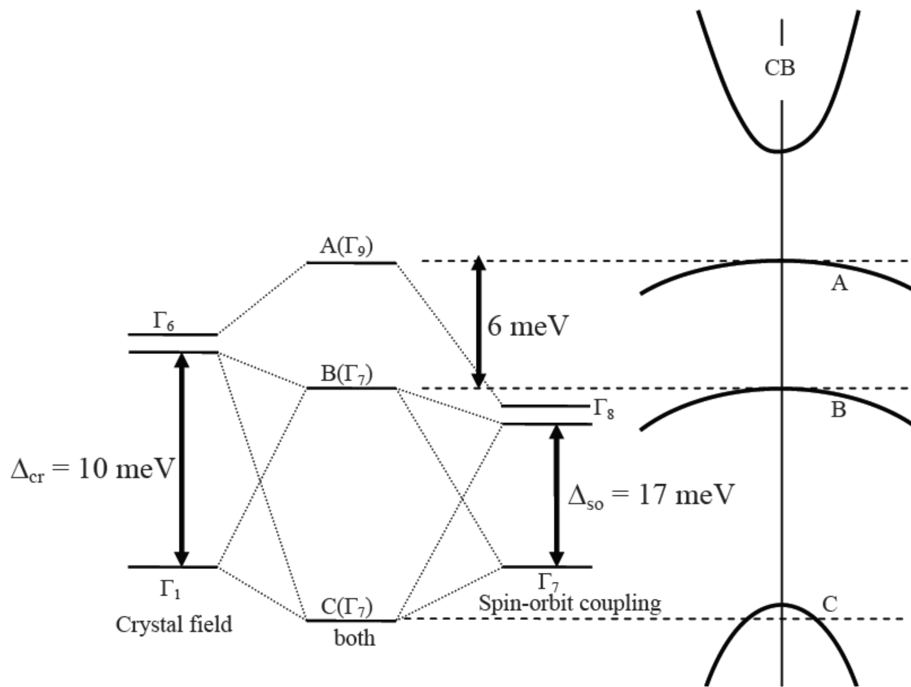

Figure 2.13 Schematic representation of the valence band splitting in wurtzite GaN

The band gap of binary compounds like GaN and AlN have been well established long back, but lot of ambiguity surrounded InN until the year 2001. Now a consensus has been reached on a value 50% lesser than previously obtained values of 1.9 eV [42]. Advances in epitaxial growth techniques have allowed fabrication of single crystal InN exhibiting a fundamental gap of ~ 0.62 eV. The band parameters for GaN, AlN and InN have been summed up in Table 2.II. For ternary compounds like AlGaN or InGaN the band gap is approximated by a quadratic equation:

$$E_g\,(AB) = xE_g\,(A) + (1-x)E_G\,(B) - x(1-x)b \qquad (2.17)$$

where, where $E_g\,(A)$ and $E_g\,(B)$ are the bandgap values for the two binary compounds. Various values can be found in the literature for the bowing parameter b as it strongly depends on the sample strain state and quality. The bowing parameter has value of 1- 1.5 eV [43, 44] in the case of AlGaN. In that context, some recent works have succeeded in establishing widely accepted values: 1.4 eV for InGaN alloys and 5-6 eV for the AlInN alloy. One nevertheless should keep in mind that Equation (2.17) is a phenomenological description. Recently, the bandgap of AlInN was successfully described with a composition dependent bowing parameter of the form b_{AlInN}=15.3/(1+4.8 x) [45].

Table 2. IV Band parameters of InN, GaN and AlN

	InN	**GaN**	**AlN**
E_g (@ 300 K)	0.66± 0.02	3.40	6.2
E_g (@ 0 K)	0.62± 0.02	3.48	6.28
α	0.414	0.909	1.999
β	454	830	1429
ε_0	15.3	8.9	8.5
ε_∞	8.4	5.35	4.77

In semiconductors, the band gap depends upon the temperature mainly due to the lattice expansion and the electron-lattice interaction. The evolution of the band gap with temperature can be represented by the expression below proposed by Varshni *et al.* [46]:

$$E_g(T) = E_g(0\,K) - \frac{\alpha T^2}{\beta + T} \qquad (2.18)$$

where, α and β are constants calculated taking into account the electron-phonon interaction. There are widespread values reported in the literature. In my calculations, I used the values published in ref. 41 for simulation of GaN and AlN heterostructures.

b) Effective masses

Figure 2.14 shows the bands around the Γ point for GaN and AlN. We observe that Γ9 symmetry is heavy along all the k directions, but Γ7 is strongly anisotropic, for instance, light along k_x and k_y directions and heavy along k_z for GaN. It is therefore important to account for such anisotropic effective masses during band engineering design of heterostructures. Table 2.V lists reported values of the average electron and hole effective masses of AlN and GaN materials.

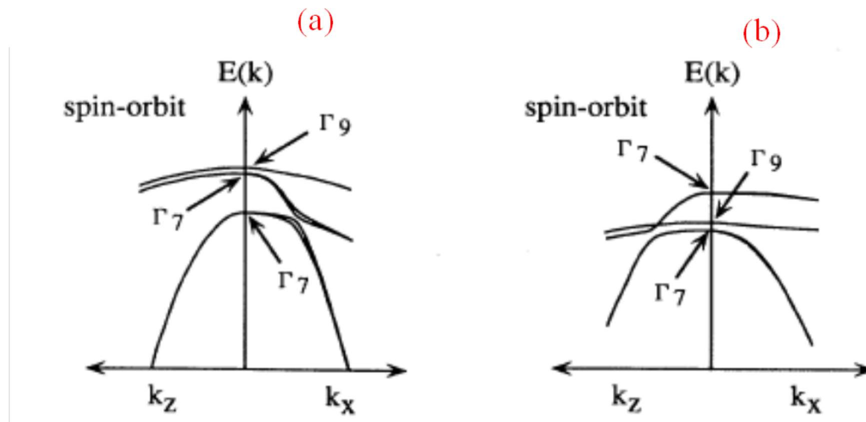

Figure 2.14 Valence band structure of (a) GaN (b) AlN, indicating the anisotropy

For small values of the ***k*** vector near the center of the Brillouin zone (Γ) the dispersion of the bands is expressed within the parabolic approximation

$$E(e,h) = E_{e,h}(k=0) - \frac{\hbar^2 k^2}{2m^*_{e,h}} \qquad (2.19)$$

where, m_e* and m_h* are the effective masses of the valence and conduction band, respectively.

Table 2.V Effectives masses for electrons (*me*/m0*), heavy (*mhh*/m0*) and light (*mlh*/m0*) hole parallel (‖) and perpendicular (⊥) to the polar [0001] axis in isotropic approximation around the point. Values are taken from ref.47

	m_e^*/m_0 (⊥)	m_e^*/m_0 (‖)	m_{hh}^*/m_0 (⊥)	m_{hh}^*/m_0 (‖)	m_{lh}^*/m_0 (⊥)	m_{lh}^*/m_0 (‖)
GaN	0.2	0.2	1.6	1.1	0.15	1.1
AlN	0.4	0.4	10.42	3.53	0.24	3.53
InN	0.07		1.63		0.27	

c) Band offsets

Heterostructures, with band discontinuities for valence band (VBO) and conduction band (CBO), have dual importance optically and electrically: optically they can be used to form waveguides and electrically to observe quantum phenomena. For the GaN/AlN, InN/GaN and InN/AlN systems, the band offset presents a type I configuration, i.e. in a quantum well, both electrons and holes are confined in the smaller band gap material. Tables 2.VI, 2.VII and 2.VIII give the theoretical and experimental values of band offsets for different binary compound combinations.

Table 2. VI GaN/AlN valence band offset (VBO) and conduction band offset (CBO)

CBO (eV)	**VBO (eV)**	**Details and refs.**
1.8	0.8	GaN in-plane lattice [48]
-	0.87	Relaxed GaN/AlN[49]
2.1	0.7±0.24	[50]
1.78	**-**	[51]

Table 2. VII InN/GaN band offsets

CBO (eV)	**VBO (eV)**	**Details and refs.**
2.2±0.1	0.5	[52]
2.22±0.1	0.58±0.08	[53]
1.82	0.85	[54]

Table 2. VIII InN/AlN band offsets

CBO (eV)	**VBO (eV)**	**Details and refs.**
4.0±0.2	1.52±0.17	[53]
2.45	1.81±0.2	[47] ,[52]

2.2 Defects in III-nitrides structures

In general, a defect in a semiconductor crystal is defined as a lack of crystal perfection in a certain region of the material. The properties of materials are often controlled by defects and impurities. This is particularly true in the case of semiconductors, where the incorporation of impurities in small concentrations determines the electrical conductivity. Defects in semiconductors can be classified according to their geometrical configuration into two categories: (a) point defects (0

dimensional) and (b) extended defects (1–3 dimensional). Point defects are usually constrained to one, or at most a few atoms and can be divided into native defects and impurities, as well as their complexes. In later case, region of defects can be extended to whole thickness of the materials. Extended defects include dislocations (1D), stacking faults and grain- or phase boundaries (2D), as well as larger structures such as atomic precipitates or larger voids (vacancy clusters) in the crystal structure (3D). The fabrication of *p*-type and *n*-type doped layers underlies the design of virtually all electronic and optoelectronic devices. To achieve such control, comprehensive knowledge of the fundamental processes that control doping is required. In order to understand the physics of defects and their role and control, one needs to understand the following topics which are still open in semiconductor research community:

a) **Defects Observation** with various Spectroscopy techniques such as Deep Level Transient Spectroscopy (DLTS), Noise measurement spectroscopy (NS), Photoluminescence (PL), Positron Annhilation Spectroscopy (PAS) and microscopy techniques such as Transmission Electron microscopy (TEM), Scanning Electron microscopy (SEM), Atomic Force Microscopy (AFM) etc.

b) **Defects correlation** with theoretical calculation such as Density Functional Theory (DFT) in correlation with Local Density Approximation (LDA) and experimental results

c) **Role of Defects** on materials/device properties in order to understand the problems and improvement

d) **Control on Defects** by acquiring enough information from above mentioned points in order to achieve better properties in materials/devices

2.2.1 Type of Defects

Here we, revise the brief information on different type of defects:

a) Point Defects

Point defects are usually constrained to one or at most a few atoms and can be divided into native defects and impurities, as well as their complexes. Impurities are foreign atoms in the lattice of the host material, and can be present either on lattice sites, i.e. substitutional or interstitial positions. Native defects are formed by mere modifications of the ideal
lattice structure. These can be empty lattice sites, i.e. vacancies, or host atoms which are displaced into interstitial positions, i.e. self-interstitials. In the case of compound semiconductors such as InN, GaN also antisite defects can be formed by atoms occupying opposite sub-lattice sites. Frenkel defects are nearby pairs of vacancies and interstitials. Schottky defects are vacancy pairs created by the simultaneous removal of a two opposite
atoms in compound semiconductors.

b) Shallow and Deep levels

In order to understand the influence of defects on electronic properties they need to classified in terms of the electronic states within the bandgap. The electrical characteristics of defects are mainly given by the position of their electron states in the energy gap. Shallow defects are called those whose levels lie in close vicinity of band edges (few tens of milli-electronvolts (meV) from the

respective band edges), while deep defects have electron states lying further from the bands. Shallow states resemble hydrogenic atoms, with energy levels and Bohr radii correspondingly scaled due to the relative dielectric constant of the material and to the effective electron mass. Shallow level defects are efficient donors (acceptors) and can be introduced intentionally for n- (p-) doping of a semiconductor. In contrast, deep level defects are highly localized defects that constitute severe perturbations of the local electronic structure and induce energy levels deep inside the bandgap. As the energy required to induce transitions from the nearest band edges to the defect level is usually much larger than the thermal energy (25 meV at 300 K), thus deep level states do not enhance the conductivity. However, they can act as efficient carrier traps and recombination centers. One typical example is shown for GaN in Fig. 2.15 [55].

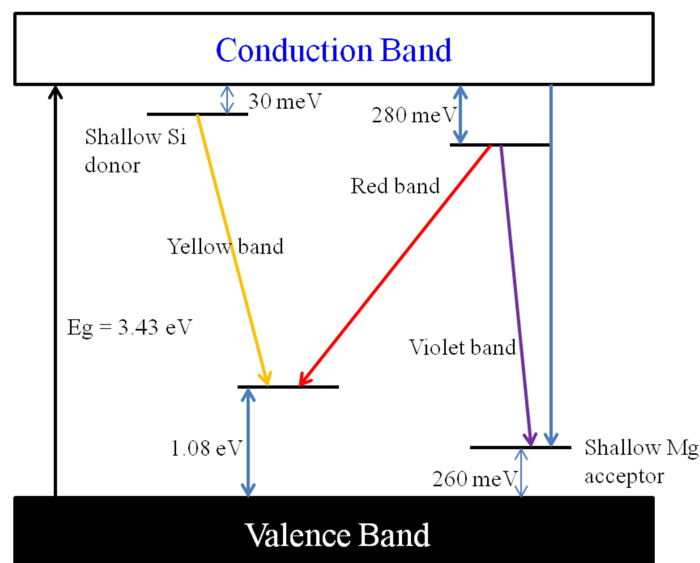

Figure 2.15 Presence of shallow and deep levels in GaN semiconductor

c) Extended Defects

Extended defects include dislocations (1D), stacking faults and grain- or phase boundaries (2D), as well as larger structures such as atomic precipitates or larger voids (vacancy clusters) in the crystal structure (3D).

Dislocations can be divided into two extreme cases, i.e., screw and edge-type dislocations. A dislocation can be described by the so-called Burgers vector. The edge dislocation has ***b*** orthogonal to the dislocation line, whereas the screw dislocation has ***b*** parallel to the dislocation line, shown in Fig. 2.16. Edge dislocations can be imagined as an extra half-plane of atoms inserted midway through the crystal lattice. To visualize a screw dislocation, a crystal is cut half-way along a lattice plane with one half slipped across the other. Edge and screw dislocations can be identified by their Burgers vector, which represents the magnitude and direction of the lattice distortion connected to the introduction of the dislocation. In edge dislocations, the Burgers vector is normal to the dislocation line direction, in screw dislocations parallel. Dislocations with both parallel and perpendicular component in the burgers vector are mixed dislocations.

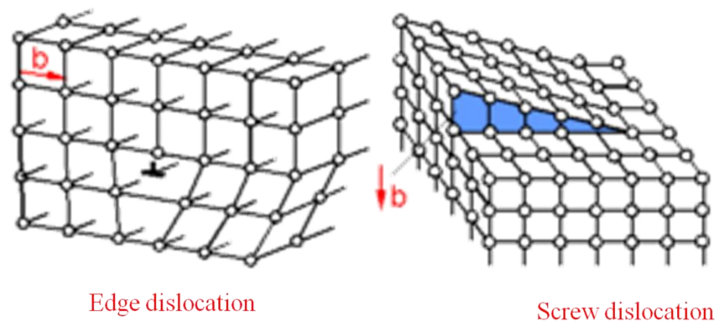

Figure 2.16 Representation of Edge and Screw dislocation with respect to burger vector

The electrical activity of dislocations is an important parameter similar to point defects; it has been proposed that dislocations may introduce electronic states in the bandgap. Scattering at dislocations can affect the electron mobility. In GaN, it is found that, due to the high dislocation density, vertical transport is favoured with respect to lateral transport. Moreover, the scattering efficiency of dislocations depends on their charge, which, in turn, depends on the free carrier concentration. In III-nitride, dislocation has been main cause of leakage in HEMT devices and efficiency droop in optoelectronic devices. Similarly to point defects, dislocations provide non-radiative recombination paths which can be harmful in optoelectronic devices, and represented one of the major degradation and failure sources in GaAs based LEDs and lasers. Despite huge dislocation densities, GaN-based LEDs show very efficient luminescence properties.

Stacking faults and grain- or phase boundaries are the main planar defects. A stacking fault is formed by a spatially limited alteration of the stacking order of the atomic planes. Grain and phase boundaries describe the sudden change of the crystallographic direction or phase. Three dimensional defects include, e.g., atomic precipitates or larger voids (vacancy clusters) in the crystal structure. One typical example is shown in Fig. 2.17 as proposed by Potin et al. [56] for GaN on sapphire.

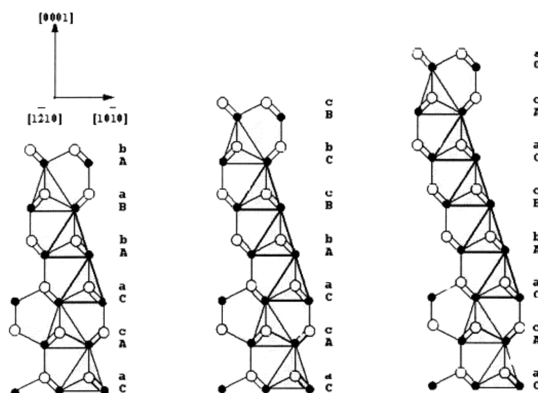

Figure 2.17 Representation of stacking faults for GaN/sapphire [56]

2.2.2 Thermodynamics of Defects

Thermodynamics is an essential tool for understanding the thermal properties of defects. In general, all kind of properties of defects can be characterized by using thermodynamics laws. The parameters such as defect concentration, diffusivity of impurity atoms and annihilation strongly depends on temperature variation.The concentration of charged defects (particularly in GaN and

alloys), moreover, depends on the Fermi energy, which, in turn, depends mostly on the concentration of shallow dopants in the material.

At thermal equilibrium, the Gibbs free energy *G* of a system is defined as the difference between the enthalpy *H* and the product of absolute temperature *T* and entropy *S*. The change in Gibbs free energy formation of a defect, ΔG_F, in a chemical reaction is given as:

$$\Delta G_F = \Delta H_F - T\Delta S_F \qquad (2.20)$$

where, H_F is the defect formation energy enthalpy, S_F is the formation entropy. The introduction of defects increases the crystal's enthalpy as well as its entropy. Therefore, defects will be formed or annihilated until the thermal equilibrium is reached, i.e., the Gibbs free energy is minimized (ΔG_F= 0). At thermal equilibrium, the concentration of a defect can be calculated as

$$C = N_{conf} N_{sites} \exp(-G_F / k_B T) \qquad (2.21)$$

Where, N_{conf} is number of equivalent configuration of defects and the N_{sites} is number of available sites per unit volume and k_B is the boltzman's constant. For practical calculations using DFT, G_F is often identified with defect formation energy, E_f.
If the defect is charged, as in the case of a donor-like defect which can donate *s* electrons, the formation enthalpy depends on the Fermi energy as:

$$H_F = H_{F0} + \sum_{n=0}^{s-1} (E_F - E^{n+}) \qquad (2.22)$$

where E^{n+} is the energy of the n+1/n transition state, E_F is the Fermi energy and H_{F0} is the formation enthalpy of the neutral defect.

The defect formation energy E_f , defines the equilibrium concentration of a certain defect at a particular temperature; a high formation energy corresponds to a low defect concentration etc. For increasing Fermi level, the formation energy of a negatively (positively) charged defect decreases (increases). Therefore, the formation of charged donors (acceptors) is less favorable under n-type (p-type) conditions, but becomes advantageous when approaching p-type (n-type) conductivity. This leads to the concept of self-compensation, i.e., the compensation of dopant-induced free carriers by the formation of native point defects.

2.2.3 Defects and HEMTs key problems

As an emerging technology, nitrides has shown very good success in some area of markets but still lag with some key problems to achieve its full potential for various applications. As mentioned in above discussions that high number of dislocations causes high leakage current in HEMTs devices and degrades the device performances which are an important issue for reliability. The key issues with Nitride semiconductors are (a) problems with growth of high quality structures, (b) defect formation/generation at high temperature in devices. Thus, temperature control needs to be optimized for better growth and device design depending on the defect generation source. The main problem with growth of nitrides has been the lack of a native substrate for the growth. The common substrates are sapphire, SiC, and Si which are commonly used for HEMT devices and as a consequence Dislocation density is really high and order of 10^8 -10^9 cm^{-2}. These substrates do not have wurtzitic structure, so growth and optimization on these substrates has been a long standing area of research. In last years, near-native substrates have been achieved through growth of thick GaN films, typically grown by MOCVD or HVPE, on a foreign substrate, which is then removed

using laser ablation, removal of a sacrificial layer, or other mechanism. These near-native substrates have low threading dislocation densities in the order of 10^6 cm^{-2}, but their cost is so high which can't be used for commercialization as per now. The evidence of the leakage caused by dislocations is evident in Fig. 2.18 where the threading dislocation-mediated carrier transport in heterojunction bipolar transistors (HBT) causes a pronounced increase in leakage current over the window region where the TDD concentration is significantly higher than the wing region [57]. Further evidence of the role of dislocations is found in several scanning probe and transmission electron microscopy experiments. Hsu *et al.* used scanning Kelvin force, scanning capacitance, and conductive atomic force microscopy to suggest that screw dislocations are the primary source of leakage current in Ga-rich MBE-grown films while mixed and pure edge dislocations are negatively charged [58, 59]. Cherns *et al.* determined that edge dislocations were negatively charged in *n*-type MOCVD-grown GaN and positively charged in *p*-type material using electron holography [60].

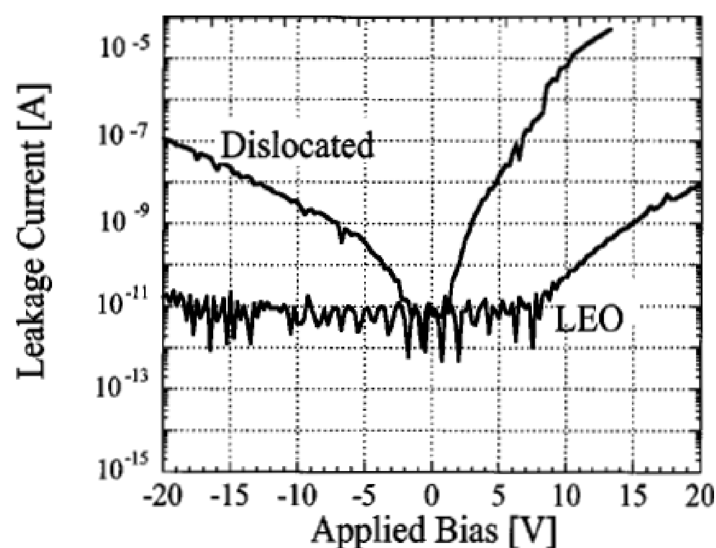

Figure 2.18 Variation of leakage current of heterojunction bipolar transistors (HBT) on lateral epitaxial overgrowth (LEO) window and wing regions. The leakage is reduced for the wing region by four orders of magnitude as compared to the window region [57].

Several issues can arise in HEMT devices that can affect device performance and operation. Many of these problems dictate device design considerations such as field plating to mitigate the problems, but this is done at the expense of reduced max operating frequency. These defects can be categorized as DC or RF according to which frequency range where they are primarily seen. Gate and buffer leakage (DC phenomena) reduce the operating voltage range by limiting the gate voltage for gate leakage and the drain-source voltage for buffer leakage. Several deviations from the expected RF performance of HEMTs exist and are generally termed as dispersion. The dispersive effects can only be caused by defects and self-heating, so although the focus here is on defect-related phenomena self-heating should not be avoided.

According to Morkoç [61], the most common and pronounced effect in HEMTs is gate lag. Gate lag is used to describe the slow transient response of the drain current and typically refers to a change in gate voltage to more positive values with a corresponding slow increase in drain current. Because the drain current increases with time, self-heating cannot be the source as increased temperature results in increased electron-phonon scattering that results in decreased current flow [61]. Therefore variations in the gate potential must cause trapping/detrapping of defects under the

gate or in the access regions, but specific defects have yet to be identified [61]. An example of the temporal dependence of the drain current on the gate switching is shown in Fig. 2.19. The gate lag exhibits a bias dependence evidenced by the differences in response in Fig. 2.19 *a* and *b* where it is clear that multiple onsets are visible indicative of multiple traps contributing to the drain current response. Several type of failures are observed by researcher in recent years on HEMT devices such as High voltage gate stress, high voltage drain-source, high time stress and found the generation of defects and appearance of some spots near Drain-Gate region [62, 63] and confirmed these tests with various experimental techniques such as Scanning probe microscopy (SPM), Electroluminescence (EL) etc. The passivation and surface treatments themselves can also be a potential source of degradation as SiN_x has been shown to potentially deteriorate with time [61]. Surface passivation has been an integral part of reducing dispersion increasing output power density [64] but the long term reliability is not as well understood yet.

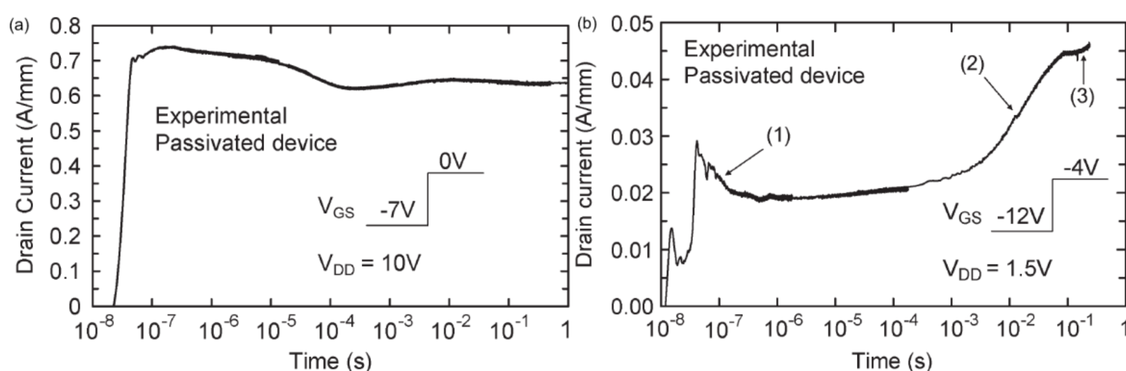

Figure 2.19 Experimental drain-current versus time waveformin response to a constant drain voltage of 10 V and gate-source voltage stepped from (a) -7 to 0 V and (b) -12 to -4 V. The HEMT was in series with a 50 - resistor attached to the drain terminal. This HEMT exhibits varying degrees of gate-induced lag due to trapped charge [65].

The source of these failures is an open question with many possible reasons. Fig. 2.20 shows potential mechanisms contributing to HEMT failure and the regions of the device where this is from a more device perspective. From a more materials aspect, the role of point defects, point defect formation, the high dislocation densities, interface and surface-related defects, and the sources of the defects is highly essential to be well understood.

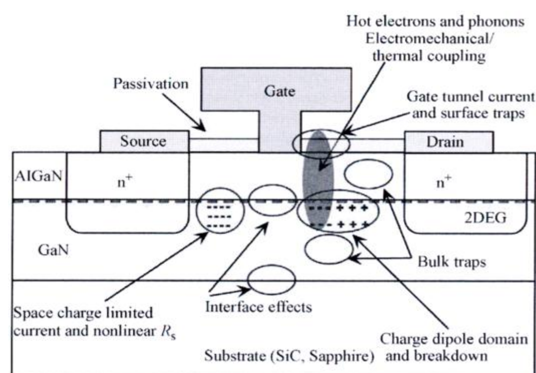

Figure 2.20 Possible mechanisms contributing to HEMT degradation and failure are represented [60]

References

1. O. Ambacher, *J. Phys. D*, 31, 2653 (1998)
2. N. Biyikli, O. Aytur, I. Kimukin, T. Tut, and E. Ozbay, Appl. Phys. Lett. 81, 3272 (2000)
3. H. Morkoç, "*Handbook of nitride semiconductors and devices: electronic and optical processes in nitrides* " Weinheim:Wiley-VCH, vol. 1 (2008)
4. S. J. Pearton, C. R. Abernathy, and F. Ren, "*Gallium nitride processing for electronics, sensors, and spintronics*" Springer-Verlag: London (2006)
5. V. Cimalla, J. Pezoldt, and O. Ambacher,J. Phys. D 40, 6386 (2007)
6. R. D. Shannon and C. T. Prewit, Acta Crysta B 25, 925 (1969)
7. K. Lorentz, N. Franco, E. Alves, I. M. Watson, R.W. Martin and K.P. O'Donnell, Phys. Rev. Lett. 97, 085501 (2006)
8. http://www.inlustra.com/technology/nonpolar.html
9. M. Seelmann-Eggebert, J. L. Weyher, H. Obloh, H. Zimmermann, A. Rar, S. Porowski, Appl. Phys. Lett. 71, 2635 (1997)
10. M. Sumiya, M. Tanaka, K. Ohtsuka, S. Fuke, T. Ohnishi, I. Onkubo, M. Yoshimoto, H. Koinuma, M. Kawasaki, Appl. Phys. Lett. 75, 674 (1999)
11. X. Q. Shen, T. Ide, S.-H. Cho, M. Shimizu, S. Hara, H. Okumura, S. Sonoda, S. Shimizu, Jpn. J. Appl. Phys. 39, L16 (1999)
12. P. Han, Z. Wang, X. Duan, and Z. Zhang, Appl. Phys. Lett. 78, 3974 (2001)
13. D. Huang, P. Visconti, K. M. Jones, M. A. Reshchikov, F. Yun, A. A. Baski, T. King, and H. Morkoç, Appl. Phys. Lett. 78, 4145 (2001)
14. T. Sasaki and T. Matsuoka, J. Appl. Phys. 64, 4531 (1988)
15. R. B. Capaz, H. Lim, and J. D. Joannopoulos, Phys. Rev. B 51, 17755 (1995)
16. J. Lu, L. Haworth, D. I. Westwood, and J. E. Macdonald, Appl. Phys. Lett. 78, 1080 (2001)
17. E. Monroy, E. Sarigiannidou, F. Fossard, N. Gogneau, E. Bellet-Amalric, J.-L. Rouvière, S. Monnoye, H. Mank, and B. Daudin, Appl. Phys. Lett. 84, 3684 (2004)
18. H. Morkoç Roberto Cingolani Bernard Gil Solid-State Electronics 43, 1753 (1999)
19. C. Wood, D. Jena, "*Polarization Effects in Semiconductors: From Ab InitioTheory to Device Applications*", Springer USA (2010)
20. F. Bernardini, V. Fiorentini and D. Vanderbilt Phys. Rev. B 56 R10 024 (1997)
21. O. Ambacher, J. Majewski, C. Miskys, A. Link, M. Hermann, M. Eickhoff, M. Stutzmann, F. Bernardini, V. Fiorentini, V. Tilak, B. Schaff and L. F. Eastman, J. Phys.: Condens. Matter 14, 3399 (2002)
22. K. Kim, W. R. L. Lambrecht, and B. Segall, Phys. Rev. B 53, 16310 (1996)
23. A. F. Wright, J. Appl. Phys. 82, 2833 (1997)
24. Y. Takagi, M. Ahart, T. Azuhato, T. Sota, K. Suzuki, and S. Nakamura, Physica B 219, 547 (1996).
25. C. Deger, E. Born, H. Angerer, O. Ambacher, M. Stutzmann, J. Hornsteiner, E.Riha, and G. Fischerauer, Appl. Phys. Lett. 72, 2400 (1998)
26. R. Neuberger, G. M¨uller, O. Ambacher and M. Stutzmann, Phys. Status Solidi RRL016 (2001)
27. U. Karrer, O. Ambacher and M. Stutzmann, Appl. Phys. Lett. **77,** 2012 (2000)
28. H. Amano, N. Sawaki, L. Akasaki, and Y. Toyoda, Appl. Phys. Lett., 48, 353 (1986).
29. S. Nakamura, S. Pearton, and G. Fasol, "*The Blue Laser Diode : The Complete Story"* (Springer-Verlag, Berlin, (2000)
30. J. Jang, C. Lee, S. Park, T. Seong, and I. Ferguson, Journal of Electronic Materials, 31, 903 (2002)
31. P. Hartlieb, A. Roskowski, R. Davis, and R. Nemanich, J. App. Phys., 91,9151 (2002)

32. D. Wang, S. Feng, C. Lu, A. Motayed, M. Jah, S. Mohammad, K. Jones, and L. Salamanca-Riba, J. App. Phys, 89, 6214 (2001)
33. C. Lee and H. Kao, Appl. Phys. Lett., 76, 2364 (2000).
34. W. Lu, J. Yang, M. Khan, and I. Adesida, IEEE Transactions on Electron Devices, 48,581 (2001)
35. H. Xing, S. Keller, Y. Wu, L. McCarthy, I. Smorchkova, D. Buttari, R. Coffie, D. Green, G. Parish, S. Heikman, L. Shen, N. Zhang, J. Xu, B. Keller, S. DenBaars, and U. Mishra, Journal of Physics: Condensed Matter, 13, 7139 (2001)
36. V. Tilak, B. Green, V. Kaper, H. Kim, T. Prunty, J. Smart, J. Shealy, and L. Eastman, IEEE Electron Device Letters, 22, 504 (2001)
37. R. Armitage, Q. Yang, H. Feick, J. Gebauer, E. Weber, S. Shinkai, and K. Sasaki, Appl. Phys. Lett.,, 81, 1450 (2002)
38. L. Liu and J. Edgar, Materials Science & Engineering R, 37, 61 (2002).
39. M. Suzuki, T. Uenoyama, A. Yanase, Phys. Rev. B 52, 11 (1995), 8132 (1995)
40. Y. Chen and J. Washburn. Phys. Rev. Lett. 77, 4046 (1996)
41. I. Vurgaftman, J. R. Meyer, L. R. Ram-Mohan, J. Appl. Phys. 89 (11), 5815 (2001)
42. Q. Guo and A. Yoshida, Jpn. J. Appl. Phys. 33, 2454 (1994)
43. G. Steude, D.M. Hofmann, B.K.Meyer, H. Amano, and I. Akasaki, phys. stat. sol. (b) 205, R7 (1998)
44. S. R. Lee, A. F. Wright, M. H. Crawford, G. A. Petersen, J. Han and R. M. Biefeld, Appl. Phys. Lett. 74, 3344 (1999)
45. E. Iliopoulos, A. Adikimenakis, C. Giesen, M. Heuken, and A. Georgakilas, Appl. Phys. Lett. 92, 191907 (2008).
46. Y. P. Varshini, Phys.34, 149 (1967)
47. J. Wu, W. Walukiewicz, K. M. Yu, J. W. Ager, E. E. Haller, Hai Lu, William J. Schaff, Y. Saito, and Y. Nanishi, Appl. Phys. Lett. 80, 3967 (2002)
48. D. Cociorva, W. G. Aulbur and J. W. Wilkins, Solid State Communications 124, 63 (2002)
49. N. Binggeli, P. Ferrara and A. Baldereschi, Phys. Rev. B 63, 245306 (2001)
50. G. Martin, A. Botchkarev, A. Rockett, and H. Morkoç, Appl. Phys. Lett. 68, 2541 (1996)
51. A. Helman, M. Tchernycheva, A. Lusson, E. Warde, F. H. Julien, Kh. Moumanis, G. Fishman, E. Monroy, B. Daudin, Le Si Dang, E. Bellet-Amalric, D. Jalabert, Appl. Phys. Lett. 83, 5196 (2003)
52. C. F. Shih, N. C. Chen, P. H. Chang and K. S. Liu, Appl. Phys. 44, 7892 (2005)
53. P. D. C. King, T. D. Veal, C. E. Kendrick, L. R. Bailey, S. M. Durbin, and C. F. McConville, Phys. Rev. B 78, 033308 (2008)
54. Z. H. Mahmood, A. P. Shah, A. Kadir, M. R. Gokhale, S. Ghosh, A. Bhattacharya, B. M. Arora, Appl. Phys. Lett. 91, 152108 (2007)
55. B.K. Meyer, D.M. Hofmann, H. Alves, Materials Science and Engineering B71, 69 (2000)
56. V. Potin, B. Gil, S. Charar, P. Ruterana, G. Nouet, Materials Science and Engineering B 82, 114 (2001)
57. L. McCarthy, I. Smorchkova, H. Xing, P. Fini, S. Keller, J. Speck, S. P. DenBaars, M. J. W. Rodwell, and U. K. Mishra, Appl. Phys. Lett., 78, 2235 (2001)
58. J. W. P. Hsu, M. J. Manfra, R. J. Molnar, B. Heying, and J. S. Speck, Appl. Phys. Lett., 81, 79 (2002)
59. B. S. Simpkins, E. T. Yu, P. Walteriet, and J. S. Speck, Appl. Phys. Lett., 94, 1448 (2003)
60. D. Cherns and C. G. Jiao, Phys. Rev. Lett. 87, 205504 (2001)
61. Morkoç, "*Handbook of nitride semiconductors and devices: electronic and optical processes in nitrides*" Weinheim: Wiley-VCH, vol. 3.(2008)
62. R. Coffie, Y. Chen, I. Smorchkova, M.Wojtowicz, Y. Chou, B. Heying, and A. Oki, *44th Annual IEEE Internationa Reliability Physics Symposium Proceedings*, (2006).

63. G. Meneghesso, G. Verzellesi, F. Danesin, F. Rampazzo, F. Zanon, A. Tazzoli,M. Meneghini,and E. Zanoni, IEEE Trans. Device Mater. Rel. 8, 332 (2008)
64. B. Green, K. Chu, E. Chumbes, J. Smart, J. Shealy, and L. Eastma, IEEE Electron Device Lett., vol. 21, 268 (2000)
65. M. Faqir, G. Verzellesi, A. Chini, F. Fantini, F. Danesin, G. Meneghesso, E. Zanoni, and C. Dua, IEEE Trans. Device Mater. Rel. 8, 240 (2008)

Chapter 3

Experimental techniques

In this chapter, I mainly discuss the primary tools which have been used for characterization in this thesis. The chapter mainly discusses the electrical characterization tool like IV, CV and defect related characterization-DLTS and optical characterization by absorption based spectroscopy methods.

3.1 Current-voltage characterization

Current-Voltage (I-V) characterization is a basic and important experimental technique in semiconductor device physics. First, the I-V characteristics give information about the operation of the sample as a device. For example, the I-V characteristics of a diode, evidencing its rectifying properties, significantly differ from the I-V of an Ohmic resistor; the I-V of a transistor evidences which the amplification or logical capabilities of the device are, and many other examples could be mentioned. Secondly, the I-V characteristics give a significant amount of physical information. From the analysis of I-V data it is possible to draw conclusions about the presence of defects, about the quality of the contacts, the potential barriers governing the transport of charge, the presence of hetero-interfaces, etc. In the following, the main applications of this characterization will be shortly revised. For an in-depth analysis, many handbooks on semiconductor materials and devices offer the details [1, 2, 3]

3.1.1 Schottky Contacts

Schottky and Mott independently suggested a model for the rectification mechanism and pointed out that the observed direction of rectification could be explained by supposing that electrons passed over a potential barrier through the normal process of drift and diffusion.

Theory of Rectifying Metal-Semiconductor Contacts

The basic theory of these contacts is presented in ref. 3 and 4. Figure 3.1 shows a schematic of the band structure of an unbiased metal semiconductor contact.
The Schottky-Mott theory is expressed as follows:

$$\phi_b = \phi_m - \chi_s \qquad (3.1)$$

where,

$\phi_b = contact\, barrier\, height\, (at\, zero\, bias)$

$\phi_m = work\ function\, of\ the\, metal$

$\chi_s = electron\, affinity\, of\ the\, semiconductor$

Electron affinity can be expressed as

$$\chi_s = \phi_s - (E_c - E_f) \tag{3.2}$$

where,

$\phi s = work\ function\, of\ the\, semiconductor$

$E_c = conductiona\, band\, energy, in\, eV$

$E_f = Fermi\, energy\, level, in\, eV$

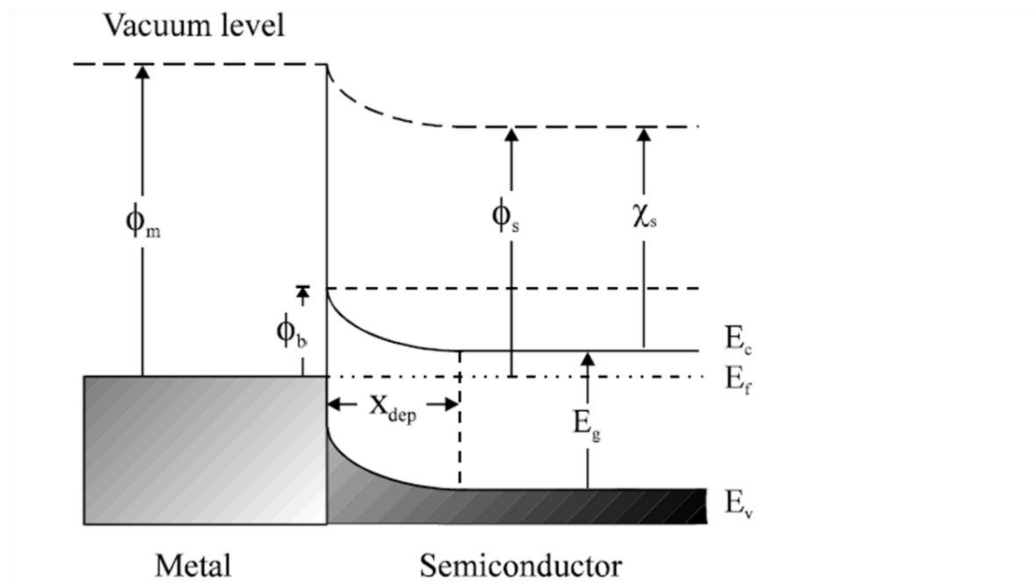

Figure 3.1 Unbiased band structure of a metal/n-type semiconductor contact

ϕ_b is the barrier encountered by electrons in the metal whereas the built-in potential V_{bi}, encountered by electrons in the semiconductor, is given by:

$$\begin{aligned} V_{bi} &= \phi_m - \phi_s \\ &= \phi_b - (E_c - E_f) \end{aligned} \tag{3.3}$$

This theory is rather simplistic since it assumes ideal conditions where dipole surface contributions to the barrier height and the electron affinity are thought to be unchanged when the metal and the semiconductor are brought into contact. It also assumed that there are no chemical reactions or physical strains created between the two when they are brought into contact.

In practice, however, surface dipole layers do arise. This is because at the surface of a solid the atoms have neighbours on one side only. This causes a distortion of the electron cloud belonging to the surface atoms, so that the centres of the positive and negative charge do not coincide. It was discovered that φ_b does not depend on φm in contradiction to (eqn. 3.1). Thus, the assumption that the surface dipole keeps constant is not corrected. One of the first explanations for the departure of experiments from this theory was given in terms of localised surface states or "dangling bonds". The surface states are continuously distributed in energy [3] within the forbidden gap and are characterised by a neutral level, ϕ_0, such that if the surface states are occupied up to ϕ_0 and empty above ϕ_0, the surface is electrically neutral.

In general, the Fermi level does not coincide with the neutral level. Consequently, a net charge exists at the surface. In figure 3.1 an n-type semiconductor is brought into contact with a metal to form a Schottky diode. After the transfer of electrons to the conduction band of the metal the Fermi levels are coincident. Positively charged donor ions are left behind in this region which is practically stripped of electrons. If, in addition (and often in practice due to chemical etching/cleaning of the semiconductor prior to processing) there is a thin oxide layer between the metal and the semiconductor due to ambient conditions, the charge at the surface states together with its image charge on the surface of the metal will form a dipole layer. This dipole layer alters the potential difference between the semiconductor and the metal. Thus the modification to the Schottky-Mott theory is expressed as follows [4]:

$$\phi_b = \gamma(\phi_m - \chi_s) + (1-\gamma)(E_g - \phi_0) \qquad (3.4)$$

where,

$E_g = band\ gap\ of\ the\ semicondcutor, in\ eV$

$\phi_0 = position\ of\ neutral\ level (measured\ from\ the\ top\ of\ the\ valence\ band)$

and,

$$\gamma = \frac{\varepsilon_i}{\varepsilon_i + q\delta D_s} \qquad (3.5)$$

where,

$\varepsilon_i = permittivity\ of\ the\ oxide\ layer$

$\delta = thickness\ of\ oxide\ layer$

$D_s = density\ of\ surface\ states$

Hence if there are no surface states, Ds = 0 and γ= 1, (eqn. 3.4) becomes identical to (eqn. 2.1) (Original Schottky-Mott approximation). If the density of states is significantly high, γ is very small and ϕ_b approaches the value $(E_g - \phi_0)$. The small deviation from the Fermi level from the neutral level can produce a large dipole moment, which stabilises the barrier height by a negative feedback effect [4, 5]. When this occurs, the Fermi level is said to be "*pinned*" relative to the band edges by the surface states.

3.1.2 Current transport mechanisms in Schottky diodes

a) Thermionic Emission

The current transport through the device by emission over the Schottky barrier is a two-step process. First, the electrons are transported through the depletion region. by the mechanisms of diffusion and drift; secondly, they must undergo the emission over the barrier into the metal. This latter process is controlled by the number of electrons that impinge on unit area of the metal per second.

This is expressed in (eqn.3.6):

$$I = AA^*T^2.\exp(\frac{-q\phi_b}{kT}).(\exp(\frac{V_{eff}}{nkT})-1) \qquad (3.6)$$

where,

A= cross-sectional area of metal-semiconductor interface

$A^* = \frac{4\pi e m^* k^2}{h^3}$ = Modified Richardson's constant for metal/semiconductor interface
T =Temperature in kelvin
K= Boltzmann constant
q= electron charge
$V_{eff.}$= effective bias across the interface
n= ideality factor
The ideality factor (*n*) in (eqn. 3.6) gives a measure of the quality of the junction, which is highly metal deposition process dependent. For an ideal Schottky junction, n = 1. In practice, however, larger values are obtained due to the presence of non-ideal effects or components to the current through the junction. This type of current transport is commonly referred to as "*thermionic emission*" [6, 7].

b) Diffusion

The expression for the diffusion current is similar to that for the thermionic current; however, the saturation current has a weak dependence on the temperature and a strong dependence on the applied voltage in the diffusive model, while it depends mostly on the temperature in the thermionic model.
According to the the diffusion model the current-voltage characteristics are described by [1]

$$J = J_D \left\{ \exp\left(\frac{eV}{kT}\right) - 1 \right\} \quad where,$$
$$J_D = \frac{e^2 D_n N_c}{kT} \left(\frac{e(V_{bi} - V) 2N_D}{\varepsilon_s} \right)^{0.5} \exp\left(-\frac{e\phi_b}{kT} \right) \qquad (3.7)$$

where, D_n is the diffusion coefficient for electrons, N_C is the equivalent density of states in the conduction band, V_{bi} is the built-in potential.

c) Quantum Mechanical Tunneling

For a moderately to heavily doped semiconductor or for operation at low temperatures, the current due to quantum mechanical tunneling of carriers through the metal-semiconductor barrier may become the dominant transport process [6, 8]. For all except very low biases, the tunneling current, I_{tn}, can be represented by:

$$I_{tn} = I_{tns} \left(\exp\left(\frac{qV_{eff}}{E_0} \right) - 1 \right) \qquad (3.8)$$

where,
I_{tn} = Tunneling saturation current
E_0 = tunneling constant

The tunneling saturation current depends on temperature, barrier height and other semiconductor parameters. In the notation of Padovani and Stratton [6], E_o is given by

$$E_0 = E_{00} \coth\left(\frac{E_{00}}{kT}\right) \qquad (3.9)$$

where, E_{00} is tunneling parameter inherently related to material properties of the semiconductor and is expressed as:

$$E_{00} = \frac{qh}{4\pi} \cdot \sqrt{\frac{N_D}{m_n^* \varepsilon_0 \varepsilon_r}} \qquad (3.10)$$

where, h is the Planck's constant, N_D the doping concentration, m_n^* the effective mass of electron.

In the following we are mention some cases over mechanisms:

d) Soft breakdown: Dislocation-assisted tunneling

In certain circumstances, for example in case of a device with high dislocation density, tunneling mechanisms can be enhanced under reverse bias, which is also called *soft breakdown*. This case has been reported in InGaN blue LEDs grown on sapphire [9]. When this dislocation-assisted tunnelling occurs, the reverse I-V characteristics tend to have the form $I = V^m$.

e) Leakage current

The leakage current, I_{lk}, is another parallel component of the total current. It is caused by surface leakage and can usually be significantly reduced by various designs and fabrication techniques. In practice, it is the component monitors the metal/semiconductor interface altogether and is often thought of as a large leakage resistor, R_{lk}, in parallel to it. Thus, the leakage current can be expressed as :

$$I_{lk} = \frac{V_{eff.}}{R_{lk}} \qquad (3.11)$$

where, $V_{eff.}$ is the applied bias across the interface.

f) *Anomalously* high ideality factors

When the ideality factor is $n >> 2.0$, other factors than diffusion or recombination of carriers must be taken into account. One of the factors is tunnelling, as already mentioned. Another model [10] takes into account the formation of potential barriers at every heterointerface, from the metal-semiconductor contacts to the semiconductor-semiconductor junctions. Each of these junctions is characterized by its own ideality factor n_j. The current and the voltage drop $V_j >> kT$ at each junction are given by:

$$I = I_{sj} \exp\left[\frac{eV_j}{n_j kT}\right] \qquad (3.12)$$

The total votage drop can be expressed as $V = \sum_j V_j$, hence the I-V characteristics of the structure is described by

$$V = \sum_j V_j = \sum_j \left[n_j (kT/e) \ln I - n_j (kT/e) \ln I_{sj}\right] \qquad (3.13)$$

Thus, rearranging the terms, one has

$$\ln I = \frac{(e/kT)}{\sum_j n_j} V + \frac{\sum_j n_j \ln I_{sj}}{\sum_j n_j} \tag{3.14}$$

As the second summand in the above equation is constant, one obtains an effective ideality factor for the heterostructure given by the sum of the single ideality factors of each junction (p-n junction, unipolar heterojunctions and metal-semiconductor junctions).

3.1.3 Experimental setup

The I-V measurements have been performed with a Keithley 2400 sourcemeter. The computer program sets the following measurement parameters:

- bias interval V_{max}, V_{min}
- scanning step ΔV
- Δ_t time interval between bias change and meter reading.

The temperature at which the measurement is performed is controlled by the home made ISTA temperature controller. The typical experimental setup for the I-V characterization is shown in fig. 3.2.

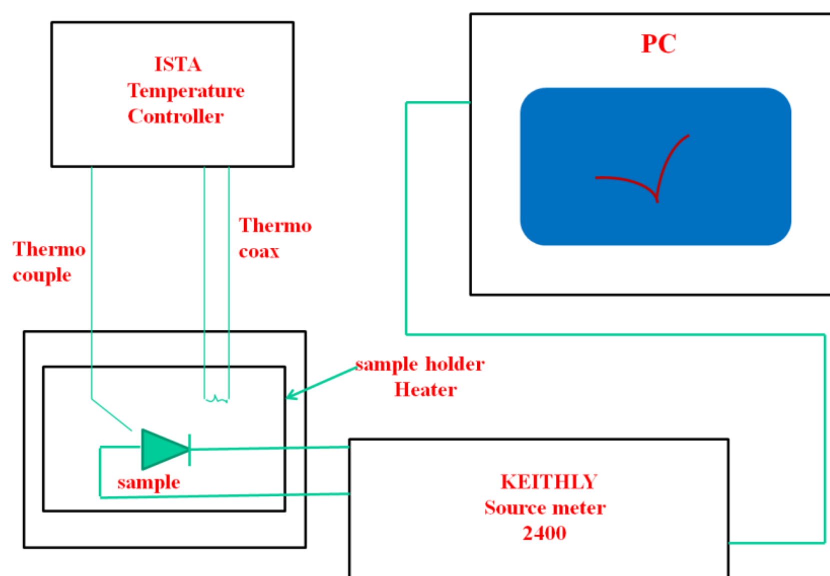

Figure 3.2 Block diagram for the I-V characterization

3.2 Capacitance-Voltage (C-V) characterization

The Schottky diode has characteristics that are similar to those of the p-n junction, except that for many applications it has a much faster response which can be desirable and depends on type of applications. The capacitance measurement allows calculating doping concentration, depletion layer width, trap concentration etc. The capacitance measurements change influenced by electronic

(trap) states during the reverse bias which is used for Deep level transient spectroscopy (DLTS) which will be explained in next section. A p-n as well as a Schottky junction in reverse bias are characterized by a capacitance, which it will be referred to as “depletion capacitance”. In the following, we will always consider the case of n-type semiconductors.

When a semiconductor is brought into contact with a metal, a barrier is formed in the semiconductor from which charge carriers are severaly depleted. The barrier layer is called the depletion layer and can be seen in figures 3.1. There is also depletion layer in the metal which is so small that it can be ignored in most of the cases [11]. We may consider the bulk region to be electrically neutral and approximate the boundary between the bulk and the depletion region to be sharp.

Here, the Pöisson’s equation is

$$\nabla D = \frac{N_d e}{\varepsilon_0} \qquad (3.15)$$

Where, D is the electric displacement and N_d is the doping concentration. From 3.15 the electric potential is determined as

$$\frac{d^2\phi}{dx^2} = -\frac{N_d e}{\varepsilon\varepsilon_0} \qquad (3.16a)$$

Where, x is the distance from the junction into the semiconductor. If we assume N_d to be constant we get

$$\phi = -\frac{N_d e}{2\varepsilon\varepsilon_0} x^2 \qquad (3.16b)$$

when we apply a reverse bias $V_{eff.}$ to the Schottky diode, the total potential becomes $V_{bi} + V_{eff.}$ where V_{bi} is the built-in potential of the junction. From 3.16b, the thickness of the layer (see fig. 3.1) is

$$W = \sqrt{\frac{2\varepsilon\varepsilon_0 (V_{bi} + V_{eff.})}{N_d e}} \qquad (3.17)$$

Therefore the stored charge in the depletion region results

$$Q = W N_d e A = A\sqrt{2\varepsilon\varepsilon_0 N_d e (V_{bi} + V_{eff.})} \qquad (3.18)$$

where, A is the cross sectional area of junction.

The capacitance of the junction is given by

$$C = \frac{dQ}{dV_{eff.}} = \frac{1}{2} A\sqrt{\frac{2\varepsilon\varepsilon_0 N_d e}{V_{bi} + V_{eff.}}} = \varepsilon\varepsilon 0 \frac{A}{W} \Rightarrow W = \varepsilon\varepsilon_0 \frac{A}{C} \qquad (3.19)$$

From eq. 3.19, it can be written that

$$\frac{1}{C^2} = \frac{2(V_{bi} + V_{eff.})}{A^2 e \varepsilon N_d} \qquad (3.20)$$

Thus, N_d can also be expressed as

$$N_d(W) = -\frac{C^3}{e\varepsilon\varepsilon_0 A^2}\left(\frac{dC}{dV_{eff.}}\right)^{-1} \qquad (3.21)$$

It turns out that these equations give accurate results despite the assumption that N_d is constant. With the known capacitance, it is necessary to develop the theory for capacitance transient spectroscopy-based techniques i.e. Deep level transient spectroscopy (DLTS) etc.

3.2.1 Series resistance and equivalent circuit of a Schottky diode in C-V measurements

Figure 3.3 shows the equivalent circuit of a Schottky diode. Two resistances, R_l are connected in parallel (nonlinear leakage resistance) and R_s is connected in series. The total impedance is then [3]

$$Z = \frac{R_l + R_s(1+\omega^2 C^2 R_l^{\ 2}) + j\omega C R_l}{1+\omega^2 C^2 R_l^2} \qquad (3.22)$$

In the LCR meter we have to use the approximation that we have a resistance connected either serial or parallel, not both. If we define C_m the value measured by the LCR meter (where we ignore R_s) we can calculate the real capacitance C by

$$\frac{C_m}{C} = \frac{1}{(1+\frac{R_s}{R_l})^2 + \omega^2 C^2 R_s^{\ 2}} \qquad (3.23)$$

If we know the approximated value of R_s. Where, ω is the test frequency during measurement.
If $R_s \ll R_l$, As expected at reverse voltage, then $C_m \approx C$.

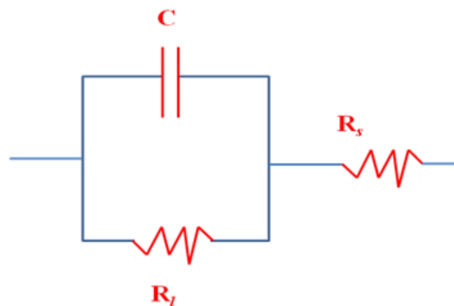

Figure 3.3 Equivalent circuit for Schottky diode

From the above eq. 3.23, one can see that for high values of the series resistance the measured capacitance is a decreasing function of the real capacitance. If not accounted for, this can seriously affect the interpretation of DLTS results, which are based on measurements of capacitance differences occurring at low temperatures.

3.2.2 Experimental setup

The block diagram of the instrumentation used for the C-V characterization of the samples analysed in this thesis is depicted in fig. 3.4. The building blocks of the setup are the Lakeshore 330 temperature controller, which makes it possible to perform measurements at different controlled temperatures, the Keithley 230 bias generator and the Keithley 3330 LCZ meter. The LCZ meter has operating frequencies ranging from 120 Hz to 105 Hz. Measurements with frequency 1MHz have also been performed by using a Boonton capacitance meter to optimize the

bias condition and DLTS results analysis. The measurements are driven by software, with the following parameters:

- The bias interval V_{max}, V_{min}
- The bias step ΔV
- The time interval Δt between two successive bias values
- The LCZ meter operating frequency f_{CAP}

The same setup can be used for slightly different measurements, such as capacitance-frequency (C-*f*) characterization and admittance spectroscopy.

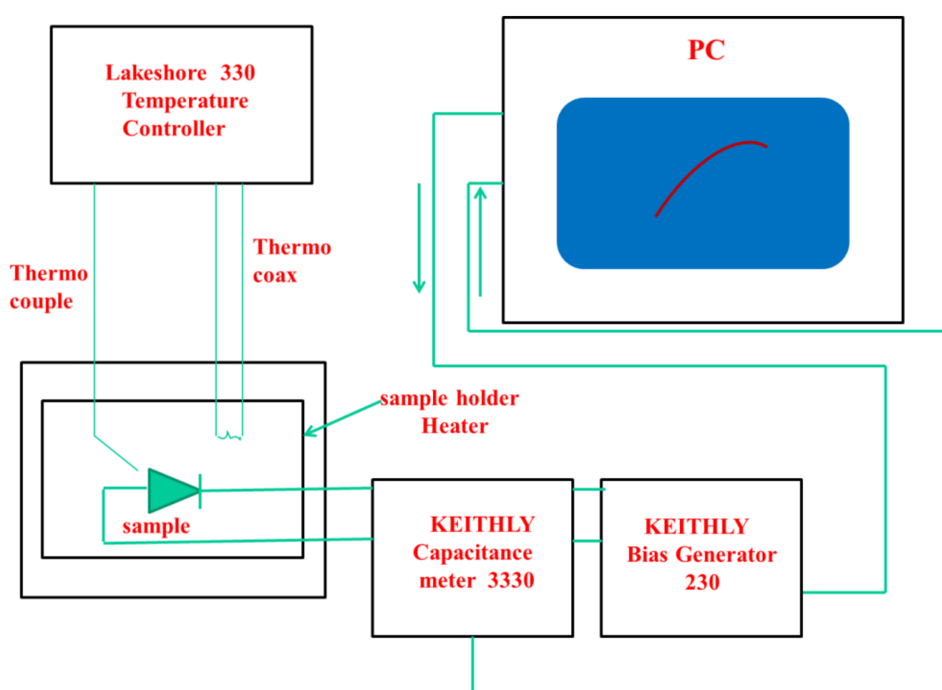

Figure 3.4 Block diagram for capacitance-voltage characterization

3.3 Thermal Spectroscopy

In order to understand the deep level transient spectroscopy (DLTS) working condition and analysis, it is important to understand the physics of carrier emission and capture which is discussed following:

3.3.1. Physics of Carrier emission and capture

The electronic levels within the gap of semiconducting materials can be determined by the emission and capture of carriers to trap levels. Electronic states are classified as shallow and deep states (details in chapter 1). Varying trap occupancy within the depletion region changes the fixed charge density to maintain the charge balance with a fixed bias applied to the sample, the depletion edge moves slightly. The small change in the depletion edge is detected by the change in capacitance, according to eq. (3.24). This section will introduce these relations and expand upon them to include all the concepts necessary for the basic understanding of processes involved in DLTS.

Four processes can occur at a deep level within the bandgap of a semiconductor to affect its occupancy. They are electron capture, electron emission, hole capture, and hole emission from the trap as depicted in processes (a)-(d) in Fig. 3.5, respectively. To solve for the rate at which the density of occupied traps n_T changes with time, the relationship between all of these possible events needs to be considered. The rate of electron capture is proportional to both the number of electrons in the conduction band n and the number of empty trap states p_T . The number of trap states empty of electrons p_T is equal to the total number of defect states n_T minus the number of defect states filled with electrons n_T . Since capture always increases the electron concentration of the defect, the rate of change is always positive and given by

$$\left.\frac{\partial n_T}{\partial t}\right|_{capture} = c_n | p_T n \qquad (3.24)$$

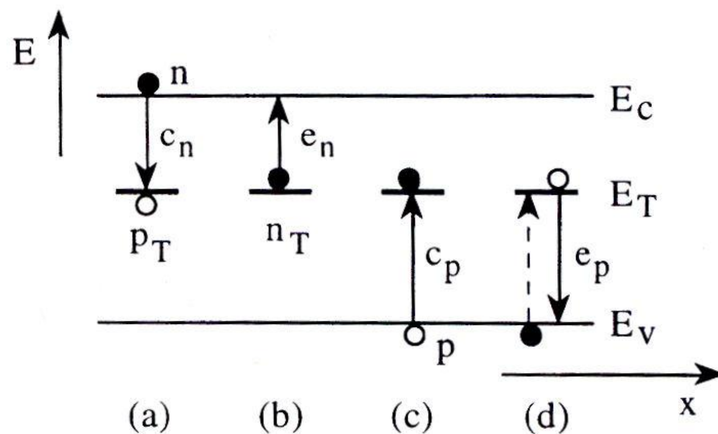

Figure 3.5 The processes possible for a deep level involving transitions to or from a band are (a) electron capture and (b) electron emission to conduction band and (c) hole capture and (d) hole emission to the valence band [12].

The constant c_n is known as the *electron capture coefficient* and has units of cm^3s^{-1}. Now, electron emission from the defect level to the conduction band is considered. Because the conduction band is mostly empty, the rate of emission is independent of the number of empty final states, and the rate is limited by the number of defects occupied by electrons. Thus,

$$\left.\frac{\partial n_T}{\partial t}\right|_{emission} = -e_n n_T \qquad (3.25)$$

In this case, e_n is the *electron emission rate* and has units of s^{-1}. Following the same argument for the valence band,

$$\left.\frac{\partial n_T}{\partial t}\right|_{capture} = -c_p n_T p$$
$$and \qquad (3.26)$$
$$\left.\frac{\partial n_T}{\partial t}\right|_{emission} = e_p p_T$$

where c_p is the *hole capture coefficient* and e_p is the *hole emission rate*. The change in occupancy of the defect considering all recombination-generation (R-G) processes is

$$\frac{\partial n_T}{\partial t} = \underbrace{\left(c_n n p_T - e_n n_T\right)}_{conduction\,band} - \underbrace{\left(c_p p n_T - e_p p_T\right)}_{valence\,band} \qquad (3.27)$$

Considering the *principle of detailed balance* under equilibrium conditions, the rate of capture and emission to each band must equal zero. This concept can be used to determine THE relationship between the capture coefficient and the emission rate

$$e_n = c_n n \tfrac{p_T}{n_T} = c_n n\left(\frac{N_T}{n_T} - 1\right) \qquad (3.28)$$

The Fermi-Dirac statistics can be used to establish the relationship between n_T and N_T in equilibrium where

$$\frac{n_T}{N_T} = \frac{1}{1+\exp\left(\frac{E_T - E_F}{kT}\right)} \qquad (3.29)$$

Fermi level position also dictates n and n_i yielding,

$$n = n_i \exp\left(\frac{E_F - E_i}{kT}\right) \qquad (3.30a)$$

$$n_i = N_C \exp\left(\frac{E_i - E_C}{kT}\right) \qquad (3.30b)$$

Thus, the relationship between c_n and e_n can be written as,

$$e_n = c_n N_c \exp\left(\frac{E_T - E_C}{kT}\right) \qquad (3.31a)$$

or for the valence band using similar arguments,

$$e_p = c_p N_V \exp\left(\frac{E_V - E_T}{kT}\right) \qquad (3.31b)$$

As the capture rate is defined as,

$$c_n = \sigma_n v_{th} n \qquad (3.32)$$

where σ_n is the *electron capture cross-section* and v_{th} is the *thermal velocity*. The latter can be defined as,

$$v_{th} = \left(\frac{3kT}{m_n}\right)^{1/2} \qquad (3.33)$$

where k is Boltzmann's constant and m_n is the electron effective mass. Additionally, the *effective density of states in the conduction band* N_C is

$$N_C = 2\left(\frac{2\pi m_n kT}{h^2}\right)^{3/2} \qquad (3.34)$$

where h is Planck's constant. This can all be substituted into eq. (3.31a) to determine the *electron emission time constant* τ_n for a defect at E_C-E_T

$$\tau_n = \frac{\exp\left(\left(E_C - E_T\right)/kT\right)}{\sigma_n v_{th} N_C} \qquad (3.35)$$

or,

$$\tau_n T^2 = \frac{\exp\left(\left(E_C - E_T\right)/kT\right)}{\gamma_n \sigma_n} \; where \; \gamma_n = \left(\frac{v_{th}}{T^{1/2}}\right)\left(\frac{N_C}{T^{3/2}}\right) \qquad (3.36)$$

where τ_n is simply the inverse of e_n. The γ term is generated by dividing out the temperature dependencies from the v_{th} and N_C terms and multiplying the left side of the equation by T^2 to maintain balance. On simplifying '*gamma'* with all the constants, it becomes 3.25 x 10^{21} (m_n/m_0) $cm^{-2}s^{-1}K^{-2}$ for an n-type majority carrier defect. Equation (3.36) is The fundamental equation for DLTS and is used to determine both the energy within the bandgap and the thermal cross-section of the defects. To determine τ_n and the defect concentration, more knowledge of how the defect concentration Affects the capacitance is needed.

Relaxing the restrictions from steady-state, quasi-steady-state relationships, which are more likely to real situations are considered. Under these conditions, the population of carriers is still constant in time, but the requirement that this balance is due to an exact balance between each process and its inverse (e.g. electron capture and electron emission) is relaxed. These conditions are useful for determining steady-state current, recombination-generation minority carrier lifetime, and most importantly for capacitive studies the steady state occupancy of the deep levels. Rearranging eq. (3.27) gives

$$\frac{\partial n_T}{\partial t} = \left(c_n n + e_p\right)\left(N_T - n_T\right) - \left(c_p pn + e_n\right) n_T \qquad (3.37)$$

On solving the differential equation results in

$$n_T(t) = n_T(0)\exp\left(\frac{-t}{\tau}\right) + \frac{\left(c_n n + e_p\right) N_T}{c_n + e_p + c_p p + e_n}\left[1 - \exp\left(\frac{-t}{\tau}\right)\right] \qquad (3.38)$$

where n_T (0) is initial density of filled states and τ is defined as,

$$\tau = \frac{1}{c_n n + e_p + c_p p + e_n} \qquad (3.39)$$

Based on this it is a simple matter to determine the steady-state occupancy of the deep level by checking the limit as '*t'* approaches ∞

$$n_T(t = \infty) = \frac{c_n n + e_p}{c_n n + e_p + c_p p + e_n} N_T \qquad (3.40)$$

This general solution is difficult to use in practice because there are so many variables that are not known at every moment is space and time. Several reasonable assumptions are possible in the case for a Schottky or p-n diode that allow for great simplification of this result. In the depletion region, *n* and *p* are negligible, so capture events can be ignored and the equation simplifies to

$$n_T(t = \infty) = \frac{e_p}{e_p + e_n} N_T \qquad (3.41)$$

From this point on, the discussion will be limited to the depletion region in an *n*-type semiconductor . It is assumed that n-type Schottky diode or abrupt *p+/n* diode is being measured. This assumption allows for the majority of the change in depletion depth to occur on one-side of the junction. Studying an *n*-type depletion region with a majority carrier trap above E_i , e_p is negligible compared to e_n. Therefore, the steady-state condition is n_T ($t=\infty$) = 0. It is also important to note a that these equations hold true for both thermal and optical processes.

We will consider a defect initially filled by electrons. This could be the case for a DLTS trap that has recently been filled with electrons during the fill pulse. In such a case, electron and hole capture are negligible within the depletion region and hole emission to the valence band is assumed negligible because the thermal energy required for this to occur is extremely high. In such a case, eq. (3.27) reduces to

$$\frac{dn_T}{dt} = -e_n n_T \tag{3.42}$$

The solution to this equation is

$$n_T(t) = n_T(0)\exp(-e_n t) \tag{3.43}$$

The emission of electrons as a function of time leads to increased positive fixed charge in the depletion region. Since the net charge remains the same for a given voltage, this leads to decrease in the depletion width and an increase in the capacitance. Using the equation for capacitance and assuming a uniformly-doped n-type Schottky or abrupt, one-sided *p+/n* junction, the following is educed from eq. (3.19)

$$C = \frac{\varepsilon A}{W} = \varepsilon A\left[\frac{qN}{2\varepsilon\left(V_{bi}-V\right)}\right]^{1/2} = \varepsilon A\left[\frac{q(N_d - n_T)}{2\varepsilon\left(V_{bi}-V\right)}\right]^{1/2} \tag{3.44}$$

where N_D is the n-type doping concentration, V_{bi} is the built-in voltage or Schottky barrier height, and V is the applied voltage. This can be rearranged to

$$C = C_\infty\left(1-\frac{n_T}{N_d}\right)^{1/2} \quad where\, C_\infty = \varepsilon A\left[\frac{qN_d}{2\varepsilon(V_{bi}-V)}\right]^{1/2} \tag{3.45}$$

When the trap concentration N_T is much lower than the doping concentration N_d, the equation can be further simplified by the binomial approximation (i.e. $(1+x)^n = 1+nx$, for x less than 0.1) . It results as

$$C(t) = C_\infty(1-\frac{n_T(t)}{2N_d} \tag{3.46}$$

In the steady-state change of capacitance from an initial occupancy to a final occupancy, this equation becomes

$$\frac{C(\infty)-C(0)}{C_\infty} = \frac{n_T(0)-N_T(\infty)}{2N_d} \tag{3.47}$$

using eq. (3.43). Typically one assumes the level is completely filled at $t = 0$ such that $n_T(0) = N_T$ and $e_p \rightarrow 0$ so $n_T(\infty) = 0$. Additionally, the total change in capacitance $C(\infty)$-$C(0)$ is typically written as ΔC. Using these relations and rearranging, the more common form of this equation is arrived at where,

$$N_T = \frac{2N_d\Delta C}{C_\infty} \tag{3.48}$$

The above expression shows the general form which one might expect for DLTS based on thermal emission rate. In summary, the majority and minority carrier emission/capture can be realized from from Fig. 3.5 and Fig. 3.6 respectively.

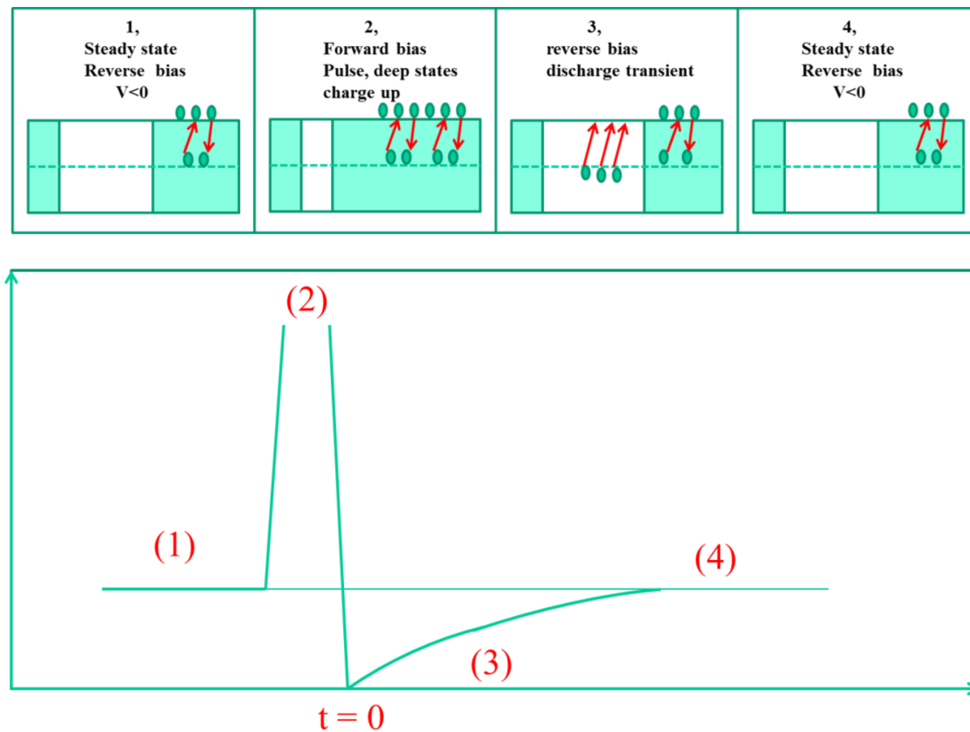

Figure 3.6 Effect of a forward bias pulse with *V'>0* applied on a reversely biased junction in presence of a majority carrier trap

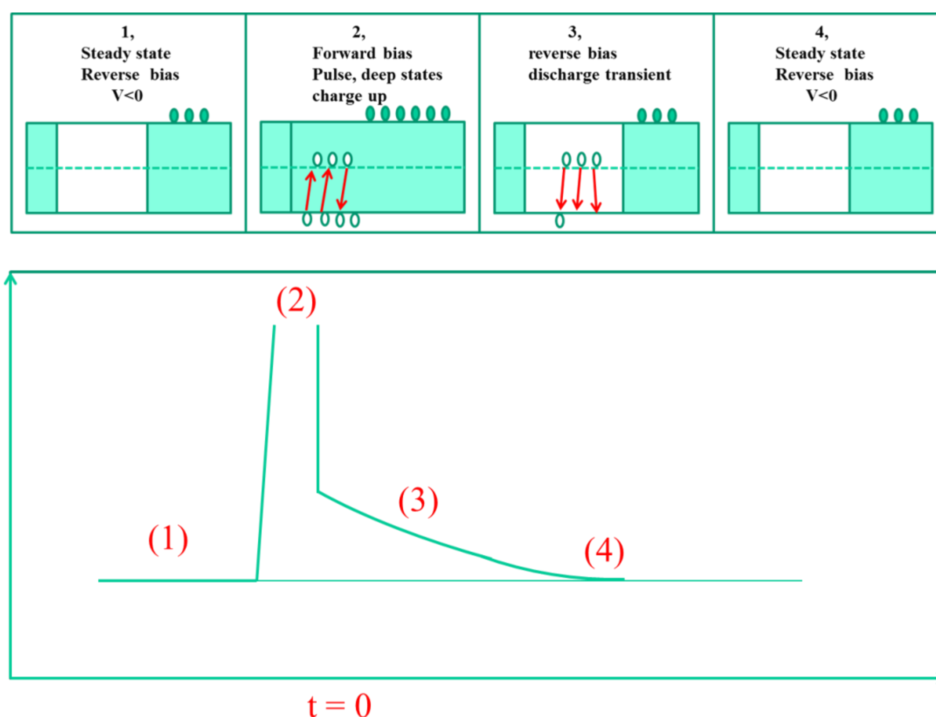

Figure 3.7 Effect of a forward bias pulse with *V'>0* applied on a reversely biased junction in presence of a minority carrier trap

3.3.2 Deep Level Transient Spectroscopy (DLTS)

Deep level transient spectroscopy (DLTS), developed by D. V. Lang in 1974, is a powerful and well known technique for identifying deep level thermal cross-section, concentration, and energy position in the bandgap [13]. The basic concept of DLTS has changed relatively little since its inception, and most of the advances have resulted from the increased capability of computers to do complex storage and analysis of the transient data. There are a few exceptions to this including applying the technique to conductance and current type measurements, for example [14–17]. Many developments to the DLTS theory have involved improving the analysis, but improving upon the original boxcar integration in terms of signal-to-noise ratio have been limited. A myriad of variations of DLTS are available including the standard boxcar DLTS, Fourier transform DLTS (FTDLTS), Laplace-transform DLTS, and covariance method of linear predictive modeling (CMLPM) to name a few [13, 18–21]. Each method has its advantages and disadvantages with regard to required signal-to-noise ratio (SNR), ability to separate defect levels closely spaced in energy, accuracy, and ease-of-use.

DLTS is based on a temperature scan of the capacitance transient of the analysed sample. The experimental setup of the DLTS system is rather simple. The sample is mounted in a temperature-controlled cryostat and connected to a capacitance meter and voltage function generator. The DLTS signal is univocally related to e_n by means of the *rate window* concept, which will be illustrated in the following. The measurement procedure is illustrated in fig. 3.8. A negative bias is applied to the sample, so that a certain region is depleted of free carriers. At each period *P* a pulse of duration t_{Fp} and amplitude V_{FP} is applied to the junction. The duration of the
pulse affects the filling level of the traps, while the amplitude can be related to the region probed by the bias pulse:

- $V_{Fp} < V$: in this case an interval inside the space charge region is selected. This can be useful if one is interested in concentration profiles of traps close to the surface or to the junction region, although more sophisticated techniques, such as Double DLTS, should be used for that.
- $V_{Fp} \approx V + V_{bi}$: the whole space charge region is depleted with free carriers.
- $V_{Fp} > V + V_{bi}$: In p-n junctions, minority carriers are injected from the opposite side of the junction, thus making possible the observation of minority carrier traps.

During the fill pulse, a majority carrier trap in n-type material below the Fermi level will fill with electrons as can be seen in Fig. 3.8a. After the fill pulse, the quiescent bias is applied, typically -0.5 V and always less (more negative) than the fill pulse bias, so the depletion region extends deeper into the material (see Fig. 3.8b). Now most of the filled traps in the depletion region are above the quasi-Fermi level and would prefer to be empty, so electron emission to the conduction band occurs according to eq. (3.46). As the emission occurs, the fixed charge density increases for an electron trap in n-type material, but because the applied bias is constant the total charge is constant the depletion depth must decrease to maintain the total charge. As the depletion region decreases, the capacitance increases, which is shown in Fig. 3.8c and d. As this process is repeated at higher and higher temperatures, the emission rate increases according to eq. (3.19) and is shown here rearranged for clarity:

$$e_n(T) = \sigma_n v_{th} N_C \exp\left(-\frac{E_C - E_T}{kT}\right) \tag{3.49}$$

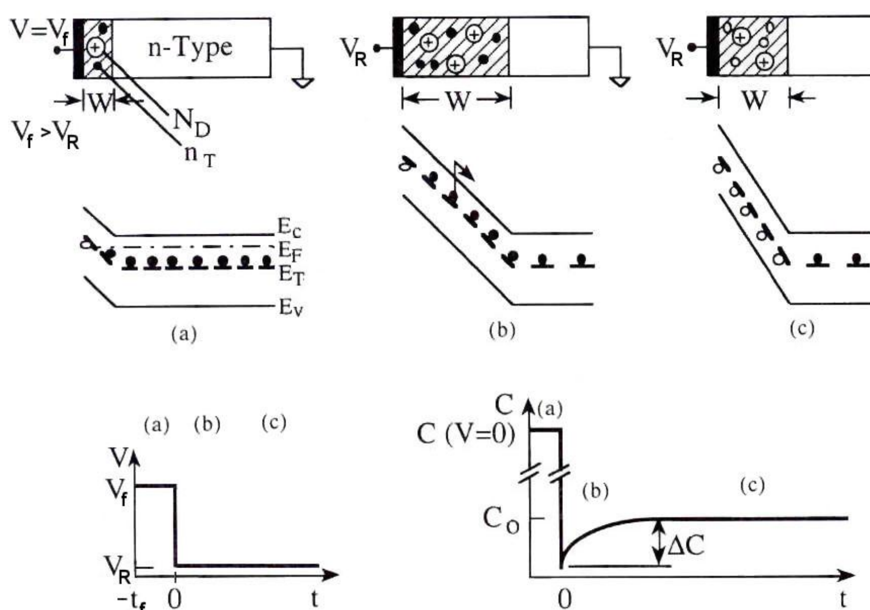

Figure 3.8: Schematic illustration of the effect of capture and emission of electrons from an electron trap. ***(a)*** The sample is biased in the fill pulse regime to allow *ET* to fill with electrons. The fill pulse bias is always greater than the measurement bias to allow traps to fill. The bottom part of the figure shows the bias scheme as a function of time while the other graph shows the resulting capacitance. ***(b)*** At the start of the measurement, the levels are completely filled resulting in a lower charge density in the depletion region. This dictates the depletion depth and capacitance. ***(c)*** As the traps emit, the charge density increases due to the uncovered fixed charge of the traps. In this case, the depletion region shrinks as the same total charge can be uncovered in a smaller volume, and the capacitance increases. This is the standard intuitive process for a deep level exposed to a voltage change. [12].

Again, remember that the emission rate constant τ_n is simply $1/e_n$ assuming negligible emission to the valence band. The emission rate varies exponentially with temperature, so the challenge is to develop a system that can determine this rate from the capacitance transient, which is given by

$$C(t) = C_\infty\left(1 - \frac{N_T}{2N_d}\right) = C_\infty\left[1 - \frac{N_T}{2N_d}\exp\left(-\frac{t}{\tau_n}\right)\right] \tag{3.50}$$

which is similar to Eq. (3.46) but $n_T(0)$ is assumed N_T .With today's computing power and memory capacity, recording parts or all of the transients is relatively simple. The difficult part is extracting the emission rate/time constant from recorded data especially considering that more than one trap can have similar time constant that would need to be extracted separately and this is where the double boxcar, Fourier transform, Padé-Laplace, and other analysis methods are used. Once the emission rate vs. temperature is extracted, the trap activation energy and capture-cross section can be determined by modifying eq. (3.45) to Plotting $1/kT$ vs. $\ln(\tau T^2)$ gives trap energy from the slope and the cross-section is extracted from the y-intercept. This is very straight forward so far, but as alluded to earlier the extraction of the emission rate constants is nontrivial and this has been the basis for the plethera of analysis techniques. The following sections will describe three of these techniques.

The original DLTS analysis method used a boxcar integrator to determine the temperature for a given emission rate.[13] Stated more simply, the DLTS signal ΔC_0 is simply $C(t_2)$-$C(t_1)$, Better signal-to-noise ratio is possible without significant distortion of the signal by averaging the capacitance around t_2 and t_1.

The change in capacitance for a given rate window is given by

$$\Delta C_0 = C(t_2) - C(t_1) = \frac{C_\infty N_T}{2N_d}\left[\exp\left(\frac{-t_1}{\tau_n}\right) - \exp\left(\frac{-t_2}{\tau_n}\right)\right] \tag{3.51}$$

Taking the derivative of Eq. 3.51 and setting it to 0 to find the maxima or minima, the peak in the ΔC_0 signal can be found as

$$\tau_n{}^* = e_n = \frac{t_2 - t_1}{\ln(t_2/t_1)} \tag{3.52}$$

One can sees that e_n is a quantity depending on the constants t_1 and t_2, which are fixed at the beginning of the measurement. The time interval t_2-t_1 is also called rate window, and the procedure is summarized in fig 3.9.

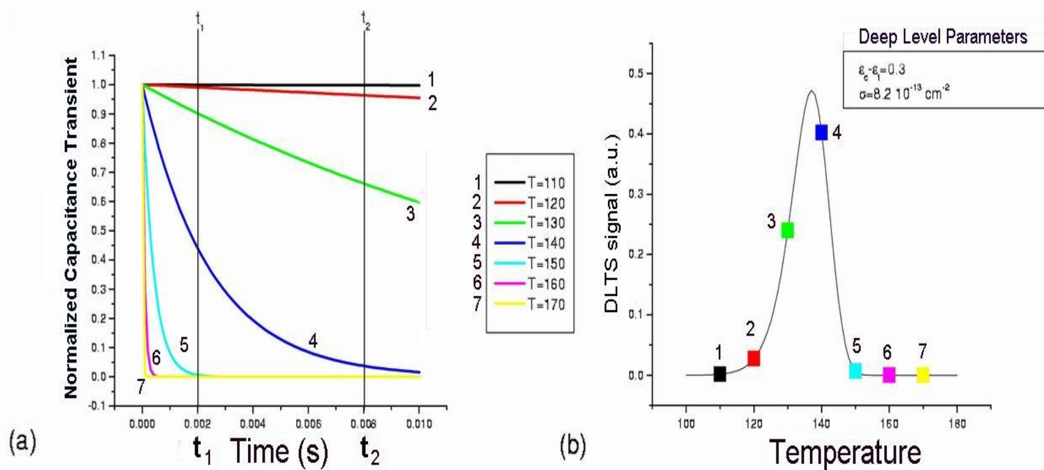

Figure 3.9 a) Discharge capacitance transients at different temperatures, with the rate window t_1-t_2 in evidence; ***b)*** associated DLTS signal [22]

3.3.3 Capture kinetics via DLTS

Under ideal situations, defects are randomly distributed and in low enough concentration such that the no defect occupancy affects any other defect occupancy. If defects are present in very high concentrations, clustered, or decorate dislocations, for example, the defects can be physically close enough that the Coulombic barrier associated with one defect can influence the occupancy of other defects. Interacting defects vs. ideal non-interacting defects can be determined via differences manifested in the DLTS spectra. Studying the capture kinetic behavior allows one distinguish ideal point defects from interacting ones. Another non-ideality that can arise for multiple reasons is a distribution of energy levels for a given defect instead of the ideal discrete energy level. Determination of the energy distribution is also possible using capture kinetic analysis although a few modifications to the ideal theory previously presented is required.

In capture kinetics the fill pulse time is varied to measure the change in the DLTS peak height. The changes that occur here are a result of incomplete filling of the level where in the past it was assumed $n_T(0) = N_T$, so it is necessary to focus on fill pulse time when capture is the dominant process. Keeping the discussion restricted to n-type material, the change in n_T is [23]

$$\frac{dn_T}{dt} = c_n n p_T = c_n n (N_T - n_T) \qquad (3.55)$$

assuming the level is completely empty at the start of the fill pulse the solution is

$$n_T(t) = N_T \left[1 - \exp(-c_n n t') \right] \qquad (3.56)$$

The t' is used to signify a difference between the measurement time t that starts at the end of the fill pulse and t' that starts at the beginning of the fill pulse. This expression is evaluated at the end of the fill pulse t_{FP} right before the bias changes and emission becomes the dominant process. The value of nT ($t' = t_{FP}$) will be called n_{T0} and corresponds to n_T ($t = 0$) in previous equations. For a sufficiently long fill pulse time, $c_n n t_{FP}$ is large and $n_{T0} \rightarrow N_T$. Conversely, as $c_n n t_{FP} \rightarrow 0$, $n_{T0} \rightarrow 0$. If the

change in capacitance ΔC_F with a fill pulse t_{FP} is compared to the change in capacitance for an infinitely long fill pulse ΔC_∞, the ratio is

$$\frac{\Delta C_F}{\Delta C_\infty}=\frac{n_{T0,F}}{N_T}=1-\exp(-c_n n t_{FP}) \qquad (3.57)$$

This can be rearranged to a more usable form

$$\ln\left(1-\frac{\Delta C_F}{\Delta C_\infty}\right)=-c_n n t_{FP} \qquad (3.58)$$

Because $c_n n$ is constant, the left side of the above expression should be linear with t_{FP} for an ideal, non-interacting defect to the point where the time is long enough for the level to completely saturate. This measurement can be performed by finding the saturation point where ΔC_F no longer increases with t_{FP} , which defines $\Delta C\infty$. Then measuring ΔC_F at several shorter fill pulse times, a plot can be generated to determine if the defect is ideal.

When the defects are non-uniformly distributed and closely spaced due to linear arrangements or clustering for example, a Coulombic interaction can occur influencing the

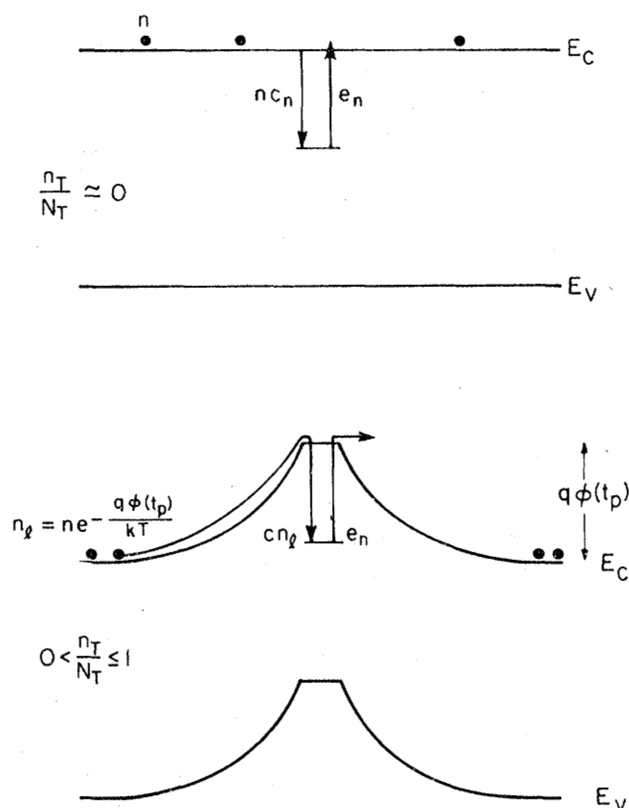

Figure 3.10 Before capture (top), the defect is uncharged and has no Coulombic barrier associated with it. After capture begins (bottom), a time dependent barrier forms reducing the capture rate of the next electron. In order for the effect to be observed, neighboring defects have to be close enough to be influenced by the resultant Coulombic potential [24]

electron capture of neighboring defects. This Coulombic barrier to capture is modeled as a time-dependent potential $\phi(t)$ that builds up around the defects and reduces the subsequent electron capture as in Fig. 3.10.

Further understanding of interacting defects is possible considering the theory of Schröter *et al.*, which allows one to distinguish bandlike and localized states [25-30]. This model shows that continuous energy bands are likely to result from pure dislocation states due to wave function overlap. In contrast, for the case where point defects decorate a dislocation, Schröter showed that such wavefunction overlap would be minimal and a deep level associated with this type of defect formation would manifest as a localized state and not exhibit band-like character [25, 30–32]. Figure 3.11 a and b shows simulation and experimentally observed behavior of bandlike levels, respectively. The band like level in Fig. 3.11 is distinguished by the peak shifting to lower temperatures for longer fill pulse times. As the fill pulse increases, more of the defect band fills starting furthest from the conduction band then filling available states above this.

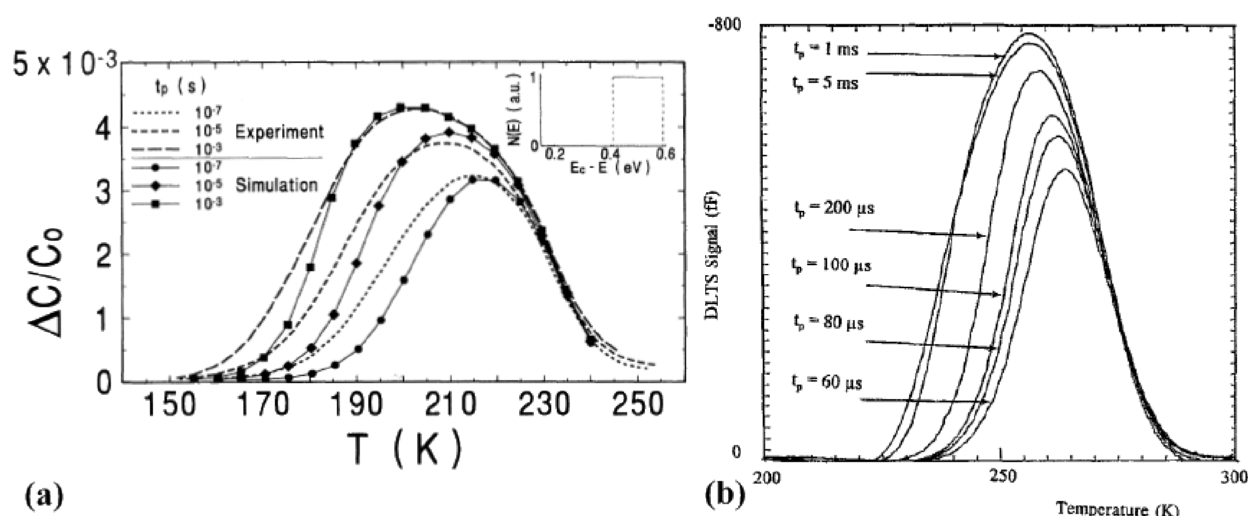

Figure 3.11 (a) Simulated DLTS spectra of interacting levels for a bandlike energy distribution [30]. ***(b)*** Measured minority carrier bandlike distribution of states in $Si_{0.7}Ge_{0.3}/Si$ [32]. The simulation uses a broader distribution of states, which causes the larger distortion of the DLTS curve at larger fill pulse times. The features of the bandlike distribution are the decrease in peak temperature and increase in peak height at longer fill pulse times and the high temperature side of the curves typically nearly overlap.

The defect band can be considered as an infinite series of discrete levels with their own $E_C - E_T$ and cross-section. Assuming the cross-section is constant, the emission rate will vary exponentially with E_C-E_T. For a short fill pulse where only the bottom of the band fills, the DLTS will approximate the peak of a discrete level. As the fill pulse is increased, the bottom part of the band will have the same emission response but additional parts of the band will emit faster (i.e. at lower temperatures) due to a lower E_C-E_T. The result of this is three-fold. First, the peak temperature will shift to lower temperatures as the averaged band E_C-E_T decreases for longer fill pulse times. Second, the peak height will increase because more defects are captured and emitted at the longer fill pulse times. Third, the high temperature side of the DLTS peak will nearly line up. This is because of the exponential dependence of the emission rate on temperature meaning that the bottom part of the band dominates this part of the spectra [29]. On the other hand, a discrete interacting level has the same "effective" E_C-E_T independent of the fill pulse length, by definition, so the emission rate is constant and therefore the peak temperature is also constant.

3.3.4. Experimental setup

The DLTS measurements have been performed as follows: the sample temperature varies slowly, while the sample bias varies in a fashion like that described in fig. 3.8, with a fixed period *P*. Moreover, the capacitance of the sample at reverse bias V_{rev}, and the capacitances during the transient at t_1 and t_2 are measured. In order to achieve this, we make use of the following experimental equipment, which is depicted in fig. 3.12.

Temperature controller and cryogenic apparatus

This instrument, a Lake Shore DRC91C, allows one to set and control the temperature of the sample. It is interfaced to a computer by means of a NI board and Visual Basic software. The user 4-24 determines the temperature interval and heating rate through the software. For our setup, the heating rate must be lower than 0.083K/s. The temperature interval can vary from 77 K, i.e. the liquid nitrogen temperature, to about 700 K for GaN devices. The lower maximum temperatures are employed for more materials and devices, such as GaN-based HEMTs, LEDs. The sample is Kept in a cryogenic apparatus, consisting of a dewar containing liquid nitrogen, and a sample holder. A thermocouple measures the temperature, while the sample holder can be heated by a Thermocoax cable with resistivity 12.5 W/cm.

Pulse generator and capacitance meter

The pulse generator and the capacitance meter are, together with the exponential correlators, building blocks of the Sula Technologies Deep Level Spectrometer. The impulse parameters are mentionend below:

- the period *P*
- the reverse bias V_{rev}
- the filling pulse bias V_{fill}
- the pulse duration (pulse width) t_p.

The capacitance meter works at a frequency of 1 MHz, thus being able to reproduce accurately capacitance transients with time constants of the order of some tens of ms. The output of this instrument yield the reverse-bias capacitance C_0, and the capacitance transient, which is further processed by the correlators.

Exponential correlators and boxcar averager

The deep level spectrometer incorporates four correlators, which play the role of reducing the noise affecting the capacitance transient. The output of each correlator is then processed by a boxcar averager, which, in turn, yield as output the signal $\Delta C=C(t_1)-C(t_2)$. To each double boxcar averager correspond four different values of the couple (t_1,t_2), so that in a single measurement it is possible to collect four spectra speeding up the experimental procedure. The ratio t_1/t_2 is fixed and equal to 2.5. The values of the emission rate en corresponding to the different values of the rate windows range from 1.16 x 10^4 s^{-1} to 2.33 s^{-1}.

The correlator performs the following operations: the periodic signal consists of the sum of noise $N(t)$ and ideal signal, described by an unknown amplitude *A* multiplying the function $s(t)$ = exp[$-e_n t$]. The signal is filtered by means of a weighting function $W(t)$= exp[-*t/*t], produced by an exponential function generator with variable time constant. The best measure S of the unknown

amplitude A

$$S = \int_0^P \left[A \exp\left(-e_n t\right) + N(t) \right] W(t) dt \qquad (3.59)$$

occurs just when $s(t)=W(t)$. This provides the best SNR.

The signal is the processed by the double boxcar averager. Here two input channels correspond to two linear gates which sample the signal at instants t_1 and t_2, while a differential block yields at the output the difference of the signals measured by the two gates. The measurement setup is illustrated in fig 3.12

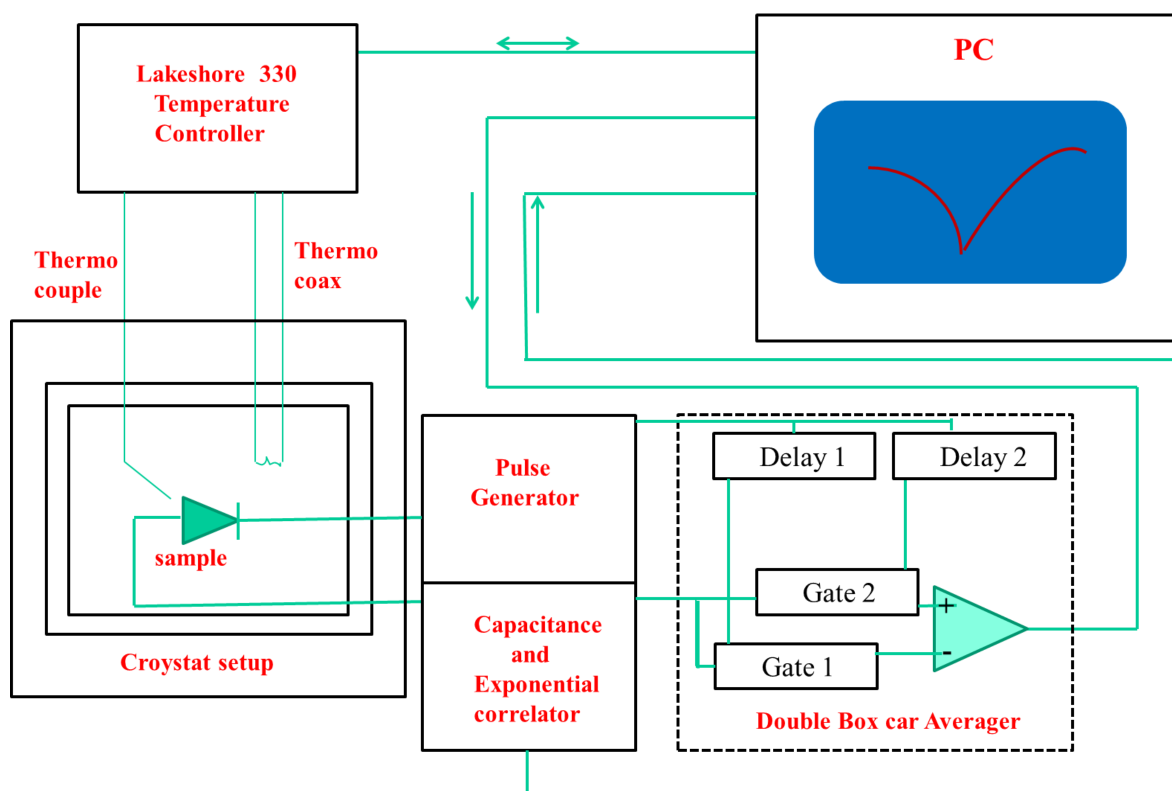

Figure 3.12 Block diagram of the instrumentation for the DLTS measurements, evidencing the correlator and the double boxcar average

Optical Spectroscopy methods

In order to extract the results on Band gap, defect related transition, polarization induced transition and optoelectronic devices efficiency calculation, different optical methods have been used in this thesis, which is discussed below. The idea has been taken also to correlate electrical properties with optical properties as the thesis is mainly focused on high polarization field materials, i.e. high carrier density structures with defects/dislocations.

3.4 Surface Photovoltage Spectroscopy

In 1839, Becquerel has discovered experimentally the photovoltaic effect [33], which consists, in general, of an illumination-induced change in the potential distribution of a given structure, due to the transfer and/or redistribution of some charge within the structure caused by an incident illumination.A specific variant of the photovoltaic effect is the surface photovoltaic effect, which is defined as the illumination-induced change in the surface potential, and named as the surface photovoltage (SPV).

Monitoring the change in the surface voltage as a function of the incident photon energy is a technique based on the SPV effect: the surface photo voltage spectroscopy (SPS). This method makes it possible to have a detailed picture of the electronic structure, due to its sensibility of the change in band bending in function of an external illumination, and so information about the bulk properties, such as band gap and type of semiconductor, which allow to reconstruction of the surface and interface band diagrams. It also allows the analysis and the measurement of surface and bulk defect state and energy levels in quantum structures.

3.4.1 Surface electrical properties of semiconductor

The boundary of media with different physical properties is generally defined as an interface. Especially the surface between a semiconductor and a solid is usually named “interface”, and between a semiconductor and vacuum or a gas “free surface”.
Ideal crystalline semiconductor presents, in general, a periodic structure of allowed energy bands separated by forbidden energy gaps. Its termination at free surface or interface creates surface- or interface-localized electronic states, within the semiconductors band gaps, and/or a surface dipole, a double layer of charge. Breaking the symmetry of lattice termination is not the unique phenomena involved in the creation of electronic states, also the presence of surface atom that are not tied with an upper one, steps, kinks, adsorbed impurity atoms and the effect of the surface reconstruction or relaxation, such as a change in the bonding configuration of surface atoms to minimize the surface energy, are involved in this process.

The presence of the surface-localized states makes the semiconductor bulk and surface not more in thermal equilibrium. In order to establish equilibrium, there is a charge transfer of free carrier between the two, therefore the carrier density deviates from its equilibrium value in the vicinity of the surface and the result is a surface space-charge region (SCR). Thus, this region is electrically non-neutral and a potential drop occurs across it, to underline the fact that the surface potential is different form the electric one in the bulk even in equilibrium conditions.
Associated to the semiconductor surface is also the presence of a surface barrier, which is defined by the electron affinity χ, the energy needed to release an electron from the conduction band into the vacuum, and by the surface dipole $\Delta\Phi_s$, determined by additional microscopic dipole contributions, such as reconstruction, stoichiometry changes [1].

Introducing the concept of the local vacuum level E_l, defined as the energy of an electron at rest in a given point free from the influence of the crystal potential but not from the macroscopic potentials due to the electric field in SCR, the different effect of surface and surface dipoles is illustrated in fig. 3.13.

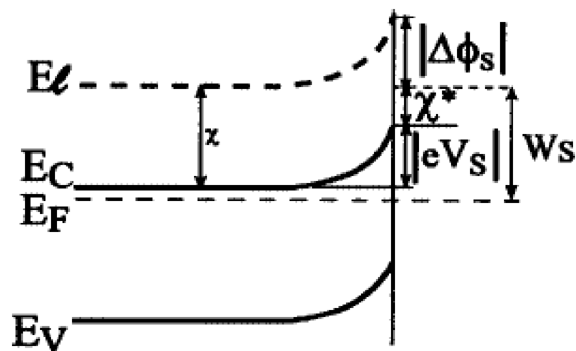

Figure 3.13 Schematic band diagram of semiconductor surface SCR at equilibrium.

So the electron affinity is defined as $\chi = E_l - E_c$, where E_c is the conduction band energy, but at the surface the effective electron affinity χ^* may deviate from the bulk value due to the various dipole effect. Also fig. 3.13 shows the work function W_s, defined as the separation energy between the local vacuum E_l at the surface and the Fermi level E_F.

3.4.2 Surface Photovoltage (SPV) effect

Under illumination, a transfer and/or redistribution of charge in the structure is typically of the photovoltaic effect and a specific variant is the surface photovoltage effect, defined as the illumination-induced change in the surface potential.

Generally there are two way of formation of free carrier by creating electron-hole pairs, due to the illumination and so to the absorbed photons: via band-to-band transitions, typically for photons energy above the energy gap, named super-bandgap photons, and/or release captured carriers via trap-to-band transitions, typically for sub-bandgap photons. Thus a significant transfer and/or redistribution of charge occur between the surface and the bulk or vice versa in an illuminated device. It's important to note that SPV is present only if carrier generation is followed by net charge redistribution.

Such redistribution normally affects only the surface charge region and so its potential drop across. The underlying bulk region remains quasi-neutral, only the presence of significantly non-uniform generation or recombination may also cause a potential drop in the quasi-neutral region, this effect is known as the Dember potential [34].

Therefore the SPV mechanism strongly depends on the energy of the incident photon. Super-bandgap and sub-bandgap mechanisms are all demonstrated for a depleted n-type surface in figure 3.14.

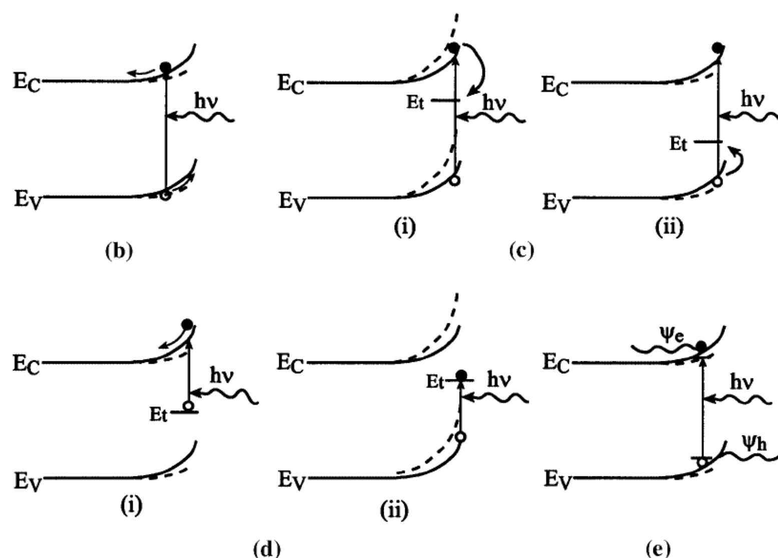

Figure 3.14 Schematic band diagrams of the semiconductor depleted n-type surface space-region under different illumination conditions

The most common super-bandgap mechanism is demonstrated in figure 3.14 (b): the electric field in the SCR causes the excess electrons to be swept away from the surface and the excess holes to be swept towards it, this reduce the density of surface trapped electrons and decreases the band-bending. A second mechanism in figure 3.14 (c) presents the situation in which electrons (i) or holes (ii) are trapped at surface defects. This transfer charges the surface and increases the band-bending in the electrons case and decreases the band-bending in the hole one.

Figure 3.14(d) shows the effect of sub-bandgap SPV illumination, in which the surface charge region and its potential is directly modified by excitation of trapped carriers. In case (i) the photons have an energy $h\nu > E_c - E_t$ and this produces electrons transition from a surface state of energy E_t to the conduction band, here the electrons are swept quickly away by the electric field to the semiconductor bulk. So the negative surface charge is reduced and the band-bending is decreased. By analogy, photons with energy $h\nu > E_t - E_v$ cause electrons transition from the valence band to the surface state of energy E_t, this is equivalent to hole transitions from the surface state to the valence band like in figure (ii). This results in an increase of both the surface negative charge and the surface band-bending. In this case SPV is necessary to have a significant diffusion of the excess holes into the bulk and/or recombination of electrons and holes inside SCR, because there is no field-assisted driving force of holes into the bulk.

Finally, there are other mechanisms based on band-to-band transitions due to sub-bandgap photons. The most important is the Franz-Keldish effect, shown in figure 3.14 (e), in which photons with sub-bandgap energy produce band-to-band transitions via photon-assisted tunneling in a sufficiently large electric field [35]. In this circumstance the photon energy is typically close to energy gap.

3.4.3 SPV effect on buried interfaces

The previous section has taken in consideration only semi-infinite, uniform bulk semiconductors. Nowadays semiconductor samples may be thin, not much larger than the diffusion length and/or absorption length, so that the excess carriers may be present near their back part as well and also presents a multi-layer structure: several buried interfaces due to homojunctions and heterojunctions within the sample.

The screening by quasi-neutral region seems to make unable the buried interfaces, deep enough in the sample, to contribute to the measured of the SPV signal. This idea is erroneous. Considering a semiconductor thin film grown on a semiconducting bulk, defined by different material parameters, the schematic band line-up of this structure, reported in figure 3.16, underlines the fact that also the interface contributes to the SPV effect [36].

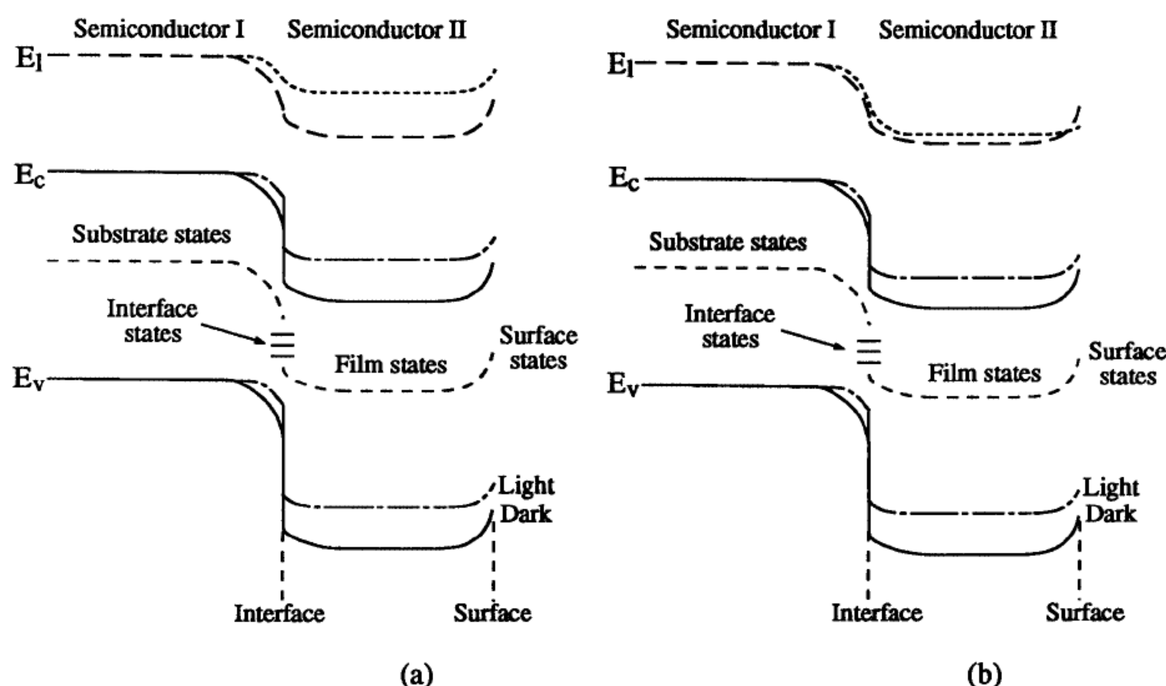

Figure 3.15 Schematic band diagrams of thin film structure in the dark (solid curve) and under illumination (dashed curve), where the interface SCR (a) is the dominated contribution and the surface SCR (b) to the SPV effect

In this structure there are two different surface charge regions: interface SCR, between the substrate and the film, and surface SCR, between the film and the ambient. Figure 3.15 clearly shows the sensitivity of the SPV to interface and surface SCR, especially, there are changes in the band-bending of either the SCR that produce SPV. However in case (a) the interface-related SPV dominates, in the other case (b) the surface-related SPV dominates, as evident from the surface position of local vacuum energy E_l. Thus optical absorption in any non-neutral region, present in the sample, may contribute to the measured SPV signal because the potential of the free surface is strictly linked to any other illuminated region, no matter how deep within the sample.

The sensitivity of SPV measurements to a certain region of a semiconductor is limited only by the absorption length of the photons, or rather the possibility of introducing an excess of free carrier in the a particular region, thus by proper design and interpretation of experiments, may be used to gain information about the various semiconductor interface and bulk properties (via the Dember effect), in addition to semiconductor surface properties.

3.4.4 SPV experimental measurements

The surface potential is a built in potential, rather than an external potential, in other words is not equal to the difference in Fermi levels between the front and the back part of a sample, and thus it cannot be measured by a simple voltmeter. Moreover any contact alters the surface properties and hence the quantity under measurement. Consequently many elaborate techniques for measuring

the surface potential without applying direct electrical contact have emerged and here the two most famous are presented.

3.4.4.1 Kelvin probe method

Figure 3.15 shows the schematic band diagram of a semiconductor SCR at the equilibrium, or rather in the absence of photochemical activity, and so the surface band-bending eV_s causes a change of equal magnitude in the surface work function W_s. Therefore, in the absence of photochemical activity, the change in the surface work function is equivalent to a direct SPV measurement, in absolute value terms.

The oldest method for measuring the relative changes in work functions is measuring the work function difference between two materials forming the two sides of a parallel plate capacitor. Figure 3.16 reported this situation for two metals. Prior the connections (a) the metals are electrically neutral, no macroscopic electrical field arise, and share the same local vacuum energy level. Short-circuiting the metals (b), charge must flow from the smaller work function metal to the other one until the equilibration of the Fermi level. This transfer of charge results in an electric field in the gap between the two plates and a drop in the local vacuum across it. Finally the potential energy drop is equal to the difference in the work functions of the two metals and is usually known as the contact potential difference (CPD) [37].

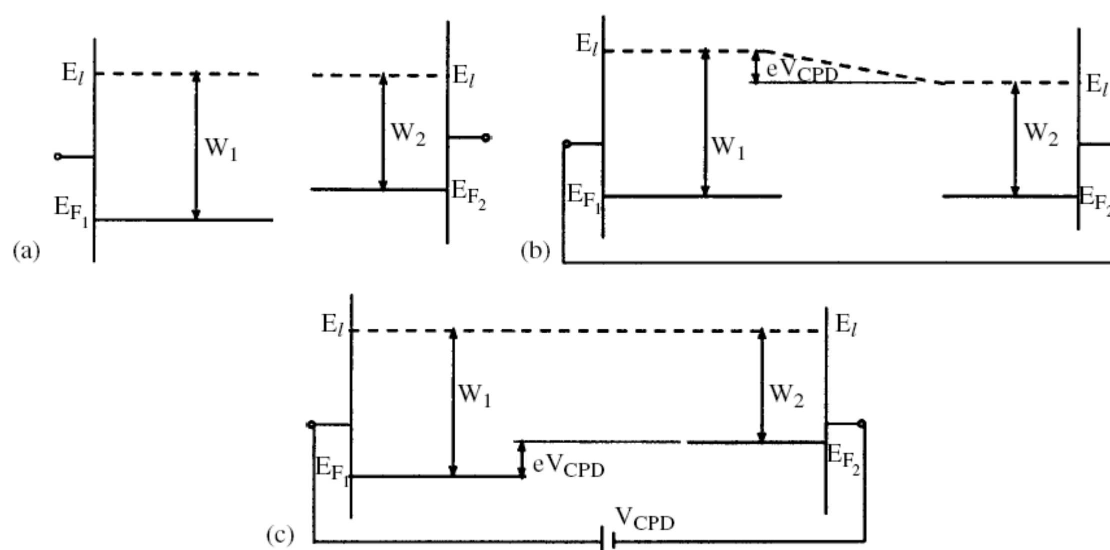

Figure 3.16 Parallel plate capacitor band diagram formed from two different metals with the two plates isolated (a), short-circuited (b) and connected through a d.c. bias equal and opposite to the contact potential difference (c)

A method for measuring CPD was suggested by Lord Kelvin applying to the capacitor an external d.c. bias equal and opposite to the CPD, figure 3.16 (c). In this condition the Fermi levels in both materials differ by eV_{CPD}, just as in the isolated case, no charge exchange between them need take place and so the capacitor is discharged. Therefore for determining the CPD is sufficient to calculate the applied bias that discharges the capacitor, even if neither the capacitor charge nor capacitance is known. This method is named Kelvin probe and nowadays rely on a periodically vibrated plate brought in proximity to the sample surface, such that a steady-state a.c. current develops in the effective a.c. capacitor formed. This current can be zero if, the capacitor is

discharged, and thus, the CPD can be determined by determining the d.c. bias for which the external a.c. current is nullified.

3.4.4.2 The metal-insulator-semiconductor structure

Metal-insulator-semicondutor (MIS) structure is an alternative way for measuring directly SPV. Assuming that after the equilibrium a MIS structure is brought into the open-circuit mode by disconnecting the two terminals, the surface voltage Vs may change due to the photovoltaic effect, applying an illumination to the capacitor. The change in Vs must produce an equal change in the voltage measured between the plates of the capacitor, thus the SPV at the semiconductor/insulator interface in a MIS structure can be found by measuring the photo induced voltage between the MIS capacitor terminals. Experimentally this is easily applicable to the study of free semiconductor by placing a static metallic grid in proximity of the sample, with air or vacuum gap functioning as the insulator, and using chopped illumination with lock-in detection of the ensuing SPV signal.

The application choice between the two different approaches is based on their own physical properties. The MIS method is more suitable for experiment that involves fast relaxation phenomena, allows for a systematic modification of the surface band-bending in the dark as an extra degree of freedom and alleviates the need for an ohmic back contact. On the other hand, the Kelvin probe is more suitable for following phenomena with large time constants, as in particular surface states with long time-relaxation. This does not perturb the true band-bending of the free surface and the extra information afforded by the work function is extremely useful in experiments involving surface chemistry and/or film deposition [38].

3.4.4.3 SPS set-up

The surface photo voltage spectroscopy (SPS) is defined as the measurement of the SPV signal for various values of photon energy. The data give us information about the behavior of the sample for a specific spectrum of various wavelength.

The SPV signal is generated using a broadly tunable light source. The most suitable set-up is to use of a “white” light source in conjunction with a monochromator, because the super-bandgap absorption coefficients is typically orders of magnitude larger than the sub-bandgap coefficient makes SPS is vulnerable to the spurious contribution of high-order diffraction peaks and stray light and so the using of monochromator results in making these effects small as possible.

Typically the sample under study is placed in a metallic box, which results as a dark box and a Faraday cage, and this box must include the probe, a vibrating plane as in the Kelvin probes or static one in the case of the MIS structure. In the last case, static metal plane, the illumination must be also periodically chopped to allow for lock-in detection of the signal.

Real-time computer program records the SPV spectrum, controls the monochromator motor and thus the wavelength changes, operates the control electronics of the probe, reads the measurement result by interfacing with the probe read-out electronics via an analogue-to-digital converter and finally stores the obtained spectrum for subsequent display and analysis. The SPS set-up schematic is given in figure 3.17.

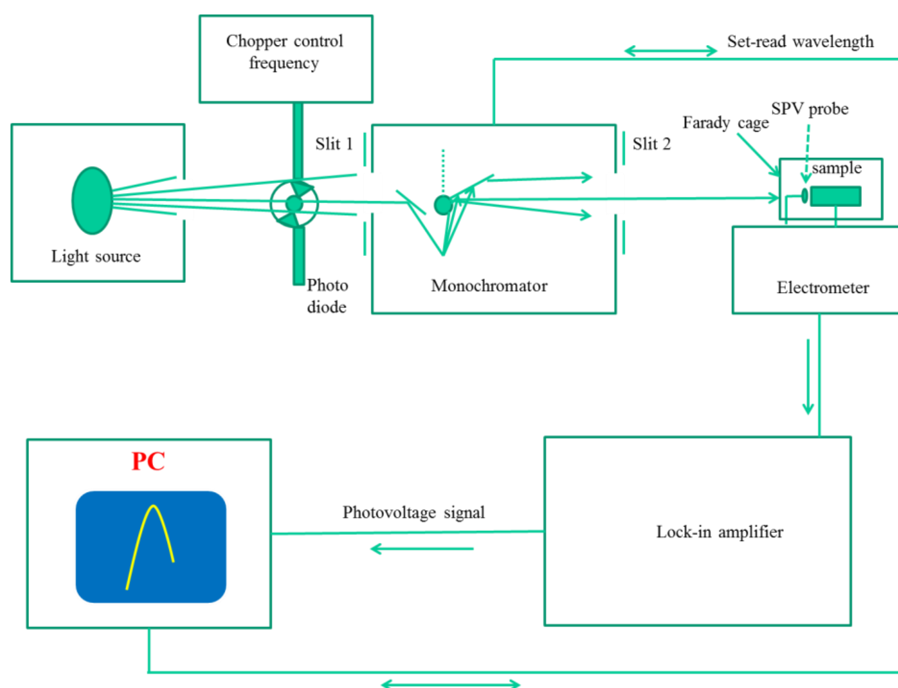

Figure 3.17 Block diagram of SPS set-up

In Kelvin probe method the use of the chopper is avoided because the lock-in can detect the vibrational signal from probe and so that's why in figure 3.16 is written as "if applicable", and also the use of an auxiliary light-source, such as white, laser or UV light, allows for "photo-bias" of the system and for additional quantitative analysis [38].

3.4.5 Applications of SPS

The analysis of the SPS spectra gives information about the semiconductor bandgap, the type of the sample, the gap state and characterization of multiplayer structures and eventually quantum wells. This tool makes the SPS an important technique in the fields of the surface electronic structure, surface reactions, metal-semiconductor interface, bulk and surface defects and more.

The method has been applied to study different materials and structures such as Si, CdS, GaAs, ZnO etc. and their heterostructures [38-41], while the GaN and it's heterostructures studies have been limited in literatures so far due to different issues such as materials quality, high polarization field etc. so far. There are some literatures which had reported some results on GaN layer which is shown in Fig 3.18 [42], but still there hasn't been any report on heterostructures which is an important field of study in this thesis and shown in next chapters.

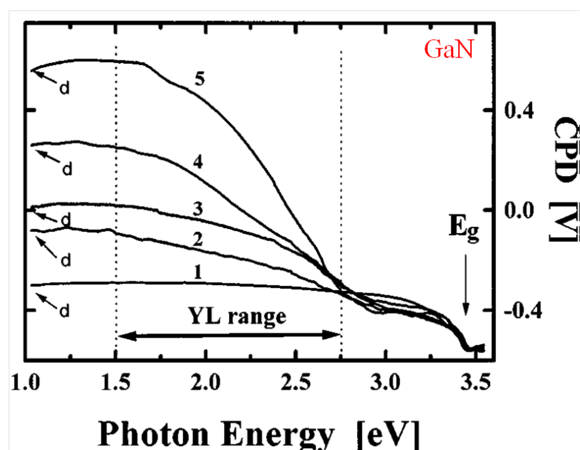

Figure 3.18 SPV spectra showing the GaN band gap and YL related transition [42]

Thus he SPV analysis offers the possibility of performing contactless and non-destructive characterization of buried and surface interfaces and quantum wells, resulting in a complete description of the electrical and optical properties of the sample.

3.5 Photocurrent Spectroscopy

Photoconductivity is an optical and electric phenomena, where a material/substance shows the increase in conductivity on absorption of the light radiation such as visible, ultraviolet etc. Photocurrent spectroscopy, also known as the spectral photoconductivity (SP) method, has been used to investigate the photoconductivity changes [43] subsequent to extrinsic or intrinsic photon-absorption processes that induce charge transitions in semiconductor materials or devices.

In a semiconductor, intrinsic absorption occurs due to larger or equal photon energy to the bandgap value ($h\nu \geq Eg$), so that carriers of both types are generated. Differently, extrinsic absorption is generated by below-bandgap energy light, able to excite transitions of carriers from deep levels to either bands, as schematically shown in Figure 3.19. SP may allow for distinguishing surface or bulk defect states from the analysis of the relevant spectra. In fact, spectral photocurrent measurements carried out by sub-bandgap light [44, 45] might be used to study deep levels in the bulk as these measurements are less sensitive to surface effects in comparison to above-bandgap illumination because the photocurrent is collected from the whole bulk, so that the contribution of the surface region is usually negligible

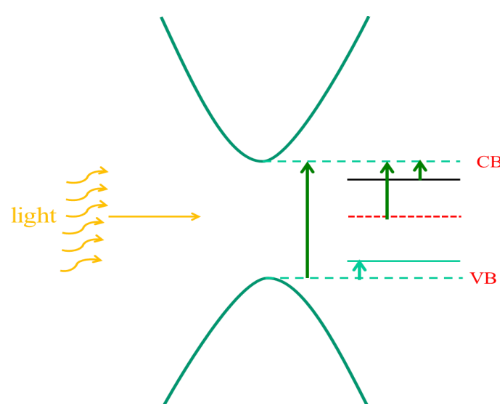

Figure 3.19 Band-to- band and intraband transitions induced by photons

Conversely, spectral photocurrent measurements carried out by above-bandgap light [45] might be eminently used to study the surface states.

3. 5.1 Basic Principles

Photoconductivity effects in solids were discovered by Smith [46] at the end of the nineteenth century. In the 1920s, Gudden [47] developed the photoconductivity theory demonstrating the dependence of photoconductivity, light absorption and luminescence on the light wavelength and assessing that the interaction occurs between one photon and one electron.
The dark conductivity σ of a semiconductor is given by:

$$\sigma = e(n\mu n + p\mu p) \qquad (3.60)$$

where, μ_n and μ_p the electrons and holes mobility, respectively, and n and p their concentrations, respectively.

Photoconductivity [43] $\Delta\sigma$ is defined as the increase of conductivity occurring in a semiconductor under optical excitation. When light of near-bandgap energy hits a homogeneous semiconductor, the conductivity increases by an amount $\Delta\sigma$ due, in most cases, to the increase of the free-carrier densities Δp and Δn:

$$\Delta\sigma = e(\Delta n\mu_n + \Delta p\mu_p) \qquad (3.61)$$

It should be reminded that only the majority carrier transport, electrons for n-type and holes for p-type semiconductors, is usually considered since low injection conditions are used. Moreover, the charge neutrality is assumed to be maintained during illumination, i.e., $\Delta p = \Delta n$. Photogenerated excess carriers in semiconductors are typically or ders of magnitude lower than their density in the dark ($\Delta p \ll p$ and $\Delta n \ll n$); conversely in semi-insulators the excess carriers are much higher than the dark density. Photo-carrier densities $\Delta n = f\,\tau_n$; $\Delta p = f\,\tau_p$ depend on the number f of electron–hole pairs generated per second per unit volume. The parameter f is, in turn, related to the excitation intensity $\Phi(\lambda)$ and to the absorption coefficient α (λ). The spectral response is therefore a function of λ.
From the Beer's law

$$A_{abs.} = \alpha(\lambda) d N_t \qquad (3.62)$$

where, $A_{abs.}$ is the absorbance, $\alpha(\lambda)$ is the absorption coefficient, d is the penetration depth and N_t is the absorbing species concentration, f can be expressed by:

$$f = \beta\alpha(\lambda)\phi(\lambda) \qquad (3.63)$$

where β is the number of carrier-pairs generated by each photon (typically $\beta < 1$) [48]. The photoconductivity $\Delta\sigma$ can be finally expressed, taking into account reflection

$$\Delta\sigma = e\beta\alpha\phi(1-R)(1-e^{-\alpha d})(\mu_n\tau_n + \mu_p\tau_p) \qquad (3.64)$$

A strict correlation thus exists between α (hν) and $\Delta\sigma$ (hν), as depicted in Fig. 3.20 [44].

For photon energies $h\nu > E_g$, corresponding to the high absorption region I in Figure 3.20 the light is mainly absorbed close to the surface, hence the photoconductivity $\Delta\sigma$ is controlled by the surface carrier lifetime. In the intermediate region $h\nu \approx E_g$, (region II) the photoconductivity is

controlled by the bulk lifetime, with a maximum occurring for $\alpha \approx 1/d$, d being the sample thickness. For $h\nu \ll E_g$ (region III) the bulk lifetime still controls the photoconductivity, which decreases by orders of magnitude as absorption coefficient does. In this region, however, the impinging light induces transitions involving deep levels (DL) in the bandgap. Here, the absorption coefficient α is proportional to the density of deep levels centers N_{DL} by the relation:

$$\alpha = s_0 N_{DL} \tag{3.65}$$

with s_o the optical capture cross section of the centers [44].

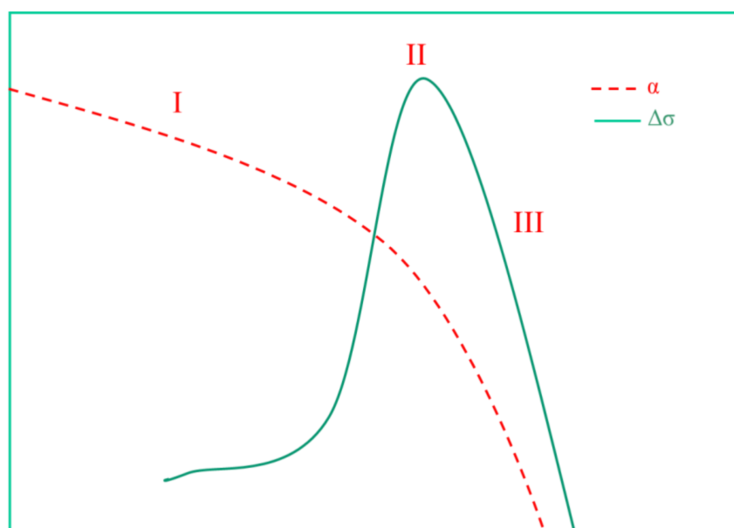

Figure 3.20 Light wavelength dependence of the absorption coefficient α and of the photoconductivity σ in the regions above (I), near (II) and below (III) bandgap [49]

At photon energy exciting extrinsic transitions, the photoconductivity spectra show peaks, the height of which is related to the density N_{DL} of the deep levels involved in the process. Usually, photoconductivity measurements are carried out in an ohmic planar configuration, The use of a rectifying Schottky contact configuration sensibly increases the signal intensity. The high collection efficiency, due to the electric field acting across the depletion region, allows well-resolved spectra to be obtained from which many details can be inferred. The Schottky contact configuration, however, limits the exploration to the depletion region W [1] also when W is much lower than the light-penetration depth. Light absorption can induce processes other than the intrinsic and extrinsic transitions [44], as for instance intraband transitions, i.e., transitions between internal levels. Intraband transitions cannot be, however, detected by photoconductivity measurements since they do not involve carrier transfer to the conduction or valence band, hence do not affect the free-carrier concentration.

3.5.2 Experimental tools/setup for Photocurrent Spectroscopy

Photocurrent setup consists of following major tools:

1. **Light sources** are one of the basic building blocks of many optical spectroscopy experiments. The spectrum can be discrete, as in Hg lamps, continuous, as in Quartz

Tungsten Halogen (QTH) lamps, or a superposition of continuous and discrete spectrum, as in Xenon Arc lamps.

2. The **monochromator** is the element which allows the selection of a narrow band $\Delta\lambda$ of wavelengths from a source of radiation. The selected wavelengths can be directed to the sample to analyse, as in absorption or photocurrent spectroscopy, or can be extracted from the emission of the sample.

3. A **thermopillar**, which is a series connection of a certain number of thermocouple junction. A thermocouple junction consists of two dissimilar metals connected in series. To detect the radiation, one junction is blackened to absorb the radiation. The temperature rise of the junction generates a voltage. An increase in the output voltage is obtained by increasing the number of thermocouple junctions.

4. The **lock-in technique** is used to measure very small AC signals, even when they are buried in noise. A lock-in is a filter with a very narrow bandwidth, tuned to the frequency of the signal. The filter rejects most of the noise, having Q factors as high as 10^6. In addition to filtering, the lock-in also provides gain, up to 10^9. The basic principle of the lock-in is that the experiment is performed at a fixed frequency, possibly far from the frequency regions where significant noise source can be present. In the present experiments a reference signal is fed to the lock-in by means of a photodiode sensing the on- and off-states of the chopper. The reference signal enters a Phase-Lock Loop (PLL) circuit which tracks the input signal frequency. The lock-in is then capable to extract the first harmonic of this square wave, in form of a sinusoidal function. The other signal may be either the photocurrent signal from the sample or the signal from the light detector.

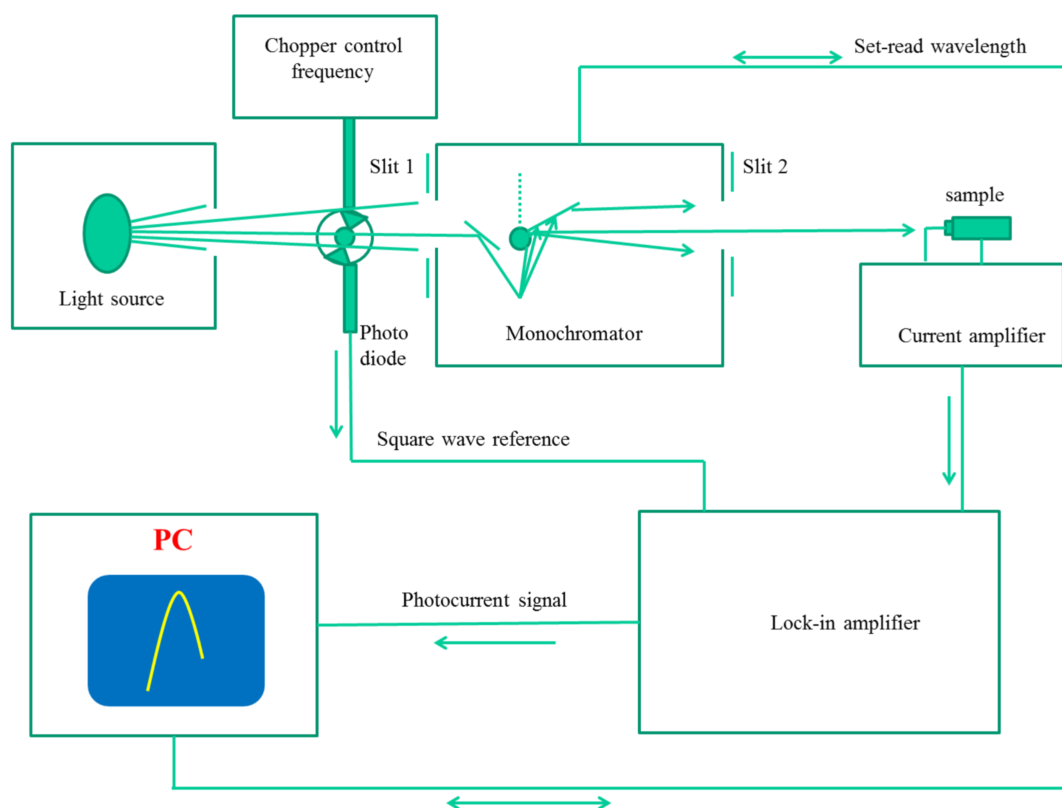

Figure 3.21 Block diagram of Photocurrent setup

3.5.3 Applications in GaN and heterostructures/quantum wells

Spectral photoconductivity has been an advanced tool for characterization the GaN materials and heterostructures. In recent years, it has been used for defect characterizations in GaN layers [50] and also for GaN based heterostructures for various applications such as LEDs, solar cells etc [51]. Fig. 3.22 shows the deep levels in GaN responsible for different luminescence. Fig. 3.23 shows the 2DEG related peak in AlGaN/GaN based HEMT structure with variable chopper frequence which is one of the main area of interest in this thesis.

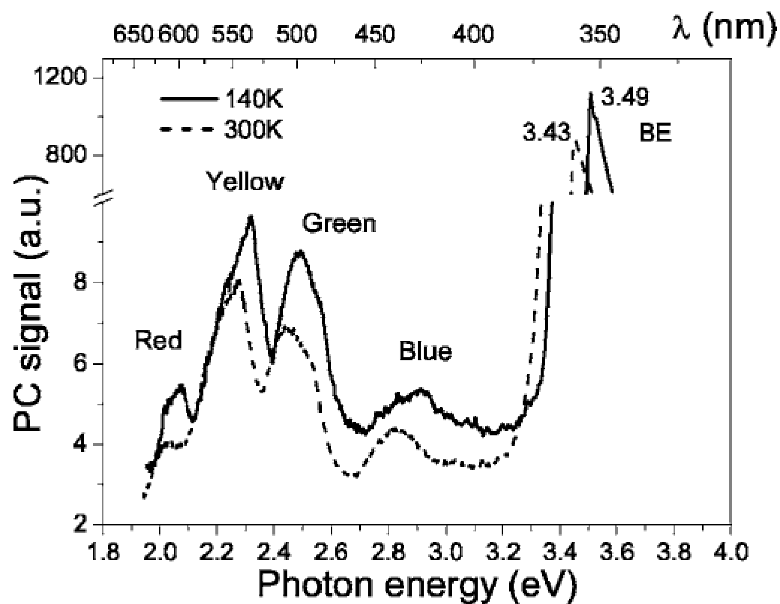

Figure 3.22 Showing Deep levels in GaN layers [50]

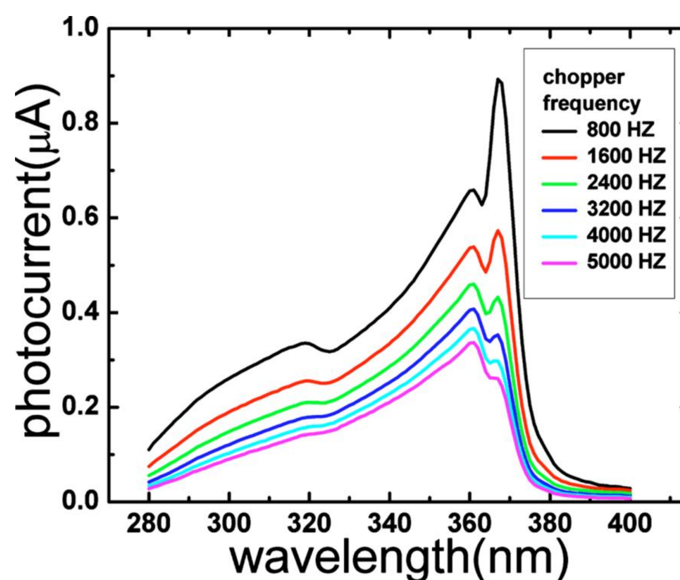

Figure 3.23 Showing presence of 2DEG related absorption in AlGaN/GaN based HEMTs [51]

References

1. S. M. Sze, Physics of semiconductor devices, Wiley, (1981)
2. J.P. McKelvey, Solid state and semiconductor physics, Harper publications (1967)
3. D.A. Neamen, Semiconductor physics and devices, McGraw Hill, New York (2003)
4. E. H. Rhoderick, “Metal-Semiconductor Contacts” IEE Proceedings-I Solid-State and Electron Devices, 129, 1 – 14 (1982)
5. E. H. Rhoderick and R. H. Williams, “Metal-Semiconductor Contacts”, (Publishers: Clarendon Press, Oxford), 2nd Edition, (1988)
6. F. A. Padovani and R. Stratton, , Solid State Electronics, 9, 695, (1966)
7. D. Donoval, M. Barus and M. Zdimal, Solid State Electronics, 34, 1365 (1991)
8. C. R. Crowell and V. L. Rideout, Solid State Electronics, 12, 89, (1969)
9. Z.Q. Fang, D.C. Reynolds and D.C. Look, J. Elec. Mater. 29, 448 (2000)
10. J.M. Shah, Y.L. Li, T. Gessmann and E.F. Schubert, J. Appl. Phys. 94, 2627 (2003)
11. C. Kittel, Solid State Physics. John Wileys & Sons, USA, (2005)
12. D. K. Schroder, Semiconductor material and device characterization. New York: Wiley, (1990).
13. D. V. Lang, J. Appl. Phys., vol. 45, pp. 3023 (1974).
14. R. Magno, R. Shelby, W. T. Anderson, J. Appl. Phys., 66, 5613, 1989
15. T. Mizutani, T. Okino, K. Kawada, Y. Ohno, S. Kishimoto, K.Maezawa, Phys. Stat. Sol. A, 200, 195 (2003)
16. T. Mizutani, A. Kawano, S. Kishimoto, and K. Maeazawa,” Phys. Stat. Sol. C, 4, 1536, (2007)
17. H. Kim, A. Vertiatchikh, R. M. Thompson, V. Tilak, T. R. Prunty, J. R. Shealy, L. F. Eastman, "Microelec.Reliability, 43, 823, (2003)
18. K. Ikeda and H. Takaoka, Jap. J. Appl. Phys., 21, 462, (1982)
19. S.Weiss and R. Kassing, Solid-State Electron., 31, 1733 (1988)
20. L. Dobaczewski, P. Kaczor, I. D. Hawkins, and A. R. Peaker, J. Appl. Phys.,76, 194 (1994)
21. W. A. Doolittle and A. Rohatgi, J. Appl.Phys., vol. 75, 4560 (1994)
22. L. Rigutti, Ph. D. dissertation, University of Bologna, (2008)
23. P. Blood and J. W. Orton, “The electrical characterization of semiconductors: majority carriers and electron states”. San Diego :Academic Press (1992)
24. P. Omling, E. R.Weber, L.Montelius, H. Alexander, and J.Michel, Phys. Rev. B, 32, 6571 (1985)
25. V. V. Kveder, Y. A. Osipyan,W. Schröter, and G. Zoth, Phys. Stat. Sol. A, 72, 701, (1982).
26. T. Wosiński, J. Appl. Phys., 65, 1566, (1989)
27. P. N. Grillot, S. A. Ringel, E. A. Fitzgerald, G. P. Watson, Y. H. Xie, J. Appl. Phys., 77, 676, (1995)
28. A. R. Arehart, Ph.D. dissertation, The Ohio State University, (2009)
29. W. Schröter, J. Kronewitz, U. Gnauert, F. Riedel, and M. Seibt, Phys. Rev. B, vol. 52pp. 52, 726, (1995)
30. Hierro, A. R. Arehart, B. Heying, M. Hansen, J. S. Speck, U. K.Mishra, S. P. DenBaars, S. A. Ringel, Phys. Stat.Sol. B, 228, 309 (2001)
31. T. Figielski, Solid-State Electron., 21, 1403 (1978)
32. P. N. Grillot, S. A. Ringel, E. A. Fitzgerald, G. P.Watson, Y. H. Xie, J. Appl. Phys., 77, 3248 (1995)
33. K.K. Ng., “Complete Guide to the Semiconductor Devices”, McGraw-Hill, New York, (1995)
34. L. Kronik, Y. Shapira, Surface Science Reports, 37, 206 (1999)

35. C M Wolfe, N. Holonyak, G E Stillman.,“Physical Properties of Semiconductors”, Prentice Hall, New Jersey, (1989)
36. M. Leibovitch, L. Kronik, E. Fefer, L. Burstein,V. Korobov, Y. Shapira, J. Appl. Phys. 79, 8549 (1996)
37. H. Luth, “Surfaces and Interfaces of Solids.” Springer-Verlag: Berlin (1993)
38. L. Kronik, Y. Shapira, Surface Interface Analysis; 31, 954 (2001).
39. L. Burstein, J. Bregman, Y. Shapira, J. Appl. Phys, 69, 15 (1991)
40. Gal D. et al., Proc. AIP; 353, 453, (1995)
41. Kronik L. et al., Appl. Phys. Lett., 68, 879, (1996)
42. I. Shalish, L. Kronik, G. Segal, Y. Rosenwaks, .Y. Shapira, U. Tisch and J. Salzman, Phys. Rev. B, 59,9748 (1999)
43. R. H. Bube, “Photoconductivity of Solids, John Wiley and Sons”, New York (1960).
44. R. H. Bube, Photoelectronic, “Properties of Semiconductors”, Cambridge University Press, New York, US (1992)
45. J. J. Pankove, “Optical Processes in Semiconductors Dover Publications”, Inc. New York, US. (1971)
46. W. Smith, “Effect of light on selenium during the passage of an electric current”, Nature, 7, 303 (1873)
47. B. Gudden, “Photoelectric Phenomena (Lichtelektrische Erscheinungen)”, Springer, Berlin, Germany (1928)
48. S. M. Ryvkin, “Photoelectric Effects in Semiconductors”, Consultant Bureau, (1964)
49. A. Cavallini, D. Cavalcoli, L. Polenta, “Advanced Characterization Techniques, in Advanced Silicon Materials for Photovoltaic Applications”, John Wiley & Sons, Ltd, Chichester, UK (2012)
50. L. polenta, A. Castaldini, A. Cavallini, J. App. Phys. 102, 063702 (2007)
51. Y. Huang, D. J. Chen, H. Lu, H. B. Shi, P. Han, R. Zhang, Y. D. Zheng, Appl. Phys. Lett. 96, 243503 (2010)

Chapter 4

Characterization of GaN layer

In this chapter I report on how GaN layer has been characterized with various electrical and optical methods. As in this thesis GaN layer has been used as reference material in order to understand the results of GaN based heterostructures, it is significant to explore the electrical and optical properties of GaN. The chapter starts with experimental results from basic electrical techniques like I-V, C-V to understand the electronic transport properties and proceeded with defect characterization by DLTS method. The electrically active defects and their capture cross section iare investigated and compared with various references. Optical spectroscopy methods like Surface Photovoltage, Photocurrent and Photoluminescence have been used to investigate the optical properties and to correlate the defect related transitions/emission with DLTS results.

4.1 Sample details and growth information

GaN layer was grown on sapphire (Al_2O_3) by Metal-Organic Chemical Vapor Deposition (MOCVD) technique. The grown Ga-face (0001) GaN layer thickness was 3 µm and confirmed by Reflection and transmission analysis by X-ray Diffraction method by sample provider. The thick GaN layers (0001) was grown on sapphire at 1050 °C using LT (low temperature) GaN nucleation layer. This leads to the formation of semi-insulating (unintentionally doped) n-type GaN. The experimentally measured Hall carrier concentration at 300 K is around ~ 4 x 10^{17} cm^{-3}. The carrier concentration has been also measured by Capacitance-Voltage analysis which is discussed in next sections.

Electrical measurements are performed on semitransparent ‘Pt’ Schottky contacts (dots of 1mm diameter) and Ti/Al/Ni/Au Ohmic contacts (dots of 1 mm diameter). The ohmic and Schottky contacts are prepared by Ti/ Al/Ni/Au and Pt evaporation, respectively; for ohmic metallization, further annealing was performed at 850^0 C for 30 s in N_2 ambient. Ohmic contacts have been checked and found quasi-Ohmic behavior, probably due to semi-insulating nature of GaN layer as it’s not doped, consequently with lower carrier concentration.

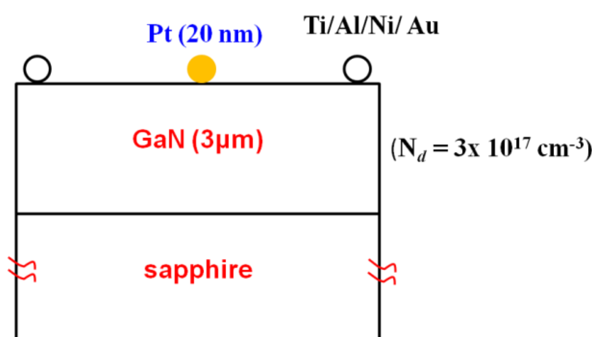

Figure 4.1 Schematic of GaN layer on sapphire with Schottky (filled dot) and Ohmic contacts (empty dots)

4. 2 Current - Voltage (I-V) characterization

The Current-voltage measurements have been performed vs. temperature (218 K – 403 K). The measurements have been performed in range of -2 V to 2 V. shown in Fig. 4.2 it can be seen that the current rises with temperature in forward and reverse bias. A very high leakage current is observed at low bias (for instance 100 nA at 1V) which is still an open issue in GaN based device as leaky devices suffer with several problems like current collapse, early degradation etc. due to presence of traps/defects [1]. The conduction mechanism involved for higher reverse leakage and forward bias current is discussed in order to understand the role of dislocations and metal-semiconductor interface related properties, respectively.

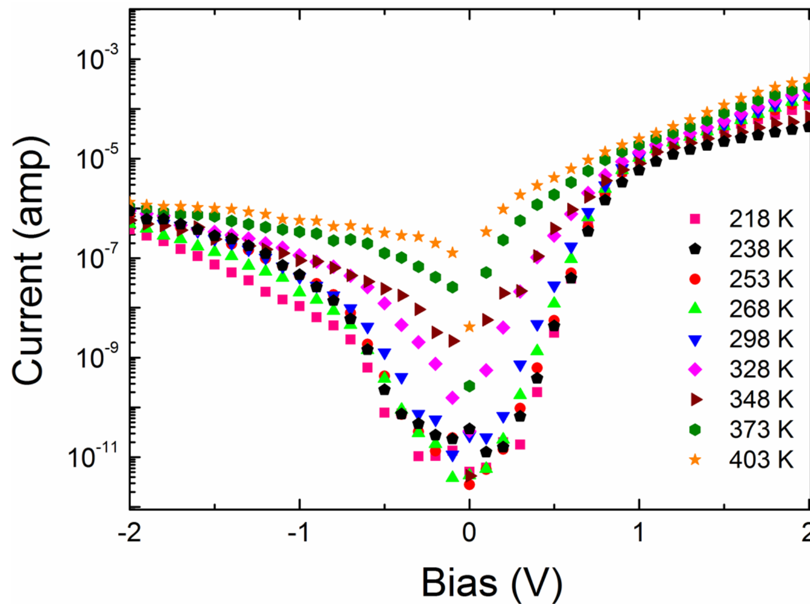

Figure 4.2 Forward and reverse bias characteristics of Pt-GaN at different tempearatures

Forward bias analysis

The forward bias characteristics is analyzed with the Thermionic emission (TE) model, as explained in chapter 3.. The apparent Schottky barrier height (SBH) ϕ_b and ideality factor (n) have been calculated with TE model from eq. 4.1 and 4.2, shown in Fig. 4.3a. It shows the variation of barrier height and ideality factor with temperature

$$I = I_0 AA^* T^2.\exp(\frac{-q\phi_b}{kT}).(\exp(\frac{V_{eff}}{nkT})-1) \quad (4.1)$$

where, $$I_0 = A^* T^2.\exp\left(\frac{-q\phi_b}{kT}\right) \quad (4.2)$$

where, I_0 is the saturation current density, k is the Boltzman's constant, ϕ_b is the apparent Schottky barrier height, n is the ideality factor, A is the Schottky diode area, A^* is the effective Richardson's constant (~ 26.4 A/cm^{2}K^2).

The experimental values of the barrier height, ϕ_b and the ideality factor, n, are determined from intercepts and slope of the forward-bias ln I vs V plot at each temperature.

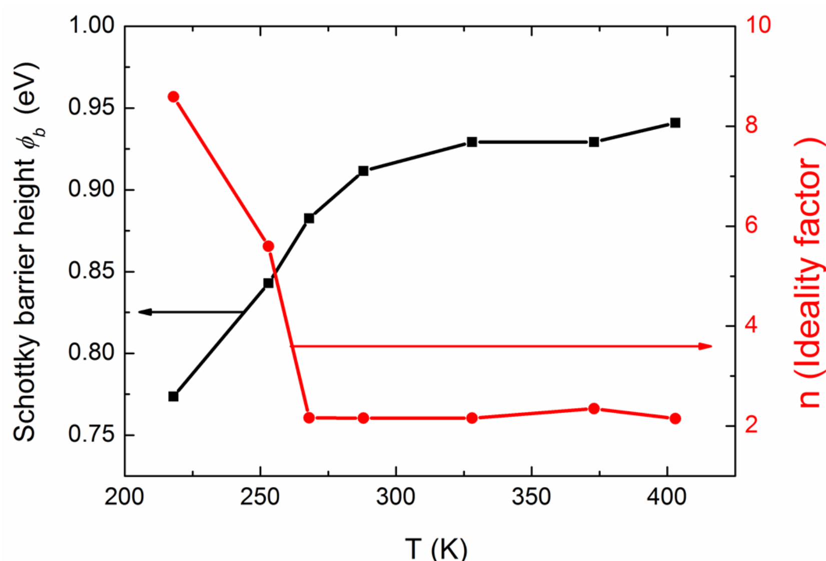

Figure 4.3a Apparent Schottky barrier height and ideality factor variation versus tempearature

An apparent increase in the ideality factor and decrease in the Schottky barrier height moving towards low temperatures are possibly caused by structural defects in the semiconductor, inhomogeneous doping (which is not the case in the sample as it's undoped), interface roughness, interfacial reactions and diffusion/interdiffusion of the contamination of applied material on semiconductor surface. Other possible effects are due to inhomogeneities of thickness and composition of the layer, non-uniformity of interfacial charges or presence of a thin insulating layer between metal and semiconductor [2, 3, 4, 5, 6]. Since current transport across the metal/semiconductor (MS) interface is a temperature activated process, at low temperature electrons having lower energy can surmount such barrier and the dominant current flow is through the regions of the low Schottky barrier height (SBH). As the temperature increases, more number of electrons having sufficient energy to surmount higher SBH at higher temperature activated process, which results in increase of the barrier height. This is evident by plotting SBH variation with 1/T, which is shown in Fig. 3b. It can be observed that at low temperature (218- 300 K) SBH varies significantly while at higher temperature (300 K-403 K) it's almost constant.

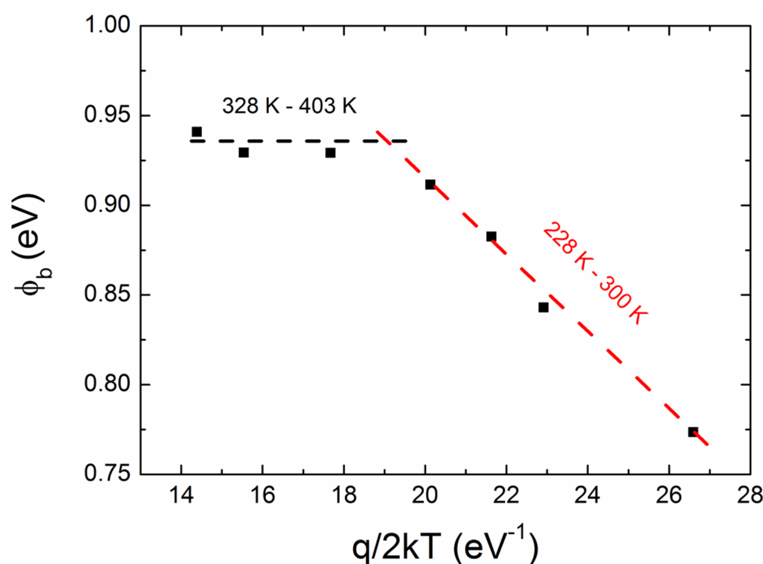

Figure 4.3b Apparent Schottky barrier height variation with temperature

According to [7], a linear relationship between experimental SBH and ideality factor (*n)* values is an indication of the barrier irregularity and can be explained by lateral inhomogeneities of BHs. The value of homogeneous barrier height can be obtained from the extrapolation of the experimental Schottky barrier heights vs ideality factors plot to n = 1 [7, 8, 9]. Thus, for *Pt*-GaN, homogenous a barrier height value is obtained around 0.97 eV, shown in Fig.4.

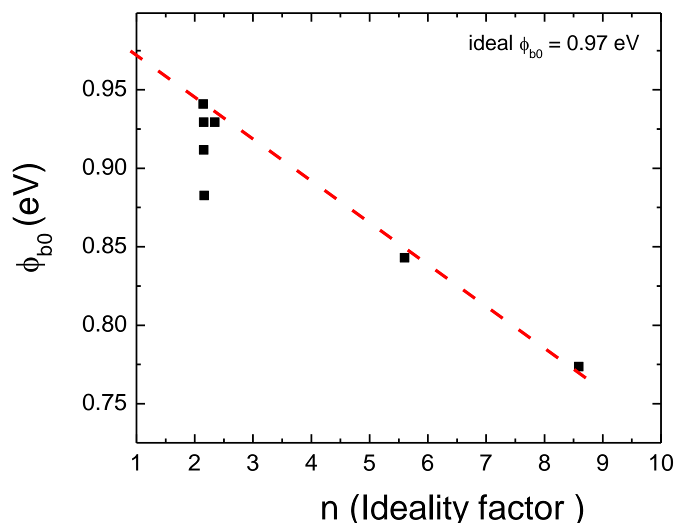

Figure 4.4 Variation of Schottky barrier height with ideality factor. The linear extrapolation for n = 1 gives the ideal barrier height for *Pt*-GaN.

Another way to determine the Schottky barrier height and the Richardson constant is to use the activation energy plot. Using the values of the saturation current density, J_0, at each temperature from the *I*/*J*–*V* data (ig. 5), the conventional Richardson plot of ln(J_0/T^2) vs 1000/*T* is obtained in the temperature range 228–403 K. From the linear fit fig. 4)Schottky barrier height and Richardson constant are calculated to be 0·81 eV and 1·8 A/cm^{2}K^2, respectively. The estimated value of the Richardson constant is much lower than the theoretical value of *n*-GaN (26·4 A/cm^{2}K^2*)*. The deviation in the conventional Richardson plot may be due to the spatially inhomogeneous barrier heights and potential fluctuations at the interface that consists of low and high barrier areas [2, 3, 10, 11] reported that the A^* value obtained from the temperature-dependent *I*–*V* characteristics may be affected by lateral inhomogeneity of the barrier.

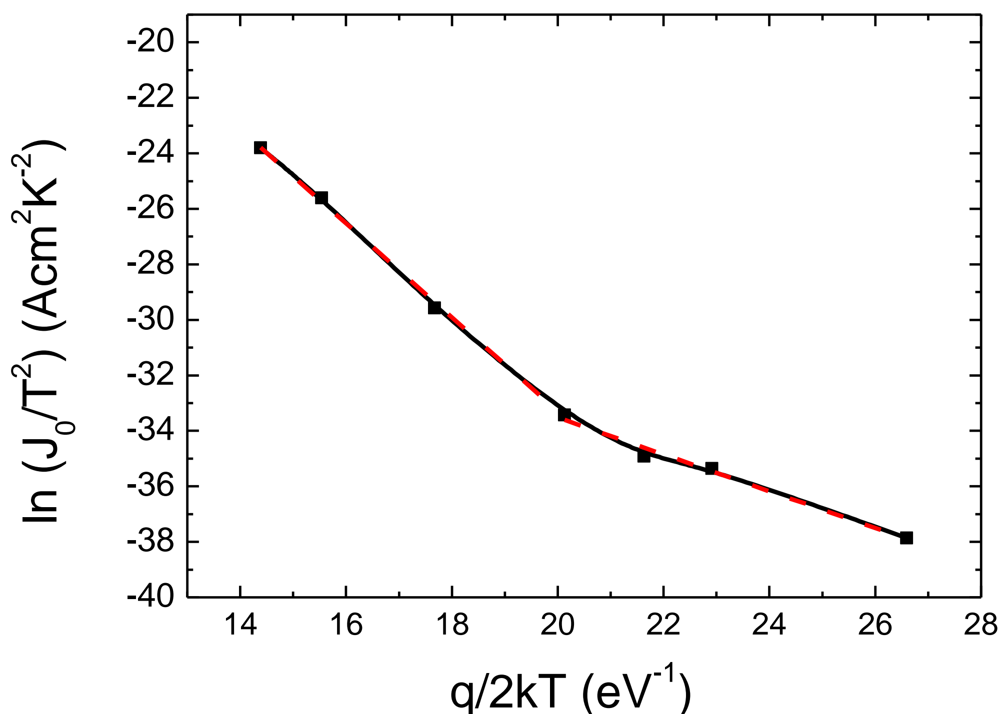

Figure 4.5 Conventional Richardson plot for the measurement of barrier height and Richardson constant

The conventional Richardson's plot, however, is based on the thermionic emission mechanism in eq. (4.1) and, hence, assumes an almost ideal barrier, with ideality factor and the Schottky barrier height independent of the temperature. Hence, the nonlinearity of the conventional Richardson's plot can be associated with the previously shown experimental evidences, namely, the temperature dependence of S*BH* and *n*. In order to take into account the deviation from the ideality and the experimentally observed dependence of *n* and SBH on the temperature, a "modified" Richardson's plot, ln(J_0 /T^2) versus q/2*nkT*, is also reported in Fig. 4.6. This approach was proposed by Hackam and Harrop [12] in order to consider the effects of deviation from $n = 1$ at zero bias voltage as well. In this case, a better linear fit has been obtained, giving a barrier height value of 0.85 eV and a Richardson's constant of 1.8 x 10^{-2} A/cm^{2}K^2. This value of A^*, however, is still significantly lower than the theoretical predictions (26.4 A/cm^{2}K^2) [13] found that the value of A^* determined by a modified Richardson's plot in freestanding GaN material is close to the theoretical value. On the other hand, [14] found a reasonable value of Richardson's constant A^* through a conventional Richardson's plot. Clearly, the wide range of variability of these results can be ascribed to the different interface quality, which, in turn, depends on several factors such as the surface defects density, the surface treatment (cleaning, etching, etc.), the metal and the deposition process (evaporation, sputtering, etc.). As an example, [15] observed a dependence of A^* on the dislocation density of the material, in Ni/GaN Schottky diodes. In our case, it can be argued that the underestimation of the A^* value, even after considering the non-ideality of the
barrier in the Richardson's plot, can be related to the formation of a laterally inhomogeneous Schottky barrier which, in turn, may result into an effective area for the current conduction lower than the total area of the diode.

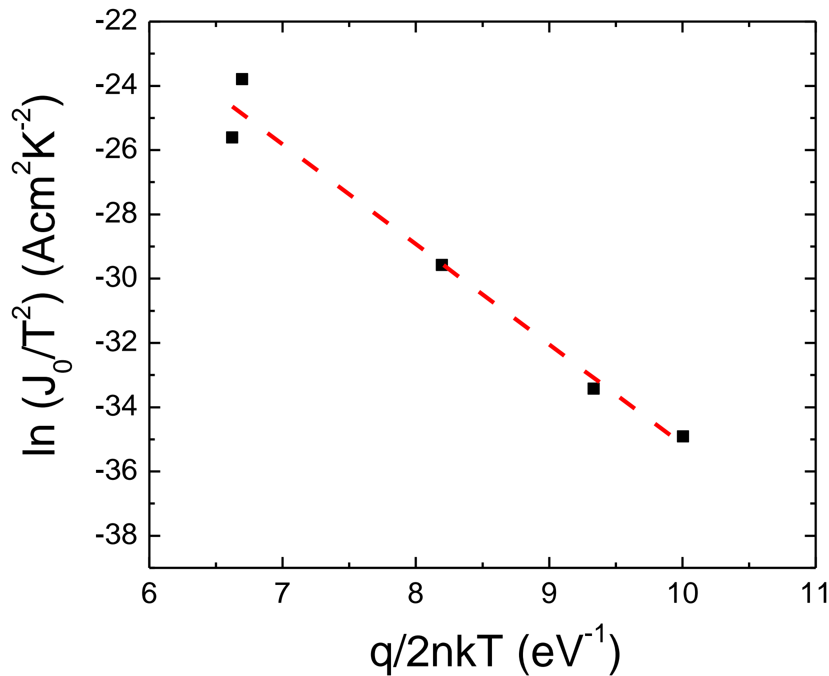

Figure 4.6 Conventional Richardson's plot for calculation of barrier height and Richardson constant

For the tunneling dominated current-transport equation 4.3, the slope of the ln I versus V plot ($q/E_0=q/nkT$) is essentially temperature independent and is called a voltage factor or tunneling constant. In addition, at a constant bias voltage, ln I is more of a linear function of temperature than an inverse temperature. According to the tunneling model, which was developed for Schottky barriers, the band bending works as a barrier for carriers tunneling into interface states or dislocations, where various traps may be involved in multi-tunneling steps [16]. Thermally activated carriers make (stepwise) tunneling into the interface states.

$$I_t = I_{t0}\left[\exp\left(\frac{q(V-IR_s)}{E_0}\right)-1\right] \quad (4.3)$$

where, $E_0 = nkT$ is the tunneling parameter and I_{t0} is tunneling saturation current.

However, E_0 values remains almost unchanged over the same temperature range with an average of 0.15 eV, shown in Fig.4.7. The high value of n can been attributed to several effects such as interface states, tunneling currents in the high dislocations [17–19] image force lowering of the Schottky barrier in the high electric field at a MS interface, and generation currents within the space charge region [20]. The TFE mechanism can be ruled out in this region, since E_0 is more or less constant in the measured temperature range.

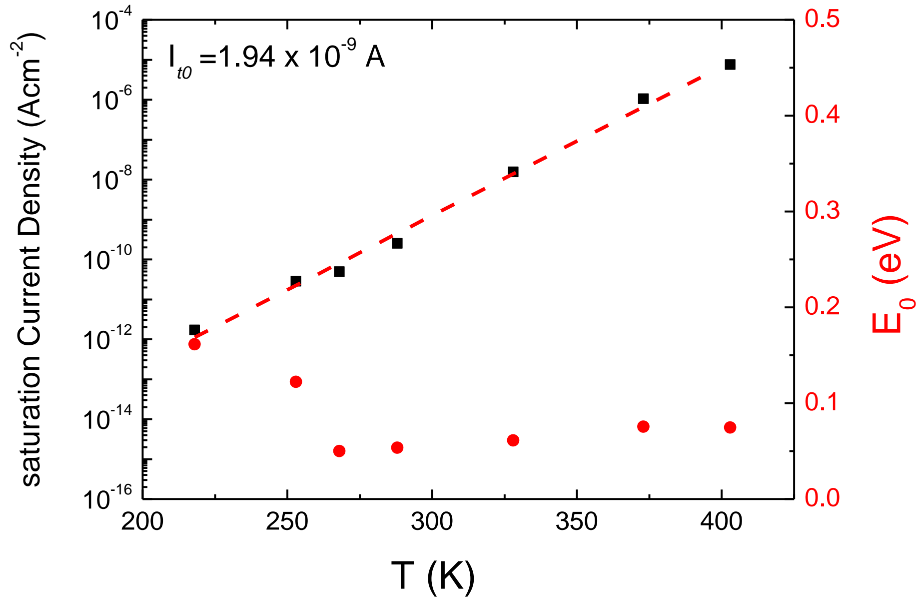

Figure 4.7 Variation of saturation current and tunneling parameter with temperature varitaion with TFE model

Reverse Bias analysis

We studied reverse bias leakage current mechanisms in Pt/Au Schottky contacts on Ga-polarity GaN. In this study, we assume that the main mechanism for leakage current occurs through Poole-Frenkel Emission (FPE) and focus on reverse bias current density and electric field characteristics. In FPE, leakage current is mainly governed by the emission of electrons via trap states into a continuum of states associated with the presence of conductive dislocations. It is successfully explained by the FPE model, in which, usually, the conduction band need not necessarily be in an insulator and its emission refers to the electrical-field-enhanced thermal emission from a trap state into a continuum of electronic states. The current density associated with FPE is given by [21, 22]

$$J = CE_s \exp\left[-\frac{q\left(\phi_t - \sqrt{\frac{qE_s}{\pi\varepsilon_s\varepsilon_0}}\right)}{kT} \right] \tag{4.4}$$

where E_s is the electric field in the semiconductor barrier at the metal/semiconductor interface, Φ_t is the barrier height for electron emission from the trapped state, ε_s is the relative dielectric permittivity, T is the absolute temperature, ε_0 is the permittivity of free space, k is the Boltzmann's constant, and K is a constant. From Eq. (4), ln(J/E_s) should be a linear function of sqrt (E_s), i.e,

$$\ln(J/E_s) = R(T)\sqrt{E_s} + S(T) \tag{4.5}$$

where,

$$R(T) = \frac{q}{kT}\sqrt{\frac{q}{\pi\varepsilon_0\varepsilon_s}} \qquad S(T) = -\frac{q\phi_t}{kT} + \ln C \tag{4.6}$$

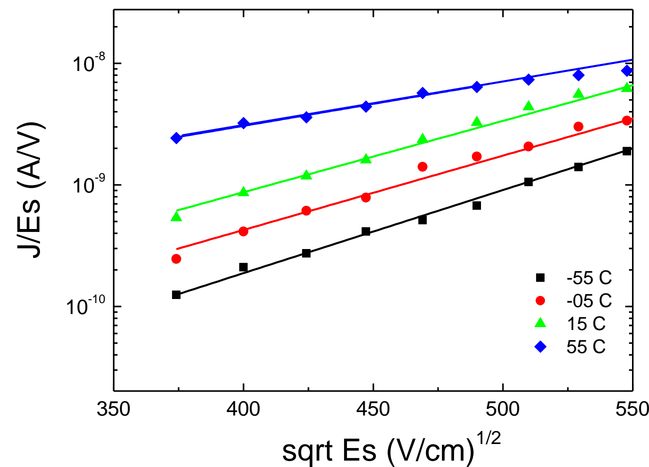

Figure 4.8 Variation ln(J/Es) with electric field for 218 K- 318 K

Figure 4.8 shows the plot of ln(J/Es) versus sqrt(Es) as linear in the temperature range 218-318 K for Pt Schottky contact on GaN; this is a proof for a Frenkel- Poole effect. As defined in eqs. 4.6, we also plotted R(T) and S(T) as functions of 1/T for Pt/GaN Schottky diode. The calculated relative dielectric constant from the slope of R(T) versus 1000/T (figure 4.9a) is 6.0±1 and the emission barrier Φ_t from the slope of S(T) versus 1000/T (the inset of Fig. 4.9b) is 0.14±.04 eV, respectively. The extracted value of ε_s for Ga-polarity GaN is in good agreement with the previously reported [23, 24]. Recently, Arslan et al. [25] reported that dielectric constant and emission barrier are 5.8 and 0.12 eV for AlInN/AlN/GaN hetero-structures, respectively.

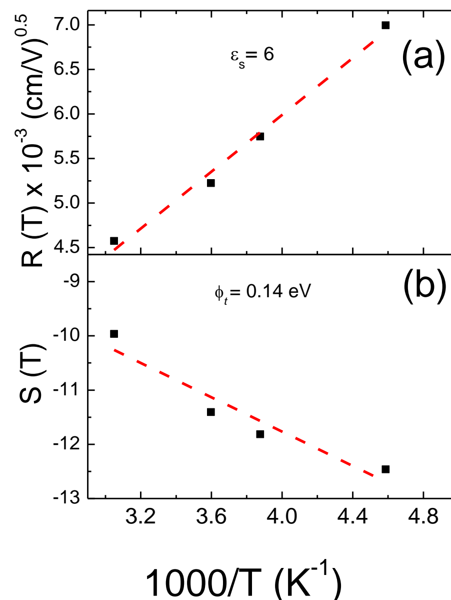

Figure 4.9 Variation of R(T) and S(T) with 1000/T to calculate high frequency constant for GaN (a) and trap barrier height (b)

4. 3 Capacitance -Voltage (C-V) characterization

The C-V measurements have been performed at 300 K to calculate the carrier concentration in GaN layer, depletion region and barrier height as mentioned in chapter 3. The C-V measurements have been carried out at 1 MHz in order to use the C-V results for DLTS characterization.. As can be seen from Fig. 4.10a , the Schottky barrier starts depleting (plateau) around 3 V , shows full depletion at very high reverse bias (~ 15 V) and step-like features. It can be observed from the C-V characteristics Schottky junctions are not completely depleted which is probably due to inhomegenies in the Schottky layer (metal-semiconductor interface) or to the quality of the Ohmic contacts on the GaN layer, that it is undoped and semi insulating. The C-V characteristics are used for calculation of the Schottky barrier height , SBH, by plotting $1/C^2$ vs V, as explained in chapter 3 [20]. The obtained SBH value ~ 0.78±.02 eV (Fig. 4.10b) is in very good agreement with calculations by Current-Voltage analysis, as mentioned above.

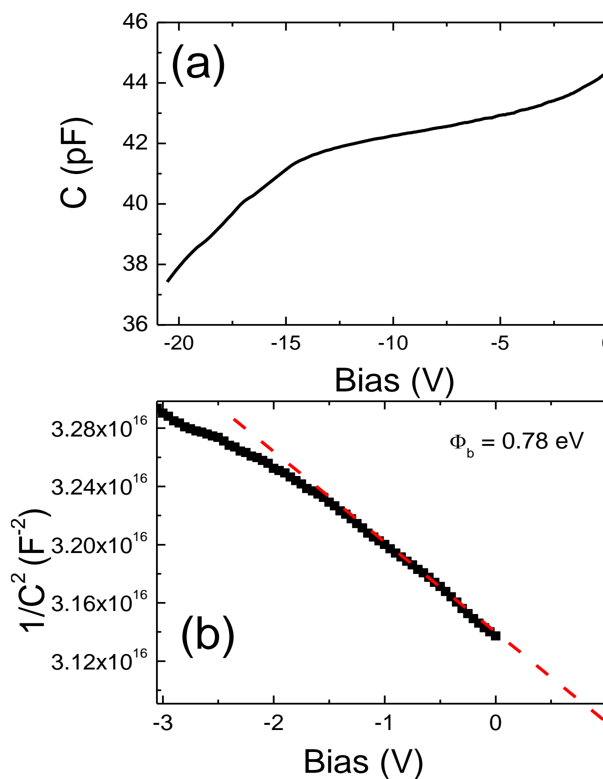

Figure 4.10 C-V characteristics of Pt-GaN at 300 K (a) diagram of 1/C2 vs V (b)

The results of the C-V measurements have been used in order to obtain $n_{CV(x)}$ and $n_{CV(V)}$ profiles, which are shown in Fig 4.11. The Schottky junction is at x = 0 μm. The distribution of carriers with reverse bias and depth indicates that reverse bias increase shows that carrier concentration starts decreases at higher bias. It's shown in fig. 4.9a that depletion starts around 3V, which can be correlated with decrease in carrier concentration with depletion and reaches to lower value with higher bias, evidenced with fig. 4.11. Moreover, the carrier concentration value is in good agreement with Hall effect measurements as provided by the sample grower.

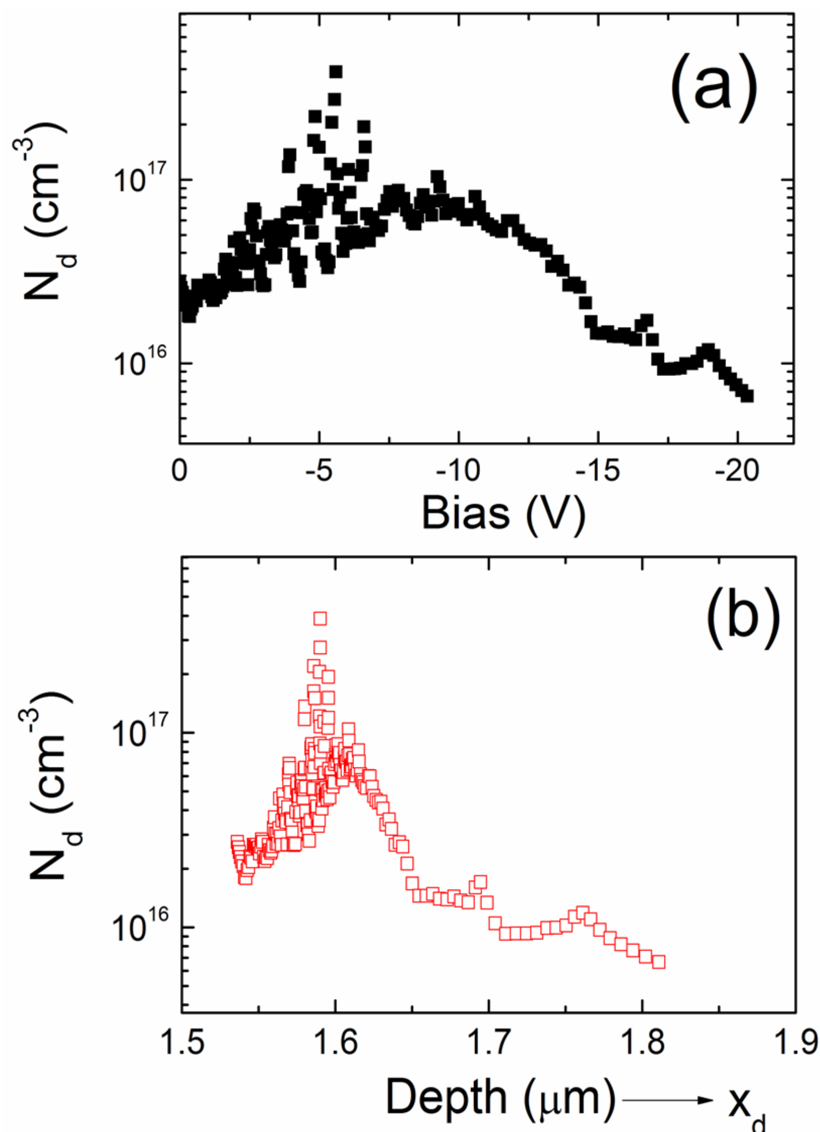

Figure 4.11 Carrier concentration profile with depth (a) and reverse bias (b)

4.4 Deep Level Transient Spectroscopy (DLTS)

Deep level transient spectroscopy has been performed to obtain information on defects/traps level in the band gap of GaN, that is very essential for understanding the electronic and optical properties of GaN devices and GaN based devices in view of their applications. DLTS is performed using a SULA TECH system, to detect the presence of deep levels in unintentionally doped GaN over a temperature range 100 - 500 K. Samples have been biased with -1 V, -3 V, -5 V for different tests with 1 V as filling pulse for trap filling with pulse width = 10 ms. The transient signal has been recorded for different emission rates, as shown in Fig. 4.12. The capacitance, C', and its variation, ΔC, with temperature is also shown in Fig. 4.12. We have observed three different defect levels and calculated their energy levels by plotting Arrhenius plot. The calculated energy level values and capture cross section values are shown in Fig. 4.13.

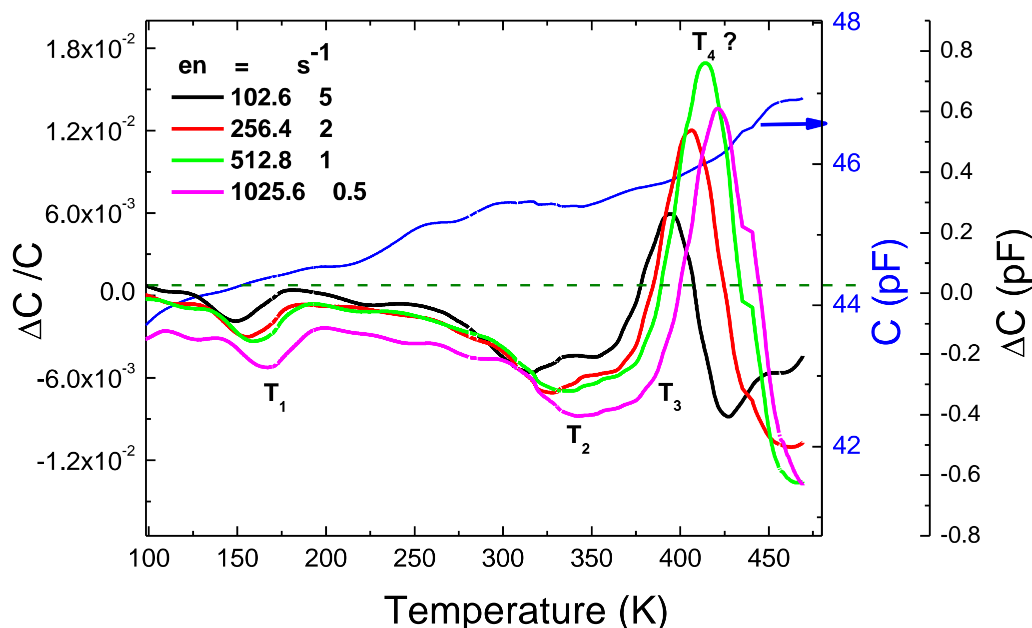

Figure 4.12 DLTS spectra for Pt-GaN (left axes), and ΔC vs. temperature (right axes)

It is worth discussing the evolution of the positive peak in DLTS spectra which should in general to be associated the 'minority carrier trap emission' [26] which turns to be "hole trap" in i/n-GaN layer. However, this 'analomous nature of positive peak' can't be explained in terms of minority carrier trap emission as [26]

a) Capacitance DLTS method does not allow to detect minority carriers in n-type of GaN layer
b) The evolution positive peak could be due to high leakage in Schottky layer i.e. high impedence and also to lack of the high quality Ohmic contacts as explained above. It could be due to the increase in current at high temperature which increases the impedence too which can affect the capacitance measurements and inverse the capacitance transient which results in positive peak evolution in DLTS spectra [26].

However, such appearance of positive peak in DLTS spectra had also been discussed in some studies in GaN [26, 27]

The calculated activation energy values of defects have also compared with earlier reported results on Ga-polar GaN layers by DLTS and Deep level transient optical (DLOS) spectroscopy method [28, 29, 30]. The defect levels present in GaN are mainly associated with charged dislocations which is also responsible for high leakage in GaN based devices as shown in an earlier part of this chapter (see Pool-Frenkel analysis on the trap level at 0.14 eV). Other authors attributed these defect levels mainly due to Gallium (Ga) or Carbon (C) vacancies or complexes in GaN [28]. In the next part of this chapter, we have performed the optical measurements by SPV, PC and PL in order to correlate the presence of defects with transitions/emissions.

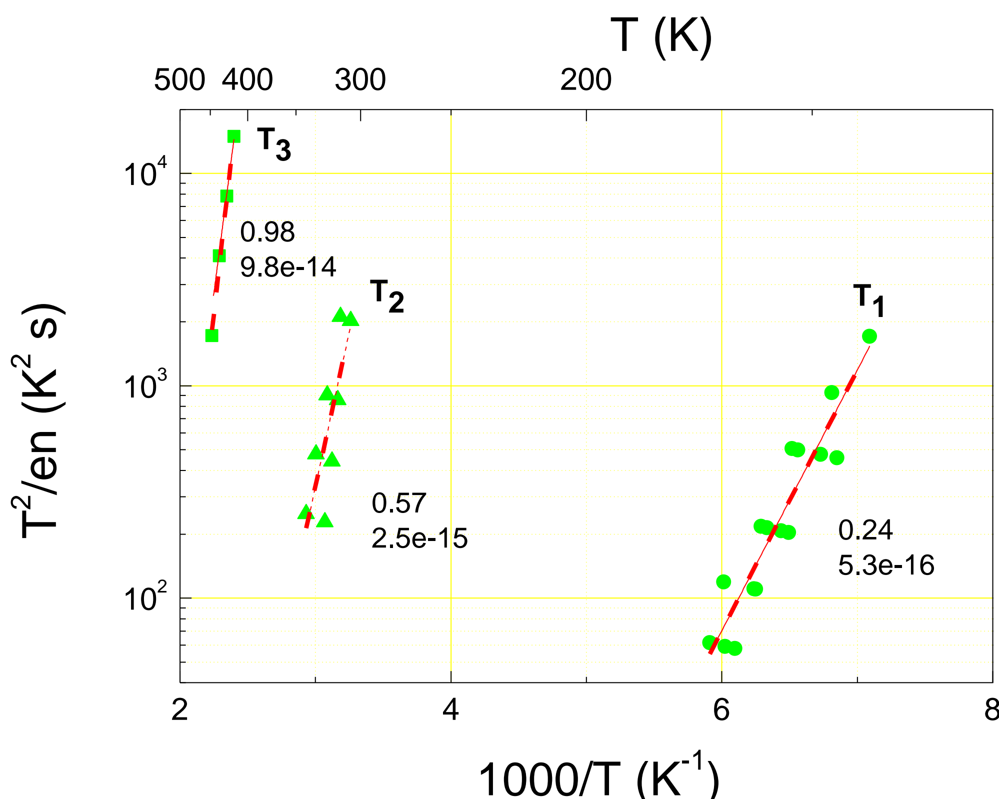

Figure 4.13 Arrhenius plot of GaN sample. Activation energy and capture cross section of the levels detected are reported

4.5 Surface Photovoltage Spectroscopy, Photocurrent and Photoluminescnece analysis

First we will discuss about SPV results obtained with two different light sources and compare their spectra. Later on, we will compare the SPV results with Photocurrent and Photoluminescence analysis for energy gap, defect related information. The aim of the study is to get further information on energy gap and defect/trap level transitions/emissions with optical methods.
In the last section, **table 4.I** has been prepared and summarized with extracted defect level positions from Conduction/Valence band in GaN with optical and DLTS mehtod as well as with some literatures.

Surafce Photovoltage (SPV) spcectroscopy measurements have been performed on GaN layer with two different lamps of QTH and Xe lamp (see chapter 3) at 300 K. SPV measurements have been performed with two different gratings A (300 lines/μm) for detection of energy gap related transition and deep levels related transition, wavelength ranges from 300 – 900 nm and grating B (1500 lines/ μm) to detect deep levels related transitions, wavelength ranges 900-2000 nm. Fig. 4.14a shows the SPV spectra for GaN with QTH and Xe lamps which clearly shows the observed band to band transition related to GaN energy gap. It should be reminded that by changing the photon energy also the optical absorption coefficient α, and in turn the penetration depth α^{-1}, varies. For photon energies ranging from 3 to 4 eV, α^{-1} ranges from 0.07 to 1 μm in GaN [31]. This means that from 3 to 4 eV the carrier generation and collection occurs mainly within the GaN layer.

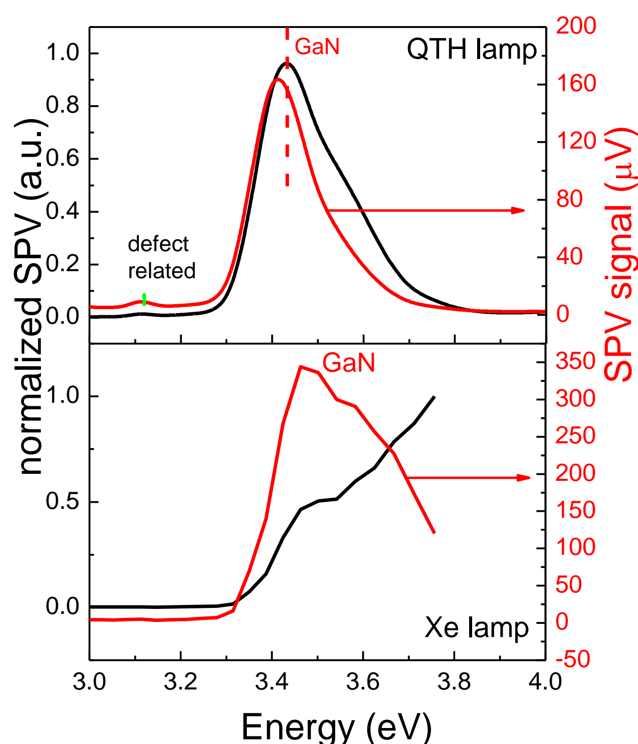

Figure 4.14a SPV spectra of GaN layer recorded by using QTH and Xe lamps

Thus from Figure 4.14a, comparing the both lamps spectra GaN energy gap related information is achieved. It can also be observed the peak at 3.16 eV in the QTH lamp spectrum while it cannot be observed the using Xe lamp, probably because of the very low intensity/absorption compared to GaN gap peak. This peak at 3.16 eV could be related to defect level transition in GaN by considering the data from DLTS analysis which show the one defect level at Ec-0.24 eV. This defect level is mainly attributed [32] to dislocation core level in GaN layer as discussed in DLTS analysis section above.

Photocurrent and Photoluminescence measurements have also been performed at 300 K and 5 K with QTH lamp and He-Cd laser to get information on energy gap and observation of bound and free excitonic emission in PL spectra (fig. 4.13b)). The comparison of SPV, PC and PL spectra is shown in fig.4.14b. Photocurrent measurements have been performed in Schottky-Ohmic contact configuration with bias = -2 V as shown below. A sharp peak has been observed in PC spectra at 3.43 eV, which shows the electron-hole recombination feature and then the signal starts decreasing. In case of PL, measurements have been done at 300 K and 5 K both in order to observe the transitions related to bound exciton and free exciton (FE) near to GaN energy [33]

Figure 4.14b presents PL spectra of GaN on c-plane sapphire measured at 300 & 5 K. The PL spectrum at 5 K exhibits the dominant transition of near band-edge (NBE) band at 3.489eV, together with shoulder at higher energy of 3.502 eV and another at lower energy of 3.496 eV. The spectra exhibit three emission lines identifying the shallow neutral donor-bound (D^oX) and free exciton (FX_A and FX_B), the bound exciton (D^oX) level at 6.7 meV below the free exciton (FX_A) energy. The splitting of FX_A and FX_B levels is 6.8 meV. Our results are in agreement with literature

results [34, 35], and the linewidths of D^oX, FX_A and FX_B as small as 4.0, 3.9 and 6.9 meV, respectively, show the high quality crystal of GaN layer.

The temperature dependence of GaN film has also been investigated. The redshift and broadening of all emission lines with increasing temperature have been observed. The temperature dependence of the linewidth is attributed to phonon-induced band broadening [36]. The characteristic redshift with increasing temperature is attributed to band gap reduction from lattice expansion and to electron-phonon interactions [37]. The first contribution has major importance at low temperature.

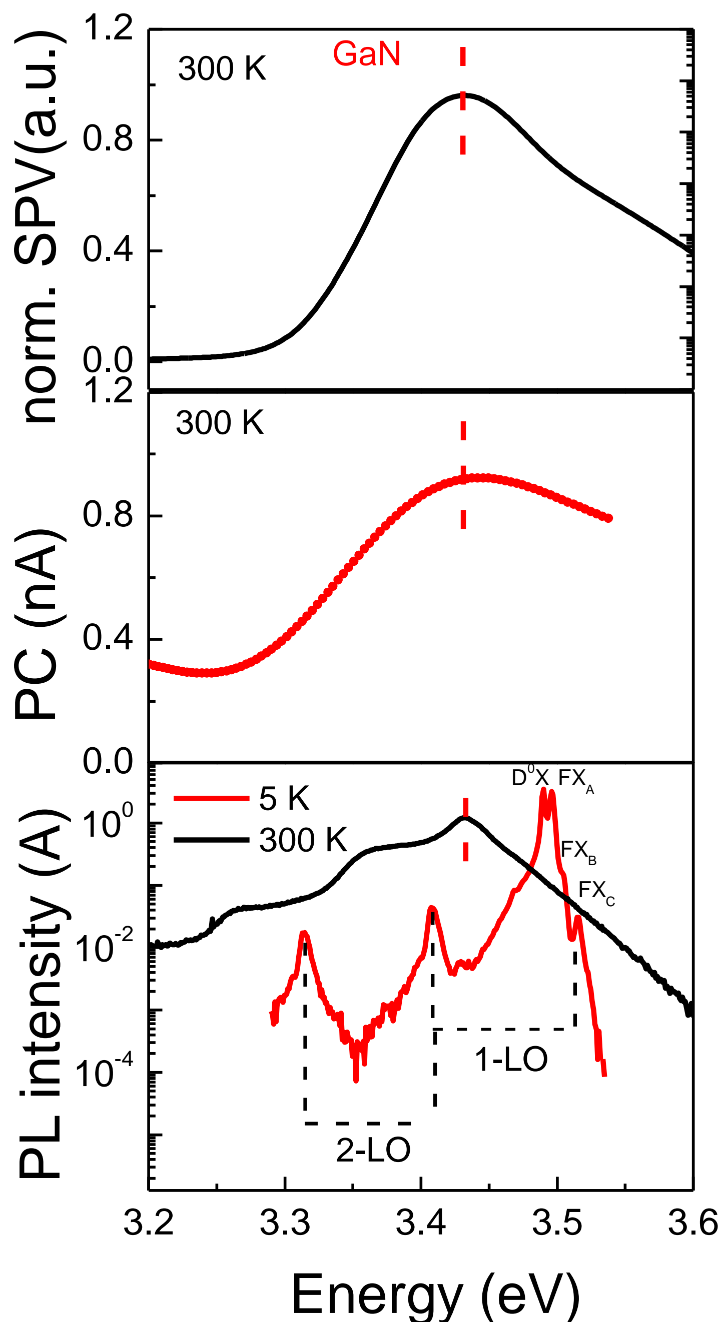

Figure 4.14b SPV, PC spectra at 300 K and PL spectra at 300 K and 5 K

Defect related information has been also achieved by performing measurements below GaN gap with all three different spectroscopies and comparison is shown in Fig. 4.15. SPV and PC measurements have been performed at 300 K and PL measurements have been performed at 5 K for defect level emissions. In SPV spectra one peak at 2.98 eV is clearly observed transition, which is usually related to Blue band (BB) emission also observed in PC and PL spectra around 2.98 eV and 3.05 eV.

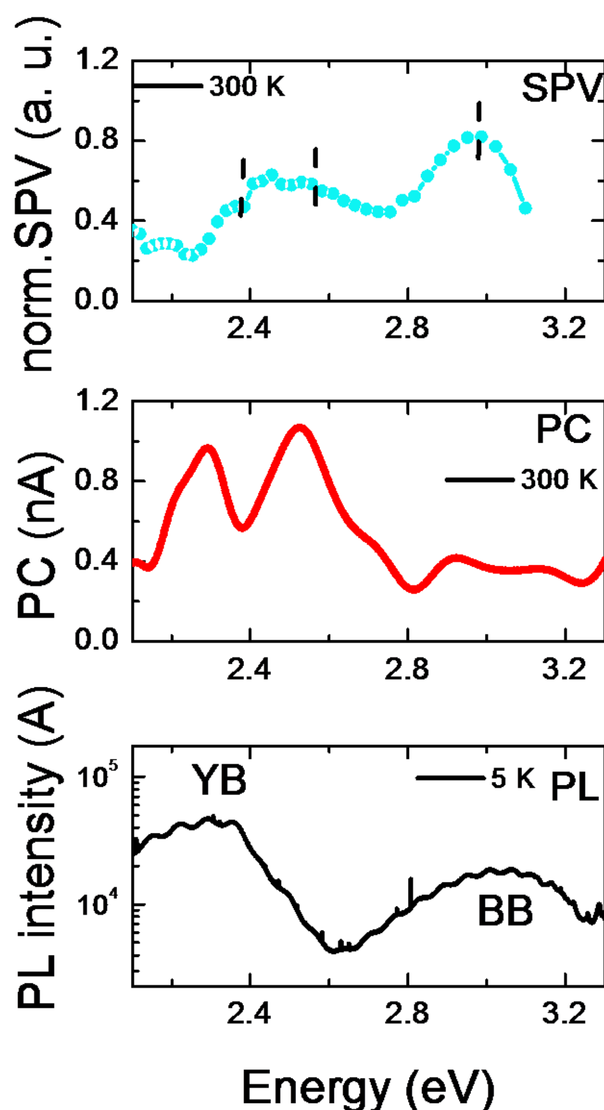

Figure 4.15 SPV, PC spectra at 300 K and PL spectra at 5 K

In case of PL spectra, the broad peak can be related to defect level response as earlier discussed which is mainly related to extrinsic feature (probably due to vacancy complexes nature) in PL spectra. This defect related transition can also be correlated with defect position analysed by DLTS at E_C-0.57 which is in good agreement with SPV, PC and PL. The other feature at 2.48 eV is observed in SPV and PC spectra while in PL spectra this peak is not observed. The peak at 2.48 eV can be due to defect related transition responsible for green band earlier reported in some reports [38]. This defect level can also be correlated with the DLTS results which show a defect level at E_C-0.98 eV. The other peak observed in SPV and PC spectra at 2.28-2.32 eV and also a broad peak in

PL spetra at similar position is observed which can be related to Yellow band (YB) emission in GaN which is still not clear about it origin due to minority carrier enhanced to majority carrier trap, originated from screw/mixed/edge dislocation. Here, I have considered both possibilities in order to explain this transition/emission with consideration of results from literature.

The case of Yellow Luminescence (YL)

I will deal with the origin of Yellow luminescence by considering two possible theories based on a) Screw/ mixed dislocation and b) Edge/mixed dislocation, which is still an open topic. It has been observed that the intensity of YL increases with the concentration of the Ga vacancy, particularly in *n*-type GaN [39]. Furthermore, the Ga vacancy is energetically the most favorable configuration in *n*-type GaN [40] . However, the Ga vacancy itself is a shallow accepter [40] and hence the Ga-vacancy/impurity complex has been suggested to be one of the sources as YL [41, 42]. Transitions between a shallow donor and a deep acceptor [43] or a deep donor and a shallow acceptor [44] could be responsible for YL. It has been suggested that YL is due to screw component of dislocation in some reports [45]. Recent theoretical calculations [46, 47] indicated that dislocations may well be charged, giving rise to deep-gap states, also discussed above with optical spectroscopies and DLTS results. Lee et al. reported that YL could also be due to edge dislocation even in absence of Ga/N vacancy or complexes where it is discussed that the dangling bonds at Ga and N atoms mostly contribute to deep-gap states and valence-band tails, respectively [32]. All the edge dislocations can act as deep trap centers except the Ga-vacancy dislocation, which may act as a source for YL. Full- and open-core dislocations show deep-gap states, which are mostly contributed by the Ga dangling bonds, located at the dislocation. Here, it is shown in Fig. 4.16 the emission mechanism for YL luminescence in undoped n-GaN with the consideration of a deep acceptor level above to valence band E_v+ (0.8-1) eV [48]. The suspected source of this YL band around 2.2 eV is a deep carbon level or gallium vacancy. It shows that YL mainly originate due to a transition from shallow donor/dislocation state to deep acceptor state which results in YL transition/emission in GaN.

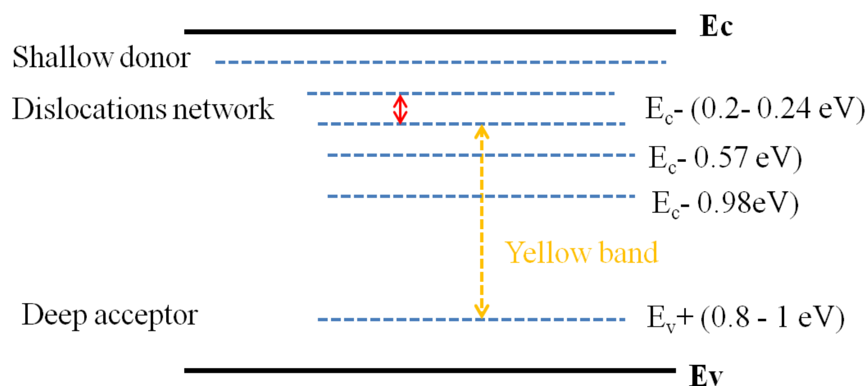

Figure 4.16 Emission mechanism of Yellow Band in GaN

Table 4.I Summary of defect levels observed by DLTS, SPV, PC and PL

Summary on defect levels in GaN

Methods	Defect levels (eV)			Capture cross section by DLTS (cm^2)	
	BB	GB	YB	BB	GB
DLTS	E_C-0.24 E_C-0.57	E_C-0.98	-	5.3×10^{-16} 2.5×10^{-15}	9.8×10^{-14}
SPV	2.98	2.48	2.28	-	-
PC	2.98	2.48	2.30	-	-
PL	3.02	-	2.32 -	-	-

References

1. J. Joh, J. D. Alamo, IEEE Dev. Lett. 29, 287 (2008)
2. P. Y. Song, R. L. Van Meirhaeghe, W. H. Lafler, F. Cardon Solid-State Electron. 29, 633(1986)
3. J. H. Werner, H. H. Guttler J. Appl. Phys. 69, 1522 (1991)
4. J. P. Sullivan, R. T. Tung, M. R. Pinto, W. R. Graham, J. Appl. Phys. 70, 7403 (1991)
5. G. Y. Chen, M. Ogura, H. Okushi Appl. Phys. Lett. 82, 4367 (2003)
6. S. Zhu, R. L. Van Meirhaeghe, S. Forment, G. P. Ru, X. P. Qu, B. Z. Li, Solid-State Electron. 48, 1205 (2004)
7. R. F. Schmitsdorf, T. U. Kampen, W. Monch Surf. Sci. 324, 249 (1995)
8. M J. Mamor. Phys. Condens. Matter 21, 335802 (2009)
9. S. H. Phark, H. Kim, K. M. Song, P. G. Kang, H. S. Shin D. W. Kim J. Phys. D: Appl. Phys. 43 165102 (2010)
10. S. Dogan, S. Duman, B. Gurbulak, S. Tuzemen, H. Morkoc, Physica E41 646 (2009)
11. J. Zs. Horvath Solid-State Electron. 39, 176 (1996)
12. R. Hackam, P. Harrop, IEEE Trans. Electron Devices 19, 1231 (1972).
13. Y. Zhou, D. Wang, C. Ahyi, C.-C. Tin, J. Williams, M. Park, N. M. Williams, A. Hanser, and E. A. Preble, J. Appl. Phys. 101, 024506 (2007).
14. H. Ishikawa, K. Nakamura, T. Egawa, T. Jimbo, and M. Umeno, Jpn. J. Appl. Phys., Part 2 37, L7 (1998).
15. A. Arehart, B. Moran, J. S. Speck, U. K. Mishra, S. P. DenBaars, and S. A. Ringel, J. Appl. Phys. 100, 023709 (2006).
16. R. Riben and D. L. Feucht, Int. J. Electron. 20, 583 (1966).
17. V. V. Evstropov, M. Dzhumaeva, Yu. V. Zhilyaev, N. Nazarov, A. A. Sitnikova, L. M. Fedorov, Fiz. Tekh. Poluprovodn. (S.-Peterburg) 34, 1357 (2000) Semiconductors 34, 1305 (2000)
18. V. V. Evstropov, Yu. V. Zhilyaev, M. Dzhumaeva, and N. Nazarov, Fiz. Tekh. Poluprovodn. (S. Peterburg) 31, 152 (1997), Semiconductors 31, 115 (1997)

19. E. Belyaev, N. S. Boltovets, V. N. Ivanov, V. P. Klad'ko, R. V. Konakova, Ya. Ya. Kudrik, A. V. Kuchuk, V. V. Milenin, Yu. N. Sveshnikov, and V. N. Sheremet, Semiconductors 42, 689 (2008).
20. S. M. Sze, Physics of Semiconductor Devices _Wiley, New York, (1981).
21. J. R. Yeargan and H. L. Taylor, J. Appl. Phys. 39, 5600 (1968).
22. J. G. Simmons, Phys. Rev. 155, 657 (1967).
23. H. Zhang, E. J. Miller, and E. T. Yu, J. Appl. Phys. 99, 023703 (2006).
24. K. H. Lee, S. J. Chang, P. C. Chang, Y. C. Wang, and C. H. Kuo, Appl. Phys. Lett. 93, 132110 (2008).
25. E. Arslan, S. Altindal, S. Ozcelik, and E. Ozbay, J. Appl. Phys. 105, 023705 (2009)
26. L. Rigutti, PhD Theis, University of Bologna, Italy (2008)
27. S. Saddoiu M. M. B. Salem, M. Gassoumi, H. Maaref, C. Gaquie`re, J. Appl. Phys. 111, 073713 (2012)
28. A. Arehart, PhD thesis, The Ohio state University (2009)
29. P. Koteswara Rao, B. Park, S-T Lee, Y-K Noh, M-D Kim, and J-E. Oh, J. Appl. Phys. 110, 013716 (2011)
30. E. J. Miller, E. T. Yu, P. Waltereit, J. S. Speck, Appl. Phys. Lett. 84, 535 (2004)
31. L. F. Jiang, W. Z. Shen, Q. X. Guo, Journal of Appl. Phys. 106, 0315 (2009)
32. S. M. Lee, M. A. Belkhir, X. Y. Zhu, Y. H. Lee, Phys. Rev. B 61, 16033 (2000)
33. M. A. Reshchikov and R. Y. Korotkov. A Phys. Rev. B 64, 115205 (2001)
34. D. Y. Song, M. Basavaraj, S. A. Nikishin, M. Holtz, V. Soukhoveev, A. Usikov, V. Dmitriev, J. Appl. Phys. 100, 113504 (2006)
35. W. Shan, T. J. Schmidt, X. H. Yang, S. J. Hwang, J. J. Song and B. Goldenberg, Appl. Phys. Lett. 66 985 (1995)
36. S. Rudin, T. L. Reinecke,B. Segall, Phys. Rev. B 42 11218 (1990)
37. R. B. Capaz, C. D. Spataru, P. Tangney, M. L. Cohen, S. G. Louie, Phys. Rev. Lett. 94 036801 (2005)
38. L. Polenta, A. Castaldini, A. Cavallini, J. Appl. Phys. 102, 063702 (2007)
39. K. Saarinen, T. Laine, S. Kuisma, J. Nissila¨, P. Hautoja¨rvi, L. Dobrzynski, J.M. Baranowski, K. Pakula, R. Stepniewski, M. Wojdak, A. Wysmolek, T. Suski, M. Leszczynski, I. Grzegory and S. Porowski, Phys. Rev. Lett. 79, 3030 (1997)
40. J. Neugebauer and C.G. Van de Walle, Phys. Rev. B 50, 8067 (1994)
41. F.A. Ponce, D.P. Bour, W. Go¨tz, and P.J. Wright, Appl. Phys. Lett. 68, 57 (1996)
42. J. Neugebauer and C.G. Van de Walle, Appl. Phys. Lett. 69, 503, (1996)
43. T. Ogino and M. Aoki, J. Appl. Phys. 19, 2395 (1980)
44. E.R. Glaser, T.A. Kennedy, K. Doverspike, L.B. Rowland, D.K. Gaskill, J.A. Freitas, Jr., M. A. Khan, D.T. Oslon, J.N. Kunznia, and D.K. Wickenden, Phys. Rev. B 51, 13 326 (1995)
45. S. Christiansen, M. Albrecht, W. Dorsch, H.P. Strunk, C. Zanotti- Fregonara, G. Salviati, A. Pelzmann, M. Mayer, M. Kamp, and K.J. Ebeling, MRS Internet J. Nitride Semicond. Res. 1, 19 (1996)
46. A.F. Wright and U. Grossner, Appl. Phys. Lett. 73, 2751 (1998)
47. D.C. Look and J.R. Sizelove, Appl. Phys. Lett. 82, 1237 (1999)
48. Y. Tokuda, Y. Yamada, T. Shibata, S. Yamaguchi, H. Ueda, T. Uesugi, T. Kachi, Phys. Stati. Solidi C 8, 2239 (2011)

Chapter 5

Characterization of InAlN/AlN/GaN based heterostructures for high electron mobility transistors

In this chapter InAlN/GaN based heterostructures for high mobility transistor (HEMT) have been characterized with various electrical and optical methods. As InAlN layer has been emerged with the possibility of lattice matching with GaN substrate/layer for HEMT and various optoelectronics applications, so it becomes quite significant to explore the electrical and optical properties of HEMT structures. The chapter starts with experimental results from basic electrical techniques like I-V, C-V to understand the electronic transport properties, different scattering mechanism for mobility variation and proceeded with defect characterization by DLTS method. The presence of electrically active defects and information on their capture cross section is explored which is still not available in literatures which makes this work in this thesis quite significant. Optical spectroscopy methods like Surface Photovoltage, Photocurrent and Photoluminescence have been used to investigate the optical properties, in particular 2DEG related transitions and emissions, which is proposed for first time on this kind of heterostructures, and to correlate the defect related transitions/emission with DLTS results.

5.1 Sample and growth details

Seven samples with AlInN/AlN/GaN heterostructures were grown in an AIXTRON metal organic chemical vapour deposition (MOCVD) reactor on c-plane sapphire substrates. AlInN was around 15 nm thick, AlN layer was varied as 0 to 7.5 nm (shown in Table I), while the 3-µm thick GaN layer has been grown on sapphire. Indium content varies from 13% to 14% as assessed by High Resolution X-Ray Diffraction (HR-XRD) [1]. Electrical measurements have been performed on semitransparent 'Ni (40 nm)/Au (50 nm)' and 'Pt (50 nm)' Schottky contacts, (dots of 1 mm diameter) and Ti (30 nm)/Al (200 nm)/Ni (50 nm)/Au (150 nm) Ohmic contacts (dots of 1 mm diameter), as shown in Fig. 5.1a as schematic. The Ohmic and Schottky contacts have been prepared by 'Ti/ Al/Ni/Au' and 'Pt' evaporation, respectively; for Ohmic metallization, further annealing is performed at 850^0 C for 30 s in N_2 ambient. Ohmic contacts have been checked and found very good Ohmic behavior, shown in Fig. 5.1b, due to high carrier concentration due to formation of two dimensional electron gas (2DEG) at (In)AlN/GaN interface. For sample 3, effect of annealing has been shown on Ohmic behavior of the contacts; similar effect has been found for other samples.

Table 5.I Sample details of InAlN/AlN/GaN structures

	Sample 1	Sample 2	Sample 3	Sample 4	Sample 5	Sample 6	Sample 7
InAlN (nm)	**15**	**15**	**15**	**15**	**15**	**15**	**15**
AlN (nm)	**0**	**0.5**	**1**	**1.5**	**2**	**2.5**	**7.5**
GaN (μm)	**3**	**3**	**3**	**3**	**3**	**3**	**3**

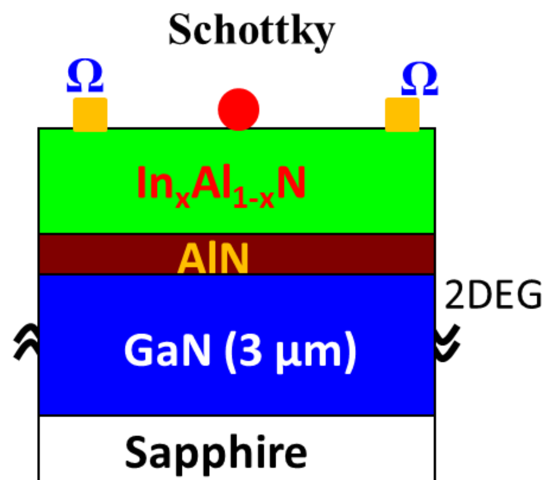

Figure 5.1a Schematic of InAlN/AlN/GaN heterostructure for electrical measurements, Ohmic contacts have been deposited by Ti/Al/Ni/Au (shown as Ω, squares in orange color) and Schottky dots of Ni/Au or Pt (circle in red color)

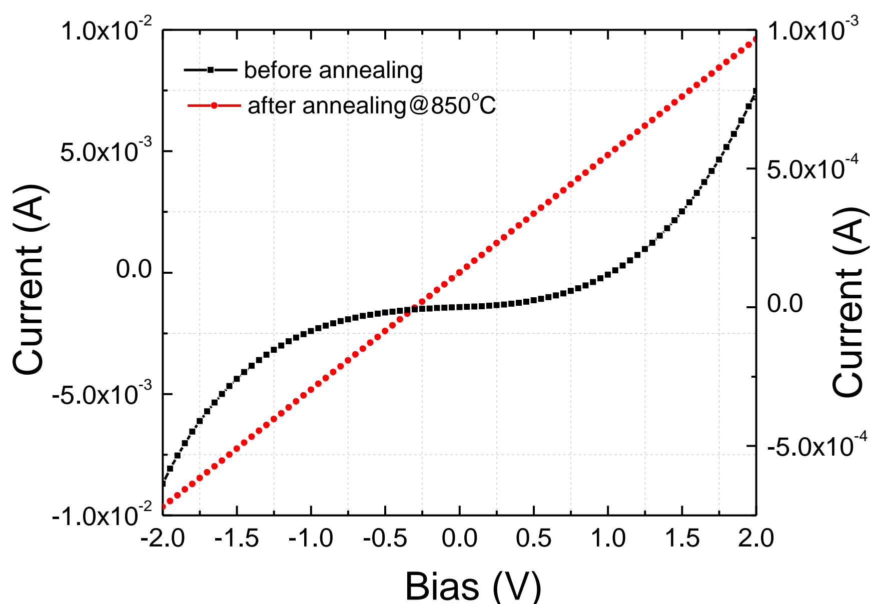

Figure 5.1b Effect of annealing on Ohmic contact behavior for sample 3, shows the achieved Ohmicity at high temperature annealing in comparison to unannelaed condition

5.2 Surface morphology analysis by Atomic force microscopy analysis (AFM)

Atomic force microscopy measurements have been performed in non-contact mode for surface morphology analysis and for the calculation of surface roughness etc. The surface morphology of all samples have been compared and found very smooth surfaces in all samples except for the sample 7, as shown in Fig. 5.2. The role of surface roughness and it's role in electrical and electronic properties have been discussed in this chapter.

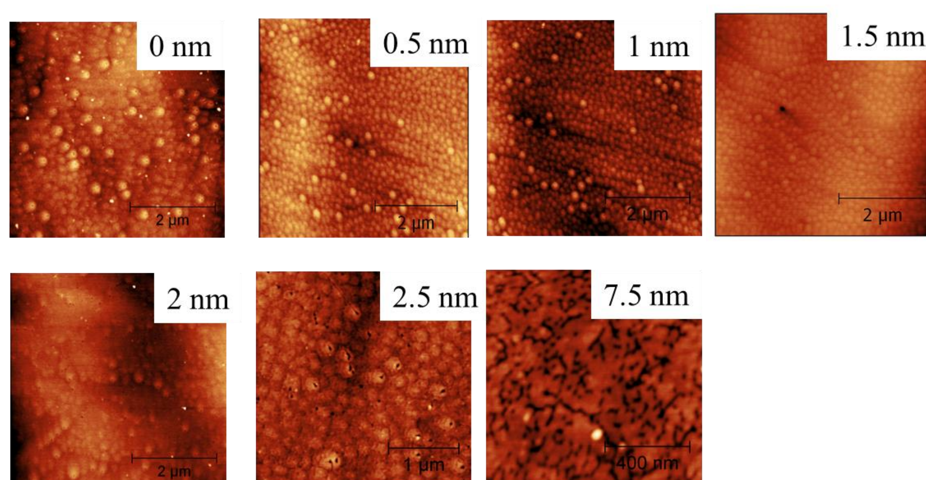

Figure5. 2 surface morphology analyses of samples with variation in AlN interlayer [2, 3]

5.3 Band diagram Simulation

Conduction band profiles have been simulated by using nextnano software [3] conduction band offset (CBO) ΔE_c= 2.1 eV for AlN/GaN, ΔE_c= 1.6 eV for AlInN/AlN as also discussed in chapter 2, metal (Schottky) thickness is taken as 10 nm for all the samples with different AlN interlayer thicknesses [5], the results are shown in Fig. 5.3. Fig. 5.3a shows the conduction band profile for all samples with variation of AlN interlayer thickness which shows the formation of 2DEG well at AlN/GaN interface and variation of depth of 2DEG well with variation in interlayer thickness (shown by arrow), while Fig. 5.3b shows the carrier concentration variation in different samples at AlN/GaN interface which also shows the variation in density with respect to interlayer thickness similarly as depth of 2DEG well as mentioned above. The Fermi level is shown as dashed line and marked as E_F in Fig. 5.3a. The detailed analysis of subband energy levels and their position and role in electrical properties are discussed later in this chapter while discussing some theories. It is to be noted that all the structures have been considered as 'in strained' condition which is explained in chapter 2 in terms of strained and relaxed nature and influence on electrical and other properties. It is shown in some earlier reports [3, 6] that thicker AlN interlayer tends to get relaxed above 6.5 nm and starts forming the cracks in surface for AlN/GaN heterostructures and we have found similar things in our case but this isn't considered in the simulation as simulations can only be performed for strained structures due to it's limitations. However, the effect of strained and relaxed nature of AlN interlayer is well explored and explained with electrical and optical measurements which has been an important feature of the thesis and discussed in next sections.

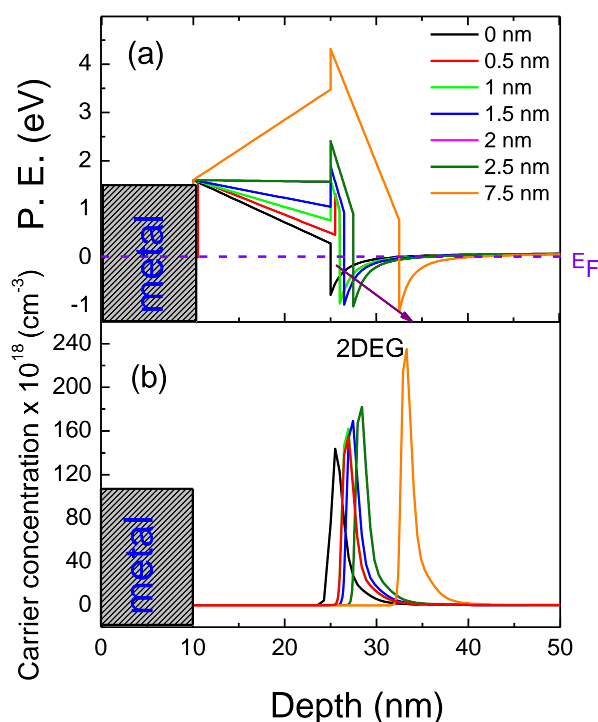

Figure 5.3 Conduction band profiles of InAlN/AlN/GaN heterostructure with varying AlN layer thickness **(a)**, and Carrier concentration variation with AlN layer thickness variation in heterostructures **(b)**

5.4 Current-Voltage (I-V) characteristics and analysis

In this section, electronic properties of the InAlN/AlN/GaN have been investigated with Current-voltage measurements for analysis of 2DEG concentration, dominant conduction mechanism, leakage analysis and mobility limiting mechanism in this kind of heterostructures.

5.4.1 'In-Ga alloy' Schottky-Schottky configuration Current-voltage measurements and 2DEG properties analysis:

Here, we examine on the current transport properties of AlInN/AlN/GaN high electron mobility transistors with different AlN interlayer thickness. We have determined the 2-dimensional electron gas (2DEG) properties directly from simple current-voltage measurements, carried out with two Schottky contacts in a planar back-to-back configuration. A model has been developed to straightforwardly extract the 2DEG electrical properties from room-temperature current-voltage curves and we correlated them to the effects of varying AlN thickness. The 2DEG properties calculated form current-voltage analyses are in very good agreement with results obtained with standard Hall effect measurements [2].

The work presented in this section is focused on the electrical characterization of $Al_{0.86}In_{0.14}N$/AlN/GaN heterostructures by means of simple, room temperature Current-Voltage (I-V) measurements which are here used to directly derive the main 2DEG electrical transport properties, such as the 2DEG carrier concentration and sheet resistance. The method we here propose offers the advantage, with respect to other methods such as Hall effect measurements, of requiring two Schottky contacts that are easier to realize than Ohmic contacts on nitride-based compounds. Moreover, it can be carried out with very common current/voltage meters, instead of requiring expensive dedicated apparatuses. We also report the effect of varying the AlN interlayer thickness in the heterostructure up to 7.5 nm.

Five samples with AlInN layer around 15 nm thick, AlN layer varied as 0, 0.5, 1, 2.5 and 7.5 nm, grown on 3-μm thick GaN layer have been used for this study. Current-Voltage measurements have been performed at room temperature with back-to-back Schottky contacts in a planar configuration directly formed by In-Ga alloy with a spacing of 2 mm, shown in the inset of Fig. 5.4a.

We have carried out I-V measurements on all samples and observed a change in the curve slope at different applied bias except for the sample with a 7.5 nm thick AlN interlayer Figure 4a reports the typical I-V curves observed for samples with 1 and 7.5 nm thick AlN structures, indicating how a change in slope is clearly visible in 1 nm thick AlN samples and less in 7.5 nm AlN samples. We can understand the I-V curves behaviour by considering that for low bias voltages the transport is limited to the top AlInN barrier layer. As the applied bias voltage increases, for one of the reverse biased schottky diode (shown in Figure 4a), the depletion region extends further through the AlInN and AlN layers, allowing the current flow to reach the interface with the GaN substrate, where the 2DEG is located [7]. The onset of the 2DEG contribution is revealed by the marked current increase observed in the S-shaped I-V curves (Figure 5.4a)

We noted that the bias value corresponding to the onset of 2DEG conduction, V_{2DEG}, varies linearly as a function of the AlN interlayer thickness for thicknesses up to 2.5 nm. Samples with a 7.5 nm AlN layer do not show an evident change in slope at this scale (Fig. 5.4b).

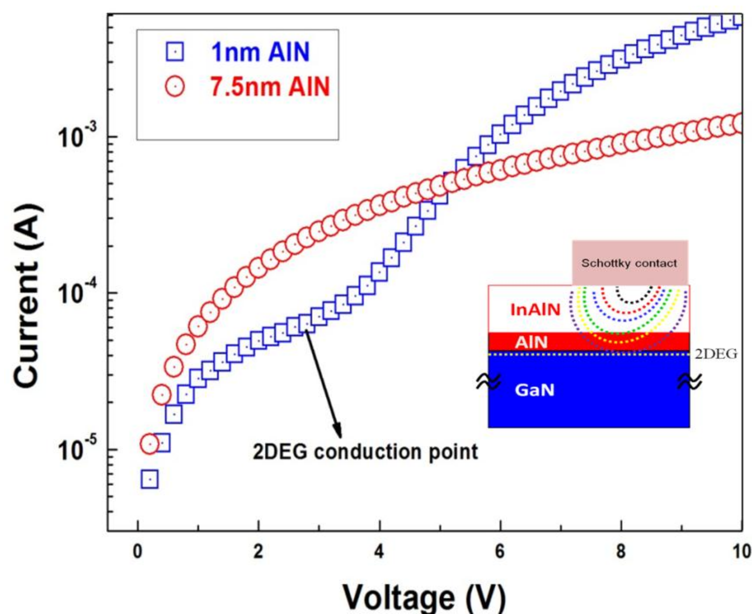

Figure 5.4a Current vs. Voltage plot showing difference between change of slope as 2DEG conduction in samples with 1 nm AlN (blue) and 7.5 nm AlN thickness (red). It also shows the depletion of reverse-biased Schottky with increasing bias (inset)

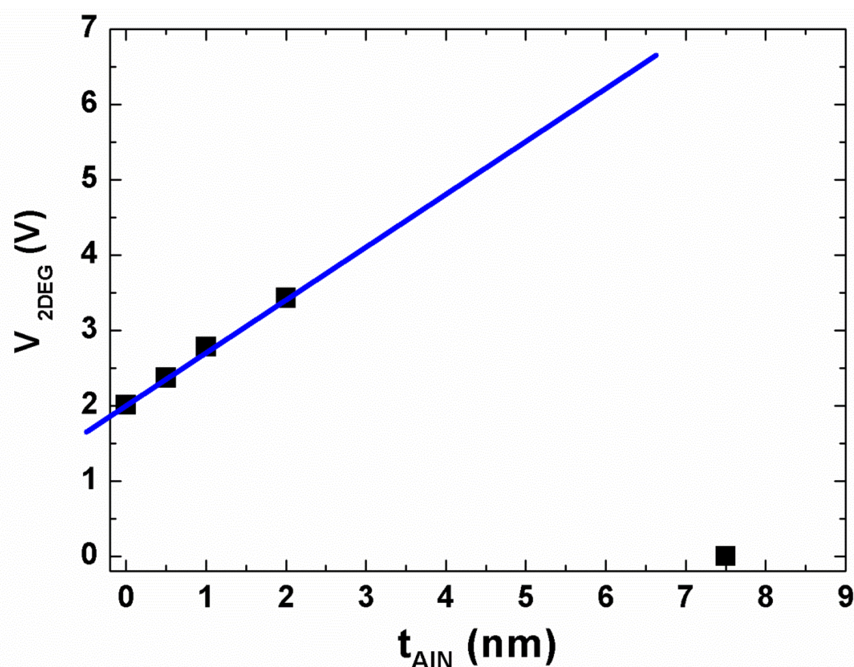

Figure 5.4b V_{2DEG} as a function of the AlN interlayer thickness

In order to understand the origin of the different behavior of samples with a 7.5 nm thick AlN layer, we have carried out Atomic Force Microscopy analyses of samples with different AlN thicknesses, reported in Figure 5.3 b and 5.3g. We have clearly identified the formation of nanocracks on the AlInN surface that become more pronounced as the AlN layer thickness increases, becoming macroscopic defects (micron-sized) in heterostructures with a 7.5 nm thick AlN layer. Other recent results report the formation of cracks in AlN/GaN heterostructures [6] and we could relate their presence in samples with a 7.5 nm thick AlN layer to the observation of large currents at very low bias voltages, due to high leakage effects.

To calculate the 2DEG sheet carrier concentration, we determine the total effective polarization charge density from the data in Figure 5.4b**.** The slope of the linear region of V_{2DEG} vs the AlN thickness (t_{AlN}) gives,

$$\frac{dV_{2DEG}}{dt_{AlN}} = \frac{e(\sigma_{AlN/GaN} + \sigma_{AlInN/AlN})}{\varepsilon_0 \varepsilon_r} \tag{5.1}$$

where, e is the electron charge, $\sigma_{AlN/GaN}$ and $\sigma_{AlInN/AlN}$ are the effective polarization charge densities of the AlN and the AlInN layers, respectively, ε_0 is the vacuum dielectric constant and ε_r is dielectric constant averaged over the AlN (~10.3) and AlInN (9.8) layers. From equation (5.1) we calculate the total effective polarization charge density ($\sigma_{AlN/GaN} + \sigma_{AlInN/AlN}$) and by calculating E_{total}, the total electric field across the AlN and AlInN layers as [2]:

$$E_{total} = \frac{V_{2DEG}}{t_{AlN} + t_{AlInN}} \tag{5.2}$$

we can then determine the 2DEG sheet carrier concentration n_{2DEG} by:

$$E_{total} = \frac{e(\sigma_{AlN/GaN} + \sigma_{AlInN/AlN} - n_{2DEG})}{\varepsilon_0 \varepsilon_r} \tag{5.3}$$

The room-temperature 2DEG carrier concentrations of the investigated AlInN/AlN/GaN structures vs. AlN thickness are plotted in Fig. 5.5a, as determined from I-V curves (solid squares) and Hall measurements (open squares). They are reported together with other experimental data from the literature for similar structures by Capacitance-Voltage (C-V) (solid triangles) [8], showing very good agreement. The error associated to our experimental data has been estimated to be $\pm 0.01 \times 10^{13}$ cm^{-2} and it's mostly due to stoichiometric and thickness fluctuations. The observed differences could be ascribed to the different growth techniques and to the different characterization methods employed (I-V, C-V and Hall). Moreover, our results are in good agreement with the theoretical calculation by Ambacher et al. [9]. The Hall measurements data reported in Fig. 5.5a from refs. 8 and 9 (circles) deviate from the behaviour of the here investigated samples possibly because the *In* concentration in their AlInN layer was ~18%. For such indium concentration, it is known that the structure becomes lattice matched and spontaneous polarization gives the major contribution to form 2DEG [8, 10], while in our samples, that are not lattice-matched, the piezoelectric polarization also plays a role.

In figure 5.5a, the last point (7.5 nm thick AlN layer) of the 2DEG concentration curve relative to our data (solid red squares) has not been directly determined from experimental data. In fact, as is clearly shown in Figure 5.4b, the I-V curves relative to the thicker AlN sample (7.5 nm) does not allow to extract the 2DEG concentration from the V_{2DEG}, possibly because of the deterioration of the AlInN barrier layer morphology that induces the flow of a very high current at very low voltages. This effect hinders the direct application of the I-V method to the study of samples with a cracked or dislocated barrier layer that acts as a lower resistance path for the injected carriers, inhibiting the direct assessment of the 2DEG properties by I-V measurements. Nonetheless, if we extrapolate the V_{2DEG} vs AlN thickness curve obtained from thinner AlN interlayers (Figure 5.4b), and we use the extrapolated values to estimate the 2DEG concentration, we obtain a very good agreement with the experimental values obtained from Hall measurements performed on the same samples (Figure 5.5a).

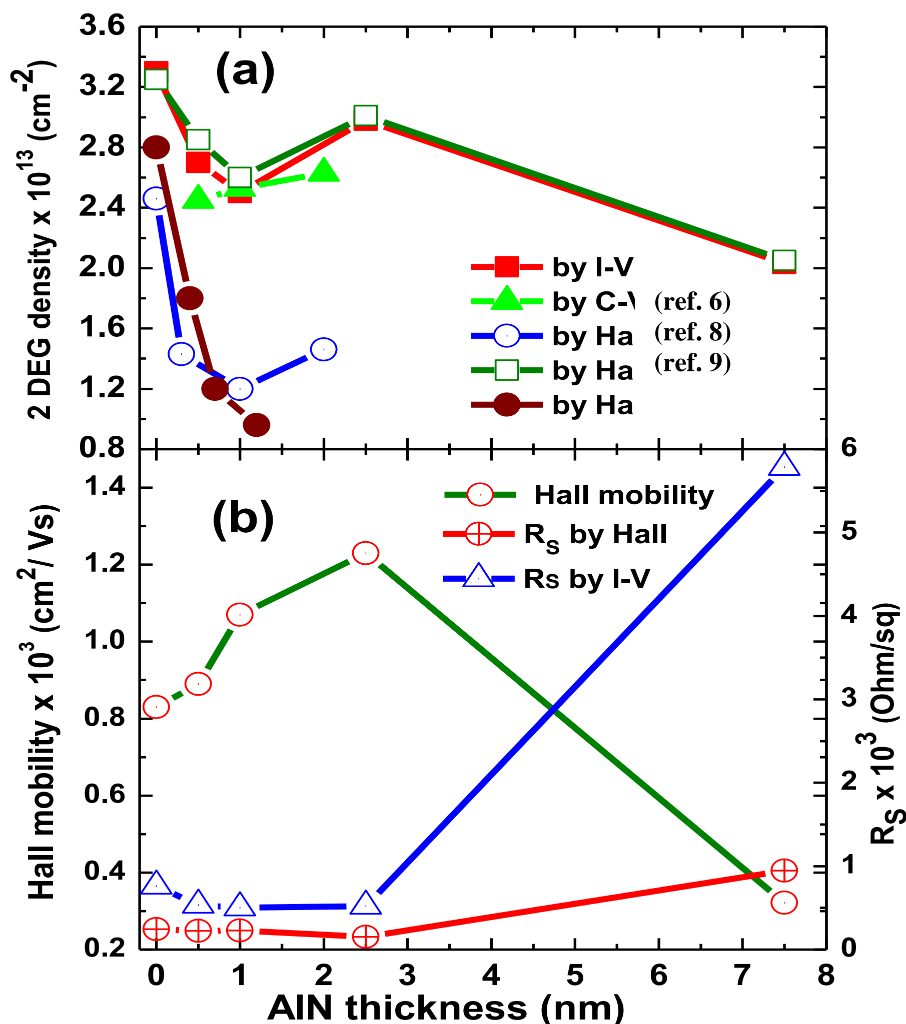

Figure 5.5 (a) 2DEG concentration as a function of the AlN interlayer thickness. Our data are obtained from I-V curves (solid squares) and Hall measurements (open squares) and they are compared with results form the literature, obtained with C-V (solid triangles) and Hall measurements (circles), on similar samples. The last point (7.5 nm) of our I-V curve has been extrapolated (see text). The lines are plotted only for eye-guidance**.** ***(b)*** 2DEG Hall mobility (left axis) and sheet resistance (right axis) variation with AlN interlayer thickness

Hall measurements have been also performed to determine the Hall mobility and the sheet resistivity as a function of the AlN interlayer thickness, shown in Figure 5.5b. The mobility increases with the AlN interlayer thickness and reaches its maximum values of 1230 $cm^2V^{-1}s^{-1}$ for an AlN thickness of 2.5 nm, while further increasing the AlN thickness (7.5 nm) induces a drastic decrease in the mobility. As the AlN thickness increases, dislocations are generated to minimize the strain induced by lattice mismatch between GaN and AlN, thus degrading the interface roughness, increasing the scattering processes and consequently, reducing the electron mobility, similarly to what has been observed in the AlGaN/GaN system [11].

The sheet resistance behaviour (Figure 5.5b) further supports the results so far discussed: the quite large value for the thickest (7.5 nm) sample well correlates to its strong morphological deterioration and significant 2DEG mobility decrease as discussed above. It is noteworthy that the sheet resistance has been measured both with the Hall effect method and with the I-V method, using the slope of the I-V curve after the onset of the 2DEG conduction, providing results in very good agreement.

In summary, we have studied the transport properties of nearly lattice-matched AlInN/AlN/GaN heterostructures with various AlN spacer layer thicknesses using I-V measurements at 300K with Schottky contacts in a planar back-to-back configuration. By comparing I-V and Hall measurements we could assess the reliability of the here proposed method based on simple I-V analyses in the determination of the major transport properties of the 2DEG. Our results confirm the beneficial role played by an AlN interlayer, provided the structural morphology of the AlInN barrier layer is preserved from the degradation induced by defects, such as extended dislocations and macroscopic cracks, that we have clearly identified by Atomic Force Microscopy analyses in samples with AlN thickness ~7.5 nm.

5.4. 2 (Ni/Au) Schottky junction behaviour

In order to clarify the effect of charged dislocations and surface donor states on the transport mechanisms in polar AlInN/AlN/GaN heterostructures, we have studied the Current-Voltage characteristics of Schottky junctions fabricated on AlInN/AlN/GaN heterostructures. The reverse-bias leakage current behaviour has been interpreted with a Poole-Frenkel emission of electrons from trap states near the metal-semiconductor junction to dislocation induced states. The variation of the Schottky barrier height as a function of the AlN layer thickness has been measured and discussed considering the role of the surface states in the formation of the two dimensional electron gas at AlN/GaN interface. A brief investigation has been also done on Schottky barrier inhomogeneity at metal-semiconductor interface in this kind of heterostructures which is a very important issue for device applications.

A surface donor model has been proposed [12, 13], even if the characteristics of such donor surface states are still debated. In this letter, we focus on the analysis of leakage current and Schottky barrier height in (Ni-Au)/ $Al_{0.86}In_{0.14}N$/AlN/GaN heterostructures obtained by current-voltage (I-V) measurements. The density and energy distribution of surface donor states were obtained and their role on the 2DEG density in pseudomorphic $Al_{0.86}In_{0.14}N$/AlN/GaN heterostructures was clarified. Moreover, such surface donor states are also found to be responsible for Poole Frenkel emission to the dislocation network which controls the reverse bias leakage current in (Ni-Au)/ $Al_{0.86}In_{0.14}N$/AlN/GaN Schottky diodes.

Pseudomorphic samples of $Al_{1-x}In_xN$/AlN/GaN heterostructures with different AlN interlayer thicknesses vary as 0, 1, 2, 2.5 and 7.5 nm. The Background doping concentration in GaN buffer layer was found of the order of 10^{17} cm^{-3} by Hall effect measurements. Another heterostructure is examined, with a nominal thickness of 30 nm AlInN layer and a ~1 nm thick AlN interlayer. All samples were pseudomorphic, except for the one with the 7.5 nm AlN interlayer, which showed partial relaxation [3, 6].

Current-voltage measurements have been performed at room temperature on Ni-Au Schottky contacts (dots of 1 mm diameter) and Ti/Al/Ni/Au Ohmic contacts (dots of 0.6 mm diameter. Forward and reverse bias current-voltage measurements performed at 300 K are shown in Fig. 5.6a. In the pseudomorphic heterostructures, the reverse bias leakage current is reduced by increasing the AlN interlayer thickness from 0 nm up to 2 nm; while for the samples where the AlN layer thickness t_{AlN} is 2.5 nm or even larger (7.5 nm) than the AlN layer critical thickness ~ 6.5 nm [6], the leakage current rapidly increases by increasing t_{AlN}.

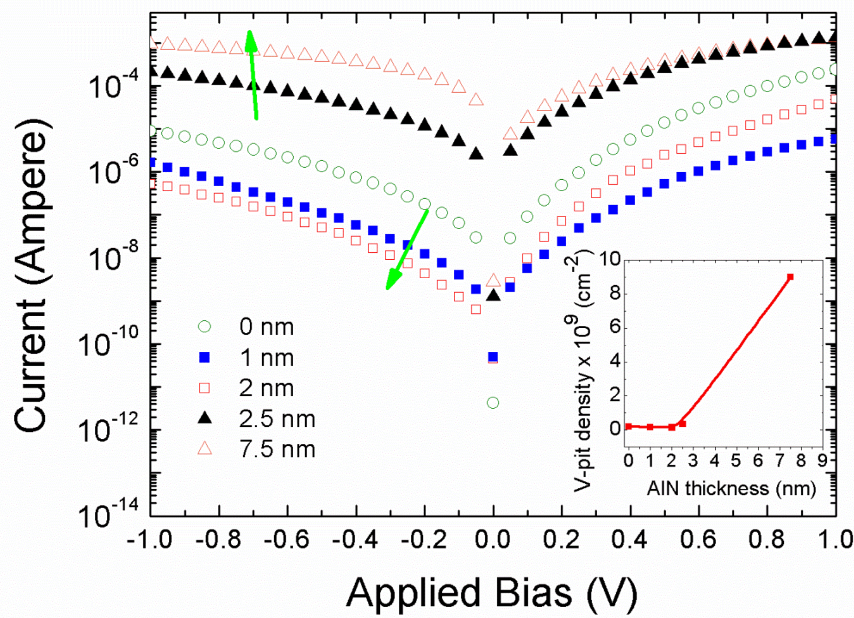

Figure 5.6 (a) Variation of reverse bias leakage current with different AlN interlayer thickness. Variation of Dislocation density (V-Pit) is also shown in the inset

5.4.2.1 Leakage and Poole-Frenkel Emission Analysis

Sample without any AlN interlayer is used as reference samples to investigate the effect of the insertion of the AlN layer on the leakage current. It has been recently suggested that the main cause of leakage in nitride based heterostructures could be due to the presence of V-pits, which are formed when screw-type threading dislocations terminate at the surface to reduce the surface energy. This phenomenon is further enhanced by the segregation of indium along the dislocation, forming a leakage path [14]. To investigate this hypothesis, we performed Atomic Force Microscopy (AFM) to directly determine the V-pit density in each sample. The V-pit density as a function of the AlN interlayer thickness is shown as inset of fig. 5.6a. It is evident that the V-pit density does not increase significantly *vs* t_{AlN} in the pseudomorphic layers while, it starts increasing at t_{AlN} =2.5 nm and reaches a high value for t_{AlN} =7.5 nm. Besides, in this relaxed structure the formation of micro/nanocracks was observed, which strongly affects the Schottky behavior [2, 3]

We have applied the Poole-Frenkel transport model [15, 16] to interpret the leakage mechanisms in such AlInN/AlN/GaN heterostructures. Poole-Frenkel emission refers to electric-field-enhanced thermal emission from a trap state into a continuum of electronic states. The current variation associated with Poole-Frenkel emission can be expressed as

$$I = CAE_s \exp\left[-\frac{q\left(\varphi_t - \sqrt{qE_s / \pi\varepsilon_0\varepsilon_s}\right)}{kT} \right] \tag{5.4}$$

which can also be written as

$$\log(J / Es) = [\frac{q}{kT}\sqrt{\frac{qEs}{\pi\varepsilon_0\varepsilon_s}}] - [\frac{q\varphi_t}{kT} + \log C] = [R(T)] + [S(T)] \tag{5.5}$$

where C is a constant, A is the area of the Schottky contact, J is the current density, E_s is the electric field at the semiconductor surface, ϕ_t is the barrier height for electron emission from trapped state, and ε_0 and ε_s are the free space permittivity and high frequency relative dielectric permittivity, respectively. The Electric field (E_s) values were calculated by dividing by the total thickness of AlInN and AlN layers the applied bias as also mentioned in ref. 16.

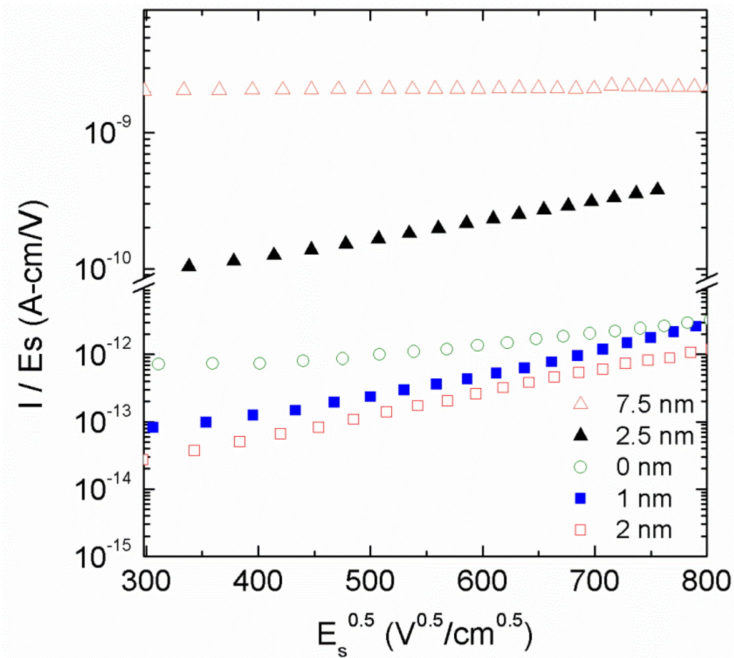

Figure 5.6 (b) Measured reverse-bias current divided by electric field vs square root of electric field for Schottky contact on the $Al_{0.86}In_{0.14}N$/AlN/GaN heterostructure (semi-log scale)

In fig. 5.6b we have plotted $(I/E_S) vs \sqrt{E_S}$ and found a linear dependence in the log scale as predicted by equation (5.4) for the pseudomorphic structures. These results indicate that the Poole-Frenkel mechanism is the dominant mechanism controlling the reverse leakage current in AlInN/GaN nearly lattice matched heterostructures. For the higher AlN layer thicknesses of 2.5 nm and 7.5 nm (relaxed structures, high dislocation density and even cracks in the case of the 7.5 nm thick layer), the reverse bias leakage current significantly increases. Actually, for the relaxed structure with 7.5 nm thick AlN layer, the current becomes nearly independent of $\sqrt{E_s}$ suggesting that other mechanisms, such for example conduction through electrically active nanocracks, could play a major role.

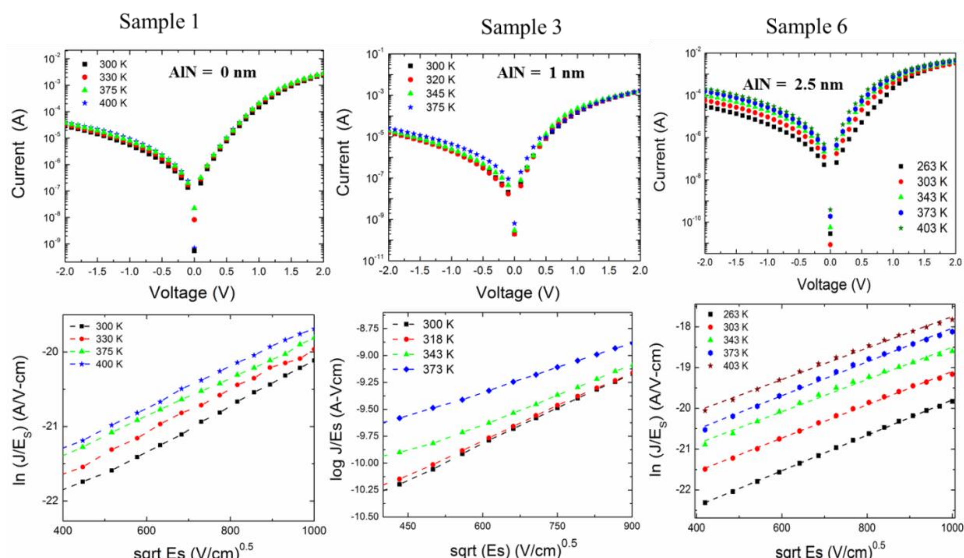

Figure 5.7 Temperature dependent I-V and ln(J/Es) vs. Es plot to show the Pool-Frenkel emission in samples 1, 3 and 6 (lines are used only for eye guide lines)

In order to confirm the Poole Frenkel mechanism responsible for high leakage current in this kind of heterostructures, 3 samples with substantial differences in AlN layer thickness have been measured with temperature variation. From temperature dependent I-V measurements (260 K- 400 K) on sample 1, 3 and 6 with varying AlN interlayer thickness, as shown in Fig. 5.7 we can observe the linear dependent plot of ln(J/Es) vs. sqrt (Es) which confirms the Poole-Frenkel mechanism. Thus, from fig.5.7 we can extract slopes and intercept to obtain the high frequency relative dielectric constant (ε_s) and emission barrier height of traps (φ_t) for the pseudomorphically grown structures, by plotting R(T) and S(T) vs. 1/T (as defined in eq. 5.5, see Fig. 5.8). The values of ranges 5.8 - 8 and ~ 0.10 - 0.167 eV were obtained for ε_s and φ_t respectively [17]. We can therefore conclude that the leakage current in these heterostructures is controlled by emission of electrons from trap states to the conductive dislocation network.

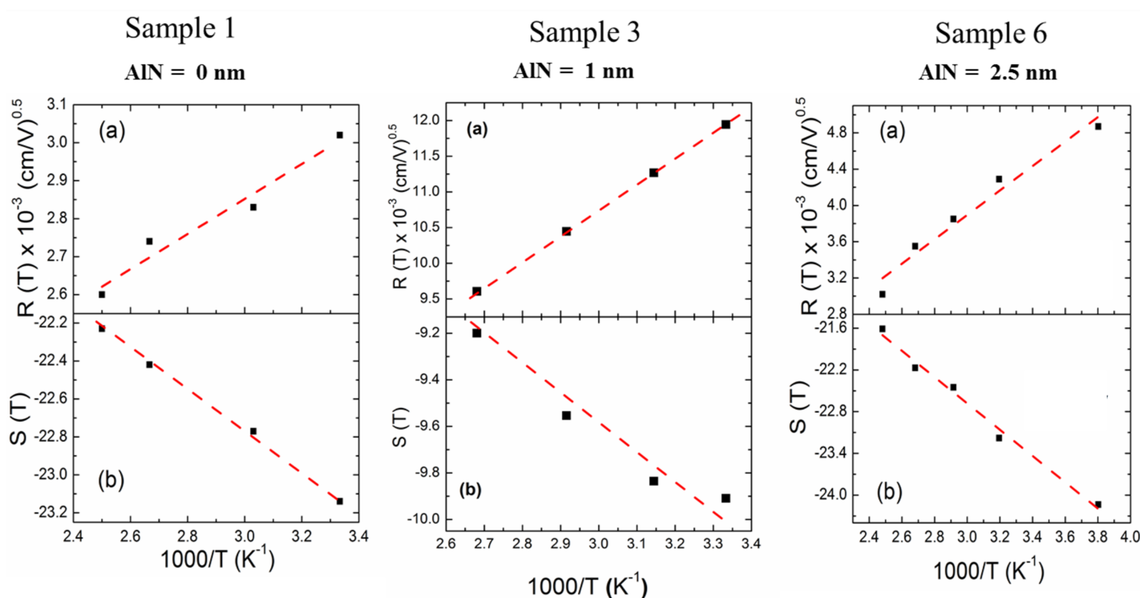

Figure 5.8 R(T) vs. 1/T allows calculating high frequency relative dielectric constant (a) and

S(T) vs. 1/T allows calculating the emission barrier height of trap (b)

5.4.2.2 Role of the surface trap states in the formation of 2DEG

Such states lie below the conduction band edge and above the Fermi level, thus they could be related to the surface donor states which are considered as the source of the 2DEG in nitride-based heterostructures [12, 13]. To validate this hypothesis, the Schottky barrier height (φ_b) is extracted by forward bias I-V plots from the thermionic emission model [18] and correlated with the 2DEG density n_{2D} directly measured for all the samples by Hall effect measurements on Van Der Pauw geometry at 300 K as reported in ref. 13 (Fig. 5.9a). Hall effect allows us to obtain a direct measurement of the 2DEG density value, as a possible contribution from the GaN substrate should be ruled out as the estimated doping of the buffer layer is around 10^{17}cm^{-3}, two orders of magnitude lower than the 2DEG related free electron density which is of the order of 10^{19}-10^{20} cm^{-3} [19]. The measured I-V curves were fitted with [15], also discussed in chapter 3:

$$I = I_0\left[\exp\left(\frac{q(V - IR_S)}{nkT}\right) - 1\right] \quad \text{where} \quad I_0 = AA^*T^2\exp\left(-\frac{q\phi_b}{kT}\right) \tag{5.6}$$

with A the Schottky contact area, A* the effective Richardson constant (~56 A cm^{-2} K^{-1}) [18], T the absolute temperature, q the electron charge, and k the Boltzmann constant.

The Schottky barrier height (φ_b) increases with AlN layer thickness for pseudomorphic heterostructures, while it decreases for the relaxed layer. From fig. 5.9a, it should be noted that the φ_b and the 2DEG density show the same trend *vs* t_{AlN}, revealing the existence of a correlation between these two parameters. However, for the sample without AlN interlayer, the n_{2D} value is higher than for the samples with AlN interlayer. Thus it doesn't follow the increasing trend in 2DEG density value with increasing AlN thickness observed for AlN layers for pseudomorphic structures. Possible reasons for such a behaviour were discussed in ref. 20. The 2DEG density is plotted against φ_b as shown in fig. 5.9b, and an almost linear relation was found. This plot can be used to investigate the energy distribution of the surface/interface donor states located at the metal-semiconductor interface. If we assume that their distribution is uniform, as earlier proposed by Gordon et. al [12], and we consider surface states as the origin of the 2DEG [13], the surface donor density can be calculated by the slope of the least-squares fit line of 2DEG density *vs* φ_b. In this study, the value of (2.7 ± 0.2) x 10^{13} cm^{-2}- eV^{-1} is estimated. The so-calculated value of surface donor density is in good agreement with earlier reports on AlGaN/GaN heterostructures [21, 22].

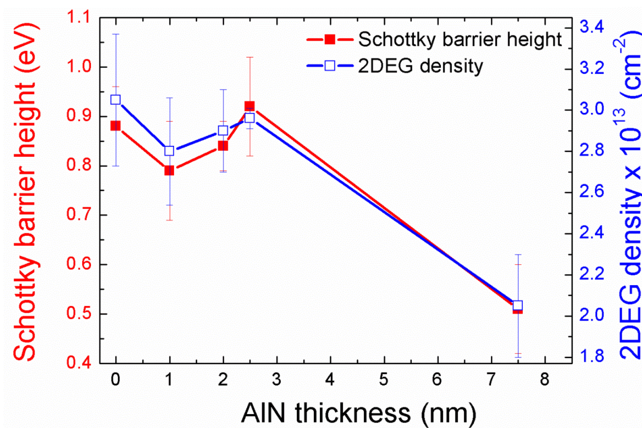

Figure 5.9 (a) Variation of Schottky barrier height (in red solid squares, left axis) and 2DEG density (in blue open squares, right axis) on AlN layer thickness variation. The lines are a guide to the eye

It should be noted that even if the Poole Frenkel mechanism does not apply to the reverse I-V curve of the relaxed sample (t_{AlN}=7.5 nm) possibly controlled by other conduction mechanisms, like conduction through threading dislocations, we have inserted the data (calculated from forward bias I-V characteristics) relevant to this sample in Fig. 5.9 to understand how the 2DEG density can be affected by the formation of cracks propagating toward the surface. It can be clearly observed that the barrier height value for this sample is significantly reduced, which means that threading dislocations propagating toward the surface can significantly affect the metal semiconductor interface through the increase in the surface states. Moreover, we have simulated by 1-D Schrödinger Poisson equations the Conduction band (CB) profile for a surface barrier height of 1.6 eV, a metal thickness of 10 nm and a conduction band offset between AlN/GaN of 2 eV [6], to show the effect induced on the band structure by the variation of the AlN interlayer thickness. The results are shown for all samples in fig. 5.3.

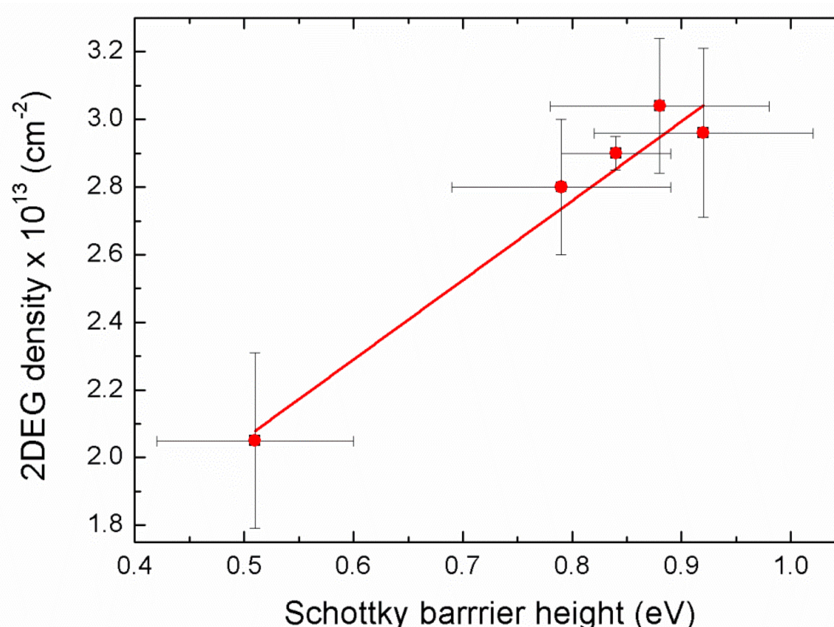

Figure 5.9 (b) Measured 2DEG density variation with barrier height (red solid circles) and linear fitting (straight line)

These results allow us to calculate the interface/surface states density value in AlInN/AlN/GaN heterostructures, and clearly demonstrate that these states are the origin of the 2DEG in nitride-based heterostructures, in agreement with results recently obtained by theoretical simulations in AlGaN/GaN structures [21 22]. In addition, we have calculated the 2DEG density value for the sample with 30 nm thick AlInN barrier layer from ref. 10. The obtained value of 2DEG density (~ 3.3 x 10^{13} cm^{-2}) is higher than the one for the 15 nm thick barrier layer, indicating that the distribution of surface donor states could indeed be important in the formation and control of the 2DEG carrier density. In fact, an increment in AlInN barrier layer thickness lowers the Fermi level below conduction band thus emptying the donor states which emits carriers in conduction band resulting in increase of 2DEG density as shown in fig. 5.4b. The conduction band (CB) profile was simulated for both structures and shown in Fig. 10 the increase in 2DEG density (n_s) value for 30 nm thick barrier sample in comparison to 15 nm thick barrier samples can be noted.

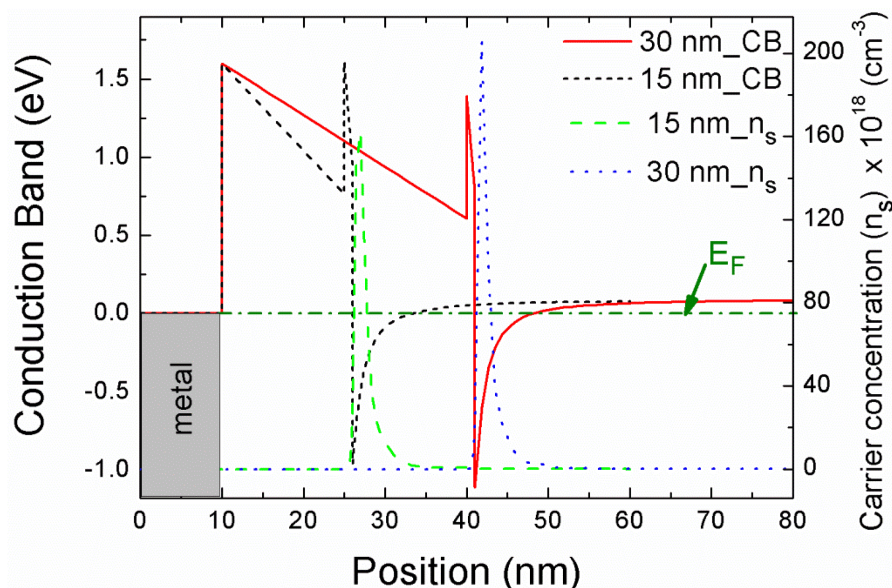

Figure 5.10 The variation in 2DEG density (dashed line for 15 nm and dotted line for 30 nm)

5.4.2.3 Barrier inhomogeneity at (Ni/Au)-InAlN/AlN/GaN interface

From above analysis and discussion, the leakage mechanism and role of surface trap states in InAlN/AlN/GaN heterostructures have been well understood and proposed. From, forward bias analysis a detailed study on Schottky barrier height has been explored to understand the metal-semicoductor interface quality as it is still an open issue in GaN based HEMT structures which has been earlier reported in very few studies [23]. To investigate this issue, Sample 6 has been considered with temperature dependent I-V analysis as shown in Fig. 5.7. as in case of other sample variation in current is quite low to conclude anything.

The forward bias characteristics is analyzed with the Thermionic emission (TE) model as explained in chapter 3 for the temperature range. The apparent Schottky barrier height (SBH) ϕ_b and ideality factor (n) have been calculated with TE model, shown in Fig. 5.11a. It shows the variation of barrier height and ideality factor with temperature. An apparent increase in the ideality factor and decrease in the Schottky barrier height at low temperatures are possibly caused by structural defects in the semiconductor, inhomogeneous doping (which is not the case in the sample as it's undoped), interface roughness, interfacial reactions and diffusion/inter-diffusion of the contamination of applied material on semiconductor surface. Other possible effects are due to inhomogeneities of thickness and composition of the layer, and non-uniformity of interfacial charges or the presence of a thin insulating layer between metal and semiconductor [24, 25, 26]. Since current transport across the metal/semiconductor (MS) interface is a temperature activated process, electrons at low temperatures can surmount the lower Schottky barrier height (SBH) and the dominant current flow is through the regions of lower Schottky barrier height (SBH). As the temperature increases, more electrons have sufficient energy to surmount higher temperature activated process, electrons at low temperatures can surmount the lower Schottky barrier height (SBH) and the dominant current flow is through the regions of lower Schottky barrier height (SBH).

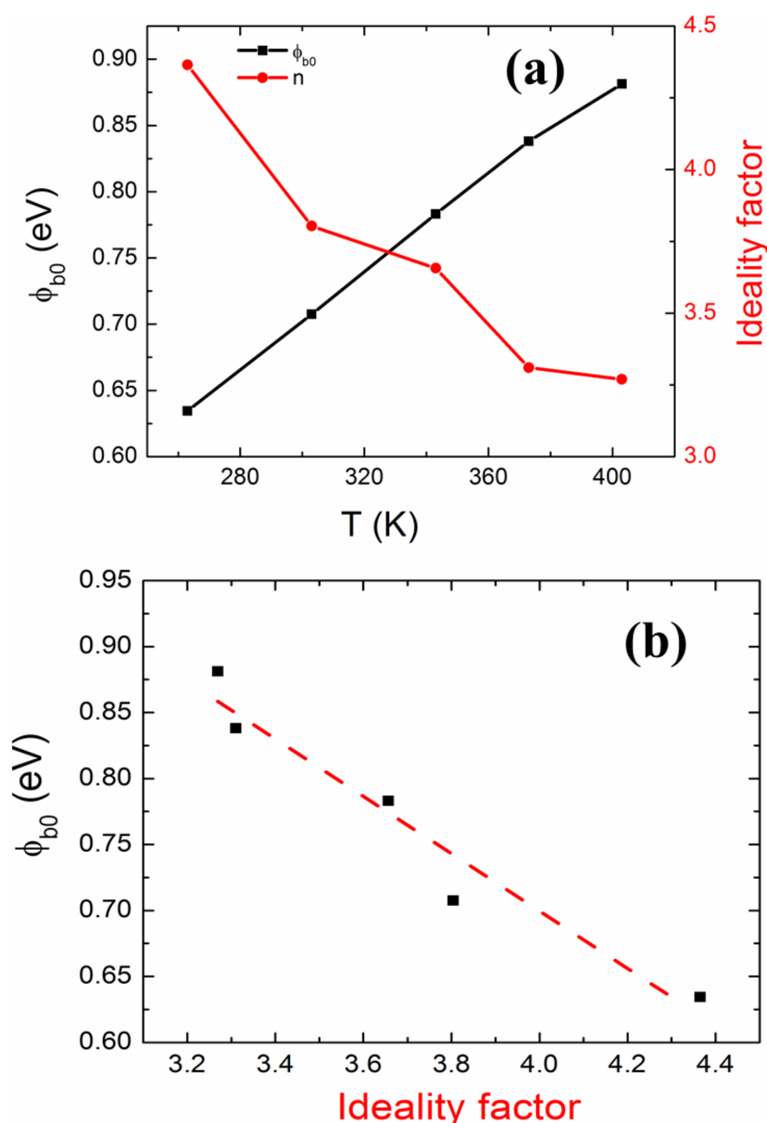

Figure 5.11 (a) Apparent Schottky barrier height and ideality factor variation with tempearature ***(b)*** Variation of Schottky barrier height with ideality factoe. The linear extrapolation for n = 1 gives the ideal barrier hright for (*Ni/Au)-InAlN/AlN/*GaN

According to [19], a linear relationship between the experimental SBH and ideality factor (*n)* values is an indication of the barrier irregularity and can be explained by lateral inhomogeneities of BHs. The value of homogeneous barrier height can be obtained from the extrapolation of the experimental Schottky barrier heights vs ideality factors plot to $n = 1$ [27, 28]. Thus, for (*Ni/Au)-InAlN/AlN/*GaN, homogenous barrier height value is obtained around 1.46 eV which is also in agreement with Mott-Schottky law [19], shown in fig. 5.11b.

In conclusion, we have investigated the characteristics of surface/interface donor states in AlInN/AlN/GaN heterostructures. We have experimentally determined the density of surface/interface donor states, which are considered the source of the 2DEG in these heterostructures, by relating the Schottky barrier height and the 2DEG density. Moreover, we have found that these surface/interface states are also responsible for Poole Frenkel emission to the dislocation network, which could be considered as the source of reverse bias leakage current observed in (Ni-Au)/AlInN/AlN/GaN Schottky diodes.

5.4.3 Mobility limiting mechanisms in polar nitride semiconductor heterostructures

The mechanisms controlling the carrier mobility of two dimensional electron gas (2DEG) in ultra-thin polar semiconductor heterostructures, such as III-V nitrides, have been analyzed. $In_xAl_{1-x}N$/AlN/GaN heterostructures with different AlN layer thicknesses have been investigated. These structures can be considered a very good benchmark for the analyses of III-V nitrides, due to the possibility to modulate the strain by varying the In composition. In order to determine an estimate of the mobility, charged dislocation and remote surface roughness scattering lifetimes have been calculated. Atomic Force Microscopy and Scanning Tunnelling Microscopy analyses have been used to measure the parameters required for the lifetime calculation, such as surface roughness, correlation length and dislocation density, and the total mobility has thus been calculated without the need of any *a priori* assumptions on the values of these parameters. The mobility of $In_xAl_{1-x}N$/AlN/GaN heterostructures has been measured at room temperature and liquid nitrogen temperature by Hall effect. The comparison between the calculated and the Hall Effect measured mobilities, allowed us to establish, without using any *ad-hoc* assumption or fitting parameters, that the remote surface roughness is the most effective factor in controlling the transport properties of 2DEGs in nitride based heterostructures at low temperature.

The identification of the dominant scattering mechanisms controlling the electron mobility in the high density 2DEG is therefore important to deepen the fundamental understanding of these systems, as well as to optimize the growth mechanisms the of the heterostructures in order to improve their electronic quality. In an ideal, defect free material the electron mobility at room temperature is mainly limited by electron-phonon interactions. In a real sample the mobility is further reduced by structural defects/impurities that interact with the electrons, in nitrides the negatively charged threading dislocation lines play a major role. Compared to other semiconductors, the nitrides have a peculiar defect: the negatively charged dislocation lines which can significantly reduce room temperature mobility [29]. Since threading dislocations propagate through the heterointerfaces, and are known to form V-pits in indium containing materials [30, 31, 14], they may also contribute to the interface roughness. Cao et al. [6] have shown that among the several scattering mechanisms that can be considered such as Coulomb scattering due to charged dislocations, surface charged states and background impurities, the dominating one at low temperature in AlN/GaN layers is the interface roughness. Similarly, Antoszewski et al. [32] showed that in AlGaN/GaN structures with 2DEG density higher than 7×10^{12} cm^{-2} the interface roughness becomes the dominant scattering mechanism. Recently, Liu et al. [33] and Cao et al. [34] showed that the remote surface roughness (RSR) scattering mechanism explains the low temperature mobility in AlGaN/GaN and in AlN/GaN 2DEG channel layers, respectively, while the scattering due to dislocations, alloy disorder, phonons, etc., plays an important role in limiting the 2DEG room temperature mobility [34]. The role of surface roughness has been also deeply discussed in ref. 35. In particular the authors discuss the role of correlation lengths on the RSR scattering in AlGaN/GaN heterostructures, and reach the conclusion that large correlation lengths (of the order of hundreds of nm or larger) control the quantum lifetime, while the transport lifetime is controlled by short (atomic level) correlation lengths.

We analyze the role of surface roughness scattering on InAlN/AlN/GaN heterostructures which have got advantages over AlGaN/GaN and AlN/GaN structures due to higher 2DEG density and mobility, and lattice matching for In~ 18%. In previous reports the RSR mechanism has been proposed [33, 34], here the values of important parameters like dislocation density, surface roughness and lateral correlation lengths, have been ad hoc assumed to calculate the mobility for AlGaN/GaN, AlN/GaN structures. On the contrary, in the present report, we have measured dislocation density, surface roughness and correlation length by scanning probe microscopy method and the measured values have been used to calculate the electron mobility. We have considered

$In_{0.14}Al_{0.86}N$ /AlN/GaN structures with different AlN thickness in order to analyze strained and relaxed structures. In polar semiconductor heterostructures the 2DEG density is function of the barrier thickness. Barrier thickness fluctuations result in variations of the electric potential in the channel and these fluctuations are the origin of the RSR scattering mechanism. The 2DEG mobility in $In_xAl_{1-x}N$/AlN/GaN heterostructures was measured by Hall effect. The morphological parameters and the dislocation density required to calculate the RSR and dislocation related mobilities were obtained by atomic force microscopy (AFM) and Scanning Tunnelling Microscopy (STM) analyses. The mobility values have been calculated by these parameters without the need of any *a priori* assumption or fitting parameters. The comparison between calculated and measured total mobility shows that in nearly lattice matched pseudomorphic $In_xAl_{1-x}N$/AlN/GaN heterostructures the surface roughness scattering is the dominant mechanism at low temperatures.

Four samples with $In_xAl_{1-x}N$/AlN/GaN heterostructures were grown by AIXTRON by metal organic chemical vapour deposition (MOCVD) on c-plane sapphire substrates. $In_xAl_{1-x}N$ thickness was around 15 nm thick, the AlN layer thickness was varied as 1, 1.5, 2.5 and 7.5 nm, while the semi-insulating GaN template was 3-μm thick. The last sample, with AlN thickness equal to 7.5 nm, is included in our investigation to study the different behaviour of mobility and surface roughness between a pseudomorphic and a relaxed layer. A sketch of the analyzed structure is shown in inset of fig. 5.12 (a).

Hall measurements have been performed on all samples at 300 K and 77 K. The surface morphology was studied by topography maps of 5 μm x 5μm by Atomic Force Microscopy (NT MDT-Solver PRO 47) in semi-contact mode. High resolution topography maps were acquired by STM in the constant current mode at room temperature in ultra-high vacuum (UHV) conditions, by using an electrochemically etched tungsten tip. By AFM and STM analyses the surface roughness Δ and the autocorrelation length Λ values are obtained by the one-dimensional height-height correlation function [35, 36]. Moreover, the density of V shaped defects was also measured by AFM. By comparison with Transmission Electron Microscopy analyses [37], the V pit density is assumed to be around one half of the threading dislocation density, as it has been recently demonstrated that only screw and mixed type dislocations form V-pits [31].

Surface roughness, V-pit density, Hall mobility and 2DEG density, measured at 300 K and at 77 K, are plotted against interlayer thickness in fig. 5.12 (a, b). It can be observed that both surface roughness and V-pit density keep almost constant for an AlN interlayer thickness t_{AlN} from 1 to 2.5 nm and increase to higher values for t_{AlN} above 2.5 nm. For t_{AlN} from 1 to 2.5 nm the surface roughness shows values around 0.25 nm (typical value in those structures, corresponding to half a GaN unit cell [33]) and the V-pit density is around 2×10^{8} cm^{-2} (of the same order of magnitude of the dislocation density in GaN). The Hall mobility also increases up to a maximum value for t_{AlN} around 1.5 nm and it starts decreasing for t_{AlN} above 2.5 nm, reaching a very low value of for t_{AlN}= 7.5 nm (relaxed growth). The variation of 2DEG density with AlN thickness measured by Hall effect at 300 K and 77 K [3] is also reported in fig. 5.12b, background concentration in GaN buffer layer is found around $10^{17}cm^{-3}$, which is quite low to influence the 2DEG density (which can reach 10^{20} cm^{-3} [17]) at AlN/GaN interface, that indicates the good confinement of electrons.

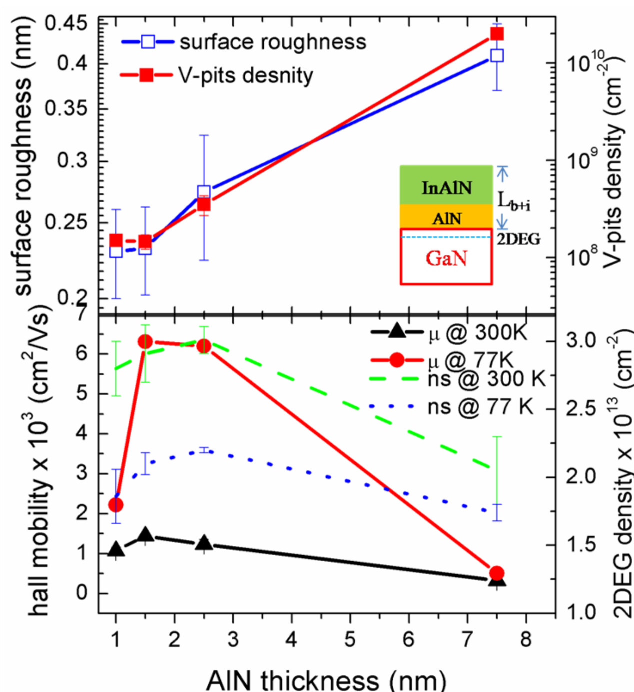

Figure 5.12 Surface roughness (open squares) V-pit density (solid squares) (top layer) and Hall mobility at 300 K (solid triangle) and 77 K (solid dots), and also 2DEG density at 300 K (in dash line) and 77 K (dot line), (bottom layer) plotted as a function of AlN layer thickness. The sketch of $In_xAl_{1-x}N$/AlN/GaN heterostructure is also shown in the inset

Here, it should be reminded that the barrier layer also plays an important role in 2DEG properties as it induces a very high electric field due to the related polarization, as discussed in ref. 14. The mobility increases as temperature decreases (fig. 5.12b) showing that strong Coulombic scattering due to charged dislocations N_{dis}($10^8/cm^2$), remote surface charged states, and background charged impurities N_{back} ($10^{17}/cm^3$) do not play a significant role. For increasing 2DEG concentration the screening of 2DEG becomes stronger, thus decreasing the contribution of the Coulombic scattering to the total mobility [38]. Thus, the increase in low temperature mobility from 1 to 1.5 nm thick AlN sample could be possibly due to better confinement of the 2DEG and the increased screening effect due to higher 2DEG density, even if the surface roughness keeps constant. At the same time, for AlN layer thickness ranging from 1.5 and 2.5 nm, the low temperature mobility remains almost constant even if the surface roughness slightly increases, this can be due to a higher n_S at 2.5 nm with respect to 1.5 nm, which enhances the screening effect.

Therefore, the combined effect of surface roughness, 2DEG density and dislocation (V-pits) density on mobility should be considered. To calculate the dependence of mobility on surface roughness, we have applied the models developed for AlGaN/GaN [33] and for AlN/GaN [34] to our $In_{.14}Al_{.86}N$/AlN/GaN heterostructures. Both models give similar values for the calculated mobility. The origin of roughness induced scattering (RSR) is due to the coupling between surface roughness and polarization. As in polar heterostructures the 2DEG density n_s is function of the layer thickness, the roughness, i.e. the fluctuation in the layer thickness affects n_s and, in turn, the electrical potential in the channel. In order to calculate the RSR limited mobility we estimated the first ground subband energy level [5]

$$E_0 = \left[\frac{9\pi\hbar e^2 n_s}{8\varepsilon_0 \varepsilon \sqrt{8m^*}} \right]^{2/3} \tag{5.7}$$

where ħ is the reduced Planck constant, m^* is the electron effective mass, e the electronic charge, ε_0 the vacuum dielectric constant and ε the GaN relative dielectric constant.

Band diagrams, subband energy levels and electronic wave functions have been simulated ΔE_c= 2.1 eV for AlN/GaN, ΔE_c= 1.6 eV for AlInN/AlN, metal thickness around 10 nm for all the samples with different AlN interlayer thicknesses [4], the results are shown in fig. 5.13. The effect of the barrier layer thickness on the subband energy levels and the localization of the electron wave functions can be noted.

The square matrix element of surface roughness scattering from k to k' state is [5]:

$$|M_R|^2 = \left(\frac{4}{9}\right) \frac{\pi\Delta^2\Lambda^2}{A} \frac{E_0^{\ 2}}{L_T^{\ 2} n_s^{\ 2}} \left(n_s - \frac{\sigma}{e}\right)^2 \exp\left(-\frac{\Lambda^2 q^2}{4}\right) \tag{5.8}$$

Where q = k-k' is the two dimensional (2D) scattering wave vector, $L_T = L_{barrier} + L_{interlayer}$ and A is the sample area.

For degenerated 2DEG, we can consider that scattering process is elastic, so k= k' and $q^2 = 2k^2\left[1-\cos\vartheta\right]$. The transport relaxation time is given by [33]:

$$\frac{1}{\tau(E)} = \frac{A}{2\pi^2}\left(\frac{2\pi}{\hbar}\right)\int |M_R|^2 S_C(1-\cos\vartheta)\delta(E_k - E_{k'})d^2k' \tag{5.9}$$

where, E_k and $E_{k'}$ are the energies to k and k', respectively, as evaluated by equation (5.7), and 1-dimensional Schrodinger-Pöisson simulations shown in fig. 5.13, and S_c is the scattering factor, that can be written to a good approximation as $\left[\frac{q}{q+q_{TF}}\right]^2$, where $q_{TF} = 2\pi a_B$ is the Thomas-Fermi wave vector and a_B, is the effective Bohr radius of 2DEG. Finally, the mobility limited by surface roughness scattering has been calculated by $\mu = \frac{e}{m}\langle\tau\rangle$ averaging τ over the Fermi-Dirac distribution function at low temperature.

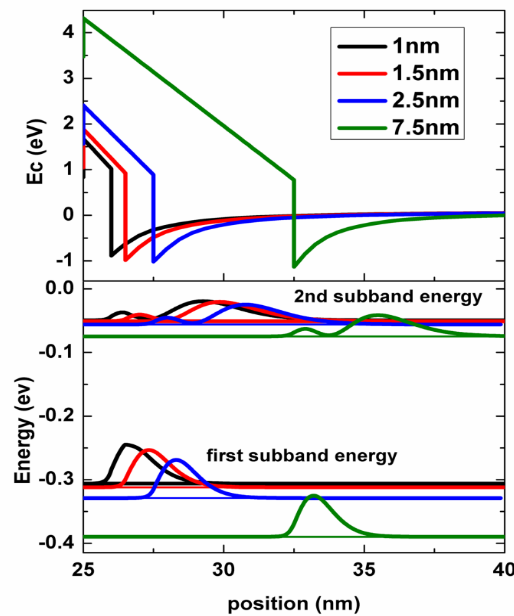

Figure 5.13 Band diagram, calculated from Schrödinger-Poisson solver, showing the fluctuation in different subband energy wave functions at heterointerface for different AlN interlayer thickness

The calculated mobility shows a monotonic increase with barrier width [33], valid for thin barrier widths. To estimate the SRS mobility two variables are needed, the lateral correlation length Λ and the roughness height Δ (eq. 5.8). Several correlation lengths can be assumed for the present structure. The problem has been deeply discussed in ref. 35 for AlGaN/GaN 2-D heterostrucures. The authors conclude that large correlation lengths (of the order of hundreds of nm or larger) control the quantum lifetime but not the transport lifetime, which is controlled by short (atomic level) correlation lengths. In order to quantify correlation length Λ and roughness height Δ values, AFM and STM topography maps were analysed (Fig 5.14a and b). The one-dimensional height-height correlation function (HHCF), defined by

$$H(r) = 2\Delta^2\left[1 - \exp\left(-\frac{r}{\Lambda}\right)\right] \tag{5.10}$$

with r as the variable corresponding to the distance between two points on the surface, has been calculated through the profiles obtained along the scanning axis, by AFM and STM maps (fig. 5.14a and b, insets). A correlation length of 55 nm was found by AFM, of the same order of magnitude of the grain size, while a correlation length of 2 nm was found by STM maps. These values do not vary significantly among the different heterostructures here studied, on the contrary to the roughness values, plotted in Fig 5.12a as a function of the AlN layer thickness. The surface roughness scattering controlled 2DEG mobility has been calculated for different values of correlation lengths and constant value of the barrier height (fig. 5.15a). It must be noted that the mobility strongly increases as a function of the correlation length, reaching, for Λ higher than 60 nm, values above 10^6 cm^2/Vs, at least two orders of magnitude higher than the experimental one. This indicates that, as already proposed by [35], scattering by surfaces with very large Λ cannot control the 2DEG transport mechanism.

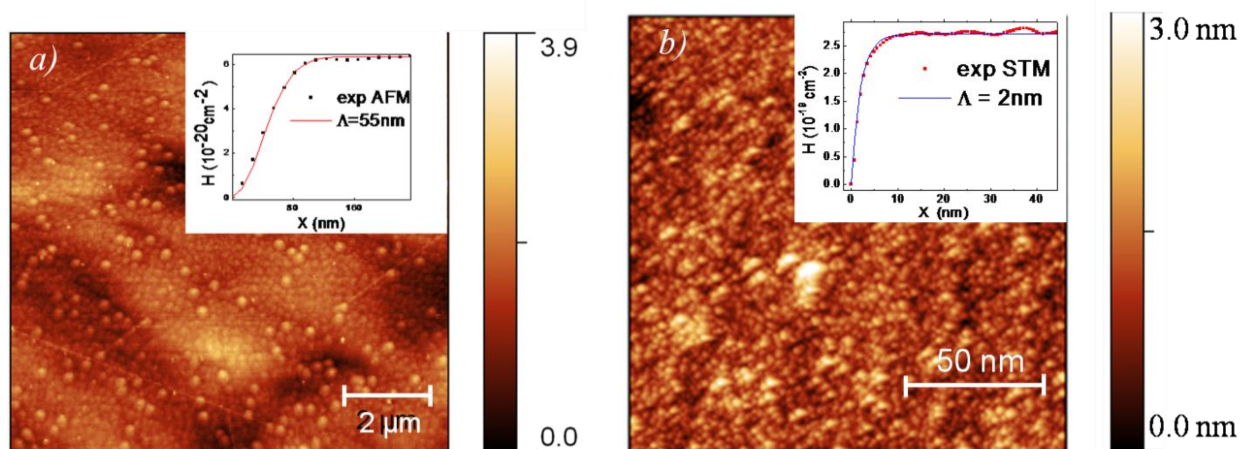

Figure 5.14 Typical topography maps of In_xAlN_{1-x}/AlN/GaN heterostructure with AlN layer thickness of 2 nm obtained by AFM ***(a)*** and STM ***(b).*** The fitting of the one-dimensional height-height correlation function H is also shown in the inset of Fig (a) for the AFM line profile, of Fig ***(b)*** for the STM line profile

Scattering by charged dislocations in 2DEG structures [38] and a GaN [6] has been also considered and calculated by:

$$\mu_{dis}^{2D} = \frac{e\tau_{dis}^{2D}}{m^*} \quad with \quad \tau_{dis}^{2D} = \frac{\hbar^3 \varepsilon_0^2 \varepsilon^2 c_0^2}{N_{dis} m^* e^4 \varphi^2} \frac{16\pi k_F^4}{I\left(\frac{q_{TF}}{2k_F}\right)} \tag{5.11}$$

with ε the relative permittivity, c the lattice spacing in the (0001) direction of wurtzite GaN, $\boldsymbol{\varphi}$ is the fraction of filled states, $\boldsymbol{K_F = \sqrt{2\pi n_s}}$ is the Fermi wave vector, N_{dis} is the dislocation density, m^* is electron effective mass in 2DEG, $\boldsymbol{q_{TF}}$ is the Thomas Fermi wave vector and $\boldsymbol{I\left(\frac{q_{TF}}{2k_F}\right)}$ is the dimensionless integral evaluated as $\boldsymbol{\frac{1.84k_F}{q_{TF}} - 0.25}$ [38], as a function of the measured value of dislocation density.

Finally, the dislocation and remote surface roughness (RSR) scattering mobilities have been combined together and the total mobility values calculated and plotted in fig 5.15b. The dislocation related mobility has been obtained by assuming that the dislocation density equals the double of the V-pit density, and by measuring the V pit density directly by AFM. The RSR mobility has been calculated by using roughness and correlation length values directly measured by AFM and STM analyses, respectively, free carrier density measured by Hall effect and barrier height obtained by the simulations. The so obtained calculated total mobility has been compared with the experimental one as measured by Hall effect at 77 K. It is noteworthy that all the parameters used for the calculation have been measured; no assumptions and no fitting parameters have been used for such a comparison. A good agreement between the experimental and calculated mobility values can be noted for all the roughness values except for the highest one. The last point corresponds to samples with barrier interlayer thickness of 7.5 nm, i.e. a thickness which exceeds the critical thickness. In these samples strain relaxation induce the formation of cracks piercing the 2DEG and thus creating electrical shunts [2]. The 2DEG electrical transport in such a sample should be strongly affected by those cracks which are not considered in the theoretical model. Moreover, we can note in fig. 5.15b that the RSR scattering mechanism is the most effective one in controlling the 2DEG mobility in $Al_{1-x}In_xN/AlN/GaN$ heterostructures, as the dislocation related mobility does not play a major role.

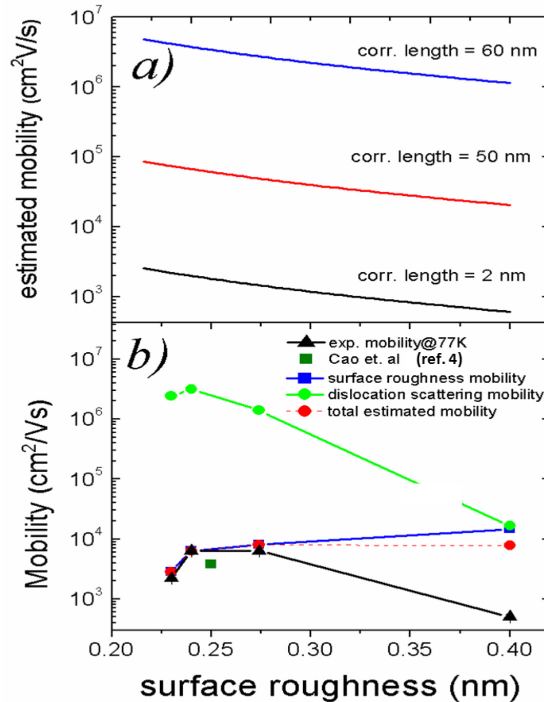

Figure 5.15 (a) Remote surface scattering mobility calculated *vs* surface roughness for different correlation length values. ***(b)*** Experimental Hall mobility at 77 K (black triangle), calculated mobility limited by surface roughness scattering (solid squares), dislocation scattering (solid circles) and total calculated mobility (solid circle) plotted as a function of surface roughness

We have measured Hall mobility, 2DEG density, surface roughness and correlation lengths by AFM and STM in $In_xAl_{1-x}N$/AlN/GaN heterostructures with increasing AlN interlayer thicknesses up to 7.5 nm. Surface roughness and dislocation scattering limited mobilities have been calculated and compared with measured values. No fitting parameters and no *a priori* assumptions have been used for the mobility evaluation, only directly measured parameters have been employed. The comparison between experimental and calculated data clearly demonstrates that surface roughness scattering is the dominant mechanism limiting the mobility in high mobility $In_xAl_{1-x}N$/AlN/GaN heterostructures.

5.5 Capacitance-Voltage (C-V) analysis

The C-V measurement has been performed at 300 K to calculate the 2DEG carrier concentration in InAlN/AlN/GaN heterostructures, depletion region width and the barrier height as mentioned in chapter 3. The C-V measurements have been performed at 1 KHz frequency mainly for use of DLTS measurements in order to be sure of applying bias and extracting the correct information on defect levels as it becomes quite complex in this kind of heterostructures to conclude precisely. The C-V measurements have been performed on 'Ni/Au' and 'Pt' Schottky diodes for different samples which is shown in Fig. 5.16 as on some samples it was so noisy signal during measurement, possible due to high leakage/conductance in structure and also the lack of good quality diodes. Fig. 5.16 shows the measured C-V curves for different samples and also the conventional C^{-2} *vs* V plot in order to calculate the Schottky barrier height for different samples for Ni/Au and Pt Schottky diodes. It can be observed that in case of Ni/Au Schottky diode depletion plateu is at low bias in comparison to Pt Schottky which could be due to differences in different interface of both metals due to their fundamental characteristics. In case of 'Pt' Schottky barrier height can be directly extracted from linear slope of C^{-2} *vs* V plot while in case Ni/Au, linear dependence is very less appeared. However, in both metal Schottky diodes case, it can be observed that capacitance. From fig. 5.16b, it can be observed that with increase in AlN interlayer thickness Schottky barrier height also increase accordingly which was also discussed in previous section and correlated with surface trap sates [18].

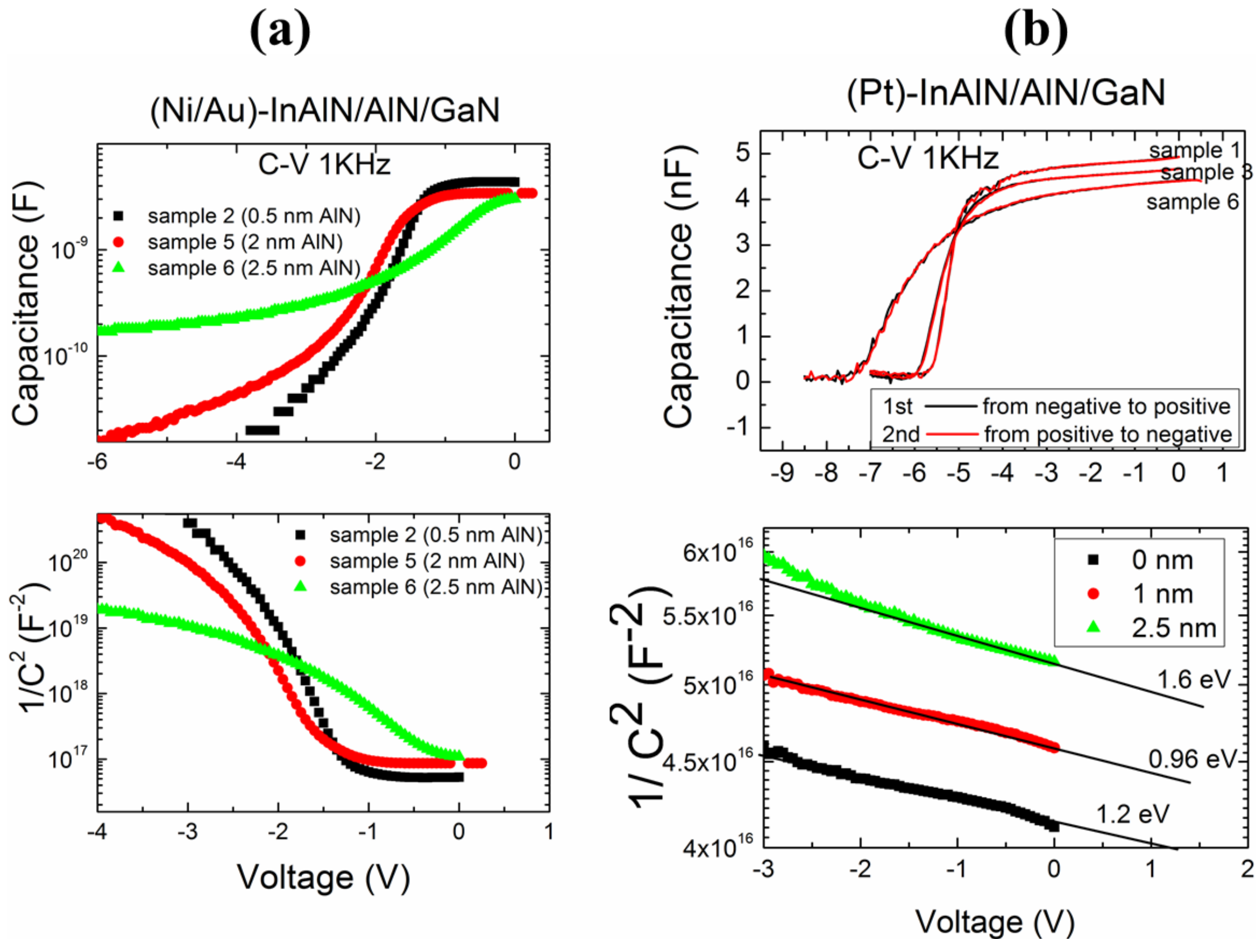

Figure 5.16 C-V characterisctics of different sampels with Ni/Au ***(a)*** and Pt ***(b)*** Schottky diodes, showing $1/C^2$ *vs V* plot to calculate Schottky barrier height

From measured C-V and C^{-2} *vs V* characteristic, it is possible to calculate the 2DEG concentration at AlN/GaN interface and also to calculate the thickness of AlInN layer and AlN layer separately. On plotting the calculated carrier concentration with thickness (depth) the total thickness of barrier and interlayer is found in very good agreement with nominal and Transmission Electron Microscopy (TEM) measured results. From fig. 5.17, it can be observed the order of carrier concentration around 10^{19}-10^{20} cm^{-3} which has been also compared with available results from previous model of I-V [2] and Hall Effect measurements, shown as fig. 5.18. The difference in values have been found to be 20-30% which can be attributed to techniques and principles related and also to different measuring conditions.

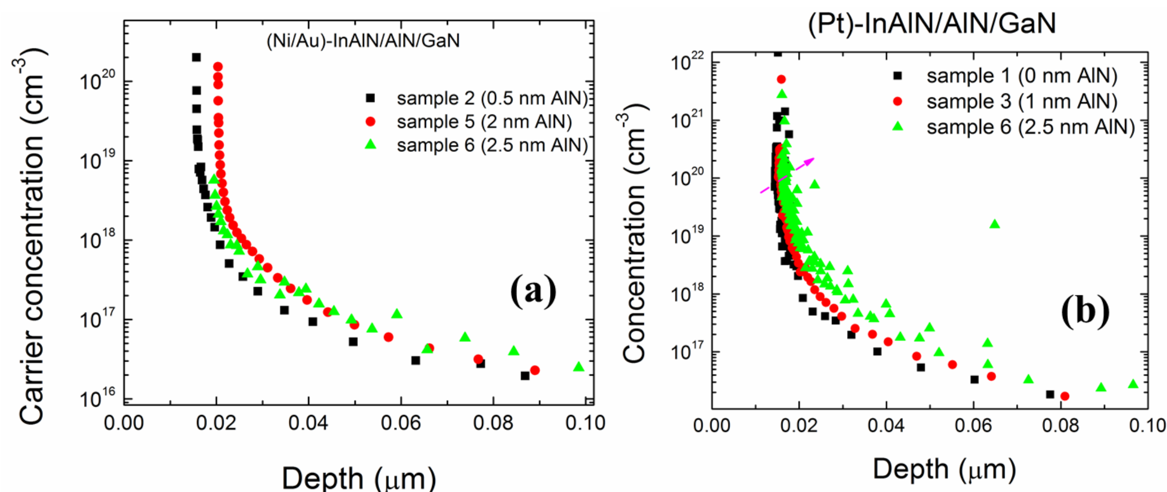

Figure 5.17 The calculated Carrier concentration (N_d) from C-V measurements with Ni/Au ***(a)*** and Pt ***(b)*** Schottky diodes

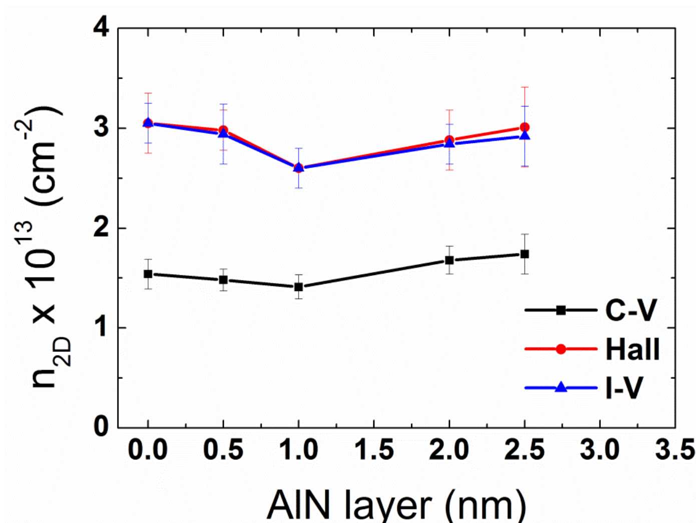

Figure 5.18 The comparison of calculated 2DEG density from conventional Hall Effect measurements (red circles), C-V measurements (black squares) and I-V model (blue triangles) [2]

5.6 Deep Level Transient Spectroscopy (DLTS) Analysis

Deep Level Transient Spectroscopy (DLTS) measurements on InAlN/GaN based heterostructures are rarely performed and very few reports are available so far. As explained above, these samples/structures suffer by high leakage current due to high number of dislocations, which makes DLTS measurements highly complex and difficult to analyze. However, 3 samples have been successfully characterized and discussed here. DLTS measurements have been performed on sample 1, sample 3 & 6 successfully by using Current-DLTS and Capacitance DLTS respectively. One of the main goal of performing DLTS measurements is to understand if insertion of AlN layer affects the defect level position/capture cross section or generation of addition defects in barrier layer or at interface.

5.6.1. Sample without 'AlN' interlayer

Current DLTS (I-DLTS) measurement on Sample 1

Despite of high leakage in sample 1, Current-DLTS measurements has been performed in order to achieve information on defect levels in structure, i.e. in barrier layer. The Capacitance mode DLTS was also applied but due to high leakage/conductance, it was not possible to record a reliable spectra. In order to achieve some reliable information from measurements, a low bias was applied with a filling pulse after confronting the leakage and CV plot.
Here is the details on applied bias and pulse [$V_{rev.}$, V_{pulse}]:

- [-0.5V, +0.5V] for probing barrier layer of InAlN layer ***(a)***
- [-0.1V, +0.5V], [-0.1V, +1.5V] and [-0.1V, +2V] for probing barrier layer of InAlN layer ***(b)***
- Constant filling pulse of 1 ms

The measured DLTS spectra for is illustrated below:

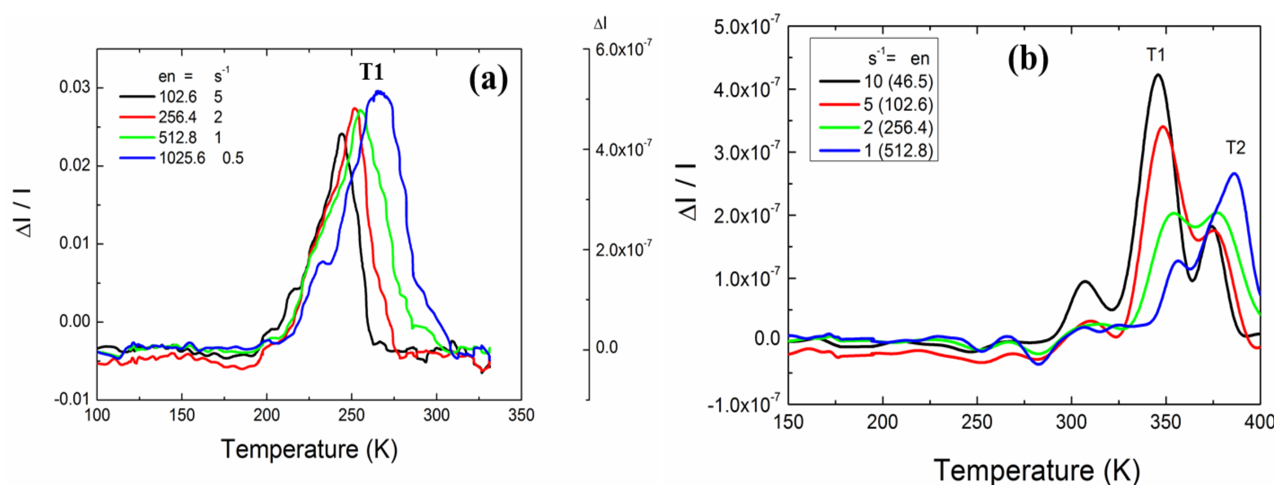

Figure 5.19 DLTS spectra for sample 1 for different emission rates at different bias and pulses

Fig. 5.19a shows the normalized DLTS spectra (ΔI/I) where, ΔI is the change in current with temperature with applied bias and pulse at [-0.5 V, +0.5 V] which shows a sharp positive peak appearance at 243 K for 102.6 s^{-1} emission rate and for other rate windows with increase in temperature which is marked as T1. In this study, as the I-DLTS spectrum is positive (increase of drain current during the transient) we are in presence of a majority carrier trap. The appearance the peak could be related to dislocation type of traps in this kind of heterostructure, responsible for higher leakage in HEMT devices. The measurements have been performed with different emission rates (not shown) in order to confirm the peak appearance and also for preparation of Arrhenius plot for calculation of it's energy position. The appearance of this sharp peak was further checked by giving different bias and pulse with [-0.1, +0.5], [-0.1V, +1.5V] and similar peak is observed with a shift in it's position with temperature (shown as fig. 5.19b). The shift in peak to higher temperature values could be due to different polarization parameters compared to previous one. Apart from this peak, an another peak is observed at higher temperature which is marked as trap 2 (T2) which is quite near to first trap position. In order to calculate the energy position and capture cross section of these traps, Arrhenius plot was prepared which is shown as fig. 20. Thus, from Arrhenius plot, the energy levels have been calculated for observed traps at, **T1: Ec-0.64 eV** with capture cross section

of 2.7e-12 cm^2 and **T2: at Ec-0.70 eV** with a capture cross section of 1.9e-13 cm^2. However these traps are found to be very close to each other in energy values and also in their capture cross section values. These traps could be related to dislocation levels in barrier layers similar like GaN. These traps could be responsible for leakage in this kind of structure and these traps can have the band of dislocation networks as also discussed above in terms of Poole-Frenkel emission. A tabulated summary and a schematic band diagram is plotted to explain this below:

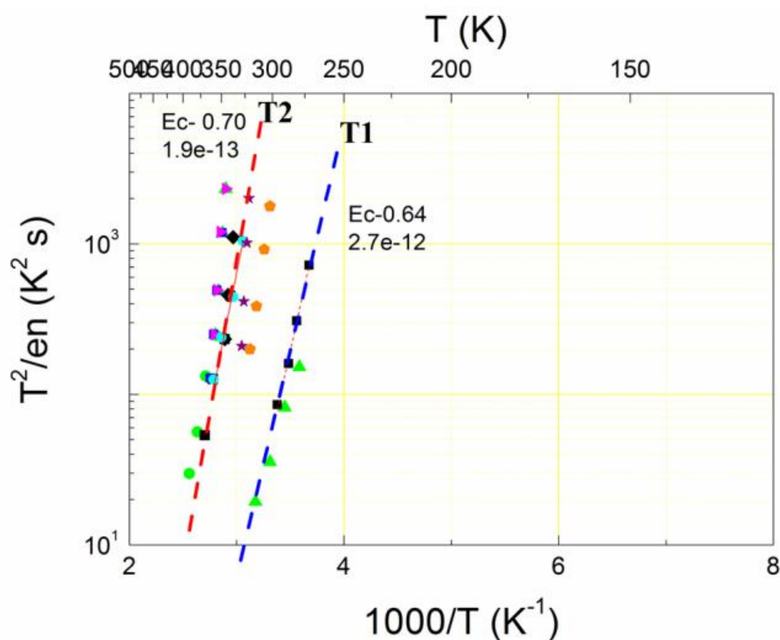

Figure 5.20 Arrhenius plot reporting the signatures of the deep levels (majority carriers) detected in sample1

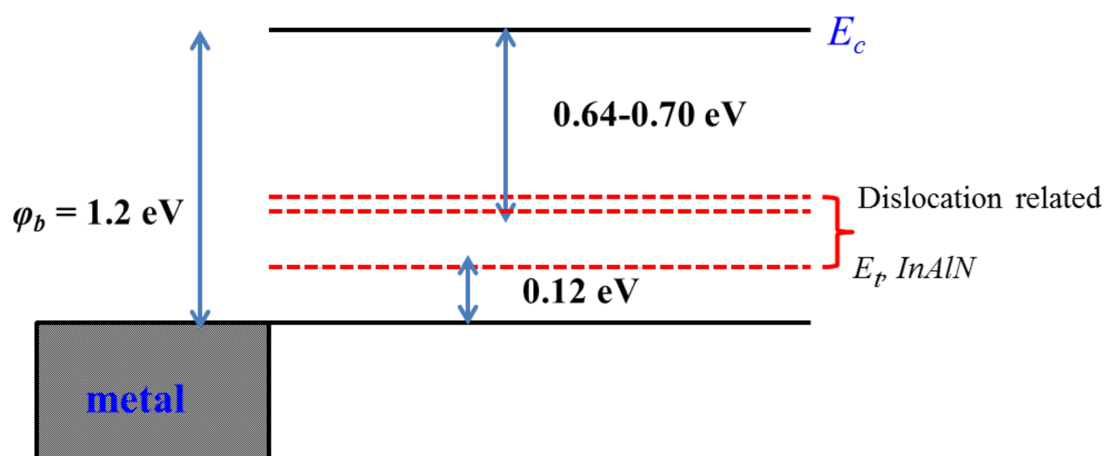

Figure 5.21 Schematic diagram of traps level position and dislocation related energy levels in InAlN barrier layer

Table 5.II Parameters of deep levels in sample 1

Deep Levels	Energy position (eV)	Capture cross section, $\sigma_{capture}$ (cm^2)
T1	E_c-0.64	2.7×10^{-12}
T2	E_c-0.70	1.9×10^{-13}

Thus, I-DLTS measurements allow identifying the deep levels in barrier layer of InAlN which have correlated to dislocations in layer. The identified traps are from majority carriers in the structure, the origin of these traps are not identified whether they have been originated from a vacancy or vacancy complexes.

5.6.2. Sample with 'AlN' interlayer

Capacitance DLTS (C-DLTS) measurement on Sample 3 and Sample 6

Capacitance DLTS method has been applied for identifying the deep levels in sample 3 and sample 6, which are the structures with interlayer of AlN to compare with sample 1 which doesn't have any interlayer of AlN in the structure. It would be interesting to remind again that an interlayer of AlN of 1 nm and 2.5 nm have been inserted in sample 3 and sample 6 in order to improve the interface properties to avoid problems like alloy scattering, penetration of wave function in order to confine the 2DEG electrons to achieve better electrical properties for devices. The main goal of performing the DLTS characterization on these structures is to compare if the presence of interlayer affects the deep levels which have been identified in sample 1 and also to see if additional deep levels have been identified.

The Capacitance mode DLTS has been applied on these samples which have also high leakage due to presence of still high dislocation but with higher mobility (as shown in Fig. 5.5). In order to achieve some reliable information from measurements, a low bias was applied with a filling pulse after confronting the leakage and CV plot.

Sample 3 (with 1 nm interlayer of AlN)

Here is the details on applied bias and pulse [$V_{rev.}$, V_{pulse}]:

- [-0.4V, +0.8V] for probing barrier layer of InAlN ***(a)***
- [-0.5V, +1.5V], [-1V, 0V] for probing barrier layer of InAlN ***(b)***
- Constant filling pulse of 1 ms

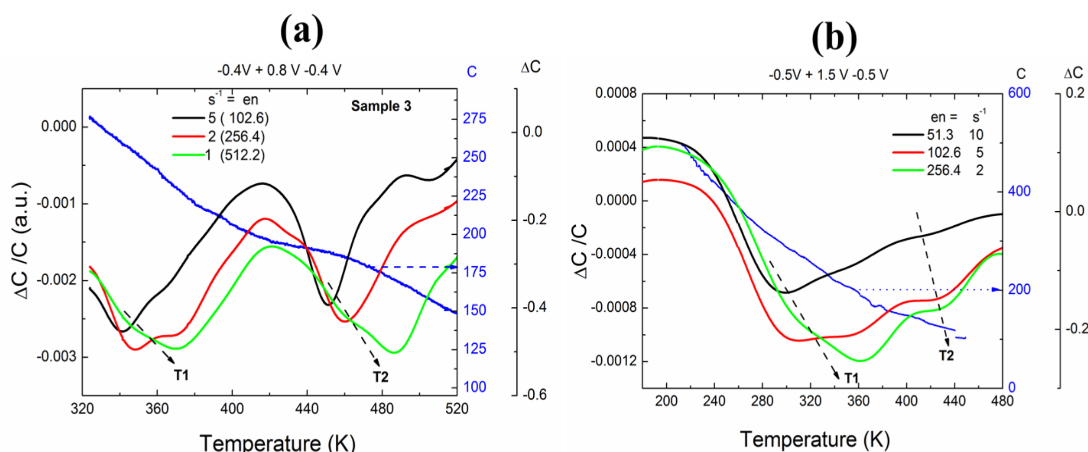

Figure 5.22 C-DLTS spectra for sample 3 for different bias conditions shown as (a) and (b) for a constant filling pulse duration

From fig. 5.22a shows the normalized DLTS spectra (ΔC/C) where, ΔC is the change in current with temperature with applied bias and pulse at [-0.4 V, +0.8 V] which shows two broad negative peak appearance at 338 K and 443 K for 102.6 s^{-1} emission rate respectively, and for other rate windows with increase in temperature which is marked as T1 and T2. In this study, as the C-DLTS spectrum is negative (decrease of gate capacitance during the transient) we are in presence of a majority carrier trap. The appearance these peaks could be related to dislocation type of traps in this kind of heterostructure as also mentioned for case of sample 1, responsible for higher leakage in HEMT devices. The measurements have been performed with different emission rates (not shown) in order to confirm the peak appearance and also for preparation of Arrhenius plot for calculation of it's energy position. The appearance of these broad peaks were further checked by giving different bias and pulse with [-0.5, +1.5], [-0.5V, +0V] and similar peak is observed with a shift in it's position with temperature (shown as fig. 5.22b). The shift in peak to higher temperature values could be due to different polarization parameters. We have not detected any other trap level at low temperatures (≤ 200 K).

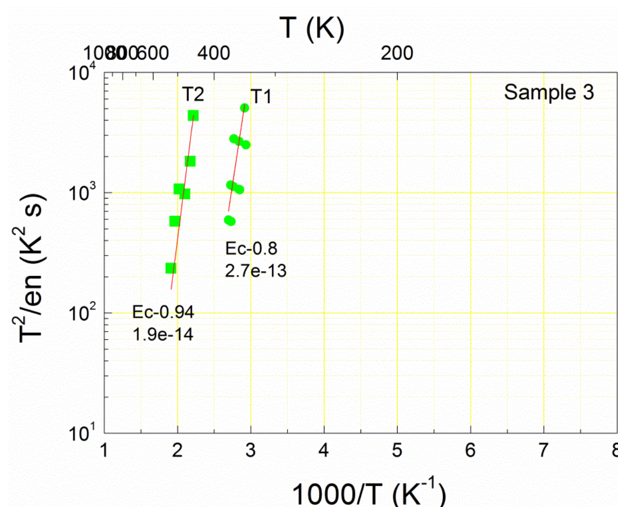

Figure 5.23 Arrhenius Plot reporting the signatures of the deep levels (majority carriers) detected in sample 3

In order to calculate the energy position and capture cross section of these traps, Arrhenius plot was prepared which is shown as fig. 5.23. Thus, from Arrhenius plot, the energy levels have been calculated for observed traps at, **T1: Ec-0.8 eV** with capture cross section of 2.7e-13 cm^2 and **T2: at Ec-0.94 eV** with a capture cross section of 1.9e-14 cm^2. However these traps are found to be very close to each other in energy values and also in their capture cross section values. It is worth to mention that these deep levels could be of same nature and from same origin as deep levels observed in sample 1 because their energy levels and capture cross sections are very close to each other. These traps could be related to dislocation levels in barrier layers similar like GaN. These traps could be responsible for leakage in this kind of structure and these traps can have the band of dislocation networks as also discussed above in terms of Poole-Frenkel emission. Thus, C-DLTS measurements allow identifying the deep levels in barrier layer of InAlN which have correlated to dislocations in layer. The identified traps are from majority carriers in the structure, the origin of these traps are not identified whether they have been originated from a vacancy or vacancy complexes.

Sample 6 (with 2.5 nm interlayer of AlN)

Here is the details on applied bias and pulse [$V_{rev.}$, V_{pulse}]:

- [-0.5V, +1V] for probing barrier layer of InAlN
- Constant filling pulse of 1 ms

From fig. 5.24 shows the normalized DLTS spectra ($\Delta C/C$) where, ΔC is the change in current with temperature with applied bias and pulse at [-0.5 V, +1 V] which shows one sharp negative peak at low temperature regime and a broad positive peak at high temperature appearance at 140 K and 390 K for 102.6 s^{-1} emission rate respectively, and for other rate windows with increase in temperature which is marked as T1 and T2. In the case of T1, as the C-DLTS spectrum is negative (decrease of gate capacitance during the transient) we are in presence of a majority carrier trap while in case of T2 which appears at C+, which could be correlated to minority carriers in this kind of structures. Apart from these deep levels signature in DLTS spectra, two small and less appeared C- peaks (negative capacitance peaks) have been also observed at 205 K and 335 K for 102.6 s^{-1} emission rate, represented as A and B respectively. It is found that these deep negative peaks are very close to each other, even at different emission rates or bias which makes the calculation for Arrhenius quite complex. The appearance of the deep level T1 could be related to dislocation type in this kind of heterostructure as also mentioned for case of sample 1& 2, responsible for higher leakage in HEMT devices, while the T2 can be correlated to interface states originating from 2DEG channel. The appearance of these broad peaks were further checked by performing another measurements with same bias and pulse of [-0.5V, +1.0V] at low and high temperature regime (shown as fig. 5.25 a & b). . The measurements have been performed with different emission rates (not shown) in order to confirm the peak appearance and also for preparation of Arrhenius plot for calculation of it’s energy position.

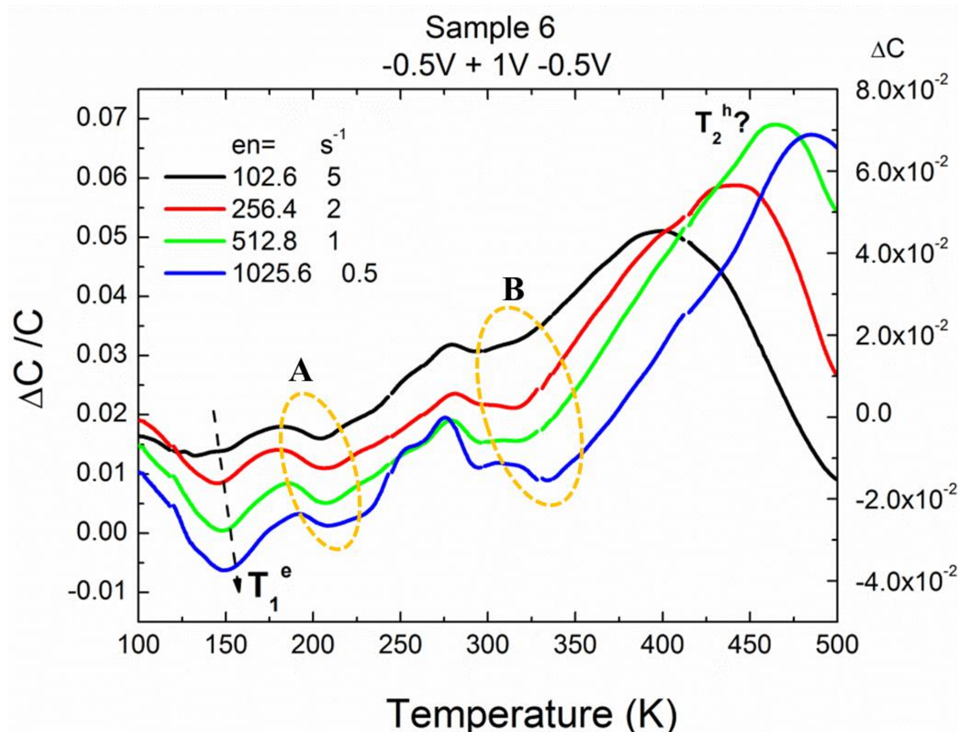

Figure5. 24 C-DLTS spectra for sample 6 for constant filling pulse duration, showing the presence of deep levels (majority and minority carriers)

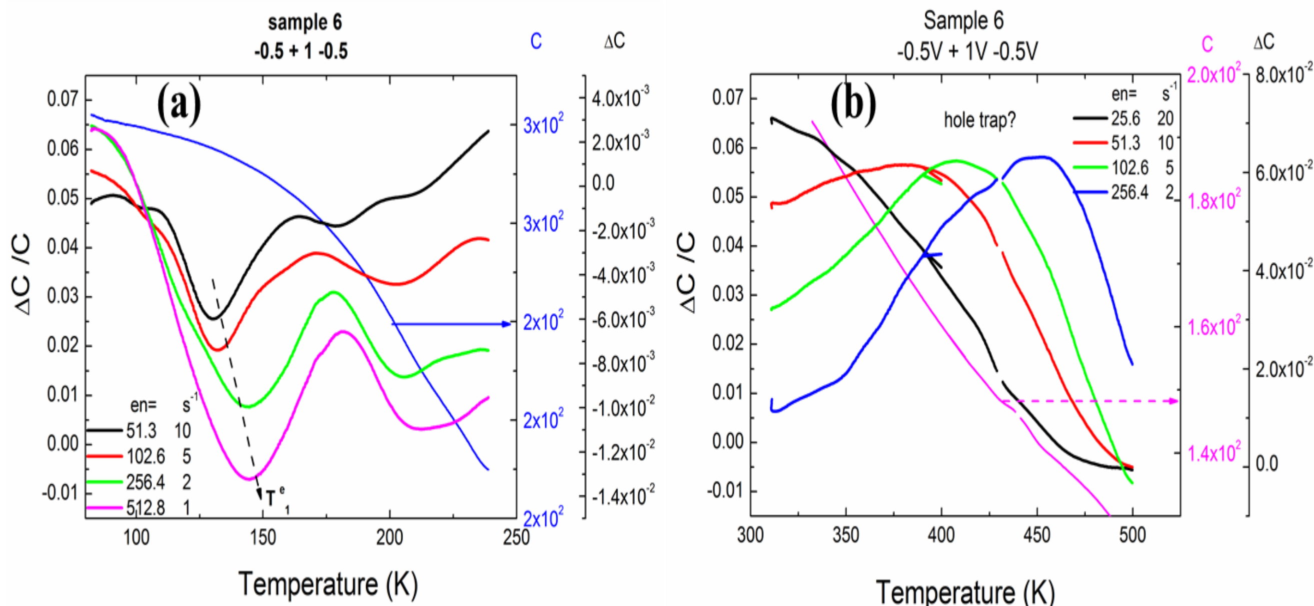

Figure 5.25 C-DLTS spectra for sample 6 in low (a) and high temperature (b) regime for constant filling pulse duration

In order to calculate the energy position and capture cross section of these traps, Arrhenius plot was prepared which is shown as fig. 5.26. Thus, from Arrhenius plot, the energy levels have been calculated for observed traps at, **T1 (majority): E_c-0.23 eV** with capture cross section of 3.0e-15 cm^2 and **T2 (minority): at E_v+0.5 eV** with a capture cross section of 1.0e-18 cm^2. However, the deep level T1 is found to be very close to the trap energy calculated by Poole-Frenkel emission

earlier in I-V analysis. While for deep levels marked as A& B in fig. 5.24, the Arrhenius calculations were very complex due to the more or less same position in temperature in spectra, which doesn't allows to calculate the reliable data and that's why they have not been included in fig. 5.26. Thus, deep level T1 could be related to dislocation levels in barrier layers similar like sample 1, 3 & GaN. On the deep level T2, which seems to be originated from minority carrier emission, mainly from 2DEG channel at AlN/GaN interface? As, it's discussed in chapter 2 that insertion of AlN layer induces the positive charges due to spontaneous polarization and balances the total charges in 2DEG channel, it could be said that due to thick AlN layer there could be some donor levels/positively charged traps of dislocation type/other type and they emit during the reverse bias and observed in DLTS spectra. While in case of sample with thinner AlN layer (sample3), it could be that thin layer doesn't induce so much positive charges in the structure and which results no appearance of such deep level in sample 3. We can not explain the real origin for this emission which would be considered for further study as future work.

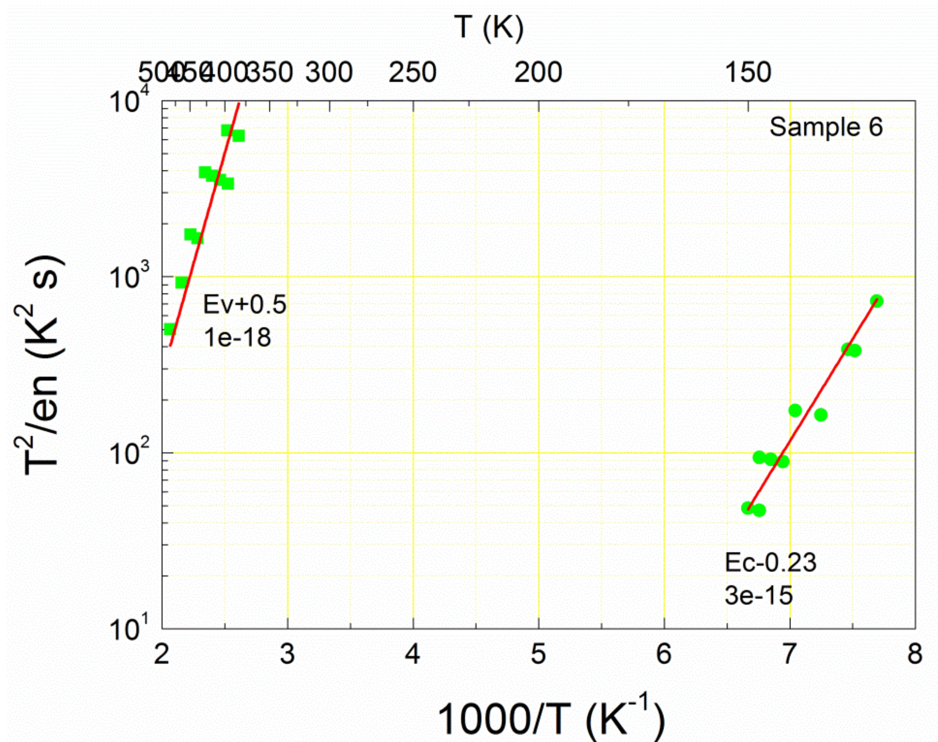

Figure5. 26 Arrhenius plot reporting the signatures of the deep levels (majority and minority carriers) detected in sample 6

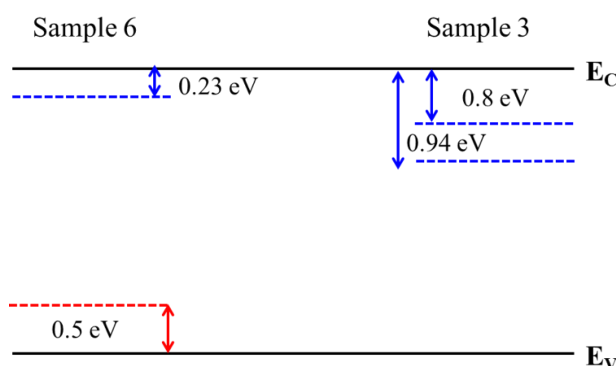

Figure 5.27 Deep level positions in sample 3 and 6

5.7 Optical characterization with SPV, PC and PL

The main focus has been given to 2DEG related or induced transitions above GaN energy gap which has not been studied before. In order to understand the mentioned phenomena different optical spectroscopy techniques have been used such as Surface Photovoltage (SPV), Photocurrent (PC) and Photoluminescence (PL) for justification and clear explanations in achieved results.

5.7.1 Band gap shift in $Al_{1-x}In_xN$/AlN/GaN heterostructures studied by Surface Photovoltage Spectroscopy

GaN based heterostructures have recently gained increased interest due to their applications for High Electron Mobility transistors. In this work AlInN/AlN/GaN heterojunctions grown by MOCVD (metal organic chemical vapor deposition) with different AlN thicknesses have been investigated by Surface Photovoltage Spectroscopy. The density of the two dimensional electron gas forming at the interface has been measured by Hall effect. A band gap shift has been detected and its dependence on the 2DEG electron density at the AlN/GaN interface has been analyzed on the basis of the Moss Burstein and renormalization effects.

The present contribution aims at the characterization of the 2DEG electron gas in AlInN/ AlN/ GaN heterostructures by Hall measurement and Surface Photovoltage Spectroscopy (SPV) at 300 K. By SPV the band to band transitions in the GaN layer was detected at an energy value close to the GaN band gap (3.4 eV). Its dependence on the AlN interlayer thickness, and on the 2DEG density evaluated by Hall effect has been discussed on the basis of the Moss-Burnstein (MB) and renormalization effects.

Samples with the AlN layer varied as 0.5, 1, 1.5, 2.5, and 5 nm have been measured for this study. Surface Photo Voltage Spectroscopy (SPS) analyses were performed at room temperature. More detailed information on the method can be found in chapter 3. Optical transmission coefficient has been also measured by the same apparatus. Hall Effect measurements have been carried out on Van der Pauw structures at room temperature.

SPV spectra measured on AlInN/AlN/GaN heterostructures and on the GaN template are shown in fig. 5.28. The most relevant peak in a SPV spectrum is usually related to band to band electronic transitions [chapter 3]. It should be reminded that by changing the photon energy also the optical absorption coefficient α, and in turn the penetration depth α^{-1}, varies. For photon energies ranging from 3 to 4 eV, α^{-1} ranges from 0.07 to 1 µm in GaN, from 1 to 96 µm for AlInN while AlN is completely transparent in this range [39]. This means that from 3 to 4 eV the carrier generation and collection occurs mainly within the GaN layer, and when the photon energy becomes comparable with the GaN band gap, it occurs mainly at the interface between GaN and AlN, or at the GaN surface in the template. Thus the peaks in fig.1 are all related to band-to band transitions at the GaN /AlN heterointerface (fig. 5.28a) or at the GaN surface (fig. 5.28b). While in the GaN template the maximum value in the spectra expectedly occurs at 3.44 eV ($E_{G,GaN}$), a value which is good agreement with the literature value of $E_{G,GaN}$ (3.45 eV), in the heterostructures the peaks are detected at higher energy values ($E_{G,\ HET}$, fig.28a). Moreover, SPV signals detected in AlInN /AlN /GaN structures are usually remarkably lower than the ones measured in GaN templates mainly due to strong recombination of e-h pairs with the 2DEG at AlN/GaN interface.

As shown in fig. 5.28a, the shift in the band gap ΔE_G , defined as $\Delta E_G = E_{G,\ HET} - E_{G,\ GaN}$, depends on the AlN interlayer thickness d_{AlN}. Moreover, it is to be noted that $\Delta E_{G,}$is not revealed by optical transmission measurements, as shown in fig. 5.29, where both optical transmittance T and SPV spectrum for the same sample are reported.

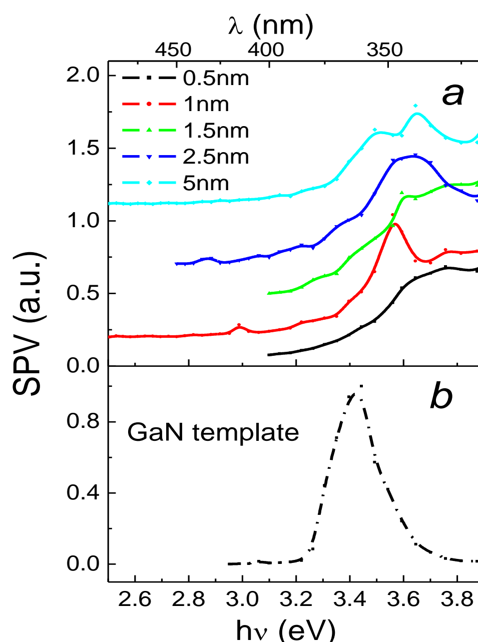

Figure 5.28 (a) SPV (a.u.) spectra, normalized to the maximum values, measured in the AlInN/AlN/GaN heterostructures (a) and in the GaN template (b). In Figure 28 (a) the spectra have been shifted with increasing AlN layer thickness for clarity

The 2DEG electron density n_{2D} in the different heterostructures has been measured by Hall Effect measurements and the results are plotted *vs* the interlayer AlN thickness in fig. 5.30. It must be noted that the 2DEG density n_{2D} initially decreases as a function of the interlayer thickness d_{AlN}, afterwards it increases up to almost 5 nm. Above this value n_{2D} again decreases, meaning that an efficient confinement is lost possibly due to crack formation. The possible reasons for this behaviour are reported [2, 3], while here we focus our attention to those samples where Hall data show good confinement due to the presence of the AlN layer, i.e. from 0.5 to 2.5 nm.

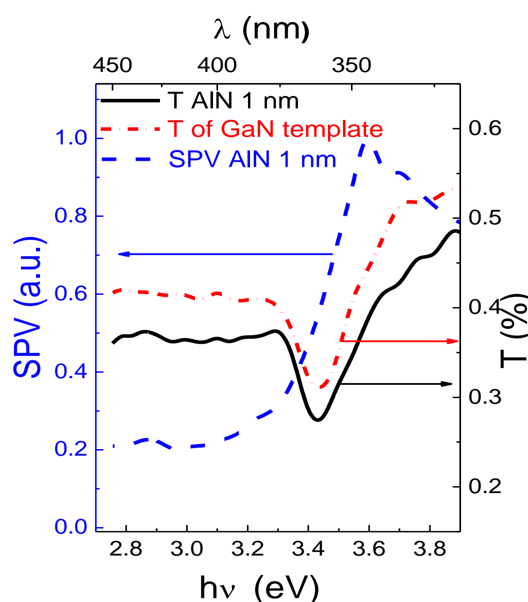

Figure 5.29 Transmission coefficient T (λ) of GaN template (red, short dashed dot) and of AlInN/AlN (1nm)/ GaN heterostructure (black, solid line), and SPV (λ) of AlInN/AlN (1 nm)/ GaN (blue, dashed line)

In order to explain the variation of ΔE_G vs d_{AlN} the volume density of the free carrier concentration n_e in the proximity of the AlN/GaN heterointerface was calculated by n_{2D}. For this purpose the "thickness" *h* of the 2DEG electron gas must be evaluated by [40]:

$$h(n_{2D}) = \frac{\varepsilon\varepsilon_0}{e^2}\frac{\partial\varepsilon_1}{\partial n_{2D}} = \frac{2}{3}c_1\left(\frac{\hbar^2}{2m^*}\right)^{1/3}\left(\frac{\varepsilon\varepsilon_0}{e^2 n_{2D}}\right)^{1/3} \tag{5.12}$$

with c_1 first coefficient of the Airy function, ε GaN relative permittivity, ε_0 vacuum permittivity, e electron charge, and ε_1 energy of the lowest energy state in the triangular potential well induced by the heterojunction. *h* depends on the n_{2D} and varies between 2.5 to about 3 nm. The electron concentration n_e, calculated as n_{2D}/h, ranges from 8 to 12×10^{19} cm^{-3}. It must be noted that GaN is degenerate at the heterointerface.

The band gap shift ΔE_G plotted *vs* n_e in fig. 5.31 shows that ΔE_G monotonically increases as a function of n_e. In order to understand this trend it should be reminded that E_G is measured by SPV close to the GaN/AlN interface where the 2DEG electron gas is confined, i.e. where GaN is degenerate. The optical band gap E_G of a degenerate semiconductor widen with increasing carrier concentration as predicted by the BM effect [41]. This effect is usually attributed to the conduction band occupation inducing optical transitions at energies higher than the minimum-energy fundamental electronic gap. The magnitude ΔE_{BM} of this shift is described by:

$$\Delta E_{BM} = \frac{\hbar^2}{2m^*}\left(3\pi^2 n_e\right)^{2/3} \tag{5.13}$$

With, n_e free electron concentration and m^* GaN effective mass.

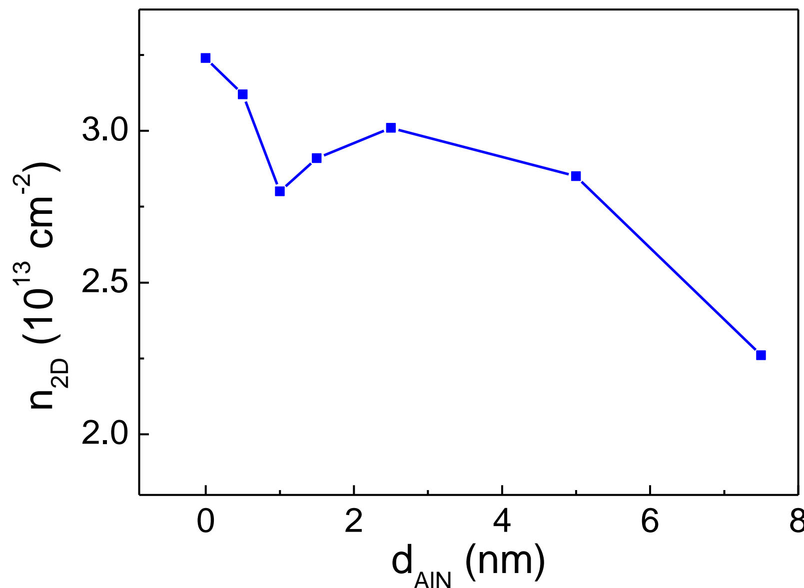

Figure 5.30 2DEG density vs interlayer AlN thickness measured by Hall Effect at 300 K [2]

In order to calculate m^* in a polar semiconductor like GaN, non-parabolic conduction band must be considered. Moreover, for degenerate semiconductors m^* at the Fermi Energy depends on n_e [42, 43 and 44]. In order to account for these effects we used for the momentum effective mass

m^*_p [14] $m_p^* = m_{e0}^*(1+2E_c/E^*)$ with E^* a constant which will be obtained in the following as a fitting parameter, m_{e0}^* the dynamical effective electron mass (for GaN 0.20 m_0 with m_0 the electron mass [45]), E_C the conduction band energy given, in the hypotheses of spherical band and degenerate semiconductor, by $E_C = \frac{\hbar^2 k_F^2}{2m_{e0}^*}$ with $k_F^2 = (3\pi^2 n_e)^{2/3}$

Finally, the dependence of m^* on n_e can be obtained:

$$m^* = m_{e0}^*\left(1+\frac{2An_e^{2/3}}{E^*}\right) \quad \text{with} \quad A = \frac{\hbar^2(3\pi^2)^{2/3}}{2m_{e0}^*} \tag{5.14}$$

and thus the dependence of ΔE_{BM} on n_e. However, the carrier concentration dependence of the measured band gap shift is usually less abrupt than that expected for free electron model (eq. (5.13)), [46]. To account for this discrepancy the band gap renormalization has been proposed, which considers a band gap shrinkage ΔE_{RN} which takes into account the Coulomb interaction between the free electrons in CB and the electron impurity scattering [47]. Therefore:

$$\Delta E_G = \Delta E_{BM} + \Delta E_{RN} \tag{5.15}$$

where ΔE_{BM} is given by equation (5.13) and ΔE_{RN} has been evaluated by the equation given by Yoshikawa [48], which is in agreement with the theoretical work of Bulutay [47]:

$$\Delta E_{RN} = -4.72\times 10^{-10} n_e^{1/3} \tag{5.16}$$

with n_e (m^{-3}) and E^* in eV .
Finally, ΔE_G was plotted as a function of n_e in fig. 31 and fitted by the following equation:

$$\Delta E_G = V_o + \frac{\hbar^2}{2m_o^*(1+2An_e^{1/3}/E^*)}\left(3\pi^2 n_e\right)^{2/3} - 4.72\times 10^{-10} n_e^{1/3} \tag{5.17}$$

obtained by the substitution of eqs. (5.13, 5.14) and (5.15) in equation (5.16) and adding V_0. V_0 has been introduced to take into account strain effects on E_G and the degeneracy of the layer. Thus the two fitting parameters used are V_0, and E^*, which takes into account the effects of non-parabolic band structure on m^* [42, 43, 44]. From the fitting procedure an E^* value of 5.8 eV has been obtained, which can be used to evaluate the dependence of the effective mass on free carrier concentration (eq. 5.14). The values shown in fig. 5.31 are in very good agreement with the variation of m^* as a function of n_e calculated and experimentally determined for GaN [44]. It is noteworthy that the V_0 value obtained by the fitting procedure allows zeroing the bandgap shift when n_e approaches the degeneracy limit of free carrier concentration.

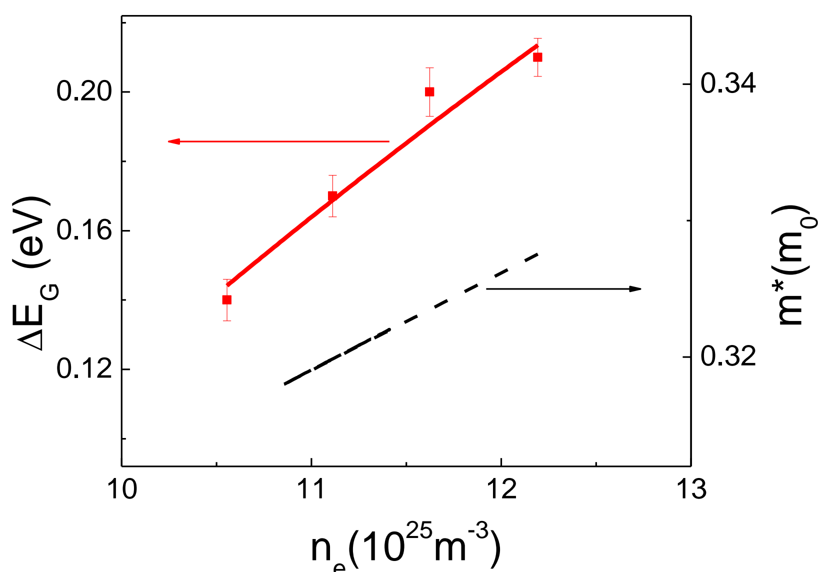

Figure 5.31Experimental values (red filled squares) and fitted curve (red solid line) of the band gap shift ΔE_G as a function of free carrier concentration n_e. Calculated values of the electron effective mass are plotted in the inset as a function of free carrier concentration n_e

The presence of the band gap shift in these structures should not be ascribed to the well-known Quantum Confined Stark Effect which usually plays a significant role in nitride based semiconductor low dimensional structures, as the polarization induced electric field should be screened out by the high density of free charges (larger than 2×10^{13} cm^{-2}) [49].

The present investigation shows the effect of quantum confinement of free carriers on band structure properties in GaN based heterostructures. The band gap shift has been measured by SPV, as the technique allows obtaining the energy gap in the close proximity of the heterointerface. The energy gap was found to increase as a function of the free carrier concentration, which is related to the 2DEG density, due to the combined Moss Burnstein and renormalization effects. The application of the model allows us to calculate a parameter which quantitatively account for the non -parabolic conduction band and to evaluate the effective mass dependence on free carrier concentration.

5.7.2 Subband Energy Levels and Fermi edge singularity in InAlN/AlN/GaN Heterostructures

An additional study has been performed on nominal lattice matched heterostructures with %In varying from 17-20 (detail are provided later in table II). In this study, optically induced electronic transitions in nitride based polar heterostrucures have been investigated by absorption and emission spectroscopy. Surface photovoltage (SPV), Photocurrent (PC) and Photo Luminescence (PL) spectroscopy have been applied to high quality InAlN/AlN/GaN structures to understand the optical properties of two dimensional electron gas. Energy levels within the two dimensional electron gas (2DEG) well at the interface between the GaN and AlN have been directly observed by SPV and PC. Moreover, a strong enhancement of the Photoluminescence intensity due to holes recombining with electrons at the Fermi Energy, known as Fermi Energy Singularity (FES), has been observed. These analyses have been carried out on InAlN/AlN/GaN heterojunctions with the InAlN barrier layer having different In content, a parameter which affects

the energy levels within the 2DEG well as well as the optical signal intensity. The measured energy values are in a very good agreement with the ones obtained by Schrodinger-Pöisson simulations.

Subband transitions in wurtzite group-III-nitride based heterostructures have been extensively studied in AlGaN/GaN systems [50, 51], but only recently in AlInN by magnetotransport measurements [52] and non-contact electroreflectance spectroscopy [53]. Radiative recombination in the 2DEG channel layer in nitride based heterostructures investigated by PL demonstrate direct recombination in the AlInN layer, while PL analyses by [54] clearly show the presence two components in the emission spectra related to AlInN layer [55].

In addition, a strong enhancement of the luminescence spectra of electrons recombining close to the Fermi level (E_F) has been theoretical predicted [56, 57] and only in a few cases experimentally observed in two dimensional structures (quantum wells [58], modulation doped heterostructures [59], and GaN/AlGaN heterointerfaces [60]). This effect, called Fermi-edge singularity, is a direct consequence of the increased electron-hole scattering rate of electrons close to E_F in an high density electron plasma (electron concentration around 10^{12} cm^{-2} and above).

The main subject of this study is the detection and identification of 2DEG related transitions above the GaN gap energy and of Fermi Edge Singularity (FES) in InAlN/AlN/GaN heterostuctures by Surface Photo Voltage spectroscopy, PhotoCurrent (PC) and Photoluminescence (PL) spectroscopy measurements. The use of these three different spectroscopical methods, allowing for the observation of absorption and emission related transitions, has allowed us to obtain an almost complete picture of the electronic states of this structure. Moreover, by detecting transitions above the GaN energy gap, we have been able to investigate the optoelectronic properties of the two dimensional electron gas, in particular the FES which can be observed only with high 2DEG.

Nearly lattice-matched AlInN/AlN/GaN heterostructures with slightly different In (%) and layer thickness, and thus different 2DEG density, have been examined in order to investigate the effect of accumulated charges in 2DEG channel layer on the surface photovoltage (SPV), photoluminescence (PL) and photocurrent (PC) spectra. The obtained results have been compared with band diagram simulation by Schrodinger-Pöisson simulation.

The nominal thickness of the InAlN layer, AlN interlayer and In%, are reported in table III. The experimentally measured 2DEG density at AlN/GaN interfaces for the different HS are also reported in table II. High crystalline quality of layers have been confirmed by XRD analysis. GaN buffer layer thickness is kept around 3 μm for all samples.

Table 5.III Sample details: nominal thickness of InAlN layer and %In, nominal thickness of AlN interlayer, experimentally measured 2DEG density by Hall Effect technique. It also shows the observed subband energy related to 2DEG well values from GaN valence band edge measured by SPV, PC and FES position by PL

Samples	%In	d_{InAlN} (nm)	d_{AlN} (nm)	2DEG density x 10^{13} (cm^{-2})	$E_{2,subband}$ by SPV (eV)	$E_{1,subband}$ by PC (eV)	FES(eV) by PL
1	19.9	10	1	1.25	3.56	3.55	3.69
2	18.5	14	1	1.35	3.64	3.57	3.73
3	17.6	10	4	1.50	3.64	3.59	3.79

Surface Photo Voltage Spectroscopy (SPS) [see chapter 3] analyses were performed at room temperature by means of a custom-made apparatus based on Xenon lamp source and a SPEX 500M monochromator. Hall Effect measurements have been carried out on Van der Pauw structures to

calculate the 2DEG density at room temperature. Photoluminescence measurements were performed by exciting the carriers with 193 nm ArF excimer lasers with at 5 K. Photocurrent analyses were performed in an Ohmic-Ohmic configuration on SiN_x passivated samples. A thin passivation layer of SiNx (~10 nm) was deposited on top of the hetrostructure to optimize the device performance. Ti/Al/Ni/Au metal stacks were fabricated to optimize Ohmic contacts and checked by I-V and Hall measurements. Photocurrent measurements were performed at +1.5 V bias using a QTH lamp and a chopper frequency at 72 Hz.

In order to shine light on the band structure and thus on the transitions at confined energy levels within the 2DEG channel, 1-D Schrodinger-Pöisson equation has been solved to calculate the energy levels within triangular 2DEG well using nextnano software [4]. The ideal HS has been simulated, with the nominal value of In%, the results are shown in fig. 5.32 for 5 and 300 K, i.e. the temperature of emission and absorption spectroscopy experiments, respectively. The energy gap and band offset values for GaN, AlN, InAlN are extracted by [5] considering unstrained structures. The first and second confined energy levels (E_1 and E_2) values are 3.7 eV and 3.8 eV, respectively. It must be noted that E_1 is located below the Fermi level, while E_2 is above, they do not change substantially with temperature between 5 and 300K.

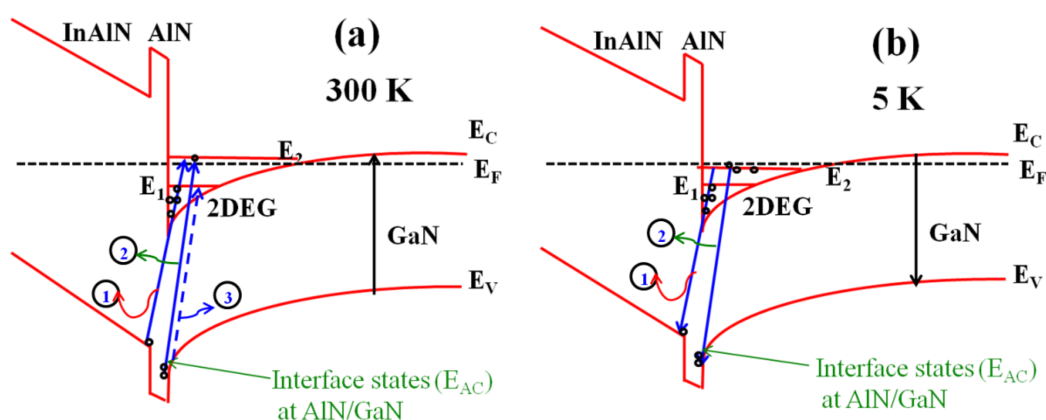

Figure 5.32 Schematic of the band structure for InAlN/AlN/GaN heterostructures calculated at 300 K (for SPV) and 5 K (for PL) from Schrodinger-Pöisson equation to show the possible photoexcited electronic transitions (marked as 1, 2, 3)

SPV spectra performed on AlInN/AlN/GaN heterostructures are shown in fig. 5.33. The peaks observed at 3.44 and 3.48 eV could be related to band-to-band transitions in the GaN layer, in very good agreement with similar values reported with previous study discussed above and also with the literature [61, 62]. The very low values of SPV signal must be noted (of the order of μV), due to the strong recombination of photogenerated electron hole pairs with the 2DEG electrons and the polarization induced charge. Nevertheless, due to the presence of piezoelectric and spontaneous polarization in wurzite nitride structures, a strong built-in electric field is induced in the region close to interface of AlN/GaN. Such an induced electric field, of the order of MV/cm as previously calculated on similar structures [2], allows for the charge collection of the e-h pairs. The observed band tails below the GaN bandgap can be related to Franz-Keldysh effect in nitrides [63]. The present analysis shows GaN band gap values not shifted with respect to the usual one, on the contrary to what has been above discussed [20], possibly due to the lower 2DEG concentration in those samples.

The SPV spectra in fig. 5.33 show different SPV signal values for samples 1, 2, 3, which can be related to differences in the 2DEG density, i.e. electric field, and surface states; we can also observe a change in slope for energies above the GaN band edge (marked by different line colours for different samples) from 3.56 eV, 3.64 eV and 3.64 eV for samples 1, 2, 3 respectively, as

reported in table II. These features could be related to transitions from valence band of GaN bulk to discrete energy levels in the 2DEG channel layer. These transitions might be attributed to electrons from the valence band are directly driven to the first or second energy level in the 2DEG well by the high electric field either from the bulk GaN (marked as (marked as 2) in fig. 5.32a) or from the AlInN layer (marked as 1 in fig. 5.32a). The second mechanism must be ruled out as AlInN is almost transparent in this spectral range, while the first mechanism should be examined in more detail: as the Fermi level almost coincides with the second level E_2, the level E_1 has a very high probability to be completely filled by electrons. Electronic transitions from the VB to E_2, which must be partially empty, are thus more probable. The reproducibility of experimental spectra has been checked and confirmed by performing several measurements on each samples. Moreover, in order to improve the SPV signal to noise ratio we tried to decrease the detrimental contribution of the e-h recombination at the 2DEG channel by illuminating the sample from the back side through the substrate for sample 1. The comparison between SPV spectra with front and back illumination (not shown here) shows that the SPV response for back illuminated surface is higher (almost 3 times) than front illumination case. Surface photovoltage spectroscopy allows also for the determination of the conductivity type of the structure. Fig. 5.34 shows the imaginary part (SPV_y) of the complex SPV signal and the phase spectrum for the sample1. The layer conductivity is extracted by the sign of the SPV_y signal close to the band gap value. The negative value of SPV_y indicates the n-type conductivity within the 2DEG channel in the GaN layer.

On the basis of above analyses, we interpret the peak at 3.44-3.48 eV as the band to band transitions in GaN and the features at 3.56, 3.64, 3.64 eV, for samples 1, 2 & 3 respectively, to transitions between the GaN valence band and the second confined energy level (E_2) within the triangular potential well.

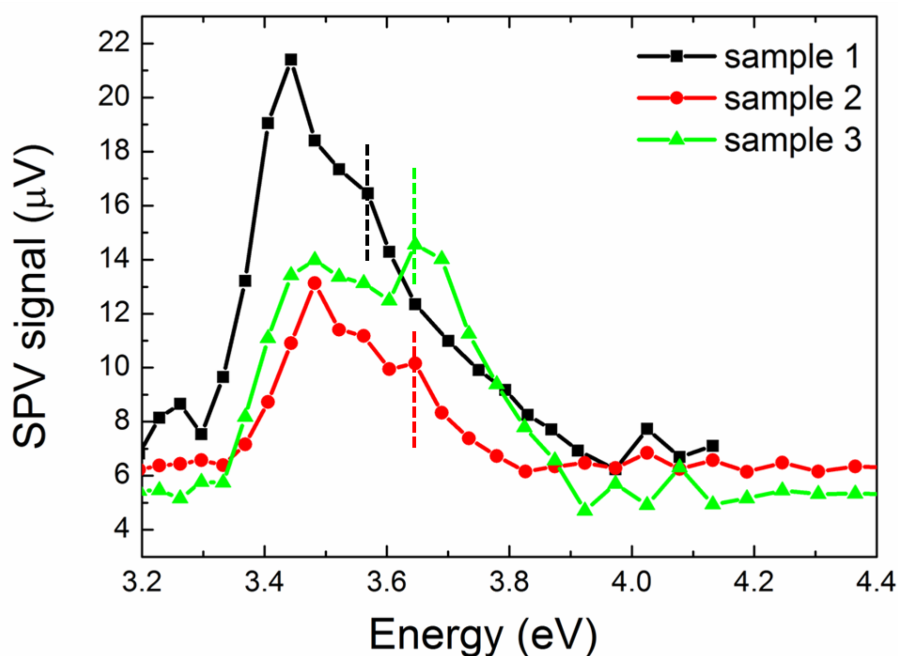

Figure 5.33 Surface Photovoltage signal plotted against photon energy for all samples. The lines are only a guide for the eyes

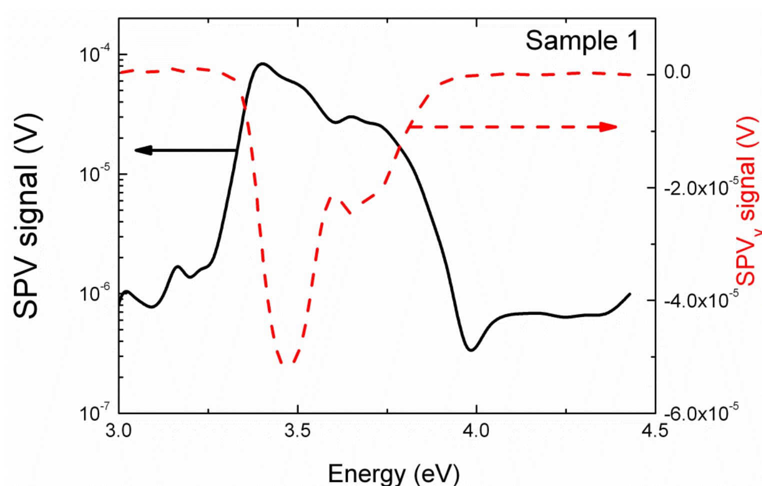

Figure 5.34 Y signal and SPV signal variation measurements for sample 1 which shows n-type of conductivity for 2DEG channel layer in within GaN layer

In addition, frequency dependent Photocurrent measurements have also been performed on the same samples with passivation layer of SiN_x on top of the surface, and a typical result is shown for sample 1 in fig. 5.35. A very intense and broad peak is observed around 3.56 eV for all the three samples examined, a value which is lower than the ones attributed to level E_2. The effect of increase in chopper frequency has been clearly observed which also indicates the fast response of 2DEG carriers. It is interesting to note that PC spectroscopy, which is based on an electron transport mechanism, allows for the detection of states filled by electrons through their photoionization. For this reason the peak observed in PC spectra can be attributed to transitions to E_1, which as demonstrated by 1-D Schrodinger-Pöisson simulations is always populated by electrons. We do not observe any peak or change of slope at the energies corresponding the GaN and InAlN layers energy gap. This indicates that the electrons, photo-generated in the GaN layer are directly collected in 2DEG channel due to the presence of the very high built-in electric field (marked as 2 in fig. 5.32a).

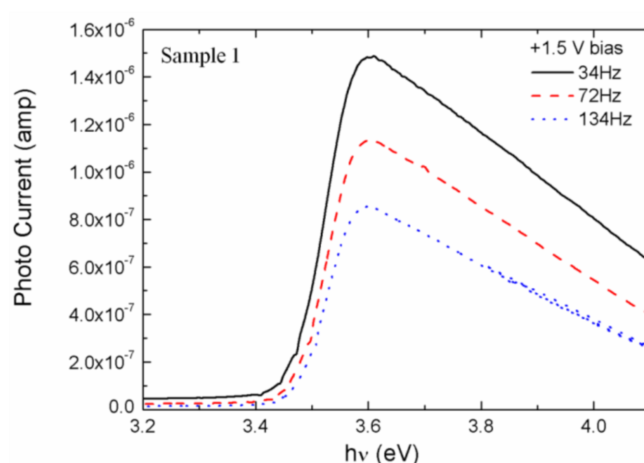

Figure 5.35 Typical measured Photocurrent spectra plotted against photon energy for sample 1, mentioned in table II

PL spectra of all samples measured at 5 K are shown in fig. 5.36a. The circled (dotted) part of the fig. 5.36a which is explained as FES, will be discussed later here. First, we explain the PL

spectra of one sample. The fig. 5.36b shows the PL spectra for sample 1 while the inset shows the known narrow PL line at 3.476 eV, related to band to band recombination at the GaN gap edge [64]. The three different peaks can be observed in the spectra above the GaN energy gap region. Starting from the higher energies a broad and asymmetric band can be noted, marked as 'InAlN related', consisting of two different peaks (marked). The much larger width of the HE band (~100 meV) is typical for ternary materials, where the emission and absorption spectra are inhomogeneously broadened by disorder induced potential fluctuations [65]. The peak at 4.2 eV can be related to a defect state in the InAlN layer, since some recent and our studies [66] on similar InAlN/AlN/GaN structures, revealed the presence of defect related states in the range of 0.37- 0.80 eV below to the conduction band, in good agreement with the present results. The peak at 4.58 eV can be attributed to the band to band emission of the InAlN, also in good agreement with earlier reported results on gap related emission [67] for similar In concentration.

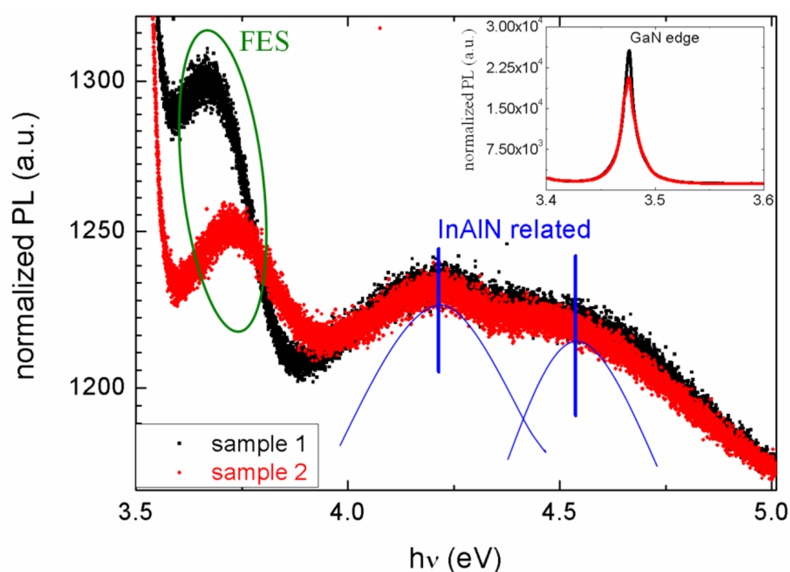

Figure 5.36 normalized PL spectra for all three samples at 5 K showing above GaN energy gap related transitions (a). The normalized PL spectra for sample 1 (b). The inset shows the GaN edge related transition for both samples (b)

Interestingly, we clearly observe a peak in the range of 3.65-3.8 eV in all three samples with a relatively narrow band superimposed on its high energy tail, as shown in fig. 5.36a. Its position is above the GaN edge and below the two peaks at higher energy (related to InAlN layer). This peak disappears at higher temperatures according to similar results obtained in AlGaN/GaN [60]. This peak appears in common for the three samples shown, while its energy increases when the 2DEG density increases. Because of these properties, this peak can be related to Fermi Edge Singularity (FES). Similar features have been previously reported in AlGaN/GaN systems etc. [60, 68] but have never been directly observed in InAlN/AlN/GaN systems up to now in our knowledge.

In order to explain the origin of this optical transition, we may consider the two possibilities shown in fig. 5.31 (b): **1)** the recombination of electrons at GaN 2DEG Fermi level with holes in the InAlN layer; **2)** their recombination with heavy holes localized as interface states at AlN/GaN interface, which could be mainly attributed due to the alloy fluctuation induced holes localization [58]. The first transition can be ruled out, as positively charged donor states have been found near the InAlN valence band edge [69] but in the energy range of 0.7 -1.3 eV, i.e. their energy values are too high to be considered responsible for the transition related to FES. On the contrary, the second transition related to heavy holes at AlN/GaN interface could be considered a possible origin for the

observed FES feature. Interface states play a fundamental role in the origin of the 2DEG, as demonstrated by [67]. Holes localized at such interface states can significantly contribute to the transitions observed by PL and attributed to FES, according to similar phenomena observed by Akopian et. al [60] in AlGaN/GaN systems. This conclusion is also well supported by the 2DEG density variation of the FES related energy level and by the very good agreement between the Fermi Energy value related to the FES feature and the one calculated by Schrödinger-Poisson simulation.

In summary, absorption and emission studies have been performed by Surface Photo Voltage, Photocurrent and photoluminescence spectroscopy on high quality lattice matched InAlN/AlN/GaN heterostructures with different In concentration and 2DEG density. Optically induced electronic transitions have been clearly observed by absorption studies and related to the first and second confined energy levels in the triangular shaped potential well at the interface between GaN and AlN. In particular the first level E_1, which is populated at room temperature, was detected by PC, while the second level E_2 which is not populated, was detected by SPV. The use of these two different spectroscopic methods allowed to directly observing transitions to empty and completely filled energy levels. Emission studies made by PL spectroscopy allowed for the detection of band to band and defect states emission in the AlInN layer, and for the first time in these heterostructures, to the detection of the Fermi Edge Singularity. The measured energy values are in good agreement with the ones obtained by Schrodinger-Pöisson simulations. The slight discrepancies between measured and simulated values can be understood taking into account the possible difference vs the nominal structure, in In% concentration, strain effects and possible Ga incorporation effect both in AlN and AlInN layers [3, 70].

The use of these different, independent and complementary methods has allowed us to obtain a complete and detailed picture of electronic transitions related to the 2DEG and to the subband energy levels, in a material system which is now subject of intense investigation both for fundamental studies as well as for many applications.

5.7.3 Photoresponse analysis of metal-semiconductor-metal (MSM) InAlN/AlN/GaN HEMT structures

We have also performed work on fabrication of metal-semiconductor-metal (MSM) photodetector (PD) fabricated on InAlN/GaN two dimensional electron gas (2DEG) HEMT structures. The electrical and photodetection properties have been compared in two structures with (sample 2) and without (sample 1) an AlN interlayer in between the barrier (InAlN) and the GaN. We obtained gain in both structures for high bias voltages. To analyze the transient behaviour we have measured time dependent evolution of the signal under energy excitation higher than the GaN band absorption and the barrier absorption for both of the samples with higher and lower leakage current. The absorption due to the GaN layer gave faster response than absorption for energy above the barrier band edge. The fabrication and improvement of this kind of device can lead to integration with the already mature HEMT technology.

As discussed above in thesis, with the presence of the 2DEG in the heterostructures, the electric field distribution below the electrodes is modified, in particular the structure results to have a strong vertical field (along the c-growth direction) [71]. When light incides on the surface the photogenerated electrons are driven toward the interface while photogenerated holes are repelled toward the substrate, which reduces the probability of recombination of the carriersleading to an improved detector responsivity with extremely high photocurrent values [72]. In fact it has been observed, since the first study on 2DEG based photoconductors [73] and the first study on nitride-based 2DEG photoconductors [74] that a huge gain is observable in such a system. However, the use of a MSM metallization scheme can highly reduce dark current, improving device characteristics [75].

In this work we studied the photoresponse of InAlN/GaN MSM devices and analysed the difference in device performance with and without the introduction of an AlN spacer in between the barrier and the GaN, which is usually used to enhance the electron mobility in the 2DEG [76] We also studied, by means of electroreflectance (ER), optical absorption of the GaN, the InAlN barrier and the 2DEG interface layer, as it has been recognized to be optically active both in absorption [77] and emission [78].

MSM structure have been processed on two different InAlN/GaN heterostructures (labelled as sample 1 & 2). Interdigitated (IDT) MSM devices have been fabricated by optical lithography patterning and Pt deposition (60 nm), assuring a good Schottky behaviour. The IDT area was 270 µm x 260 µm. The width of the contacts was 7 µm with an interspacing of 6 µm. As far as the characterization of the structure is concerned, we performed electroreflectance measurements (ER) to identify absorption edges detected in photocurrent measurements.

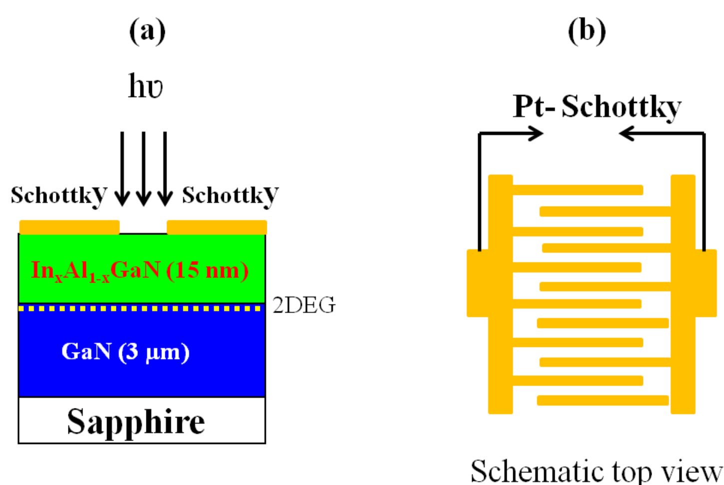

Figure 5.37 Schematic of MSM structure (a) and top view (b)

We have used a Pt-semitransparent-Schottky top contact and ohmic contact (Ti/Al/Ni/Au - 30 nm/200 nm/50 nm/150 nm) connected with the 2DEG after the annealing at 850◦ for 30 seconds. Details of the experimental technique and data analysis of ER can be found elsewhere [79, 80].

MSM photocurrent measurements have been carried out by top illumination of the sample with Xe arc lamp as source and a monochromator to select the light wavelengths (fig. 5.37). We also measure photoresponse of a calibrated commercial silicon photodiode and a thermocouple (depending on the wavelength) to estimate the total power of the incident light and, therefore, knowing the sizes, to extract the responsivity of our MSM PDs.

The electrical characterization of the two samples provide the confirmation of better blocking behavior of the sample with AlN spacer (sample 2). From the current-voltage measurements performed in dark, lower leakage current of sample 2 is revealed as shown in fig. 5.38. This can be explained by the raising of the effective Schottky barrier with the introduction of AlN spacer.

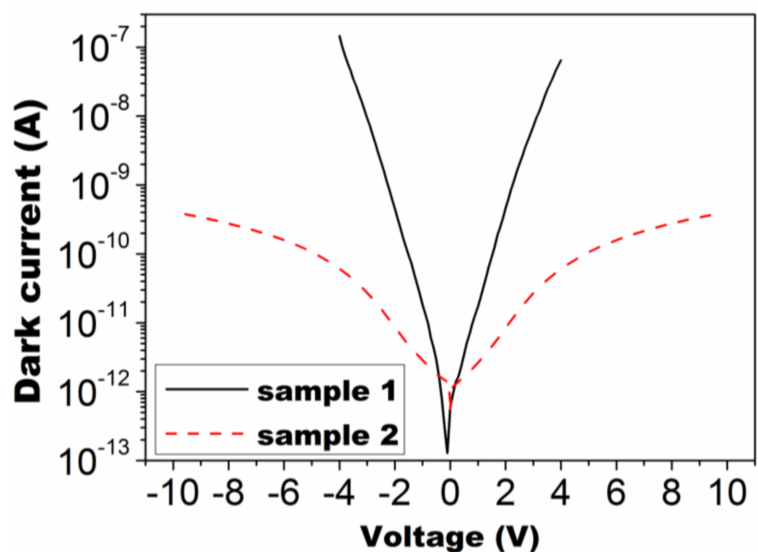

Figure 5.38 Leakage current measured for Pt-MSM on both samples

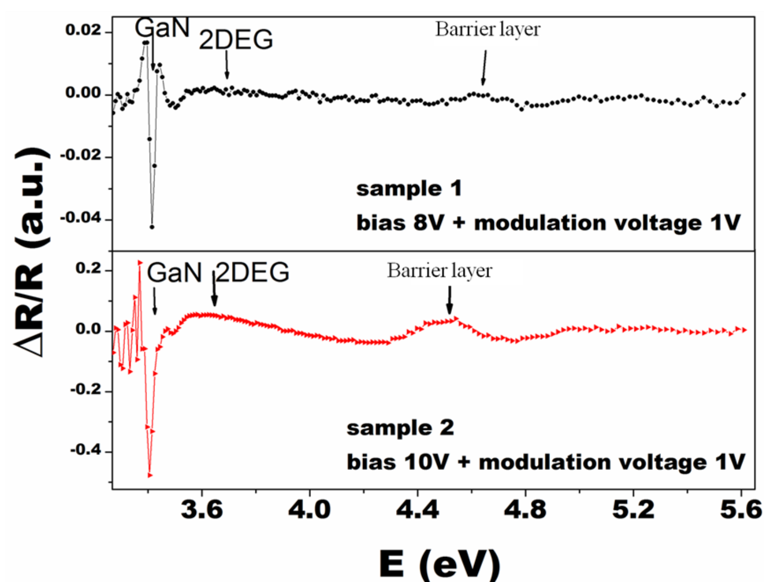

Figure 5.39 ER measurements of the two samples analysed. The measurements were performed with a bias voltage (8 V sample A and 10 V sample B) with a superposition of a modulating voltage of 1 V

ER spectroscopy determines the relative change in reflectivity (DR/R) caused by a change of electric field strength or carrier densities when applying a modulation voltage. Fig. 5.39 shows typical ER spectra of the two samples. The signals arising from the GaN band gap, the 2DEG channel layers, and the quaternary barrier layers are clearly visible. The energy positions for the latter yields band gaps of 4.725 eV and 4.595 eV for the strained barrier layers of sample 1 and 2, respectively. These values are fully consistent with the results of Sakalauskas et al. [81].

Fig. 5.40 shows spectral responses of both fabricated MSM PDs for different biases. It indicates that the responsivities measured from both PDs exhibit sharp cutoffs at the absorption edge. Since energy approximate estimation band gaps of AlInN and GaN are respectively 4.6 eV and 3.4 eV, the cutoff observed at around 3.4 eV was related to the absorption of the GaN layer. The bias increment lead to higher responsivity values due to an increase of electric field strength

and penetration in the structure. In fact, at low bias (1 V) the electric field is unable to penetrate in the GaN structure for screening effect due to the high 2DEG density, and the GaN absorption edge is not detectable. In contrast the InAlN absorption edge is observable, being directly in contact with metallization. Raising the bias has the effect of increasing GaN band edge absorption as well as barrier absorption. Interestingly, sample 1 shows a peak in the photoresponse located at around 3.35 eV, slightly lower than the GaN absorption. These peak, which shifts with the applied voltage, could be ascribed to possible defects or traps at the interface as already been observed by Huang et al.[71] These states, at least in part, are reduced with the introduction of the AlN spacer. In fact sample 2, shows only a small shoulder at energies lower than the GaN band gap, ascribable to the same cause of sample 1.

In both samples, for high voltages we observe the presence of a responsivity higher than the ideal case. In the graphs the dash-dot line is the dependency of the ideal responsivity (for quantum efficiency η equal to 1). Following the formula

$$R = \frac{\eta}{E} \tag{5.18}$$

where E is the incident photon energy, to obtain a responsivity higher than the ideal case we have to assume the presence of gain, and the responsivity becomes:

$$R = \frac{(\eta . G)}{E} \tag{5.19}$$

where G is the Gain. At energy corresponding to the GaN band edge we obtain for sample A biased at 2.5 V a gain of G = 5.5 , while for sample B biased at 15 V we obtain G = 51.

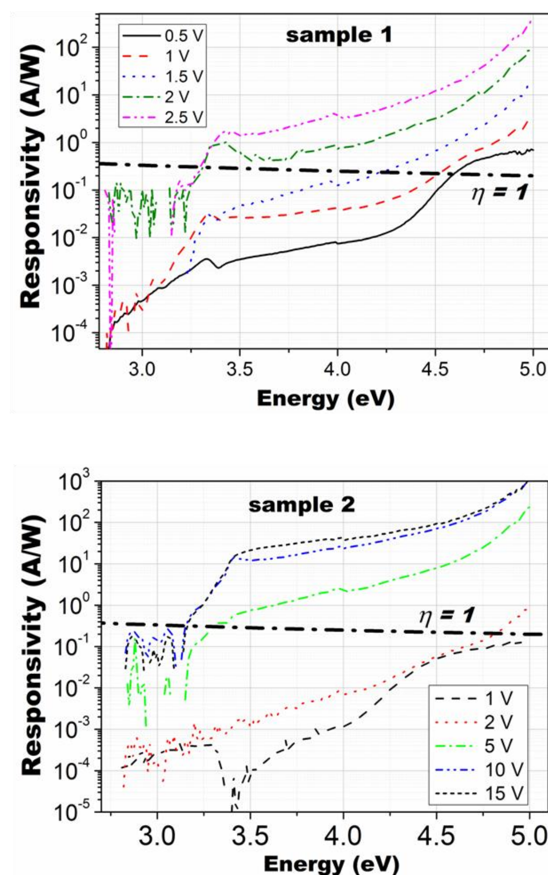

Figure 5.40 Responsivity versus applied voltage for the two samples

In order to better characterize the MSM PDs we studied the time response of sample 2 (with AlN interlayer), which presented lower leakage current and a lower noise. We analysed transient behaviour under light excitation of photon energy above the GaN band edge (but lower than the barrier) and light of photon energies above the InAlN for low bias voltages (1 V) and high bias voltages (2 and 5 V for sample 1&2 respectively), shown in fig. 5.41. For sample 1, low bias is applied due to very high leakage which doesn't allow to measure at higher bias. The photocurrent variation (ΔI_{ph}) transients for switching periods of 60 seconds are analysed.

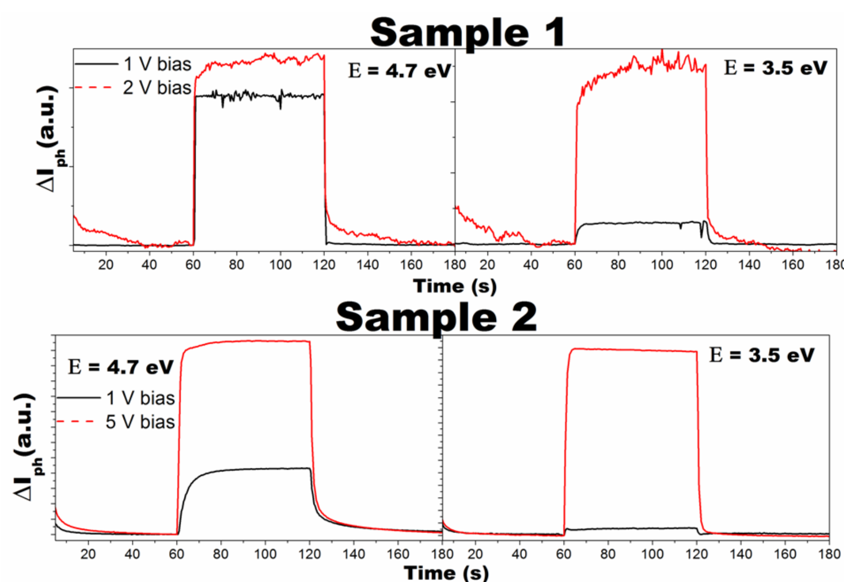

Figure 5.41 Transient behaviour of sample 1&2 analysed for two different excitation energies and two bias voltages. low (1 V) and high (2/5 V)

At low voltage bias (1 V) for photon energies above the GaN but below the InAlN band edge the photoresponse is weak. This can be understood by a short distance of band bending in the channel. However, when the photon energy is increased above the InAlN barrier edge, photogenerated carriers in barrier can contribute to the photoresponse, increasing the signal. At higher bias (2 and 5 V for sample 1 and 2 respectively) the electric field penetrates deeper in the GaN and the contribution to the photoresponse is way higher. Interestingly, the transient is slower when the photon energy is above the InAlN barrier absorption. We speculate that trap states that can originate both at the interface and inside the barrier, collect and reemit carriers delaying the photoresponse. In table III we resume the values obtained for the exponential raising fit of the signals.

Table 5.IV Time constant for the raising of the signal for the two bias voltage used and the two photon excitation energies

Bias (V)	E (eV) = 3.5	E (eV) = 4.7
1	$\tau = 0.24$ s	$\tau = 4.3$ s
2* and 5**	$\tau = 0.81$ s	$\tau = 1.13$ s

*for sample 1
**for sample 2

We have succesfully fabricated and tested high responsivity MSM PDs on 2DEG nitride structures. The structure of the two samples analysed differs only in the presence of a thin AlN spacer between the barrier and the GaN. The insertion of spacer layer results in remarkable reduction in leakage current which allows the higher voltage measurements for sample 2 in comparison to sample 1. We observed that at high voltages both structures showed gain. Transient analysis revealed different behaviours in the photodetection mechanism depending on the energy absorption range. Future work is required to better understand photogeneration and collection of carriers in these kind of structures.

References

1. A. Vilalta-Clemente, M. A. Poisson, H. Behmenburg, C. Giesen, M. Heuken, P. Ruterana, Phys. Status Solidi A 207, 1105–1108 (2010)
2. S. Pandey, B. Fraboni, D. Cavalcoli, A. Minj, A. Cavallini, Appl. Phys. Lett. 99, 012111 (2011)
3. A. Minj, D. Cavalcoli, S. Pandey, B. Fraboni, A. Cavallini, T. Brazzini, F. Calle, Scripta Materialia 66, 327 (2012)
4. www.nextnano.de
5. C. Wood, D. Jena, Polarization Effects in Semiconductors: From Ab InitioTheory to Device Applications, Springer USA (2010)
6. Y. Cao, D. Jena, Appl. Phys. Lett. 90, 182112 (2007)
7. J. Carrano, T. Li, P. Gudrowski, C. Eiting, R. Dupuis, J. Campbell, J. of Appl. Phys.83, 6148 (1998)
8. M. Gonschorek, J. F. Carlin, E. Feltin, M. A. Py, N. Grandjean, V. Darakchieva, Monemar, M. Lorenz, G. Ramm, J. of Appl. Phys. 103, 093714 (2008)
9. O. Ambacher, J. Majewski, C. Miskys, A. Link, M. Hermann, M. Eickhoff, M. Stutzmann, F. Bernardini, V. Fiorentini, V. Tilak, B. Schaff, L. F. Eastman, J. Phys.: Condens. Matter 14**,** 3399 (2002)
10. A Teke, S. Gökden, R. Tülek1, J. H. Leach, Q. Fan, J Xie, Ü. Özgür, H. Morkoç, S Lisesivdin, E. Özbay, New J. Phys**.** 11, 063031 (2009)
11. Jinqiao Xie, Xianfeng Ni, Mo Wu, Jacob H. Leach, Ümit Özgür, Hadis Morkoç, Appl. Phys. Lett. 91, 132116 (2007)
12. L. Gordon, M. S. Miao, S. Chowdhury, M. Higashiwaki, U. K. Mishra, C. G. Van de Walle, J. Phys. D: Appl. Phys. 43**,** 505501 (2010)
13. J. P. Ibbetson, P. T. Fini, K. D. Ness, S. P. DenBaars, J. S. Speck, U. K. Mishra, Appl. Phys. Lett. 77, 250 (2005)
14. A. Minj, D. Cavalcoli, A. Cavallini, Appl. Phys. Lett. 97, 132114 (2010)
15. J. Frenkel, Tech. Phys. USSR 5, 685 (1938l); Phys. Rev. 54, 647 (1938)
16. E. Arslan, S. Bütün, E. Ozbay, Appl. Phys. Lett. 94, 142106 (2009)
17. S. Pandey, D. Cavalcoli, B. Fraboni, , A. Cavallini, T. Brazzini. F. Calle, Appl. Phys. Lett. 100, 152116 (2012)
18. S. M. Sze, "*Physics of Semiconductor Devices"* (New York: Wiley), (1981)
19. D. Cavalcoli, S. Pandey, B. Fraboni. A. Cavallini, Appl. Phys. Lett. 98, 142111 (2011)
20. S. B. Lisesivdin, A. Yildiz, S. Acar, M. Kasap, S. Ozcelik, E. Ozbay, Appl. Phys. Lett. 91, 102113 (2007)
21. G. Koley, M. G. Spencer, Appl. Phys. Lett. 86, 042107 (2005).
22. M. S. Miao, A. Janotti, C. G. Van de Walle, Phys. Rev. B 80, 155319 (2009)
23. Z. T. Chen, K. Fujita, J. Ichikawa, T. Egawa, IEEE Dev. Lett. 32, 0741 (2011)

24. P. Y. Song, R. L. Van Meirhaeghe, W. H. Lafler, F. Cardon Solid-State Electron. 29, 633(1986)
25. J. H. Werner, H. H. Guttler J. Appl. Phys. 69, 1522 (1991)
26. J. P. Sullivan, R. T. Tung, M. R. Pinto, W. R. Graham, J. Appl. Phys. 70, 7403 (1991)
27. R. F. Schmitsdorf, T. U. Kampen, W. Monch Surf. Sci. 324, 249 (1995)
28. M J. Mamor. Phys. Condens. Matter 21, 335802 (2009)
29. D. C. Look, J. R. Sizelove, Phys. Rev. Lett, 82, 1237 (1999)
30. Z. L. Miao, T. J. Yu, F. J. Xu, J. Song, C. C. Huang, X. Q. Wang, Z. J. Yang, G. Y. Zhang, X. P. Zhang, D. P. Yu, B.Shen, Appl Phys Lett, 95, 231909 (2009)
31. A. Mouti, J. L. Rouviere, M. Cantoni, J. F. Carlin, E. Feltin, N. Grandjean, P. Stadelmann Phys Rev B, 83, 195309 (2011)
32. J. Antoszewski, M. Gracey, J. M. Dell, L. Faraone, T. A. Fisher, J. Appl Phys, 87, 3900 (2000)
33. B. Liu, Y W Lu, G R Jin, Y Zhao, X L Wang, Q S Zhu, Z G Wang. Appl. Phys. Lett. ; 97, 262111 (2010)
34. Y. Cao, D. Jena, Appl. Phys. Lett., 97, 222116 (2010)
35. H. Tang, J. B. Webb, P. Coleridge, J. A. Bardwell, C. H. Ko, Y. K. Su, S J. Chang, Phys Rev B, 66, 245305 (2002)
36. D. K. Ferry, Goodnick S M, Bird J. Transport in Nanostructures, 2nd ed. Cambridge: Cambridge University Press; 2009)
37. N. Kumar et al., unpublished
38. D. Jena, A. C. Gossard, U. K. Mishra, Appl. Phys. Lett.,76, 1707 (2000)
39. L. F. Jiang, W. Z. Shen, Q. X. Guo, Journal of Appl. Phys. 106, 0315 (2009)
40. J. H. Davies, “ The physics of low dimensional semiconductors- an introduction” Cambridge Univ. Press Publication (1998)
41. E. Burstein, Phys. Rev. 93, 632 (1954)
42. C Persson, Bo E Sernelius, A Ferreira da Silva, R Ahuja, B Johansson, J. Phys.: Condens. Matter 13 891(2001)
43. S. Shokhovets, O. Ambacher, G. Gobsch, Phys. Rev. B 76, 125203 (2007)
44. S. Shokhovets, O. Ambacher, B. K. Meyer, G. Gobsch, Phys. Rev. B 78, 035207 (2008)
45. Vurgaftman and J. R. Meyer, J. Appl. Phys, 54, 3675 (2003)
46. A. Walsh, Juarez L. F. Da Silva, Su-Huai Wei, Phys. Rev. B 78, 075211 (2008)
47. C. Bulutay, C. M. Turgut, N. A. Zakhleniuk, Phys. Rev. B 81, 155206 (2010)
48. M. Yoshikawa, M. Kunzer, J. Wagner, H. Obloh, P. Schlotter, R. Schmidt, N. Herres, U. Kaufmann, J. Appl. Phys, 86, 4400 (1999)
49. V. Fiorentini F Bernardini, F della Sala, A Di Carlo and P Lugli, Phys Rev B 60 (12) 8849 (1999)
50. J. Bhattacharyya, S. Ghosh, H. T. Grahn Appl. Phys. Lett. 93, 051913 (2008)
51. B. K. Li, M. J. Wang, K. J. Chen, J. N. Wang, Appl. Phys. Lett. 95, 232111 (2009)
52. H. Cheng, Ç. Kurdak, J. H. Leach, M. Wu, H. Morkoç, Appl. Phys. Lett. 97, 112113 (2010)
53. M. Motyka, R. Kudrawiec, G. Cywiński, M. Siekacz, C. Skierbiszewski, J. Misiewicz Appl. Phys. Lett. 89, 251908 (2006)
54. M. Gonschorek, D. Simeonov, J.-F. Carlin, E. Feltin, M. A. Py and N. Grandjean, The European Physical Journal Applied Physics, 47 , 30301 (2009).
55. Z. T. Chen, Y. Sakai, and T. Egawa Appl. Phys. Lett. 96, 191911 (2010)
56. P. Hawrylak, Phys. Rev. B 44, 6242 (1991)
57. D. Mahan, Many- Particle Physics (Plenum, New York, 1981)
58. M. S. Skolnick, J. M. Rorison, K. J. Nash, D. J. Mowbray, P. R. Tapster, S. J. Bass, and A. D. Pitt Phys. Rev. Lett. 58, 2130 (1987)
59. E. S. Snow, O. J. Glembocki, and B. V. Shanabrook, Phys. Rev. B 38, 12483 (1988)
60. N. Akopian, A. Vardi, G. Bahir, V. Garber, E. Ehrenfreund, D. Gershoni, C. Poblenz

C. R. Elsass, I. P. Smorchkova, J. S. Speck, Appl. Phys. Lett. 94, 223502 (2009)
61. F. Binet, J. Y. Duboz, E. Rosencher, F. Schoiz, V. Harle, Appl. Phys. Lett. 69, 1202 (1996)
62. J. F. Muth, J. H. Lee, I. K. Shmagin, R. M. Kolbas, H. C. Casely Jr., B. P. Keller, U. K. Mishra, S. P. DenBaars, Appl. Phys. Lett. 71, 2572 (1997)
63. A. Cavallini, L. Polenta, M. Rossi, T. Stoica, R. Calarco, R. J. Meijers, T. Richter, H. Lüth, Nano Lett. 7, 2166 (2007)
64. J. Bergman, T. Lundstrom, B. Monemar, H. Amano, I. Akasaki, Appl. Phys. Lett. 69, 3456 (1996)
65. D. Gershoni, E. Cohen, A. Ron, Phys. Rev. Lett. 56, 2211 (1986)
66. W. Chikhaoui, J.-M. Bluet, M.-A. Poisson, N. Sarazin, C. Dua, C. Bru-Chevallier, Appl. Phys. Lett. 96, 072107 (2010)
67. E. Iliopoulos, A. Adikimenakis, C. Giesen, M. Heuken, A. Georgakilas, Appl. Phys. Lett. 92, 191907 (2008)
68. P. Zhang, D.-Z. Sun, X.-L. Wang, M.-Y. Kong, Y.-P. Zeng, J.-M. Li, L.-Y. Lin, Appl. Phys. Lett. 73, 2471 (1998)
69. M. Tapajna, K Cico, J. Kuzmik, D. Pogany, G. Pozzovivo, G. Strasser, J. F. Carlin, N. Grandjean and K Fröhlich, Semicond. Sci. Technol. 24, 035008 (2009)
70. H. Leach, X. Ni, X. Li, M. Wu, Ü. Özgür, H. Morkoç, L. Zhou, D. A. Cullen, D. J. Smith, H. Cheng, Ç. Kurdak, J. R. Meyer, I. Vurgaftman, J. App. Phys. 107, 083706 (2010)
71. Y. Huang, D. J. Chen, H. Lu, R. Zhang, Y. D. Zheng, L. Li, X. Dong, Z. H. Li, C. Chen, and T. S. Chen: IEEE Electron Dev. Lett. 32**,** 1071 (2011)
72. T.- M. Kuan, S.- J. Chang, Y.-K. Su, C.-H. Ko, J. B. Webb, J. A. Bardwell, Y. Liu, H. Tang, W.-J. Lin, Y.-T. Cherng, W.-H. Lan: Jpn. J. Appl. Phys. 42, 5563 (2003)
73. S. Subramanian, D. Schulte, L. Ungier, P. Zhao, T. K. Plant, J. R. Arthur: IEEE Electron Dev. Lett. 16, 20 (1995)
74. M. A. Khan, M. S. Shur, Q. Chen, J. N. Kuznia and C. J. Sun : Electron. Lett. 31, 398 (1995)
75. H. Jiang,T. Egawa, H. Ishikawa, C. Shao and T. Jimbo: Jpn. J. Appl. Phys. 43, L683 (2004)
76. R. T¨ulek, A. Ilgaz, S. G¨okden, A. Teke, M. K. ¨ Ozt¨urk, M. Kasap, S. ¨Oz¸celik, E. Arslan, and E. ¨Ozbay: J. Appl. Phys. 105, 013707 (2009)
77. Y. Huang, D. J. Chen, H. Lu, H. B. Shi, P. Han, R. Zhang, Y. D. Zheng: Appl. Phys. Lett. 96, 243503 (2010)
78. M. F. Romero, M. Feneberg, P. Moser, C. Berger, J. Bla¨sing, A. Dadgar, A. Krost, E. Sakalauskas, and R. Goldhahn: Appl. Phys. Lett. 100**,** 212101 (2012)
79. R. Goldhahn, A. T. Winzer, A. Dadgar, A. Krost, O. Weidemann, M. Eickhoff: Phys. Status Solidi A 204, 447 (2007)
80. A. T. Winzer, G. Gobsch, R. Goldhahn, D. Fuhrmann, A. Hangleiter, A. Dadgar, A. Krost: Phys. Rev. B 74, 125207 (2006)
81. E. Sakalauskas, B. Reuters, L. Rahimzadeh Khoshroo, H. Kalisch, M. Heuken, A. Vescan, M. Röppischer, C. Cobet, G. Gobsch, R. Goldhahn, J. Appl. Phys. 110, 013102 (2011)

Chapter 6

Characterization of InGaN/GaN heterostructures

In this chapter I report as InGaN/GaN based heterostructures have been characterized with electrical and optical methods. InGaN based structures sre considered very important semiconductors as they offer possibility to achieve most efficient solar cell devices, various color Light emitting diodes (LEDs) and lasers ranging from red, green, blue and white colors. Moreover, understanding of the electrical properties such as optimization of good quality metal contacts for fabrication of devices, understanding of defects with properties and performance, variation of energy gap and bowing are still under debate and need to be investigated in details. Apart from above issues which have been covered in this chapter, InGaN based photodetector structures have been also studied and discussed. The optical spectroscopy methods like Surface Photovoltage, Photocurrent and Photoluminescence have been used to investigate the optical properties, and also to correlate the defect related transitions/emission with DLTS results.

6.1 Sample and growth details

InGaN/GaN heterostructures were grown in an AIXTRON metal organic chemical vapour deposition (MOCVD) reactor on c-plane sapphire substrates. $In_xGa_{1-x}N$ layer was around 45 nm thick, while the 3-μm thick GaN layer has been grown on sapphire [1]. For electrical measurement like I-V, C-V, DLTS one sample has been measured with %In ~ 19. For Photocurrent on MSM photodetector structure one sample has been measured with %In ~ 11.5, while for energy gap variation and calculation of bowing parameter calculation, Surface Photovoltage analysis has been performed on samples with varying In concentration in un-doped and n-type doped (Si), $In_xGa_{1-x}N$ (%x = 11 to 22) layer while the thickness was kept constant. Si doping was introduced through SiH_4 during growth of InGaN layer [1, 2]. Electrical measurements were performed on semitransparent ‘Pt (40 nm)’ Schottky contacts, (dots of 1 mm diameter) and ‘soldered In’ Ohmic contacts (dots of 2 mm diameter), as shown in Fig. 6.1 as schematic. The Schottky contact was prepared by ‘Pt’ evaporation by thermal evaporation technique and Ohmic contact was prepared by soldering of ‘In’ wire directly on surface of sample.

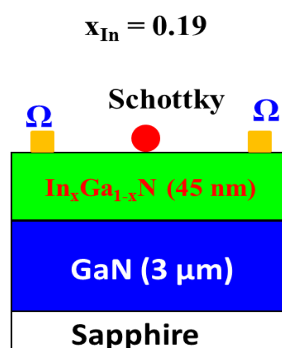

Figure 6.1 Schematic of InGaN/GaN heterostructure for electrical measurements, Ohmic contacts are shown as Ω, (squares in orange color) and Schottky dot of Pt (circle in red color)

6.2 Band diagram Simulation of $In_{0.19}Ga0_{.81}N/GaN$

Conduction band profile has been simulated by using Schrodinger-Poisson solver [3] and nextnano software [4] with parameters taken from ref. 5 which is also discussed in chapter 2. The simulated band diagram is shown in fig. 6.2 which shows the conduction and valence band profile for InGaN/GaN structure, which shows the formation of hole accumulation at interface. It can be observed that polarization induced band bending affects the structure and hole well is formed at interface. The Fermi level is shown as dashed line and marked as E_F in fig. 6.2. It is to InGaN layer is assumed to be ‘ in compressive strained’ condition which is explained in chapter 2 in terms of strained and relaxed nature and influence on electrical and other properties. The valence band edge at the interface crosses the Fermi level under zero bias and hence, the hole confinement can be realized close to the interface. On the basis of the calculation results of the band diagrams, we believe that the accumulation of holes at the InGaN/GaN interface which is induced by the strong polarization effects. For the InGaN/GaN heterostructures, the InGaN layer is grown on the top of the thick relaxed GaN layer and is under compressive strain due to the lattice mismatch between InGaN and GaN. In the cases of compressive strain and In polarity in InGaN, the piezoelectric and spontaneous polarizations are antiparallel. The piezoelectric polarization causes the negative bound sheet charges at the InGaN/GaN interface, whereas the bound charge located at the interface is not significantly affected by spontaneous polarization [5] Therefore, holes will tend to compensate the negative bound sheet charges, leading to the accumulation of holes in the hole well at the interface under certain condition.

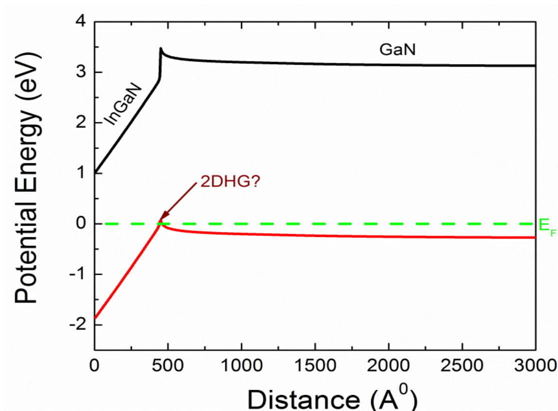

Figure 6.2 Simulated band diagram for InGaN/GaN structure showing the hole accumulation (2DHG) at interface

6.3 Electrical characterization of deep levels in $In_{0.19}Ga0_{.81}N$/GaN structure

In this section, electrical properties of the InGaN/GaN heterostructure have been investigated with I-V, C-V and DLTS measurements for analysis of deep levels. I-V and C-V masurements have been done at 300 K before performing the DLTS measurements to optimize the bias conditions. Fig. 3a shows the I-V results at 300 K which shows high leakage at low bias, possibly due to high number of dislocation, similar problems in InAlN/GaN based heterostructure and GaN based devices, also discussed in earlier chapters. As it can be observed that with increase in bias, leakage increases and tends towards saturation at higher bias (> 5V) so during DLTS measurements, it will be better to perform the measurements below this range of bias in order to achieve a good spectra. However, barrier height and ideality factor calculations have also been done by considering the Thermionic emission mechanism and the obtained values are found ~ 0.83 eV and 2.8 respectively.

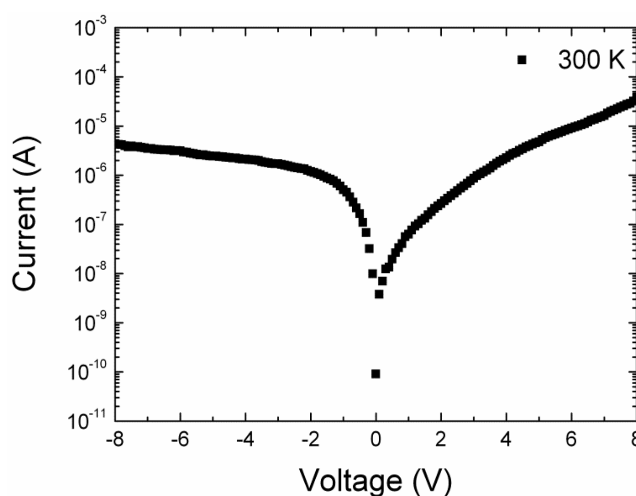

Figure 6.3a Current-voltage spectra for Pt-(InGaN/GaN) at 300 K

The CV- measurements has been also performed at 1 MHz frequency for DLTS use at 300 K. The measured C-V spectra is shown in Fig. 6.3b which shows the depletion starts at low bias and depletes the barrier and GaN layer at 10 V.

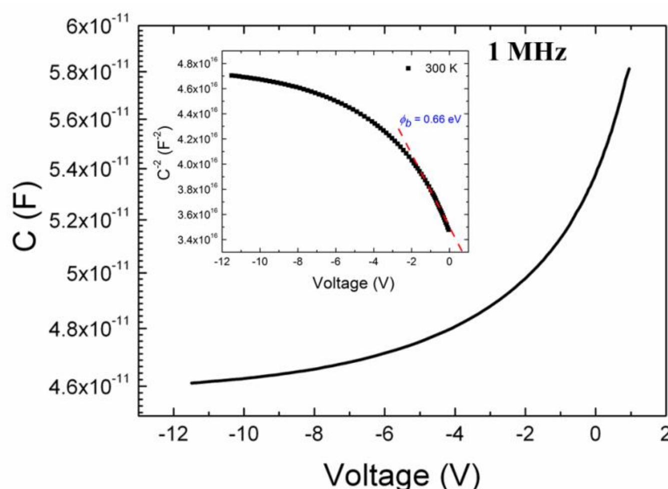

Figure 6.3b Capacitance-voltage spectra for Pt-(InGaN/GaN) at 300 K. The inset shows the calculation for barrier height from C^{-2} *vs* V plot

The barrier height value is also calculated by plotting C^{-2} *vs* V plot which gives the built in potential value ~ 0.66 eV which has been compared with value calculated from I-V measurements, shows good agreement with each other. Moreover, carrier concentration values have been also calculated by C-V plot, which is shown as Fig. 6.4. It is interesting to observe the low value of the carriers in InGaN layer with a value of $N_d \sim 5 \times 10^{15}$ cm^{-3} which shows it's semi-insulating behavior as it's not doped structure. The carrier concentration value is found to be $N_d \sim 2 \times 10^{17}$ cm^{-3} which is in good agreement with value, provided by growers.

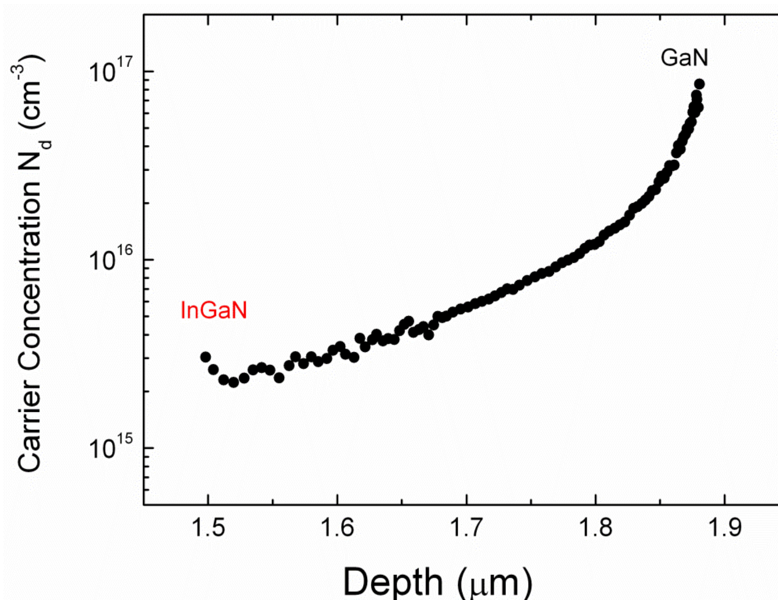

Figure 6.4 Calculated carrier concentration profiling of InGaN/GaN structure at 300 K

Thus, the DLTS measurements have been planned by considering the I-V and C-V spectra and analysis for detection of deep levels in InGaN layer. The Capacitance mode DLTS has been applied on these samples which have also high leakage due to presence of still high dislocation (as shown in fig. 6. 3a). In order to achieve reliable information from measurements, a low bias was applied with a filling pulse after confronting the leakage and CV plot.
Here is the details on applied bias and pulse [$V_{rev.}$, V_{pulse}]:

- [-2 V, +0 V] for probing barrier layer of InAlN
- Constant filling pulse of 1 ms

Fig. 6.5 shows the normalized DLTS spectra (ΔC/C) where, ΔC is the change in capacitance with temperature with applied bias and pulse at [-2 V, 0 V] which shows two sharp negative peak appearance at 118 K and 165 K for 256.4 s^{-1} emission rate respectively, and for other rate windows with increase in temperature which is marked as T1 and T2. However, the positive peaks (T3) observed at high temperature are also considered for calculations which is discussed later in this section. For T1 and T2, as the C-DLTS spectrum is negative (decrease of gate capacitance during the transient) we are in presence of a majority carrier trap. The appearance these peaks could be related to dislocation type of traps in this kind of heterostructure as also mentioned for case of HEMT devices, responsible for higher leakage. The measurements have been performed with different emission rates (not shown) in order to confirm the peak appearance and also for

preparation of Arrhenius plot for calculation of it's energy position. The appearance of these sharp peaks were further checked by giving different bias and pulse with [-3 V, +0 V].

For the case of positive peak appearance, we explained it on the basis of the band diagram shown in fig. 6.2, which shows the hole accumulation at interface (InGaN/GaN) at zero bias. This positive peak appearance can be attributed to these holes accumulated at interface, so the band structure was also simulated at -2 V and shown as fig. 6.6. In order to explain the accumulation process of minority carriers, some deep level acceptors located between the midgap band and the valence band are considered.

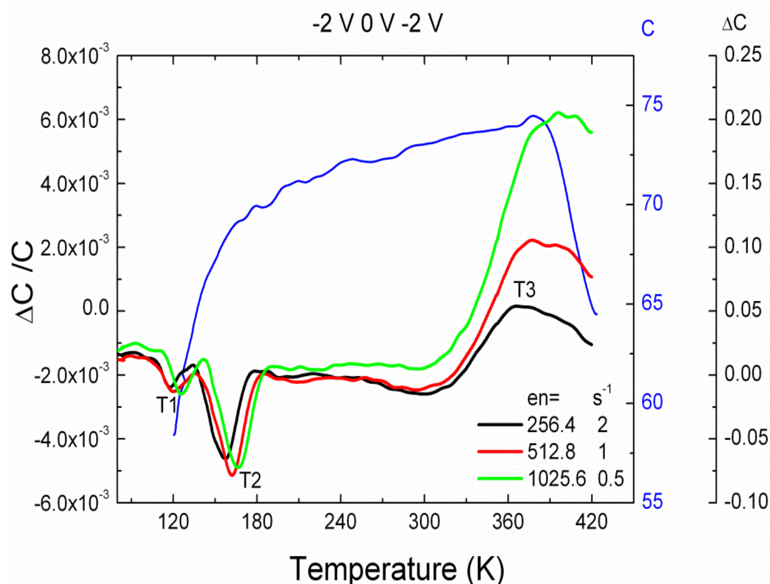

Figure 6.5 C-DLTS spectra for InGaN/GaN structure for constant filling pulse duration

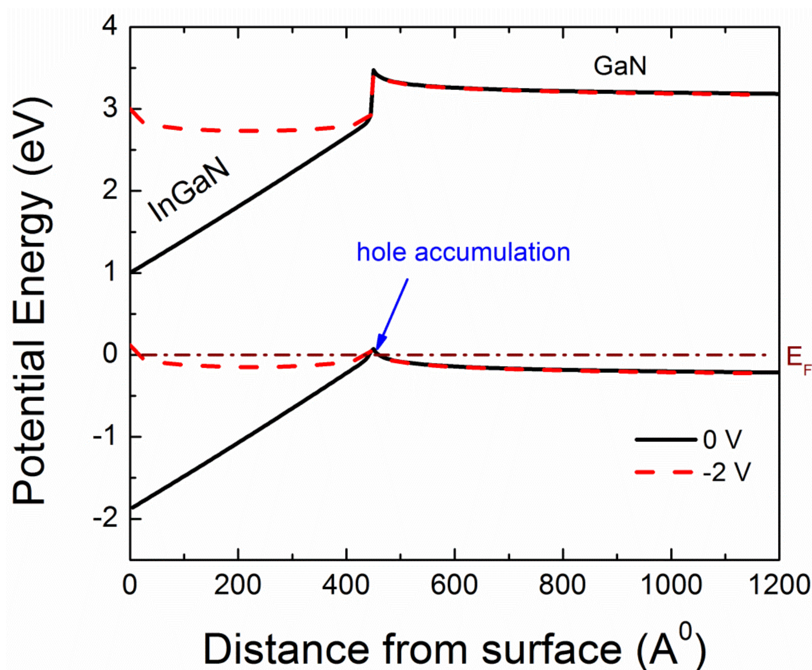

Figure 6.6 Simulated band diagram for InGaN/GaN at 0 and 2 V (in reverse bias)

It may be assumed that exist some such neutral acceptors in the InGaN layer which can trap electrons (majority carriers) and meanwhile bind valence holes under zero bias [6]. On increasing reverse bias, when the acceptor level crosses gradually over the Fermi level (E_F), those trapped electrons are emitted into the conduction band, leaving holes in the valence band and appearing as positive peak in DLTS spectra. One more interesting thing which can be noted is the dramatic change in Capacitance (shown in blue in fig. 6.5) trend which starts decreasing once the positive peaks starts appearing in DLTS spectra. These free holes are driven to the hole well at the heterointerface by the strong polarization electric field. Thus, the inversion behavior occurs when the negative bias reaches a certain value. However, when the hole of the level E_A in the InGaN layer crosses over the Fermi level, the generation of free holes decreases significantly and the strong inversion is prohibited. Therefore, the capacitance begins to decrease again with further depletion of the majority carriers when the negative bias continues to increase.

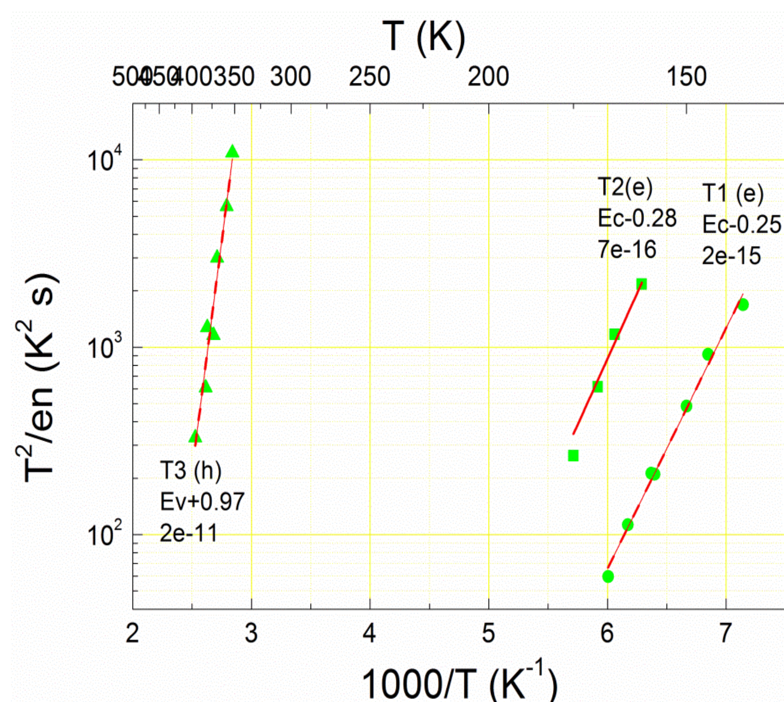

Figure 6.7 Arrhenius Plot reporting the signatures of the deep levels (majority carriers) and minority carriers detected in InGaN/GaN structure

In order to calculate the energy position and capture cross section of these traps, Arrhenius plot was prepared which is shown as fig. 6.7. Thus, from Arrhenius plot, the energy levels have been calculated for observed traps at, **T1: Ec-0.25 eV** with capture cross section of 2 e-15 cm^2 and **T2: at Ec-0.28 eV** with a capture cross section of 7 e-16 cm^2. The possible minority carrier related trap is found with Ev+0.97 eV with capture cross section 2 e-11cm^2. However the majority carrier related traps are found to be very close to each other in energy values and also in their capture cross section values. The summary is prepared for the identified traps by DLTS analysis and shown in table I.

Table 6.I Summary of deep levels in $In_{0.19}Ga_{0.81}N$ layer detected by DLTS

Deep Levels	Energy position (eV)	Capture cross section, $\sigma_{capture}$ (cm^2)
T1(e)	E_c-0.25	2.0 x 10^{-15}
T2 (e)	E_c-0.28	7.8 x 10^{-16}
T3 (h)	E_{v+}0.97	2.0 x 10^{-11}

6.4 Surface Photovoltage Spectroscopy on undoped and doped $In_xGa_{1-x}N$/GaN heterostructure with varying Indium content

Recent progress in epitaxial growth techniques has led to the availability of high quality growth of InN and InGaN layers for high efficient solar energy and optical device applications [7]. InGaN alloys are preferred semiconductors for blue lasers and light-emitting diodes [8, 9, 10]. This alloy system is particularly interesting as its band gap is tunable, i.e. energy gap can be varied in a wide spectral range and the emission and absorption wavelengths strongly depend on the composition. The InGaN alloy system has been studied extensively in recent years, nevertheless, some fundamental issues such for example surface properties, compositional variation of the band gap and doping related effects are still far to be completely understood. The tunability of the band gap as a function of the In concentration is also still debated. A number of experimental [11] and theoretical studies [12] on variation of InGaN band gap with Indium content, does not allow jet to reach an agreement on this subject. The InGaN band gap varies nonlinearly as a function of In content as follows:

$$E_g(In_xGa_{1-x}N) = (1-x)E_g^{GaN} + xE_g^{InN} - bx(1-x) \qquad (6.1)$$

where, b is the bowing parameter. Up to now no agreement has been reached on the bowing value and even on the issue if a single bowing parameter can describe the gap over its entire composition range [13, 14].

The present contribution aims at the characterization of $In_xGa_{1-x}N$/GaN structures with varying In concentration by Surface Photovoltage Spectroscopy (SPS). SPS allowed for the detection of band to band and intra band transitions in the $In_xGa_{1-x}N$/GaN structures, thus the variation of the energy gap as a function of the In content was obtained, as well as the bowing parameter. Moreover Si doped $In_xGa_{1-x}N$/GaN structures were studied, band to band and intra band electronic transitions were related the Si doping density, evaluated by Electrochemical Capacitance-Voltage (ECV). The Si donor energy level is identified for different %Indium containing InGaN layers. The InGaN/GaN band structures has been simulated by 1-D Schrodinger-Poisson equation to show the effect of doping on band structure [3, 4].

Undoped InGaN layer structures (x ranging from 0.11 to 0.22) and doped samples with nominal x = 14% (sample 1), 19% (sample 2) and 22% (sample 3) were examined. The Si doping concentration was of 7 x 10^{18} cm^{-3}, 1 x 10^{19} cm^{-3} and 3 x 10^{19} cm^{-3} respectively. The indium content in barrier layer was obtained by XRD measurements. Doping concentration was measured by Electrochemical Capacitance-Voltage (ECV) measurement. The nominal barrier layer thickness of InGaN was ~ 40- 45 nm for all samples and measured by X-ray Diffracation (XRD) measurements and buffer layer thickness of GaN was 3 μm [1, 2]. The GaN layer has been grown on sapphire.

Surface Photo Voltage Spectroscopy (SPS) analyses have been performed at room temperature by the use of light source (quartz-tungsten-halogen, QTH). The SPV data are also normalized to the photon flux of the QTH lamp.

Figure 6.8a shows some examples of the SPV spectra of InGaN/GaN structures with % In up to 22 % . While the GaN related energy gap does not change for the different samples examined, the InGaN gap changes with the In%. The variation of the InGaN gap as a function of the In content is shown in fig1b. In order to calculate the bowing parameter, the strain effect on the band gap values needs to be considered. Even if the thickness of the investigated structures exceeds the critical thickness [15] our structures could be considered as made by a strained layer close to the interface plus a nearly relaxed structure at the surface, according to ref 16.Thus the strain induced energy gap shift has been calculated from ref.17 and subtracted to the experimentally measured bandgap, the values obtained are plotted as triangles in figure 8b. The Eg variation as a function of In concentration has been also calculated by equation (1) with the band gap of GaN taken as 3.40 eV from SPV spectra in Fig. 6.8a for undoped structures and InN band gap as 0.67 eV [18] for b=2.1 eV as proposed in ref. 19 and for b=1 eV. It can be noted that the Eg values calculated from the experimental data considering the strain induced shift are in good agreement with b=2.1 eV and with ref. 20.

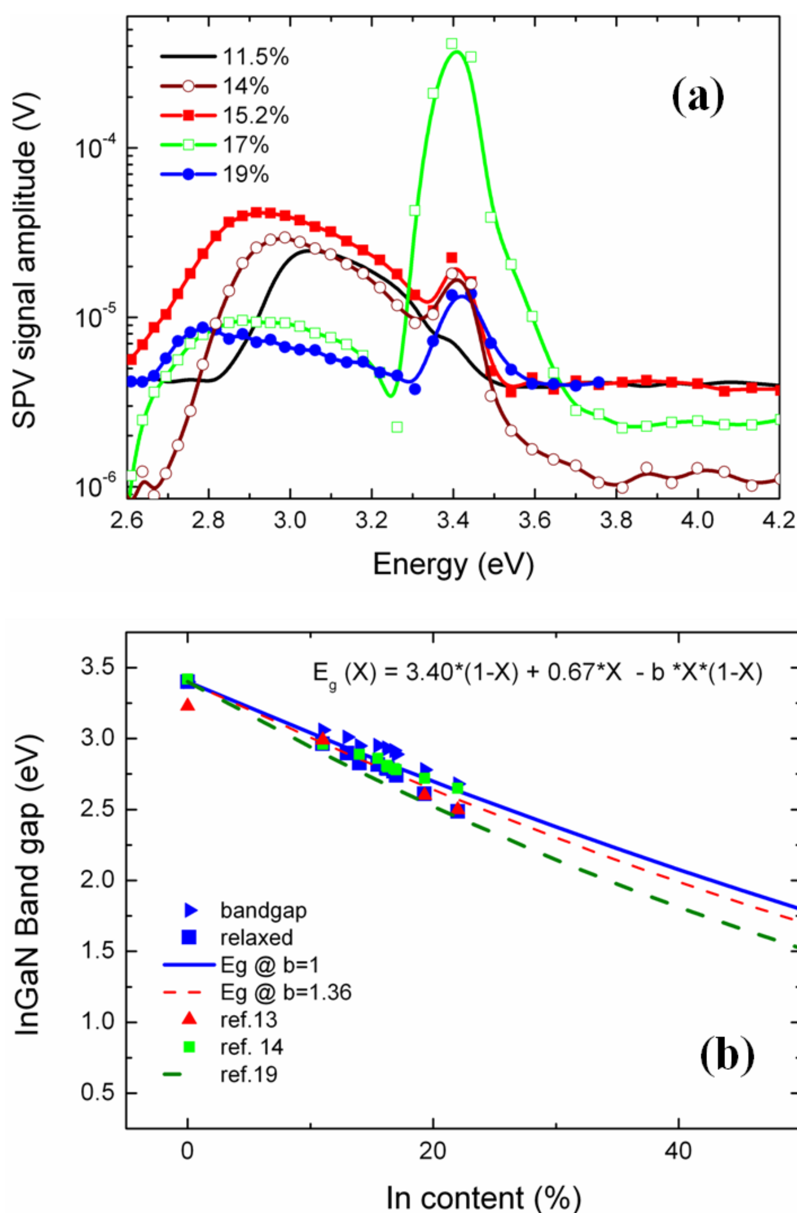

Figure 6.8 SPV spectra of some samples (a) Calculation of bowing parameter for $In_xGa_{1-x}N$ layers (%In up to 22) with experimental results (solid squares), calculated results (solid circles) and comparison with earlier reported results (solid triangle, open circles) in references. The line shows the fit for linear region (up to 20% In) (b)

Fig. 6.9a shows the Surface Photovoltage spectra for the Si doped samples. The measured SPV signal amplitude (always larger than 10 μV, which indicates the good quality of InGaN layers) has been normalized to the photon flux. The measured signal is always negative, which indicates the n-type of doping/conductivity in material. Peaks relevant to GaN can be observed at 3.43 eV for all samples. Peaks related to InGaN are observed at different positions at 2.98, 2.79, 2.67 eV due to different %In in barrier layer of InGaN (shown by arrow). It can be observed that after band to band transitions related to InGaN SPV signal decreases and then increases again and gets almost constant for samples with 14% and 19% In while for sample with 22% In, we can't distinguish such feature from spectra as the curve is also much broader.

For photon energies below the InGaN band to band transitions, slope changes can be noted in each spectra. By comparing SPV spectra of undoped and doped structures with comparable In% (fig9b) we can argue that these transitions are related to the Si donor levels. The Si activation energies can thus be obtained by the SPV spectra as

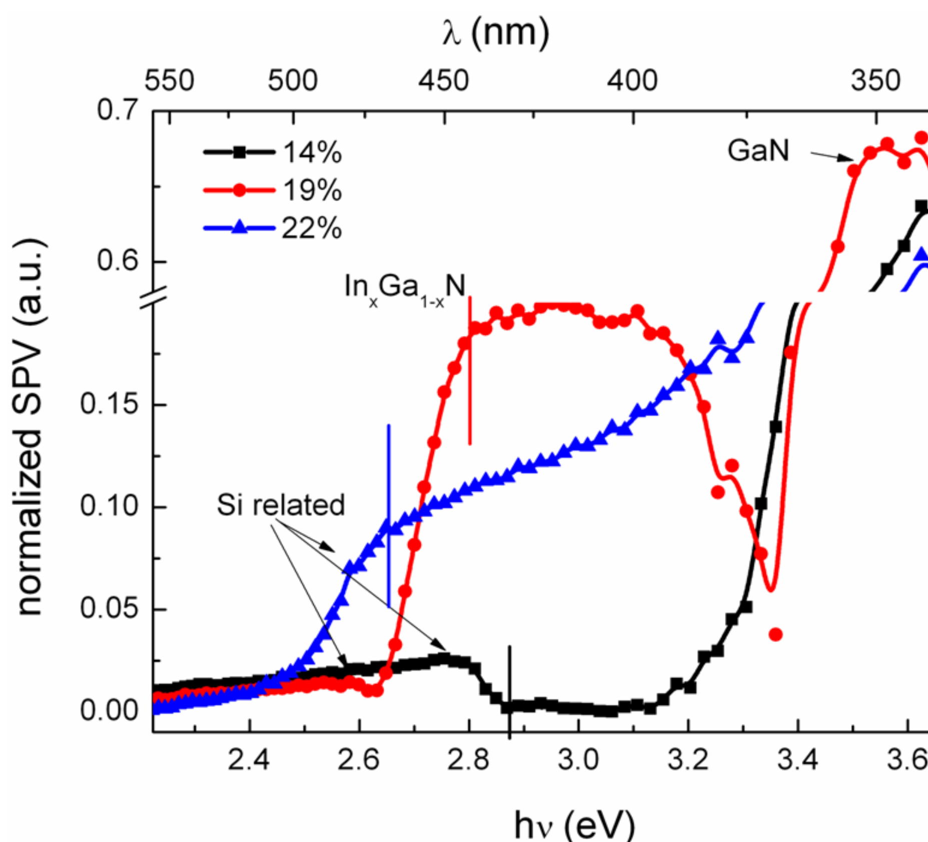

Figure 6.9a Normalized SPV spectra with photonflux showing against photon energy for all samples. GaN, InGaN band to band and Si donor related transitions are indicated in the spectra

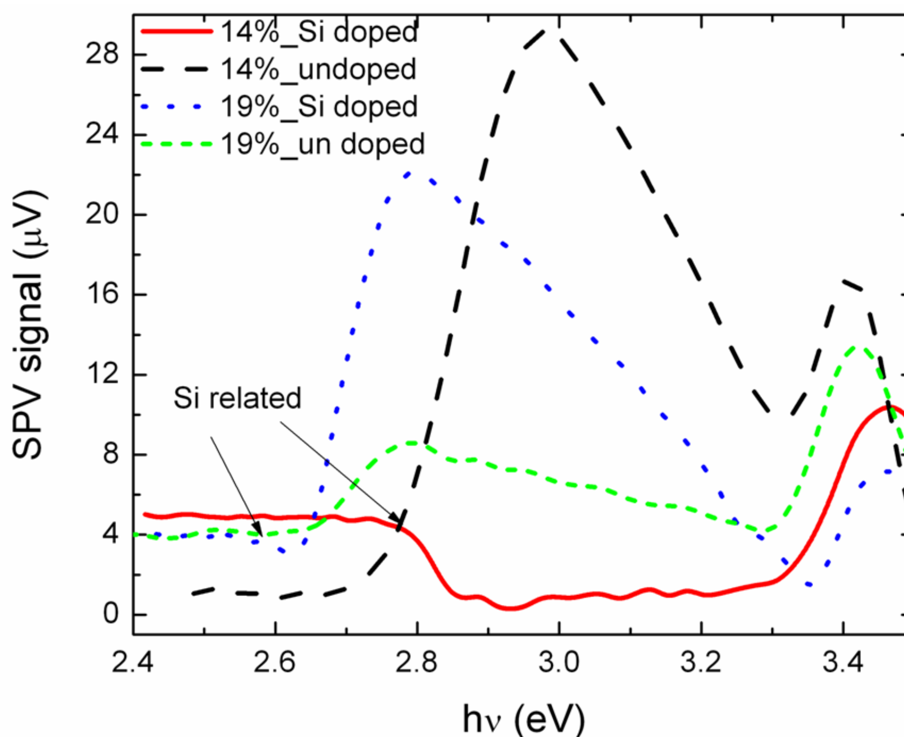

Figure 6.9b Comparison of the Surface Photovoltage (SPV) spectra of Si doped and undoped structures for 14% and 19% In in InGaN barrier layer

In order to understand the role of Si doping on band structure, 1-D Schrodinger-Poisson simulations were performed on doped and undoped [3]. From our simulation in Fig. 6.10a, we observe the existence of accumulation of hole (2DHG) at InGaN/GaN interface, as also reported by Chen et al. [21]. Meanwhile, we also observe the change in InGaN band structure with variation in %In in barrier layer of InGaN. On further simulation of Si-doped InGaN structures as shown in Fig. 10b, we interestingly observe the role of Si-doping on InGaN band structure and on heterointerface as well which is not reported yet to our knowledge. It is observed that on increment in doping density in barrier layer the conduction band minima crosses the Fermi level, thus a large free carrier concentration and an almost degenerate behavior should be expected in such a layer.

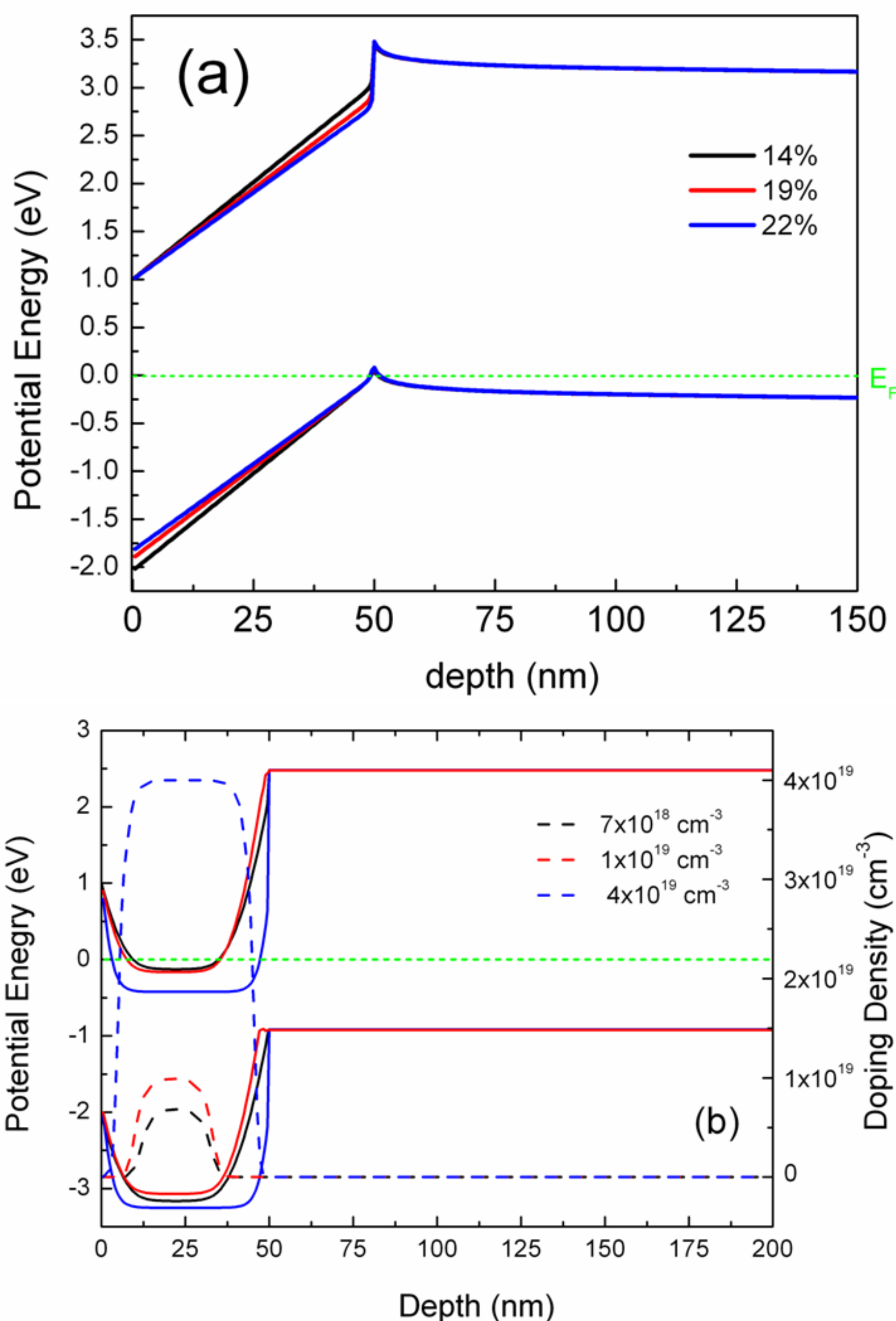

Figure 6.10 1-D Schrodinger-Pöisson simulation shows conduction and valence band profile of InGaN/GaN undoped structures (a) and Si-doped structures (b). The straight line (short dashed) drawn at 0 is just to show Fermi level of heterostructure for eye guide line

The InGaN band to band transitions energies and the Thus we confirm the transitions at lower energy values to band gap of InGaN as Si deep donor related transitions and their energy levels are shown in fig. 6.11 which shows that on increment in doping density and In% concentration position of deep donors in conduction decreases. It also confirms that these donor levels are the main cause for high carrier concentration in InGaN. Variation of doping density with increase in %In has also been shown in inset of fig. 6.11a which has also been discussed in fig. 6.10b from simulation. Moreover we have also shown the variation of bandgap of InGaN variation with increase in %In which is in good agreement with earlier reported results on undoped and doped structures [12, 18]. Recently, Pantha et al. [22] reported that the origin of background concentration

in undoped InGaN layers due to presence of shallow and deep donor levels and confirm that on increment of %In in barrier layer increases the carrier concentration due to variation in position of donor levels and their activation energy.

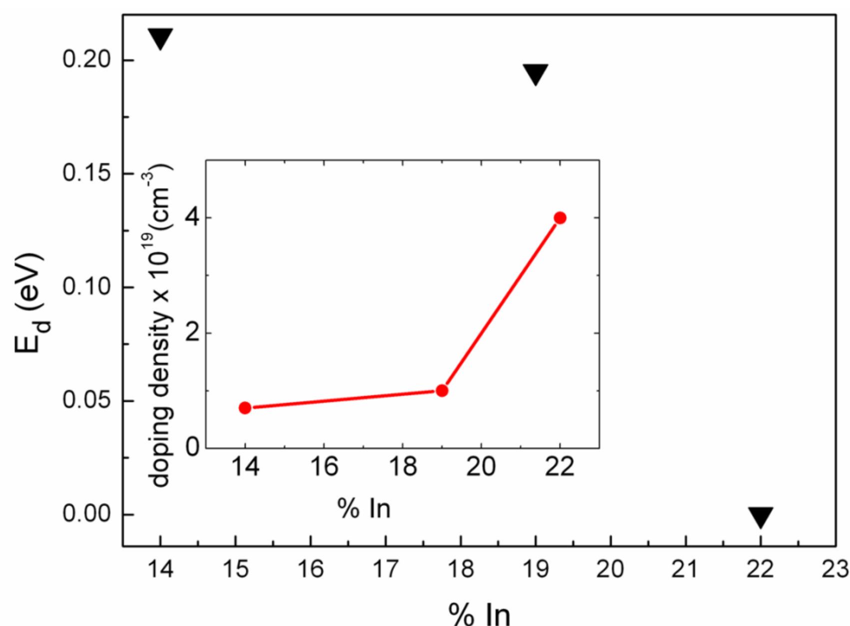

Figure 6.11 Variation of deep donor levels (solid triangle) in conduction band of InGaN with %In is shown and variation of doping density (solid circle) is also shown in inset

In conclusion, we have observed good intensity in SPV signal for undoped and doped InGaN layers which allows us to calculate the band bowing parameter which is calculated and found ~ 1eV. In calculation of bowing parameter, we have considered both cases of strain and relaxed structures of InGaN layers. For, Si doped structures we suggest that in Si doped structures, doping density has been found increasing on increasing in %In which affects the energy band diagram of heterostructure. The identification of Si donor levels has been confirmed and found responsible for high carrier concentration by comparing the results with undoped structures, and variation in their position in conduction band has been observed which is not reported yet up to our knowledge.

6.5 Mesa-InGaN/GaN based Photodetector structure

A heterojunction structure based photodetector has been fabricated by evaporating a semitransparent Pt metal film on the InGaN/GaN structure. The photocurrent (PC) spectra show that both the Schottky junction (Pt/InGaN) and the InGaN/GaN iso-type heterojunction (which will be called as surface and heterojunction respectively during further discussion) contribute to the PC signal which suggests that two junctions are connected in series and result in a broader spectral response of the device. A band diagram of the device is drawn based on the consideration of the polarization effect at the InGaN/GaN interface. The analysis is consistent with the physical mechanism of a tandem structure of two junctions connected in series.

The sample with 45 nm thick InGaN layer with Indium content of 11.5% on thick and relaxed 3 μm GaN layer template on the sapphire (0001) substrate has been considered for this study [1]. The carrier concentration in InGaN layer is assumed to be very low (of the order of 10^{15} cm^{-3}) similar like structure studied for DLTS analysis, discussed above in this chapter. A 5/10 nm

thick metal Pt film was directly deposited on the surface of the InGaN layer and then annealed at 500^0C in atmosphere environment for 5 min to form a semitransparent Schottky contact. After that a mesa structure with an electrode area of 4 mm^2 is formed, Ti/Al/Ti/Au (15/250/50/150 nm) is deposited on the GaN layer using electron beam evaporation to form a contact electrode as an Ohmic contact and annealed at 800^0C for 30 s in N_2 ambient. The device structure of the Pt/InGaN/GaN structure used in this study is shown schematically in fig. 6.12a. Fig. 6.12b shows the room-temperature *I–V* curve measured by a Agilent semiconductor parameter analyzer 4156C with the positive electrode of the electric source connected to the metal contact upon the InGaN layer. The result shows that the diode has an apparently rectifying current characteristic.

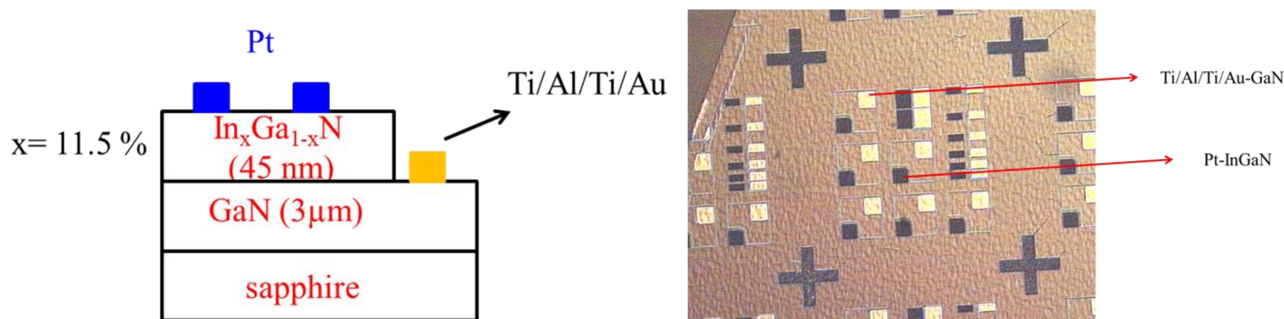

Figure 6.12a Optical microscope image of mesa structure of InGaN/GaN based photodetector structure. 'Pt' metal Schottky-InGaN, is shown in gold color while black shades show the Ti/Al/Ni/Au metal stack on GaN, as Ohmic contacts

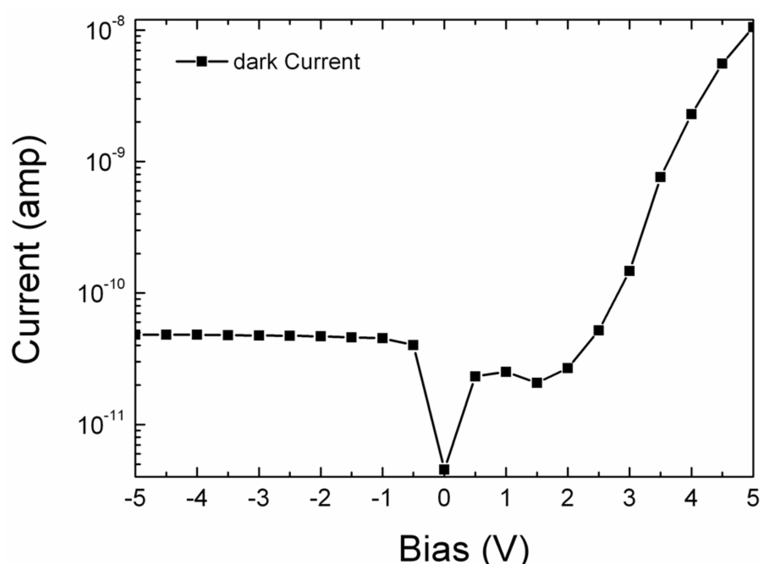

Figure 6.12b The Current-voltage characteristics of device at InGaN-GaN heterojunction

The PC spectra of the device are shown in figure 6.13(*a*) which are measured at room temperature with a zero bias by a Keithley 6430 sourcemeter, using a Xe lamp and a monochromator as a dispersed light source illuminating the front side of the device on InGaN surface (solid line) and the heterojunction of InGaN/GaN device (dashed line). The ac photovoltage signal is obtained by lock-in amplifier at 300 K. The photoresponse of the front-side illuminated PC spectrum of surface and heterojunction (shown in figure 6.13(*a*)) consists of two parts apparently.

The signal between 3.3 and 3.6 eV comes mainly from the GaN layer, which shows a peak appearance at 3.43 eV related to GaN gap (and partly from the InGaN layer) while between 2.6 and about 3.3 eV the main signal comes from the InGaN layer if the photocurrent is mainly induced by the intrinsic optical excitation of the incident light, i.e. by electronic interband transitions. The photon energy of the rising edge of these two parts of optical spectra corresponds to the band gap of GaN and InGaN at 3.43 eV and 3.12 eV, respectively. The slope of the PC curve at about 3 to 3.2 is similar steep as at 3.43 nm, indicating that the no alloy composition fluctuations and then the related band gap are relatively homogeneous in the InGaN layer. Actually, in the SPV spectra of the structure (shown above) there are two peaks of near bandedge transitions from the GaN layer at about 3.43 eV nm and the $In_{0.115}Ga_{0.885}N$ layer at about 3.05 eV, respectively, in quite good agreement with the energy gaps determined by the PC spectra. However, at 2.76 eV another peak is observed in PC spectra below InGaN gap which can be related to defect related absorption. The external quantum efficiency (%EQE) shown in figure 6.13(*b*) is calculated from the photovoltage signal which is normalized by a calibrated Si photodetector. Thus, it can be observed that EQE is quite high in case of surface based device than heterojunction and shows the maximum efficiency at InGaN-GaN interface (marked as dash) than InGaN surface (marked as dot), probably due to charge accumulation at interface.

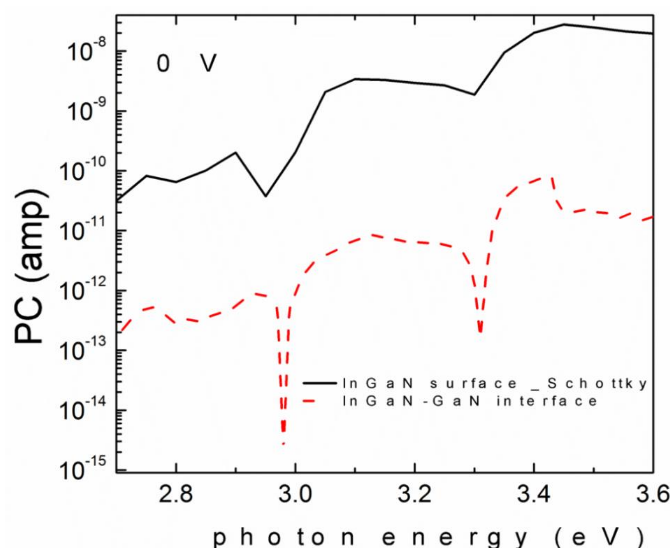

Figure 6.13a Photocurrent spectra for Pt-InGaN surface (solid) and InGaN-GaN heterojunction (dashed) without any bias

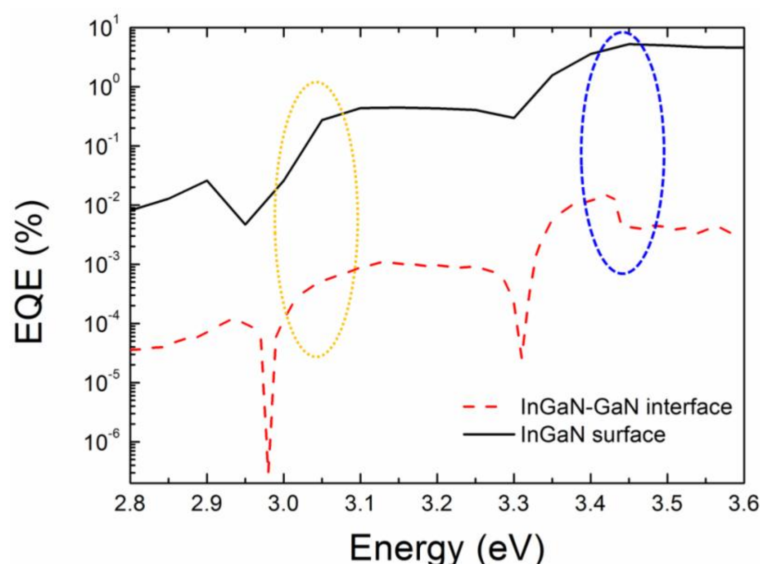

Figure 6.13b The EQE for device at Pt-InGaN surface (solid) and InGaN-GaN heterojunction (dashed), showing high efficiency at interface of InGaN-GaN

Thus, the studies show that the EQE is much higher at interface in case of Pt-InGaN based device than heterojunction based device, which gives very strong indication towards development of tendem based solar cells with further improvement in crystalline quality and optimization of high carrier density structure. A similar study was reported by Sun et al. [23] and our results are in good agreement with it.

Moreover, a high bias PC spectrum is also recorded at -5 V, shown as Fig. 6.14 to see the photoresponse. It can be observed that response from InGaN slope is not as steep as GaN which shows the effect of depletion at high bias and results more response from GaN bulk. In order to confirm the origin of defect related absorption at 2.76 eV, whether defect is present in InGaN layer or from GaN bulk, high bias PC spectra is significant and it can be observed that in case of heterojunction based device defect related transition is steeper than surface based device which indicates the presence of defect level in GaN layer rather than InGaN layer [24].

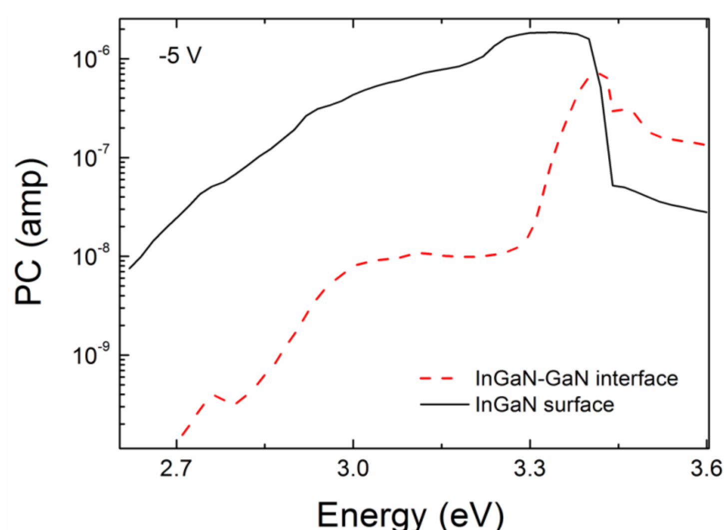

Figure 6.14 PC spectra of Pt-InGaN surface and InGaN-GaN heterojunction at -5 V

In summary, we have successfully fabricated the two junction based devices at InGaN/GaN based heterostructure. Pt-InGaN based devices shows the higher % EQE at interface than heterojuncion based device, probably due to high number of carriers at InGaN-GaN interface and also due to mixed response from surface and interface both. The defect related absorption is also observed and attributed to defect in GaN layer, possibly responsible to blue emission. Our studies gives very strong indication towards development of tendem based solar cells with further improvement in crystalline quality and optimization of high carrier density structure.

References

1. O¨. Tuna, W.M.Linhart , E.V.Lutsenko, M.V.Rzheutski, G.P.Yablonskii, T.D.Veal, C.F. McConville, C.Giesen, H.Kalisch, A.Vescan , M.Heuken, J. Crys. Growth 358, 51 (2012)
2. C. Mauder, Ö. Tuna, B. Gutrath, V. Balmes, H. Behmenburg, M. V. Rzheutskii, E. V. Lutsenko, G. P. Yablonskii, M. Noyong, U. Simon, M. Heuken, H. Kalisch, A. Vescan, Phys. Stati. Solidi C, 9, 964 (2011)
3. http://www.nd.edu/~gsnider/
4. http://www.nextnano.de/nextnano3/tutorial/1Dtutorial_SchroedingerPoisson.htm
5. O. Ambacher, J Majewski, C Miskys, A Link, M Hermann, M Eickhoff, M Stutzmann, F Bernardini, V Fiorentini, V Tilak, B Schaff and L F Eastman, J. Phys.: Condens. Matter 14 3399 (2002)
6. D. J. Chen, J. J. Xue, B. Liu, H. Lu, Z. L. Xie, P. Han, R. Zhang, Y. D. Zheng, Y. C. Kong, and J. J. Zhou, Appl. Phys. Lett. 95, 012112 (2009)
7. N. M. Johnson, A. V. Nurmikko, S. P. DenBaars, Phys. Today 53, 31 (2000)
8. S. Nakamura, J. Vac. Sci. Technol. A 13, 705 (1995)
9. I. Akasaki, S. Sota, H. Sakai, T. Tanaka, M. Koike, H. Amano, Electron. Lett. 32, 1105 (1996)
10. S. Nakamura, M. Senoh, S. Nagahama, N. Iwasa, T. Yamada, T. Matsushita, Y. Sugimoto, H. Kiyoku, Appl. Phys. Lett. 70, 1417 (1997)
11. M. D. McCluskey, C. G. Van de Walle, L. T. Romano, B. S. Krusor, N. M. Johnson, J. Appl. Phys. 93, 4340 (2003)
12. M. D. McCluskey, C. G. Van deWalle, C. P. Master, L. T. Romano, N. M. Johnson, Appl. Phys. Lett. 72, 2725 (1998)
13. P. G. Moses, C. G. Van de Walle, Appl. Phys. Lett. 96, 021908 (2010)
14. J. Wu, W. Walukiewicz, K. M. Yu, J. W. Ager III, E. E. Haller, H. Lu, W. J. Schaff, Appl. Phys. Lett. 80, 4741 (2002
15. D. Holec, P.M.F.J. Costa, M.J. Kappers, C.J Humphreys, J. Crystal Growth, 303, 314 (2007)
16. M. Leyer J.Stellmach, Ch.Meissner, M.Pristovsek, M.Kneissl, J. of Crystal Growth, 310 4913(2008)
17. W. Shan, B. D. Little, A. J. Fischer, J. J. Song, B. Goldenberg, W. G. Perry, M. D. Bremser, R. F. Davis, Phys. Rev. B 54, 16369 (1996)
18. J. Wu, W. Walukiewicz, W. Shan, K. M. Yu, J. W. Ager III, S. X. Li, E. E. Haller, H. Lu, W. J. Schaff, J. Appl. Phys. 94, 4457 (2003)
19. I. Gorczyca, T. Suski, N. E. Christensen, and A. Svane Phys. Rev. B 83, 153301 (2011)
20. J. Wu, W. Walukiewicz, K. M. Yu, J. W. Ager III, E. E. Haller, H. Lu, W. J. Schaff, Appl. Phys. Lett. 80, 4741 (2002)

21. D. J. Chen, J. J. Xue, B. Liu, H. Lu, Z. L. Xie, P. Han, R. Zhang, Y. D. Zheng, Y. C. Kong, J. J. Zhou, Appl. Phys. Lett. 95, 012112 (2009)
22. B. N. Pantha, H. Wang, N. Khan, J. Y. Lin, H. X. Jiang, Phys. Rev. B 84, 075327 (2011)
23. X Sun, W B Liu, D S Jiang, Z S Liu, S Zhang, L L Wang, H Wang, J J Zhu, L H Duan, Y T Wang, D G Zhao, S M Zhang and H Yang, J. Phys. D: Appl. Phys. 41, 165108 (2008)
24. L. Polenta, A. Castaldini, and A. Cavallini, J. App. Phys. 102, 063702 (2007)